Using Multi-omics To Study 2-Hydroxyglutarate (Patho)Biology

A thesis submitted to fulfil the requirements of the degree of Doctor of Philosophy

at The University of Sydney

Niv Vigder

THE UNIVERSITY OF SYDNEY

School of Life and Environmental Sciences

May 2026

Statement of originality

I hereby declare that this thesis is my own original work and that it has been written by me in its entirety. Except where explicitly stated otherwise, the work presented in this thesis has not been submitted for any other degree or professional qualification at this or any other institution.

All sources of information, data, figures, and ideas derived from the work of others have been appropriately acknowledged and referenced in accordance with academic standards. Where collaborative work has contributed to this thesis, my individual contributions are clearly identified.

I confirm that this thesis complies with the rules and regulations of the institution regarding academic integrity and originality.

Name: Niv Vigder

Date: February 9, 2026

Author attribution statement

Chapter 4 of this thesis contains a book chapter that has been published as [**Vigder, N.**, Cordwell, S. J., & Loscalzo, J. *Network medicine: A new paradigm for cardiovascular disease research and beyond*. In C. Banfi (Ed.), *Cardiovascular Proteomics Techniques* (Chap. 16). John Wiley & Sons (2026). https://doi.org/10.1002/9781394211166.ch16]. I conceptualized the chapter structure, developed the outline, and prepared all drafts. The results presented in Chapters 2 and 3 constitute the central body of work for a comprehensive manuscript currently in preparation for submission to *Nature Metabolism* or *Cell Metabolism*. With the exception of an Abstract presented at the 2024 American Heart Association Annual Meeting [**Vigder, N.**, He, H., Tumanov, S. *et al*. L-2-hydroxyglutarate Attenuates the Accumulation of Long Chain Acylcarnitines in Myocardial Ischemia. *Circulation* **150**, A4144377-A4144377 (2024)], these findings have not yet appeared as a primary research article, not due to insufficient data, but as a deliberate strategic decision to present the work as a single, integrated study linking 2HG metabolism with lipid metabolic reprogramming. This unified framework represents a novel and biologically significant discovery that we believe is best communicated as one cohesive publication rather than fragmented into smaller reports.

In addition to the work presented in this thesis, several publications have arisen from collaborative projects conducted during my PhD. These co-authored studies are not directly included in this thesis but reflect broader contributions to related research efforts:

1. Ziehr, D.R., Li, F., Parnell, K.M., Krah, N.M., Leahy, K.J., Guillermier, C., Gao, C., Prell, S.A., **Vigder, N.**, Poli, S., Varon, J., Baron, R.M., Maron, B.A., Philp, N.J., Hariri, L.P., Kim, E.Y., Wei, K.S., Steinhauser, M.L., Knipe, R.S., Rutter, J., and Oldham, W.M. Lactate transport inhibition therapeutically reprograms fibroblast metabolism in experimental pulmonary fibrosis. *Science Translational Medicine* (2026). [In Press] (PDF available upon request)
2. Li, F., **Vigder, N.**, Ziehr, D.R., Kamiya, M., Nguyen, H.N., Steinhauser, M.L., Kim, E.Y., and Oldham, W.M. TGF-β Coordinates Alanine Synthesis and Import for Myofibroblast Differentiation in Pulmonary Fibrosis. *bioRxiv* doi: 10.1101/2025.07.23.666333 (2025).
3. Deshmukh, T., Hume, R.D., Chen, S., Igoor, S., Foster, S.L., Barry, T., Lu, J., Tran, V., Pouliopoulos, J., Jabbour, A., **Vigder, N.**, Cordwell, S.J., Tumanov, S., Nguyen, C., Kotake, Y., Turnbull, S., Campbell, T., Pathan, F., Kumar, S., Kizana, E., and Chong, J.J.H. Platelet derived growth factor-AB modulates post-infarct myocardium leading to extended improvement in cardiac function. *npj Regenerative Medicine* **10**, 46 (2025).
4. Du, X., Wang, Y., Huang, J., **Vigder, N.**, Jin, T., Liu, Z., Hua, W., Li, W., and Li, F. Targeting glutamine catabolism suppresses eosinophil expansion and activation to alleviate allergic airway inflammation. *Biochemical Pharmacology* **242**, 117443 (2025).

5. Xiao, W., Shrimali, N., **Vigder, N.**, Oldham, W.M., Clish, C.B., He, H., Wong, S.J., Wertheim, B.M., Arons, E., Haigis, M.C., Leopold, J.A., and Loscalzo, J. Branched-chain α-ketoacids aerobically activate HIF1α signalling in vascular cells. *Nature Metabolism* **6**, 2138–2156 (2024).
6. Koay, Y.C., Liu, R.P., McIntosh, B., **Vigder, N.**, Lauren, S., Bai, A.Y., Tomita, S., Li, D., Harney, D., Hunter, B., Zhang, Y., Yang, J., Bannon, P., Philp, A., Philp, A., Kaye, D.M., Larance, M., Lal, S., and O'Sullivan, J.F. The Efficacy of Risk Factor Modification Compared to NAD^+ Repletion in Diastolic Heart Failure. *JACC: Basic to Translational Science* **9**, 733–750 (2024).

Three additional manuscripts to which I contributed LC–MS/MS-based multi-omics analyses are currently in preparation and have not yet been submitted for publication. These projects are led by Assoc. Prof. Matthew Steinhauser (University of Pittsburgh, PA, USA) on clinical human plasma metabolomics during fasting, Assoc. Prof. William Oldham (Brown University, RI, USA) on metabolomics profiling of cells exposed to hypoxia-inducible factor inhibitors and genetic manipulations, and Dr. Aaron Hakim (Harvard Medical School, MA, USA) on the characterization of a novel gene involved in lipid droplet homeostasis.

In addition to the authorship attribution statements above, in cases where I am not the corresponding author of a published item, permission to include the published material has been granted by the corresponding author.

Niv Vigder (February 24, 2026)

As supervisor for the candidature upon which this thesis is based, I can confirm that the authorship attribution statements above are correct.

Stuart Cordwell (February 24, 2026)

Artificial intelligence

During the preparation of this thesis, I used NotebookLM, Claude AI, and ChatGPT for minor supplementary purposes. NotebookLM was used to generate an initial graphical abstract, which was subsequently reviewed and substantially amended by the author using PowerPoint. Claude AI was used to expand a list of abbreviations that I identified into their complete names, which were subsequently reviewed and verified for accuracy and completeness. ChatGPT was used to address general writing convention queries during thesis preparation, including punctuation style questions such as the use of en dashes *vs.* hyphens; no text was directly generated by this tool for inclusion in the thesis. The author confirms that all generative AI output was reviewed for possible errors, inaccuracies, and bias. I take full responsibility for the submitted thesis and confirm that the work is my own and in accordance with University of Sydney guidelines and policies.

Australian Government Support

This research was supported by an Australian Government Research Training Program (RTP) offset scholarship.

Table of contents

Acknowledgements

I would like to express my deepest gratitude to my parents and family for their unwavering support, encouragement, and belief in me throughout this journey and beyond. Their constant guidance and sacrifices made this work possible, and I am profoundly thankful for their presence in my life.

I am sincerely grateful to my PhD supervisors and mentors, Prof. Joseph Loscalzo and Prof. Stuart Cordwell, for their exceptional guidance, scientific insight, and support throughout my doctoral training. This PhD began in Sydney in 2023 under the supervision of Prof. Cordwell. In 2024, I relocated to Boston, where I continued and expanded this work under the supervision of Prof. Loscalzo at Brigham and Women's Hospital and Harvard Medical School. This period marked a profound personal and professional transformation, as the relocation reshaped my life entirely and established Boston as my new home.

I would also like to acknowledge Prof. Roland Stocker, whose mentorship prior to and during my PhD played a pivotal role in my scientific formation. His emphasis on rigor, attention to detail, and critical thinking laid the foundation for the work presented in this thesis and continues to influence my approach to scientific inquiry.

I am thankful to my colleagues and collaborators in the Loscalzo Laboratory in Boston and the Cordwell Laboratory in Sydney for creating intellectually stimulating, collaborative, and supportive research environments. Their discussions, feedback, and camaraderie greatly enriched my PhD experience.

I gratefully acknowledge the support of the 2022 Cardiovascular Postgraduate Scholarship, funded by Sydney Research, Sydney Local Health District, and The University of Sydney, which supported this doctoral work.

Finally, I am grateful to everyone who contributed, directly or indirectly, to this journey. The experiences, challenges, and growth throughout this process have shaped who I am as a scientist and as a person.

Abstract

The term 2-hydroxyglutarate (2HG) is often used broadly in the biomedical literature, yet it overlooks a key biochemical nuance: chirality. 2HG exists as two enantiomers, (*R*)- and (*S*)-2HG (D2HG and L2HG, respectively), which are structurally identical except for the configuration around the chiral hydroxyl-bearing carbon at the C2 position. This enantioselectivity is biologically consequential as the two forms arise from distinct metabolic pathways engaged under different physiological and pathological stresses. Seminal work from our laboratory and beyond established that L2HG accumulates robustly under conditions of hypoxia, acidosis, and myocardial ischemia as a consequence of enzyme promiscuity within central carbon metabolism, reframing L2HG from a metabolic byproduct to a context-dependent signaling metabolite. This thesis begins with an introduction (Chapter 1) tracing the evolution of 2HG research from its early chemical characterization to its recognition as a signaling metabolite, and summarizing current understanding of stereoselective metabolism and mitochondrial clearance, as well as mechanistic paradigms through which 2HG influences cellular function, including inhibition of α-ketoglutarate (αKG)–dependent dioxygenases and protein interactions. Building on this conceptual framework, the experimental chapters examine how L2HG accumulation interfaces with lipid metabolism. The first results chapter (Chapter 2) investigates the relationship between L2HG and triglyceride / fatty acid metabolism and demonstrates that conditions promoting L2HG accumulation are accompanied by coordinated remodeling of neutral lipid pools, consistent with altered fatty acid handling and energy storage pathways. The second results chapter (Chapter 3) focuses on phosphatidylethanolamine metabolism, implicating L2HG in regulation of glycerophospholipids. The final results chapter (Chapter 4) moves beyond reductionist analysis by applying a holistic, network medicine–based framework to integrate proteomics data, leading to the identification of major vault protein (MVP), the principal structural component of vault nanoparticles, as a previously unrecognized molecular target of L2HG-associated metabolic stress. Finally, this thesis concludes with Chapter 5 aimed at integrating the L2HG-mediated phenotypic alterations identified herein, highlighting the interplay between unbiased and hypothesis-driven approaches and examining how apparent stereoselective effects may also reflect concentration-dependent, biphasic responses. Collectively, this thesis defines a connection between stereospecific L2HG metabolism and lipid and protein remodeling and establishes an integrated framework for understanding how L2HG functions as a context-dependent metabolic signal in (patho)biology.

Graphical abstract

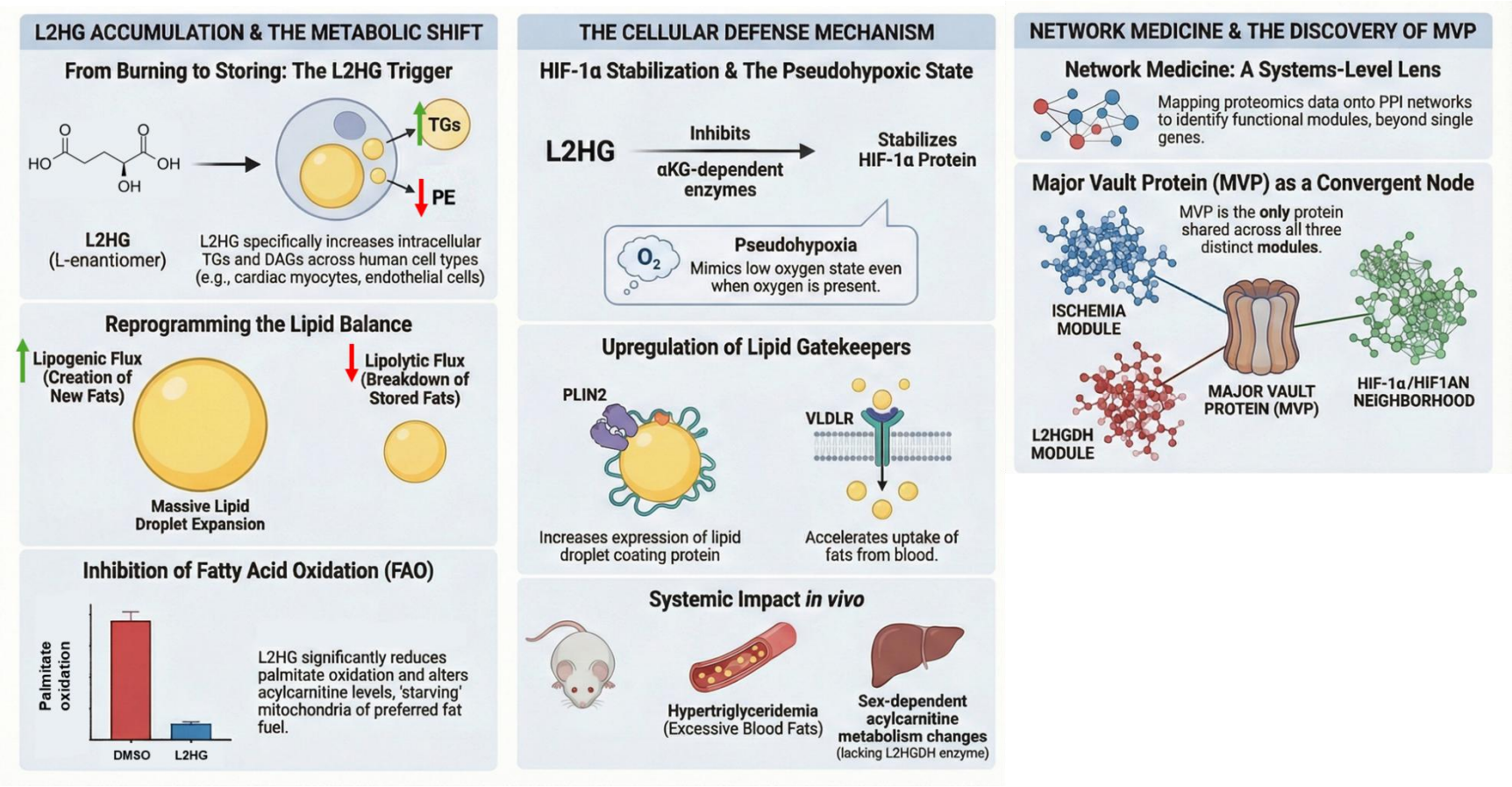

List of Figures

Chapter 1

Chapter 2

Chapter 3

Chapter 4

List of Tables

List of Supplementary Data

Chapter 2

Supplementary Data S2.1. Lipidomics dataset of HCMs treated with OL2HG.

Supplementary Data S2.2. RNA-seq dataset of HCMs treated with OL2HG.

Supplementary Data S2.3. RNA-seq dataset of PAECs treated with OL2HG.

Supplementary Data S2.4. Proteomics dataset of HCMs treated with OL2HG.

Supplementary Data S2.5. Metabolomics dataset of plasma from baseline *L2hgdh*$^{+/+}$ and *L2hgdh*$^{-/-}$ mice.

Chapter 4

Supplementary Data S4.1. Proteomics dataset of hearts obtained from male *L2hgdh*$^{+/+}$ and *L2hgdh*$^{-/-}$ mice following baseline and ischemic conditions.

Abbreviations

Note: Gene symbols are presented according to species-specific conventions: human genes are italicized and written in all capital letters (*e.g.*, *L2HGDH*), whereas murine genes are italicized with only the initial letter capitalized (*e.g.*, *L2hgdh*). Protein abbreviations are not italicized (*e.g.*, *HIF1A* gene and HIF-1α protein).

(+)-*O*,*O*′-Diacetyl-L-tartaric anhydride (DATAN); 1-acylglycerol-3-phosphate acyltransferase (AGPAT); 2-hydroxyglutarate (2HG); 2-hydroxyglutarate aciduria (2HGA); 2-hydroxyglutarate dehydrogenase (2HGDH); 4′,6-diamidino-2-phenylindole (DAPI); adipose triglyceride lipase (ATGL); alpha-ketoglutarate (αKG); analysis of covariance (ANCOVA); analysis of variance (ANOVA); area under the curve (AUC); automatic gain control (AGC); basic pH reversed-phase (BPRP); bone marrow–derived macrophage (BMDM); bovine serum albumin (BSA); carnitine palmitoyltransferase 1 (CPT1); carnitine palmitoyltransferase 2 (CPT2); carnitine–acylcarnitine translocase (CACT); choline (Chol); cholesteryl ester (CE); circularly permuted yellow fluorescent protein (cpYFP); cytidine 5′-diphosphate-choline (CDP-Chol); cytidine 5′-diphosphate-ethanolamine (CDP-Etn); CTP:phosphoethanolamine cytidylyltransferase (PCYT2); D-2-hydroxyglutarate (D2HG); diacylglycerol (DAG); diacylglycerol acyltransferase (DGAT); diacylglycerol *O*-acyltransferase 1 (DGAT1); diacylglycerol *O*-acyltransferase 2 (DGAT2); diacylglycerol *O*-acyltransferase inhibitor (DGATi); dihydroxyacetone phosphate (DHAP); dihydroxyacetone phosphate acyltransferase (DHAPAT); dimethyl sulfoxide (DMSO); disintegration per minute (DPM); dulbecco's modified Eagle medium (DMEM); dulbecco's phosphate-buffered saline (DPBS); electron transport chain (ETC); endoplasmic reticulum (ER); enzymatic assay-based L-2-hydroxyglutarate-sensing fluorescence reporter (EaLHGFR); ethanolamine (Etn); ethanolamine kinase (ETNK); ethanolamine phosphotransferase 1 (EPT1); fatty acid oxidation (FAO); false discovery rate (FDR); fetal bovine serum (FBS); field asymmetric waveform ion mobility spectrometry (FAIMS); fluorescence resonance energy transfer (FRET); glycerol-3-phosphate (G3P); glycerol-3-phosphate acyltransferase (GPAT); glycerophosphocholine (glycero-PChol); glycerophosphoethanolamine (glycero-PEtn); heated electrospray ionization (HESI); higher energy collisional dissociation (HCD); hormone-sensitive lipase (HSL); human cardiac myocyte (HCM); human embryonic kidney 293FT cell (HEK293FT); human metabolome database (HMDB); hydrophilic interaction liquid chromatography (HILIC); hypoxia-inducible factor 1 alpha (HIF-1α); hypoxia-inducible factor 1-alpha inhibitor (HIF1AN); ion mobility spectrometry (IMS); ischemia–reperfusion (I/R); isocitrate dehydrogenase (IDH); L-2-hydroxyglutarate (L2HG); L-2-hydroxyglutarate dehydrogenase (L2HGDH); L-2-hydroxyglutarate dehydrogenase knock-out (*L2hgdh*$^{-/-}$); L-2-hydroxyglutarate dehydrogenase wild-type (*L2hgdh*$^{+/+}$); L-2-hydroxyglutarate-sensing fluorescent reporter (LHGFR); lactate dehydrogenase A (LDHA); lipid droplet (LD); lipin (LPIN); liquid chromatography–mass spectrometry (LC–MS); liquid chromatography–tandem mass spectrometry (LC–MS/MS); low-flow ischemia (LFI); lysophosphatidic acid (LPA); lysosomal acid lipase (LAL); macrophage colony-stimulating factor (M-CSF); major vault protein (MVP); malate dehydrogenase (MDH); matrix-assisted laser desorption/ionization (MALDI); mean fluorescence intensity (MFI); microvascular endothelial cell (MVEC); monoacylglycerol (MAG); monoacylglycerol acyltransferase (MGAT); monoacylglycerol lipase (MGL); monomeric teal fluorescent protein (mTFP); myocardial infarction (MI); *N*-acylethanolamine-hydrolyzing acid amidase (NAAA); *N*-(p-toluenesulfonyl)-L-phenylalanyl chloride (TSPC); nicotinamide adenine dinucleotide (NAD^+); nicotinamide adenine dinucleotide phosphate ($NADP^+$); nicotinamide adenine dinucleotide

phosphate, reduced form (NADPH); nicotinamide adenine dinucleotide, reduced form (NADH); nuclear cap-binding protein subunit 1 (NCBP1); octyl-2-hydroxyglutarate (O2HG); octyl-D-2-hydroxyglutarate (OD2HG); octyl-L-2-hydroxyglutarate (OL2HG); octyl-α-ketoglutarate (OαKG); pentose phosphate pathway (PPP); perilipin (PLIN); peptide-spectrum match (PSM); phosphatidic acid (PA); phosphatidic acid phosphatase (PAP); phosphatidylcholine (PC); phosphatidylethanolamine (PE); phosphatidylglycerol (PG); phosphatidylinositol (PI); phosphatidylserine (PS); phosphocholine (PChol); phosphoethanolamine (PEtn); post-translational modification (PTM); principal component analysis (PCA); protein mono-ADP-ribosyltransferase (PARP4); protein–protein interaction (PPI); seed connector algorithm (SCA); selenoprotein I (SELENOI); small interfering RNA (siRNA); solute carrier family 1 member 1 (SLC1A1); solute carrier family 25 member 1 (SLC25A1); standard error of the mean (SEM); sterol regulatory element-binding protein 1 (SREBP1); tandem mass spectrometry (MS/MS); tandem mass tag (TMT); tandem mass tag pro 16-plex (TMTpro); telomerase protein component 1 (TEP1); transcript per million (TPM); triglyceride (TG); tricarboxylic acid cycle (TCA); ultra-high-performance liquid chromatography (UHPLC); very low-density lipoprotein (VLDL); very low-density lipoprotein receptor (VLDLR).

Chapter 1

Introduction to 2-Hydroxyglutarate Research and (Patho)Biology

1.1 Historical perspective of 2HG research

In 1868, the German biochemist Ritthausen first reported the formation of a compound with the empirical formula $C_5H_8O_5$ generated by the reaction of glutamic acid with nitrous acid, a chemical observation describing a glutamate-derived hydroxy-dicarboxylic acid, which he termed "glutansäure" (glutanic acid) and which was later recognized as 2-hydroxyglutarate (2HG)[1]. Four years later, in 1872, Ritthausen further demonstrated that this glutamate-derived acid is optically active, showing left-handed rotation of plane-polarized light, thereby establishing that the compound is chiral[2].

Early descriptions of 2HG metabolism date back to the early 20th century. In 1920, Thunberg demonstrated that 2HG reduced methylene blue in water-washed frog muscle, leading him to classify the molecule as a substrate of "intermediary metabolism", defined at the time as the set of reactions linking nutrients to the end products carbon dioxide and water[3]. In the same study, Thunberg illustrated the presence of enzymes, which he termed "hydrogentransportases" or "dehydrogenases", that can transfer a hydrogen from a donor (*e.g.,* 2HG) to an acceptor (*e.g.*, O_2). He further proposed that these enzymes exhibit substrate specificity, supported by his observation that L-, but not D-, tartaric acid functioned as a hydrogen donor under defined experimental conditions.

In 1923, Wishart reported that 2HG enhanced the reduction of methylene blue by extracts from ox and rabbit muscle and rabbit liver, although less effectively than succinic acid[4]. However, it was not until 1937 that Weil-Malherbe provided unambiguous evidence that L2HG and D2HG have distinct metabolic effects[5]. Specifically, L2HG markedly increased the respiratory rate and respiratory quotient in several rat tissues – most prominently the heart and kidney, but not the spleen or intestine – whereas D2HG failed to alter respiration in rat brain and kidney slices[5]. Consistent with Thunberg's earlier proposal of substrate-specific dehydrogenases, Weil-Malherbe was the first to report an animal dehydrogenase capable of reversibly metabolizing L2HG but not D2HG, although the coupling of this reaction to α-ketoglutarate (αKG) formation was not demonstrated experimentally. Notably, tissues from pig, rabbit, and rat exhibited marked differences in the activity of this enzyme, with the highest activity observed in heart, as assessed by the extent to which exogenous L2HG stimulated oxygen uptake during one-hour incubations. In contrast, the first evidence for a dehydrogenase capable of metabolizing D2HG emerged in

1961, when Tubbs and Greville proposed that a mitochondrial D-α-hydroxyacid dehydrogenase partially purified from rabbit kidney could act on D2HG, based on its activity toward the structurally related substrate D-malate, a four-carbon α-hydroxy dicarboxylic acid[6].

Despite early evidence for enzyme-mediated metabolism of both L2HG and D2HG, the specific enzymes responsible and their corresponding genes were identified only in the last three decades. In 2004, Achouri and colleagues, led by Emile Van Schaftingen, identified the mitochondrial, FAD–dependent D2HG dehydrogenase (D2HGDH), which catalyzes oxidation of D2HG to αKG, using tandem mass spectrometry (MS/MS) of partially purified rat liver preparations[7]. In parallel, the same group identified a distinct mitochondrial, FAD–dependent enzyme that selectively oxidizes L2HG to αKG in mammalian tissues and demonstrated that it is encoded by the *L2HGDH* gene located on chromosome 14q22.1[8].

1.2 2HG acidurias

2HG acidurias (2HGAs) constitute a group of rare inborn errors of metabolism characterized by pathological accumulation of 2HG in bodily fluids including urine and cerebrospinal fluid that predominantly affect neurological function at a young age[9]. The modern classification of 2HGAs emerged in 1980 with the independent description of two rare metabolic disorders characterized by enantiomer-specific accumulation of 2HG. In one report, Chalmers *et al.*[10] documented a disorder marked by elevated D2HG in a young Kenyan Asian male, whereas Duran *et al.*[11] described a separate condition distinguished by accumulation of the L2HG enantiomer in a young Moroccan male. These studies established D2HGA and L2HGA as biochemically and clinically distinct entities. The phenotypic spectrum was broadened two decades later when Muntau and colleagues identified three patients exhibiting concurrent elevation of both enantiomers, defining a third disorder termed combined DL2HGA[12].

Subsequent progress was driven by molecular genetic studies that identified the enzymes responsible for stereospecific 2HG oxidation, with *D2HGDH* and *L2HGDH* shown to encode the D2HG and L2HG dehydrogenases, respectively (see Section 1.1). Pathogenic variants in these genes were detected in a substantial proportion of affected individuals, accounting for most cases of L2HGA and a subset of D2HGA[13,14]. Notably, a significant fraction of D2HGA cases lacked mutations in *D2HGDH*[15], a discrepancy later resolved by the identification of gain-of-function

mutations in *IDH2* (isocitrate dehydrogenase 2) as an alternative genetic basis for pathological D2HG accumulation[16] (see Section 1.4). Combined DL2HGA was subsequently attributed to recessive mutations in solute carrier (SLC) family 25 member 1 (*SLC25A1*), which encodes the mitochondrial citrate transporter[17,18]. However, it remains unclear whether pathological accumulation of 2HG is mechanistically linked to impaired citrate transport *per se*, given that *SLC25A1* mutations may exert effects independent of citrate transport. Taken together, these discoveries transformed our understanding of genetic and biochemical heterogeneity underlying 2HGAs and provided a foundation for rational diagnostic approaches. For a more detailed review of 2HGA pathobiology, the reader is referred to Ref.[9].

1.3 L2HG production by enzyme promiscuity in hypoxia and myocardial ischemia

L2HG is an endogenous metabolite generated through non-canonical enzymatic reactions rather than a dedicated biosynthetic pathway. Under basal conditions, L2HG is present at low abundance – for example, reported at approximately 52.47 ± 4.97 μM in HEK293FT cells[19] – but its levels increase substantially under specific metabolic stresses. The prevailing view is that L2HG arises primarily from enzyme promiscuity (defined as the capacity of an enzyme to catalyze secondary, non-canonical reactions on alternative substrates[20]) within central carbon metabolism, reflecting altered substrate availability, redox state, and / or intracellular pH (**Fig. 1.1**).

In 2015, two independent studies reported that L2HG accumulates in mammalian cells during hypoxia. The first study, conducted by our group, demonstrated that hypoxia-mediated L2HG accumulation is driven by enhanced reductive conversion of αKG by cytosolic and mitochondrial malate dehydrogenase (MDH), with a secondary contribution from decreased L2HGDH–mediated clearance[21]. In the same study, hypoxia-driven accumulation of the reduced to oxidized nicotinamide adenine dinucleotide redox couple ($NADH/NAD^+$) was partially attributable to L2HG, as evidenced by potentiation of this increase in L2HGDH-deficient cells and its partial attenuation in cells overexpressing L2HGDH. Phenotypically, 2HG contributed to the generation of the mitochondrial potential under hypoxia, attenuated glycolytic flux and capacity, decreased basal and maximal mitochondrial oxygen consumption, and decreased mitochondrial oxidative stress[21] (**Fig. 1.1**). While some protective effects were specific to L2HG, others were reproduced

by D2HG, indicating the presence of shared mechanisms that are not strictly stereospecific[21]. In the second study, Intlekofer *et al.*[22] demonstrated that hypoxia-driven L2HG production is mediated primarily by promiscuous activity of lactate dehydrogenase A (LDHA). The authors used isotope tracing coupled to liquid chromatography tandem mass spectrometry (LC–MS/MS) to demonstrate that, under normoxic conditions, the relatively small total 2HG pool is derived predominantly from glutamine *via* glutaminolysis with a minor contribution from glucose *via* glycolysis, whereas the substantially larger pool of hypoxia-induced L2HG arises exclusively from glutaminolysis.

Structural and biochemical studies have demonstrated that acidic conditions enhance the ability of α-ketoacids (*e.g.*, αKG) and other α-hydroxyacid precursors to "fit" within the LDH and MDH catalytic pockets, enabling reduction reactions that are otherwise thermodynamically inefficient at neutral or physiological pH[23,24]. Moreover, Nadtochi *et al.*[23] showed that the activity of L2HGDH is inhibited by acidic pH, which contributes further to L2HG accumulation due to decreased clearance. These pH-dependent processes provide a plausible mechanistic basis for L2HG accumulation in contexts characterized by acidosis, such as hypoxia. However, unambiguous validation of this model is challenging, as it would require inducing hypoxia without a concomitant decrease in intracellular pH. Moreover, pH-dependent LDHA-mediated L2HG production is sufficient to drive downstream stabilization of hypoxia inducible factor 1α (HIF-1α) even under normoxic conditions[23,24].

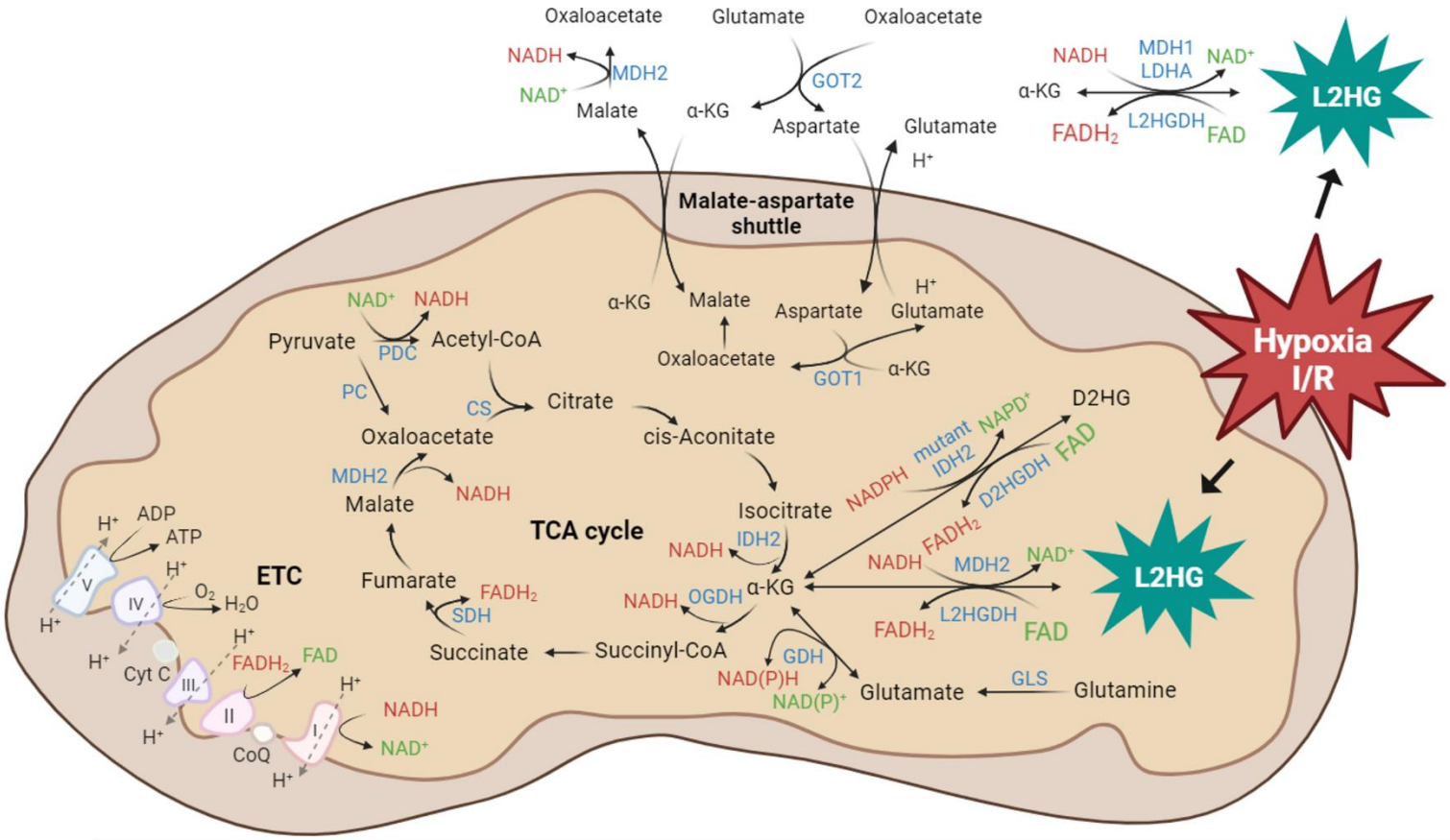

Figure 1.1. L2HG accumulation during hypoxia and ischemia–reperfusion within central carbon metabolism. Schematic representation of central carbon metabolic pathways illustrating proposed routes of L2HG production and clearance under normoxic and hypoxic or ischemia–reperfusion (I/R) conditions. The schematic highlights the tricarboxylic acid (TCA) cycle, malate–aspartate shuttle, electron transport chain (ETC), and associated redox cofactors (NAD^+/NADH, FAD/$FADH_2$). Hypoxia or I/R promote reductive stress and altered redox balance, enabling promiscuous reduction of α-ketoglutarate (αKG) to L2HG by enzymes such as lactate dehydrogenase A (LDHA) and malate dehydrogenases 1/2 (MDH1/2), while L2HG is oxidized back to αKG by L2HG dehydrogenase (L2HGDH). The corresponding reactions for D2HG are also shown. Arrows indicate metabolic fluxes, with redox cofactors shown in green and red. GOT, glutamic-oxaloacetic transaminase; IDH, isocitrate dehydrogenase; GLS, glutaminase; GDH, glutamate dehydrogenase; OGDH, αKG dehydrogenase; SDH, succinate dehydrogenase; CS, citrate synthase; PDC, pyruvate dehydrogenase complex; PC, pyruvate carboxylase; Cyt C, cytochrome *c*; CoQ, coenzyme Q. *Source*: Created with BioRender.com.

Building on prior observations that L2HG accumulates under hypoxic conditions and exerts protective effects, we investigated whether L2HG also accumulates and contributes to tissue protection in myocardial ischemia, a pathophysiological state characterized by reduced blood flow. Using both *ex vivo* and *in vivo* models of low-flow cardiac ischemia and ischemia–reperfusion injury, we demonstrated that myocardial L2HG levels increase robustly during ischemic stress[25]. Moreover, hearts from *L2hgdh*$^{-/-}$ mice, which exhibit chronically elevated systemic L2HG due to impaired clearance (see Section 1.6.1.3), display enhanced resistance to ischemic injury, as evidenced by improved cardiac function, decreased infarct size, decrease in global markers of lipid and protein oxidation, and preservation of high energy phosphates (**Fig. 1.2**). Mechanistically, *L2hgdh*$^{-/-}$ hearts showed a shift in metabolic flux away from glycolysis and toward the pentose phosphate pathway, resulting in increased generation of reduced nicotinamide adenine dinucleotide phosphate (NADPH) (**Fig. 1.3**). Consistent with this model, the L2HG-mediated improvement in cardiac function following ischemic injury required an intact pentose phosphate pathway, as these protective effects were abolished by pharmacological inhibition of the pathway with the glucose-6-phosphate dehydrogenase inhibitor, dehydroepiandrosterone[25]. Taken together, these findings identify L2HG as an ischemia-responsive metabolite and support a protective role for L2HG in the heart during ischemic stress.

1.4 D2HG production by neomorphic IDH activity in cancer

Isocitrate dehydrogenase (IDH) exists as three isoforms in mammals: cytosolic/peroxisomal IDH1, mitochondrial IDH2, and mitochondrial IDH3. IDH mediates the conversion of the ionized 2*R*,2*S* isomer of isocitrate to αKG and is dependent on the reduction of oxidized nicotinamide adenine dinucleotide phosphate ($NADP^+$) to its reduced form (NADPH). In brief, isocitrate is converted first to the enzyme-bound transitional intermediate oxalosuccinate by hydride transfer (forming NADPH), the decarboxylation and subsequent protonation of which liberates αKG as the keto acid form. Although the forward reaction (*i.e.*, isocitrate to αKG) is favored thermodynamically, IDH1/2 (but not IDH3) can also catalyze the reverse carboxylation reaction in the presence of carbon dioxide, oxidizing NADPH to $NADP^+$ and converting αKG back to isocitrate. While contributing to TCA cycle flux by generating αKG, the forward reaction by IDH also contributes to redox balance by producing the reducing equivalent NADPH.

IDH1/2 harboring somatic, heterozygous mutations (mutIDH) are frequent in a subset of cancers (*e.g.,* secondary glioblastoma and acute myeloid leukemia). Early work by Yan *et al.*[26] identified distinct mutations in *IDH1* and *IDH2* in ~70% out of ~1,000 astrocytoma and oligodendroglioma tumors, as well as in ensuing secondary glioblastoma. Such tumors, particularly those affecting the central nervous system, tend to have a common missense mutation wherein adenine replaces guanine at position 395 of the *IDH1* transcript, leading to arginine at amino acid residue 132 of the IDH protein being replaced with a histidine ($IDH1^{R132H}$)[27]. In contrast, IDH2 mutants often contain R172K or R140Q ($IDH2^{R172K}$ and $IDH2^{R140Q}$, respectively)[27]. A commonality of such mutations is that they map to phylogenetically conserved arginine residues that are required for substrate (*i.e.,* isocitrate) binding at the active site of IDH. Importantly, these mutations are different to those that occur outside of the active site, the presence of which has been reported previously in numerous cancers[28].

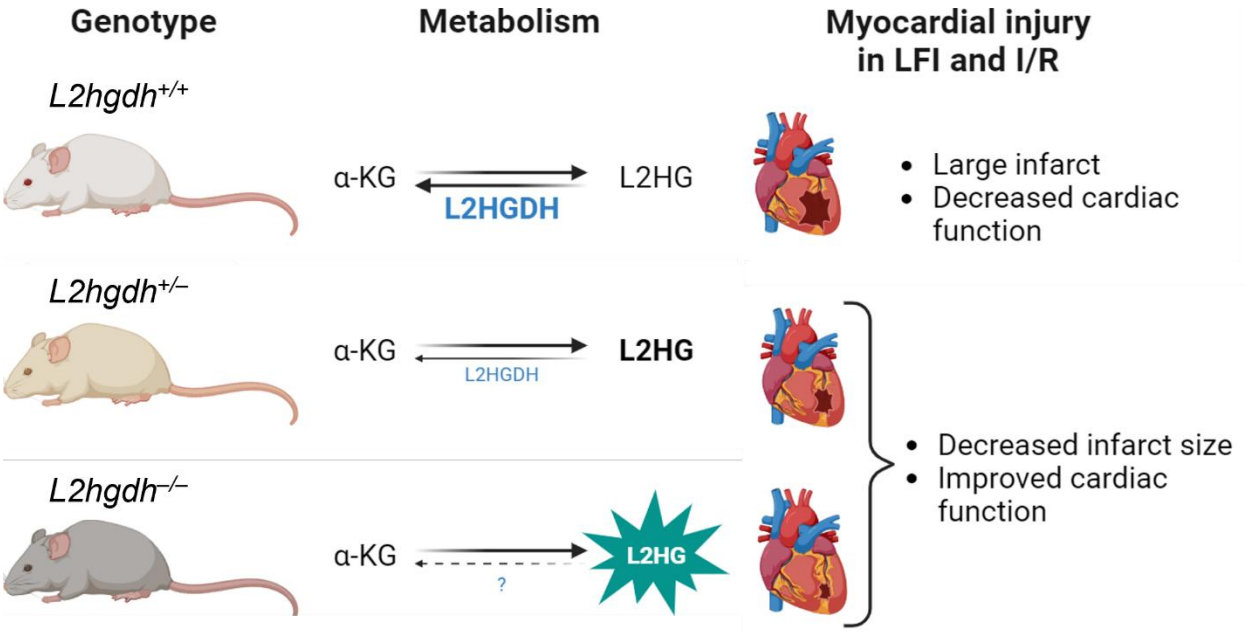

Figure 1.2. Genotype-dependent regulation of L2HG metabolism and myocardial injury. Schematic illustrating the relationship between *L2hgdh* genotype, L2HG metabolism, and myocardial injury following low-flow ischemia (LFI) or ischemia–reperfusion (I/R). In $L2hgdh^{+/+}$ mice, efficient oxidation of L2HG to α-ketoglutarate (αKG) by L2HG dehydrogenase (L2HGDH) limits L2HG accumulation and is associated with larger infarct size and impaired cardiac function. $L2hgdh^{+/–}$ mice exhibit partial oxidation of L2HG to αKG. In $L2hgdh^{–/–}$ mice, loss of L2HGDH results in elevated L2HG levels, which are associated with reduced infarct size and improved cardiac function. Dashed arrow indicates uncertainty as to whether L2HG can be oxidized by L2HGDH-independent mechanisms. *Source*: Created with BioRender.com.

In 2009, Dang and colleagues showed that mutIDH exhibits neomorphic activity enabling the reduction of αKG to 2HG *via* 2-electron reduction of the ketone at the C2 position to a hydroxyl, coupled to oxidation of NADPH to $NADP^+$ (**Fig. 1.1**)[29]. In particular, the authors showed that recombinant homodimeric $IDH1^{R132H}$ retained a catalytic-competent, active conformation and could mediate a simple hydride reduction of αKG to 2HG that was thermodynamically favored over carboxylation of αKG back to isocitrate. This contrasted with wild-type IDH1 which, in the presence of isocitrate and $NADP^+$, catalyzed only the forward reaction to form αKG. The distinct orientation in which αKG fits in the active site of mutIDH with relation to the A-face of the nicotinamide ring of NADPH (from which hydride transfer attack happens) results in the formation of D2HG but not L2HG (reviewed in Ref.[27]). Mechanistically, replacement of the arginine residues at the active site of mutIDH perturbs the binding capacity of isocitrate and, consequently, decreases the flux of the forward reaction substantially. Moreover, mutIDH exhibits a higher affinity for NADPH than for $NADP^+$, indicating a thermodynamic preference for the reverse reaction. Notably, the two subunits of heterodimeric mutIDH are catalytically independent, enabling both the forward oxidation of isocitrate to αKG and its reversed reduction to D2HG with minimal net consumption of NADPH.

Studies comparing the metabolic origin (*i.e.,* carbon source) of D2HG in mutIDH cancer cells showed that glutamine-derived αKG contributes a greater proportion of carbon for D2HG production *via* glutaminolysis than glucose-derived αKG *via* glycolysis and overflow to the TCA cycle (reviewed in Ref.[27]). Taken together, this work prompted the notion that cancer-related mutIDH produces D2HG, which was coined an oncometabolite. In addition, mutIDH are the underlying cause of a subset of D2HGA, a human disorder in which D2HG is accumulated in bodily fluids (see Section 1.2).

1.4.1 D2HG production beyond mutIDH

Beyond neomorphic IDH activity, D2HG can also be generated through several IDH-independent metabolic routes. In bacteria, D2HG can be formed from αKG as a side product of L-serine biosynthesis by 3-phosphoglyceric acid dehydrogenase (PHGDH)[30], from the catabolism of 2-aminoadipate to glutamate[31], and from the reaction of propinyl-CoA with glyoxylate[32]. Production of D2HG by PHGDH has also been reported in human cancer cells, as in the case of breast cancer

tumors without mutIDH[33]. In plants, lysine catabolism is the primary source of D2HG production, plausibly *via* glutaconyl-CoA (reviewed in Ref.[34]). In addition, Kaufman and colleagues purified a mitochondrial oxidoreductase from rat kidney and brain, which was capable of hydroxyacid-oxoacid transhydrogenase activity independent of NADP(H) or NAD(H) as cofactors, and that reversibly converted αKG and γ-hydroxybutyrate to D2HG and succinic semialdehyde[35].

1.5 Mechanisms of action of 2HG

The biological effects of 2HG cannot be understood adequately through a single mechanistic framework. Instead, its actions are best considered as a function of concentration, duration of exposure, cellular compartmentalization, and molecular context. For example, useful conceptual distinctions can be made between chronic *vs.* acute 2HG accumulation, as well as long-term transcriptional and epigenetic remodeling *vs.* direct molecular interactions.

Importantly, the biological activity of 2HG is also shaped by spatial constraints. For example, intracellular localization within the cytosol, mitochondria, or nucleus, may differentially expose the metabolite to distinct classes of protein targets, while extracellular 2HG may engage transporters or plasma membrane-associated proteins[36]. These processes, however, remain poorly defined. Moreover, the extent to which 2HG participates in covalent *vs.* non-covalent interactions is likely to vary across these compartments. Non-covalent binding events may occur rapidly and reversibly, supporting short-term signaling or allosteric regulation, whereas covalent modifications may accumulate more slowly and persist over relatively longer timescales.

These considerations underscore the need to move beyond strict scientific reductionism when evaluating the mechanisms underpinning 2HG (patho)biology. Rather than attributing its effects to a single dominant target or pathway, a more integrative framework is required – namely, one that accounts for temporal dynamics, subcellular distribution, and multi-order effects. In this context, first-order effects may arise from direct binding of 2HG to proteins or other macromolecules, while second- and third-order effects may emerge indirectly through downstream metabolism and/or signaling networks. Such a systems-level perspective is essential for understanding how the same metabolite can exert divergent effects across physiological and pathological contexts.

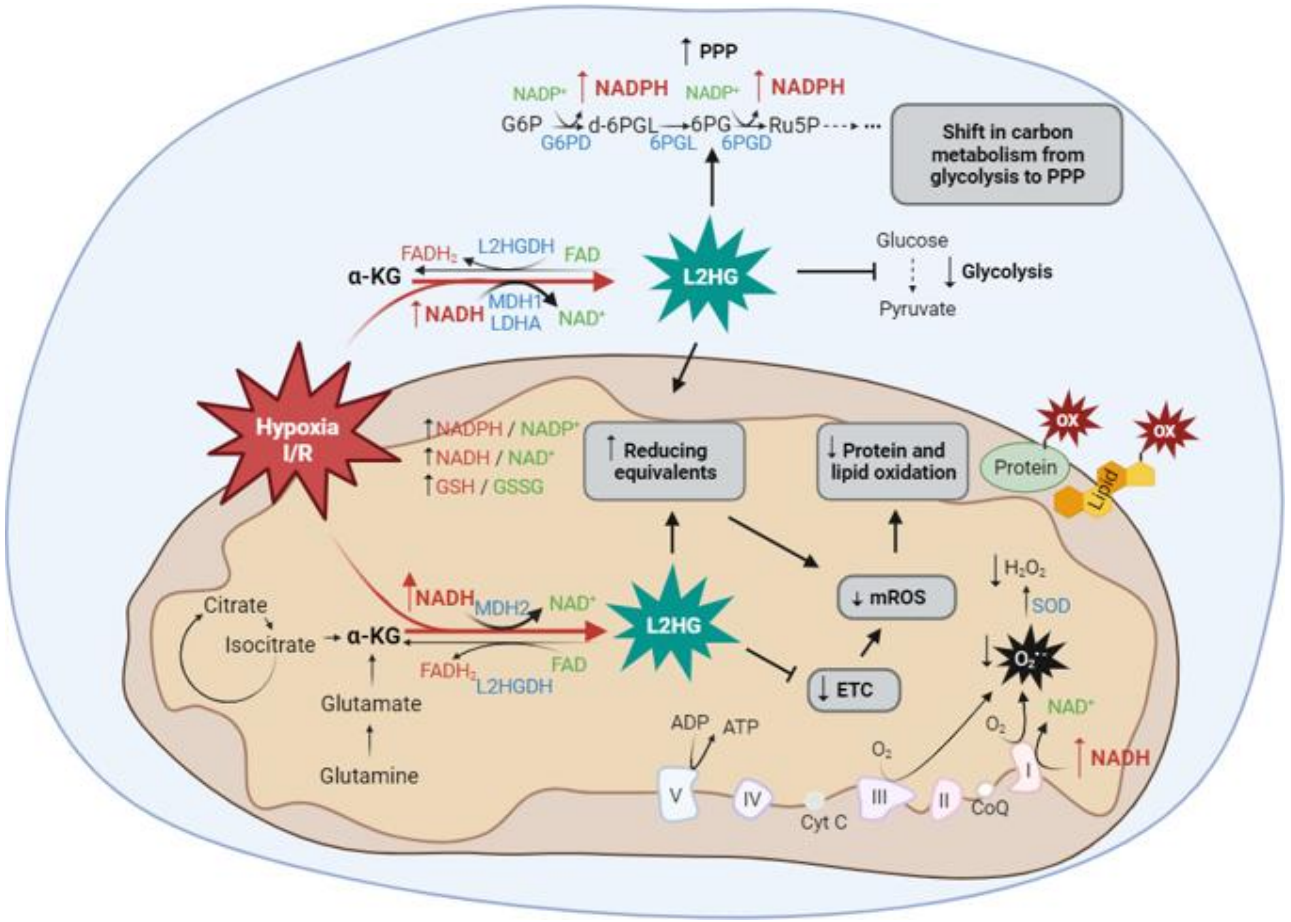

Figure 1.3. Proposed model linking L2HG accumulation to redox remodeling and altered central carbon metabolism under hypoxia and ischemia–reperfusion. Schematic illustrating proposed metabolic consequences of L2HG accumulation during hypoxia and ischemia–reperfusion (I/R). Under conditions of elevated NADH/NAD$^+$ and reduced electron transport chain (ETC) activity, α-ketoglutarate (αKG) is reduced to L2HG by promiscuous dehydrogenase activity of malate dehydrogenase 1/2 (MDH) and lactate dehydrogenase A (LDHA). Accumulated L2HG results in increased reducing equivalents (NADPH, NADH, and GSH), attenuation of mitochondrial respiration and reactive oxygen species (ROS) generation, and reduced protein and lipid oxidation. In parallel, L2HG is linked to a shift in glucose carbon flux from glycolysis toward the pentose phosphate pathway (PPP), supporting NADPH generation and redox homeostasis. Collectively, the model highlights L2HG as a metabolic node integrating redox state, mitochondrial function, and carbon partitioning during ischemic stress. *Source*: Created with BioRender.com.

1.5.1 Competitive inhibition of αKG–dependent enzymes

One of the most extensively characterized mechanisms by which 2HG exerts biological effects is through competitive inhibition of αKG–dependent dioxygenases. Due to its close structural similarity to αKG, 2HG can occupy the αKG binding pocket of these enzymes, thereby reducing their catalytic activity. In general, L2HG is a more potent inhibitor of αKG–dependent enzymes than D2HG; however, reported IC_{50} values vary substantially between targets, spanning approximately 25 μM to >10 mM[37].

The αKG/Fe(II)–dependent dioxygenase superfamily encompasses a vast array of over 60 enzymes in humans that regulate a diversity of critical biological processes through oxidative reactions. These enzymes require Fe(II) as a catalytic cofactor and utilize αKG and molecular oxygen as obligate co-substrates. Structurally, they possess a highly conserved "jellyroll" fold (a double-stranded β-helix) containing a specific His^1-X-Asp/Glu-X_n-His^2 Fe(II)-binding motif. During the catalytic cycle, the enzyme coordinates the Fe(II) center with these amino acid ligands while αKG chelates the metal *via* its C1 carboxylate and C2 ketone. The reaction proceeds through the oxidative decomposition of αKG into succinate and carbon dioxide, which generates a high-valent Fe(IV)-oxo intermediate. This reactive intermediate then performs the hydroxylation or demethylation of a primary substrate, such as a protein side chain, a methylated nucleotide, or a lipid. In addition to hydroxylation and demethylation reactions, αKG–dependent enzymes comprise subclasses capable of catalyzing desaturation, ring expansion, ring formation, and other oxidative transformations; however, the breadth of these reactions lies beyond the scope of the present review. For a more extensive review of αKG–dependent enzymes, the reader is referred to Ref.[38].

1.5.1.1 Jumonji C-domain lysine demethylases

Jumonji C-domain lysine demethylases (JmjC-KDMs) serve as master regulators of the epigenetic landscape by catalyzing the removal of methyl marks from histone tails. These enzymes target mono-, di-, and tri-methylated lysine residues on histone H3: H3K4, H3K9, H3K27, H3K36, and H3K79 (reviewed in Refs.[39,40]). By oxidizing the methyl group, JmjC-KDMs release formaldehyde and restore the unmodified lysine, thereby dictating whether a gene locus is transcriptionally active or repressed. For example, the KDM4 family demethylates the repressive H3K9me3

(trimethylated) mark, a process that is essential for maintaining cellular differentiation programs. Indeed, in glioblastomas, mutations in IDH1/2 are associated with diffuse, tumor-wide increases in H3K9me3[41]. Furthermore, Intlekofer *et al.*[24] demonstrated that hypoxia-induced L2HG drives H3K9me3 accumulation in glioblastoma through direct inhibition of JmjC-KDMs. Importantly, inhibition of KDM family histone demethylases by 2HG can result in sustained histone methylation across multiple genomic loci. For example, Gu *et al.*[42] recently showed that, by inhibiting KDM5, L2HG sustains H3K4 methylation at the MYC proto-oncogene (MYC) locus, leading to increased MYC expression in L2HGDH-deficient cells across both two-dimensional cultures and heterogeneous cortical spheroids. Interestingly, among the αKG–dependent enzymes tested, Chowdhury *et al.*[37] demonstrated that D2HG and L2HG exhibit comparable inhibitory potency toward KDM4A (JMJD2A), with an IC_{50} of approximately 25 μM.

1.5.1.2 Ten-eleven translocation DNA hydroxylases

Ten-eleven translocation (TET) DNA hydroxylases (TET1, TET2, and TET3 in humans) initiate active DNA demethylation by iteratively oxidizing 5-methylcytosine (5mC). These enzymes first convert 5mC to 5-hydroxymethylcytosine (5hmC) and can further oxidize the substrate to 5-formylcytosine and 5-carboxylcytosine, which are replaced eventually by unmethylated cytosine through the base excision repair pathway[43,44]. TET inhibition or loss of function can lead to regional DNA hypermethylation, a hallmark observed in many cancer genomes[45]. Kusi and colleagues demonstrated that L2HG and D2HG induce marked epigenetic remodeling in primary human mammary epithelial cells, including reduced 5hmC with reciprocal increases in 5mC at long interspersed nuclear element-1 sequences, consistent with inhibition of TET-mediated DNA demethylation[46]. Moreover, by competitively inhibiting TET enzymes, mutIDH-derived D2HG has been shown to affect DNA demethylation in gliomas and acute myeloid leukemias[47,48].

1.5.1.3 Prolyl hydroxylase domain proteins

Prolyl hydroxylase domain proteins (PHDs or Egl-9 homologs, EGLNs) function as the primary cellular oxygen sensors in metazoans. Under normoxic conditions, these enzymes utilize oxygen and αKG to hydroxylate specific proline residues on HIF-1α. This modification marks HIF-1α for polyubiquitination and subsequent proteasomal degradation. When oxygen or αKG levels drop, PHD activity diminishes, allowing HIF-1α to stabilize and activate gene expression programs for

adaptation to hypoxia, such as angiogenesis and metabolic reprogramming. Both D2HG and L2HG have previously been shown to inhibit PHD enzymes, albeit with cell-type specificity. For example, forced mutation in *IDH1* (*i.e., IDH1*^{R132H}) in U-87MG cells leads to decreased conversion of isocitrate to αKG, thereby stabilizing HIF-1α and, consequently, stimulating expression of its target genes[49]. In addition, we showed previously that hypoxia-induced stabilization of HIF-1α is potentiated by genetic knockdown of either *L2HGDH* or *D2HGDH* in primary human lung fibroblasts[21]. Furthermore, Williams *et al.*[50] showed that L2HG functions as an immunometabolite in lipopolysaccharide-activated macrophages, driving HIF-1α stabilization and activation through PHD inhibition to promote inflammatory and glycolytic reprogramming. In contrast, Koivunen *et al.*[51] demonstrated that D2HG, but not L2HG, can stimulate PHD activity in astrocytes by acting as an alternative co-substrate that is oxidized to αKG, thereby enhancing HIF-1α hydroxylation and reducing its stabilization to promote cell proliferation.

1.5.1.4 Alkylation repair homolog B

The AlkB family comprises dioxygenases that catalyze oxidative dealkylation reactions to reverse alkylation damage on nucleic acids, thereby preserving genomic and transcriptomic integrity. In mammals, nine AlkB homologs have been identified [ALKBH1–8 and fat mass and obesity-associated protein (FTO)], which have diverged to perform distinct functions across DNA repair, RNA modification, and protein regulation. ALKBH2 and ALKBH3 are *bona fide* DNA repair enzymes that directly reverse alkyl lesions such as 1-methyladenine and 3-methylcytosine, whereas other family members have specialized roles beyond canonical DNA repair[52]. Notably, FTO and ALKBH5 function as RNA demethylases that remove N^6-methyladenosine from mRNA, thereby regulating RNA stability and gene expression, while ALKBH8 mediates post-transcriptional tRNA modifications critical for translational fidelity. Additional homologs, including ALKBH1, ALKBH4, and ALKBH7, act on mitochondrial nucleic acids, histones, or protein substrates, underscoring the functional breadth of the AlkB family. Collectively, these enzymes illustrate how a conserved dioxygenase scaffold has been repurposed to regulate diverse aspects of nucleic acid and protein biology, with emerging implications for epigenetic regulation, metabolism, and disease. D2HG derived from IDH mutant cells has been shown to inhibit ALKBH DNA repair enzymes, thereby sensitizing cells to alkylating agents[53]. Furthermore, Chen *et al.*[54] showed that both enantiomers of 2HG inhibit ALKBH2 and ALKBH3 at pathologically relevant

concentrations (73–88% and 31–58% inhibition by D2HG and L2HG, respectively). Competitive inhibition of these enzymes in the context of IDH mutation has been shown to lead to collagen immaturation and basement membrane aberrations that may contribute to glioma progression[55].

Taken together, by competitively occupying the αKG binding pocket of Fe(II)/αKG–dependent dioxygenases, 2HG broadly modulates epigenetic regulation, hypoxia signaling, and nucleic acid repair in an enzyme-, enantiomer-, and cell-type–dependent manner; however, like other metabolites, 2HG may also interact (non-covalently or covalently) with non-αKG–dependent enzymes, modes of action that are the focus of the next sections.

1.5.2 Noncovalent, direct binding of 2HG to target proteins

Metabolites can directly bind and allosterically regulate proteins, thereby influencing gene expression, RNA metabolism, and protein–protein interaction networks[56,57]. Indeed, metabolites can act as *bona fide* signaling molecules by engaging transcription factors, chromatin-associated proteins, RNA-binding proteins, and metabolic enzymes through reversible, noncovalent interactions that modulate DNA binding, RNA association, enzymatic activity, or complex assembly (reviewed in Ref.[56]). These interactions provide a rapid and tunable mechanism for coupling metabolic state to gene regulatory outputs and are increasingly recognized as pervasive in eukaryotic cells. In this framework, 2HG should not be viewed solely as an αKG mimic, but rather as a metabolite with the potential to engage protein targets through direct binding, reshaping regulatory networks independently of dioxygenase inhibition.

Systematic proteomics and chemoproteomics studies have revealed that central carbon metabolites, including organic acids, nucleotides, lipids, and amino acids, bind hundreds of proteins across the proteome[58]. Given the high intracellular concentrations reached by 2HG in pathological settings, it is plausible that 2HG participates in analogous protein–metabolite interaction networks that remain largely unexplored. This emerging view motivated the application of unbiased, structure-sensitive approaches to systematically identify direct 2HG-binding proteins and to estimate their binding efficiencies. Li *et al.*[59] developed a modification-free, peptide-centric proteomics approach that leverages high-dose trypsin–based limited proteolysis under native conditions (termed PELSA) to detect D2HG-induced local protein stability changes across the proteome, enabling simultaneous target identification and binding-region mapping by MS. Using

this approach, the authors confirmed D2HG binding to canonical αKG–dependent enzymes, including KDMs. In addition, the authors uncovered previously unrecognized targets, including proteins involved in central carbon metabolism such as pyruvate carboxylase ($EC_{50} \approx 144$ μM), offering a potential mechanism to explain the direct link between 2HG signaling and glycolytic reprogramming, a phenotype discussed in Section 1.3.

In summary, metabolites such as 2HG can directly bind and allosterically regulate diverse proteins, a regulatory layer that is increasingly revealed by unbiased, structure-sensitive proteomics approaches such as PELSA. As these technologies continue to mature, they will likely uncover additional non-canonical 2HG targets, including interactions with non-enzymatic proteins and, potentially, other macromolecules such as lipids.

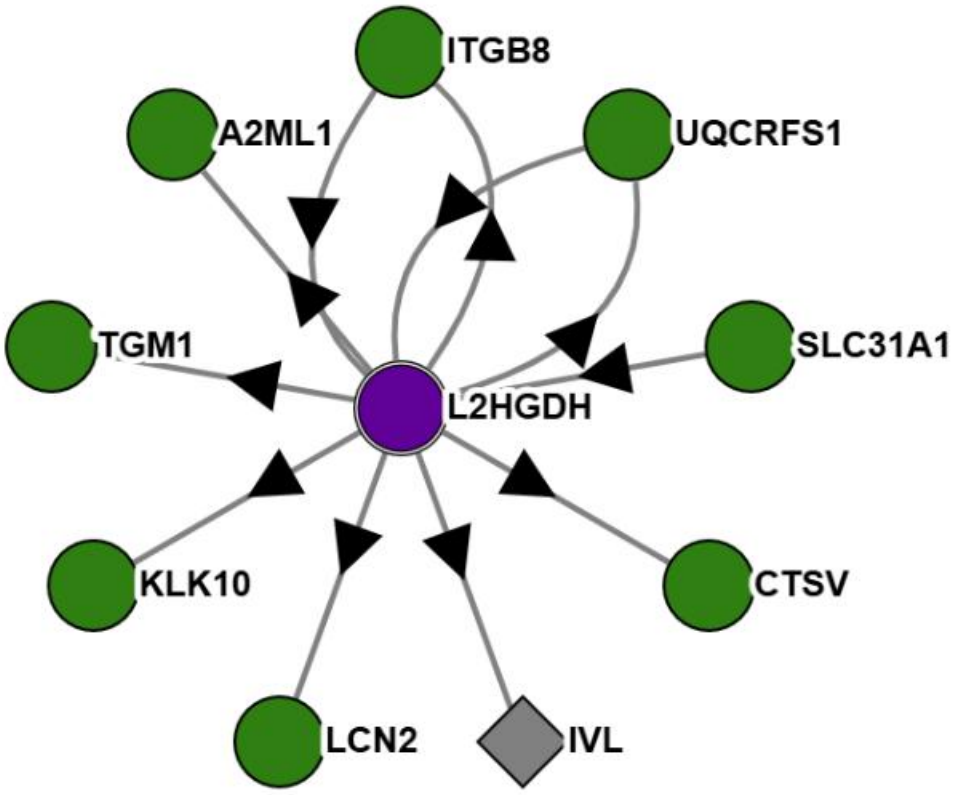

Figure 1.4. L2HGDH protein–protein interaction network. Network representation of L2HGDH and its first-order interacting proteins derived from protein–protein interaction analysis of HEK293FT cells on BioPlex[68], with nodes representing proteins and edges indicating physical interactions, as assessed by high-throughput affinity-purification mass spectrometry. Arrowheads denote directionality from the protein bait to prey. ITGB8, integrin beta-8; UQCRFS1, cytochrome *b*-c_1 complex subunit Rieske, mitochondrial; SLC31A1, high affinity copper uptake protein 1; CTSV, cathepsin L2; IVL, involucrin; LCN2, neutrophil gelatinase-associated lipocalin; KLK10, kallikrein-10; TGM1, protein-glutamine gamma-glutamyltransferase K; A2ML1, alpha-2-macroglobulin-like protein 1. *Source*: Created with Bioplex.com.

1.5.3 "2HGylation": covalent binding of 2HG to target proteins

Beyond non-covalent binding, metabolites can also regulate protein function through covalent incorporation as post-translational modifications (PTMs), providing a durable mechanism by which metabolic state is encoded into protein activity and gene regulation. Well-established examples include lysine acetylation[60,61], succinylation[62,63], malonylation[64], and lactylation[65], in which reactive acyl-CoA or acyl donors derived from central carbon metabolism covalently modify protein side chains. These PTMs are tightly coupled to intracellular metabolite abundance and flux, enabling metabolites such as acetyl-CoA, succinate, and lactate to function as direct signaling entities rather than passive metabolic intermediates alone.

Given its close structural similarity to lactate and succinate, and its ability to accumulate to millimolar concentrations in pathological contexts such as mutIDH-associated cancers and hypoxia, it is reasonable to posit that 2HG may also participate in covalent protein modification. Indeed, recent work by Zhang *et al.*[66] identified a previously unrecognized class of metabolite-driven PTMs, termed *O*-2-hydroxyglutarylation ("2HGylation"), through which D2HG and L2HG covalently modify proteins in a chiral-dependent manner. Using an integrated chemical proteomics workflow combining mass-shift screening, optimized enrichment, isotopic tracing with labeled 2HG, and MS/MS validation, the authors mapped hundreds of highly confident 2HG modification sites across the proteome, predominantly on serine, threonine, and tyrosine residues. Functionally, 2HGylation selectively modified and inhibited kinases such as serine/threonine-protein kinase MRCK alpha (CDC42BPA, D2HG–dependent) and STE20-like serine/threonine-protein kinase (SLK, L2HG–dependent), leading to reduced phosphorylation of downstream substrates. The authors used structural modeling approaches to suggest that these modifications impair kinase activity by destabilizing active site access or protein–protein interactions. In the same study, the authors showed with high confidence that L2HG, but not D2HG, post-translationally modified pyruvate dehydrogenase E1 component subunit alpha (PHDA1), thereby providing a plausible mode of action by which L2HG alters glycolytic flux[21,67] (see Section 1.3). In addition, the authors revealed that L2HG, but not D2HG, post-translationally modified C-1-tetrahydrofolate synthase (MTHFD1) and peroxiredoxin-6 (PRDX6), the functional consequence of which may contribute to the effect of L2HG on NADPH bioavailability, as reported previously[25] (see Section 1.3). In contrast, D2HG, but not L2HG, post-translationally modified glutaminase kidney isoform (GLS),

whereas both enantiomers modified α–actinin-1 (ACTN1), brain acid soluble protein 1 (BASP1), DnaJ homologous subfamily B member 1 (DNAJB1), DnaJ homologous subfamily C member 10 (DNAJC10), heat shock 70 kDa protein 1A (HSPA1A), DNA replication licensing factor 4 and 5 (MCM4/5), myosin light polypeptide 6 (MYL6), nuclear autoantigenic sperm protein (NASP), and lysine-specific demethylase 6 (RSBN1). These findings establish covalent 2HG-driven protein modification as a distinct and biologically consequential mode of action, expanding the functional repertoire of 2HG beyond competitive inhibition of αKG–dependent enzymes and noncovalent binding to target proteins.

1.5.4 2HGDH beyond 2HG

Alterations in 2HGDH are often interpreted purely through their metabolic consequence (namely, accumulation / depletion of 2HG). However, emerging protein–protein interaction (PPI) data argue that this view is incomplete. Large-scale affinity-purification MS efforts, most notably the BioPlex interactome[68], reveal that L2HGDH associates physically with a broad and functionally diverse set of proteins spanning mitochondrial biology, cytoskeletal organization, vesicular trafficking, chromatin-associated factors, and signaling components (**Fig. 1.4**). For example, both the BioPlex project and a human PPI network constructed by our laboratory[69-71] indicate that L2HGDH physically interacts with cytochrome *b*–c_1 complex subunit Rieske (UQCRFS1), a connection that may underlie the altered mitochondrial energetics we previously observed in the hearts of *L2hgdh*$^{-/-}$ mice[25] (see Section 1.3). More broadly, these interactions may not be trivially explained by L2HG turnover alone, and instead suggest that L2HGDH may participate in multiprotein complexes, potentially serving scaffolding, regulatory, or spatially organizing roles that are independent of its enzymatic activity on L2HG.

A parallel situation appears to hold for D2HGDH. BioPlex interaction maps show that D2HGDH engages a largely distinct set of binding partners compared with L2HGDH (**Fig. 1.5**), indicating isoform-specific interaction networks rather than a shared 2HG module. Indeed, none of the direct neighbors of L2HGDH and D2HGDH overlap (compare **Figs. 1.4** and **1.5**). The divergence of these interactomes is striking given the close biochemical analogy between L2HGDH and D2HGDH at the metabolite level, yet it is consistent with the surprisingly limited sequence homology shared by the two proteins. Instead, it implies that each dehydrogenase may be

embedded in unique cellular pathways, potentially linking 2HG metabolism to broader processes such as proteostasis, cytoskeletal dynamics, DNA replication, or stress signaling through direct physical interactions rather than through changes in metabolite abundance alone.

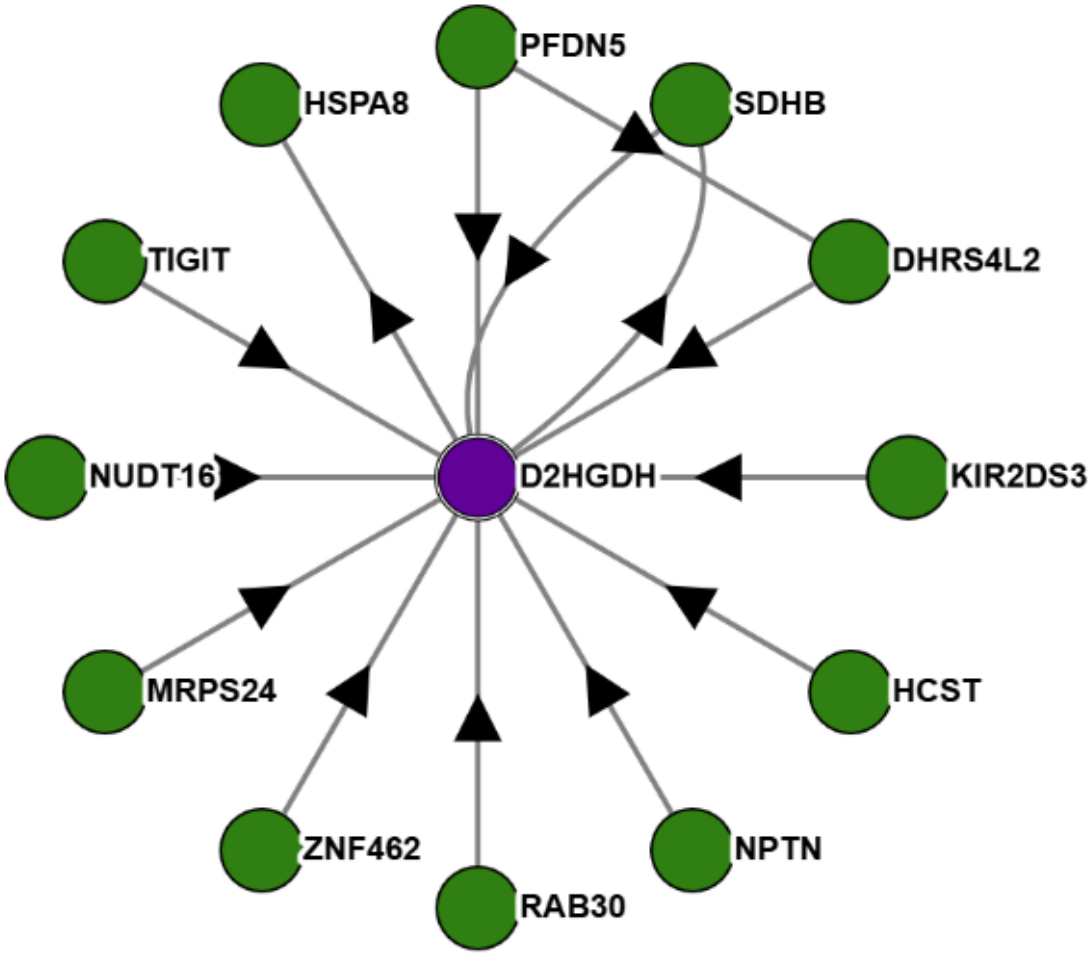

Figure 1.5. D2HGDH protein–protein interaction network. Network representation of D2HGDH and its first-order interacting proteins derived from protein–protein interaction analysis of HEK293FT cells on BioPlex[68], with nodes representing proteins and edges indicating physical interactions, as assessed by high-throughput affinity-purification mass spectrometry. Arrowheads denote directionality from the protein bait to prey. PFDN5, prefoldin subunit 5; SDHB, succinate dehydrogenase [ubiquinone] iron-sulfur subunit, mitochondrial; DHRS4L2, dehydrogenase/reductase SDR family member 4-like 2; KIR2DS3, killer cell immunoglobulin-like receptor 2DS3; HCST, hematopoietic cell signal transducer; NPTN, neuroplastin; RAB30, Ras-related protein Rab-30; ZNF462, zinc finger protein 462; MRPS24, small ribosomal subunit protein uS3m; NUDT16, U8 snoRNA-decapping enzyme; TIGIT, T-cell immunoreceptor with Ig and ITIM domains; HSPA8, heat shock cognate 71 kDa protein. *Source*: Created with Bioplex.com.

These observations have important conceptual and experimental implications. If L2HGDH and D2HGDH exert functions through PPIs that are independent of L2HG or D2HG levels, then genetic perturbation of these enzymes (*e.g.*, knock-out, knock-down, or over-expression) may introduce phenotypes that cannot be attributed solely to altered 2HG concentrations. Such effects could include epigenetic or signaling perturbations driven by disruption of protein complexes rather than by the metabolite *per se*. Consequently, experimental models that rely exclusively on manipulating L2HGDH or D2HGDH to study 2HG (patho)biology must be interpreted with caution and ideally complemented by approaches that modulate 2HG levels independently of the dehydrogenases, to disentangle metabolite-dependent effects from enzyme-intrinsic, interaction-mediated functions (see Section 1.6).

1.6 Practical considerations for the study of 2HG (patho)biology

1.6.1 2HG modeling *in vitro* and *in vivo*

There are several ways to study the role(s) of 2HG in a biological system. Broadly, these approaches are based on either accumulating or depleting 2HG. The simplest approach to accumulate 2HG intracellularly is, arguably, to supplement cells or animals with an authentic standard of L/D2HG. This approach was used by Thunberg[3], Wishart[4], and Weil-Malherbe[5] in their seminal works on 2HG metabolism in the early twentieth century (see Section 1.1). *In vitro*, cells take up 2HG from the medium. Given the relatively high polarity of 2HG owing to its two carboxylic acids and the α-hydroxyl group, its uptake is likely transporter-mediated, the kinetics of which are likely cell-type–dependent. While several studies have implicated various transporters in the cellular uptake of 2HG, there remains considerable uncertainty regarding their relative contributions and the extent of cell-type–specific transport mechanisms. For example, Wang and colleagues showed that D2HG uptake in vascular endothelial cells is mediated by SLC1A1, illustrated by the observation that its genetic knock-down decreased D2HG uptake, while its over-expression enhanced it[72]. In the same study, the authors showed that SLC1A1-mediated D2HG uptake is dependent on residues T370, R447, and N451, as illustrated by the finding that mutagenesis to these residues impaired its uptake. In a separate study by Kang and colleagues, *SLC1A1* knockdown was shown to increase cytosolic L2HG under baseline conditions in HEK293FT cells[19]. Collectively, these findings suggest that SLC1A1 may facilitate the uptake of both enantiomers of 2HG. Even if there are no transporters dedicated exclusively to 2HG, it is

not unreasonable to speculate that transporters of other α-hydroxy-dicarboxylic acids may exhibit promiscuous activity toward 2HG (reviewed in Ref.[73]).

1.6.1.1 2HG chemical modifications to improve cellular uptake

2HG can be modified chemically to facilitate its diffusion across the plasma membrane. For example, in 2011, Xu and colleagues synthesized an octyl-ester form of L2HG by diazotization of the α-amino group of *(S)*-2-amino-4-(benzyloxy)-4-oxobutanoic acid to a α-hydroxyl, alkylation of the α-hydroxyl with 1-iodooctane, and hydrogenolytic removal of the benzyl ester to yield the free octyl ester of the hydroxy-acid (*i.e.,* octyl-L2HG, hereafter referred to as OL2HG)[47]. The authors also synthesized OD2HG by activating disodium D2HG with trifluoroacetic anhydride and selectively esterifying one carboxyl group with octanol in tetrahydrofuran. Both L and D forms of O2HG are now commercially available.

The ester bond of O2HG is hydrolyzed intracellularly with the stereospecificity conserved to liberate 2HG and 1-octanol. The advantage of using octyl esters lies in their ability to enhance cellular uptake of 2HG, coupled with the assumption that intracellular esterase-mediated hydrolysis releases unmodified 2HG in a gradual manner that more closely approximates physiological production rather than a non-physiological burst. Indeed, Wang and colleagues showed that OD2HG induced both greater and time-dependent increases in the intracellular D2HG–to–αKG ratio when compared with unmodified D2HG[72], consistent with the notion that the octyl ester sustains a concentration gradient through continuous hydrolysis.

However, these assumptions are complicated by the kinetics of ester hydrolysis, which can vary substantially across chemical environments and experimental conditions. Indeed, Fets and colleagues showed that dimethyloxalylglycine, a cell-permeant ester analog of the αKG inhibitor *N*-oxalylglycine, hydrolyzes rapidly in aqueous solutions[74]. Similarly, Parker and colleagues recently showed that esterified analogs of αKG, including dimethyl- and octyl-αKG (OαKG), hydrolyze rapidly in a cell-free system[75]. In fact, these authors showed that OαKG hydrolyzes spontaneously to αKG within as little as 5 minutes. Hydrolysis rates were influenced by the hydrophobicity of the ester group, as evidenced by preferential formation of 5-methyl-αKG over 1-methyl-αKG during the initial hydrolytic step of dimethyl-αKG, which proceeded more rapidly

than the subsequent conversion of 5-methyl-αKG to free αKG. By extrapolation, 1-O2HG is likely to undergo spontaneous hydrolysis more rapidly than 5-O2HG, with kinetics potentially further influenced by stereochemistry. As such, when supplemented in culture media, esterified analogs of metabolites can hydrolyze before diffusing into cells. In our experience nonetheless, approximately 350–400 μM of O2HG remains in the culture medium after treatment of primary human cardiomyocytes and cardiac fibroblasts with 500 μM of the octyl ester for 24 hours (Vigder and Loscalzo, Brigham and Women's Hospital, Harvard Medical School, unpublished), suggesting that although some extracellular hydrolysis occurs, the octyl group likely supports a time-dependent, continuous release of 2HG. Despite these considerations, such nuances are often overlooked in experimental design and in the interpretation of findings aimed at defining the roles of 2HG in specific phenotypes.

When using modified forms of 2HG, appropriate controls are essential to ensure that observed phenotypic effects are attributable to 2HG itself rather than to the chemical modification. In our experience, O2HG and unmodified 2HG do not always elicit identical molecular responses in several primary human cell types (Vigder and Loscalzo, Brigham and Women's Hospital, Harvard Medical School, unpublished). Consistent with this principle, Swain and colleagues demonstrated that octyl-4-itaconate, but not unmodified itaconate, induced a pronounced eosinophilic stress response associated with an immunosuppressive phenotype in macrophages[76]. In addition, esterified αKG has been shown to affect cellular metabolism independently of its unmodified form[75]. This discrepancy may arise because unmodified metabolites and their esterified derivatives engage distinct protein targets, leading to non-overlapping molecular effects. Alternatively, phenotypic changes may be driven, at least in part, by octanol released during hydrolysis of the octyl ester. Indeed, octanol can be oxidized to octanoic acid *via* octanal by alcohol dehydrogenase, a metabolic sequence described both in horse liver and in human fibroblasts and termed the "fatty alcohol cycle"[77,78]. Octanoic acid can subsequently undergo further oxidation[79,80] and is a known regulator of ketogenesis, as octanoate loading increases ketone production in fasted animals[81]. In addition, octanol exhibits lipid bilayer-modifying potency[82], inhibits gap junctions[83-85], suppresses the capacitative entry of Ca^{2+} in pancreatic acinar cells and fibroblasts[86], and modulates *γ*-aminobutyric acid type A receptor activity in human embryonic kidney cells[87].

For the reasons mentioned above, inclusion of an octyl-ester form of an additional metabolite (*e.g.,* octyl acetate) can serve as a useful experimental control, although this approach assumes that (i) the different octyl esters hydrolyze at comparable rates and therefore liberate equimolar amounts of octanol with similar kinetics, and (ii) the phenotype under investigation is independent of the liberated control metabolite (*e.g.,* acetate). Nevertheless, this strategy is generally preferable to the use of octanol alone, as it more closely recapitulates the gradual release of octanol from O2HG rather than an acute bolus. Arguably, the most appropriate control is the alternative enantiomeric form of the modified compound under study (*e.g.,* using OD2HG as a control for OL2HG treatment, and *vice versa*). These considerations extend to other esterified derivatives of 2HG, including trifluoromethylphenyl esters, which have been employed previously by us and others[21,88].

In summary, investigators should specify unambiguously whether a modified form of 2HG was used and verify their findings using appropriate controls as well as unmodified 2HG. Equally important, results should be described accordingly; for example, when using OL2HG, phenotypic effects should be reported as "OL2HG-induced" rather than "L2HG-induced".

1.6.1.2 Intracellular compartmentalization of 2HG

An additional nuance in the biological roles of 2HG concerns its intracellular compartmentalization. The distribution of 2HG across subcellular compartments is likely influenced by whether it is taken up from the extracellular microenvironment or synthesized endogenously, as well as by the extent of its transport between organelles and the specific enzymes responsible for its production. Importantly, chemical modifications of 2HG can alter hydrophobicity and partition coefficient, raising the possibility that modified and unmodified forms accumulate in distinct intracellular compartments. For instance, the hydrophobic acyl chain of O2HG may facilitate diffusion across organellar membranes, enabling release of 2HG within compartments in which it would not otherwise accumulate. Because the protein composition differs substantially between compartments, such redistribution is likely to result in qualitatively distinct biological effects.

Related to this notion of 2HG compartmentalization, Gelman and colleagues showed that [$^{13}C_5$]-2HG supplemented exogenously is not readily converted to [$^{13}C_5$]-αKG in colorectal carcinoma

cells[89]. We and others have observed the same results in primary pulmonary artery endothelial cells (Vigder and Loscalzo, Brigham and Women's Hospital, Harvard Medical School, unpublished) and primary human umbilical vein endothelial cells[72]. These findings encouraged some investigators to propose that the oncometabolic effects of D2HG are mediated through direct molecular interactions rather than through its oxidation to αKG (reviewed in Ref.[27]). However, such a conclusion assumes that 2HG can diffuse freely across the entire cell. This hypothesis implicitly assumes the existence of an active transport mechanism capable of translocating cytosolic 2HG into mitochondria; however, cytosolic-to-mitochondrial exchange of 2HG remains poorly understood. One study implicated SLC1A1 in mediating D2HG uptake into mitochondria, based on increased D2HG uptake by purified mitochondria isolated from microvascular endothelial cells over-expressing SLC1A1[72]. However, to the best of our knowledge, the authors did not assess whether D2HG accumulates within mitochondria of intact cells, nor quantify its distribution relative to the cytosolic pool. Indeed, using an L2HG–specific biosensor, Kang and colleagues did not detect an increase in mitochondrial L2HG following genetic knock-down and pharmacological inhibition of SLC1A1 in intact HEK293FT cells[19].

Notably, the oxidation of 2HG to αKG is confined to the mitochondria, as both 2HGDH isoforms are mitochondrial enzymes. Therefore, the observation that cells do not oxidize exogenously supplemented [$^{13}C_5$]-2HG may reflect limited mitochondrial uptake and/or isotopic dilution due to relatively large endogenous pools of TCA cycle intermediates. To address these possibilities, it may be helpful to use a carbon labeled form of a membrane-permeant analog of 2HG (*e.g.*, octyl-[$^{13}C_5$]-2HG), followed by cellular fractionation and assessment of the relative 2HG accumulation within different organelles. For a more detailed discussion on current methodologies for assessing 2HG compartmentalization, the reader is referred to Section 1.6.2.2. Therefore, the use of unmodified and cell-permeant derivatives of 2HG requires not only the incorporation of appropriate controls but also scrutiny of the interpretations that are made.

1.6.1.3 Altering 2HGDH expression and/or activity

Another means to accumulate 2HG in biological systems is to decrease the expression and/or activity of 2HGDH. *In vitro*, this can be achieved by genetically silencing the *2HGDH* gene, as done previously by us and others[21,22,90,91]. In addition, several groups have generated mouse models

with global *L2hgdh* knock-out[92,93]. For example, the model developed by Rzem and colleagues involved insertion of a gene trapping cassette in intron 3 of the disrupted allele of the *L2hgdh* gene, leading to the production of an inactive protein comprising the first 137 residues of L2HGDH fused to the cassette[92]. As such, antibodies that target this region of the inactive protein should not be used to verify the efficiency of the genetic knock-out in this model. This model was used throughout the results chapters of the current thesis.

Again, manipulating 2HGDH has implications regarding the intracellular compartmentalization of 2HG. A corollary of 2HG compartmentalization is that the mitochondrial and non-mitochondrial pools of 2HG are, at least in part, independent of each other. In support of this, it was shown recently that extracellular-derived αKG decarboxylated to succinate primarily in the cytosol with minimal contributions to anaplerosis mitochondrially, suggestive of the presence of functionally distinct subcellular pools of αKG[75]. As such, manipulating the expression and/or activity of 2HGDH may alter the mitochondrial concentration of 2HG independently of the extra-mitochondrial pool. In addition, 2HGDH may exhibit functions other than oxidizing 2HG to αKG by, for example, interaction with other proteins (see Section 1.5.4). Collectively, modulating the expression and/or activity of 2HGDH may provide nuanced insight into the role of mitochondrial *vs.* cytosolic 2HG, and findings should be verified with supplementation of the metabolite itself.

1.6.1.4 Alternative ways to study 2HG

A less specific approach to accumulate 2HG is to increase the expression and/or activity of enzymes that are involved in 2HG synthesis (*e.g.*, LDHA as in the case of L2HG). However, this approach fails to control for effects that are independent of 2HG, particularly because these enzymes are often molecular hubs that participate in numerous chemical reactions and pathways. In addition, one could deplete 2HG intracellularly by decreasing the expression and/or activity of enzymes that are involved in 2HG synthesis. Again, this approach can induce alterations that are independent of 2HG. Nevertheless, such a tactic is useful in ascertaining the relative contributions of different enzymes to the production of 2HG, as we and others have shown[21,22].

1.6.2 Quantification of 2HG and 2HGDH activity

1.6.2.1 Liquid chromatography mass spectrometry-based approaches

The gold standard method for the detection and quantification of metabolites is arguably liquid chromatography (tandem) mass spectrometry [LC–MS(/MS)]. The chromatographic separation of 2HG from other similarly structured polar metabolites (*e.g.*, malate) is achieved with relative ease using, *e.g.*, hydrophilic interaction liquid chromatography (HILIC[94]). According to the Human Metabolome Database (HMDB), seven known, biologically relevant metabolites share the same molecular formula as 2HG ($C_5H_8O_5$): poly(lactic acid-co-glycolic acid), citramalic acid, 3HG, ribonolactone, D-xylono-1,5-lactone, 2-methylmalate, and D-arabinono-1,4-lactone. The reliable detection of 2HG requires chromatographic separation from these structural isomers, which may be achieved with diligently optimized HILIC. Alternatively, derivatization prior to LC–MS can enhance the chromatographic separation of 2HG from its structural isomers. For example, Simon and Wierenga[95] derivatized plasma and urine samples with butanol to yield butyl-ester derivatives of 2HG and 3HG, the separation of which was achieved using a C8 chromatographic column. Nevertheless, a more specialized approach is required to chromatographically separate the enantiomeric forms of 2HG.

Chiral columns can provide adequate enantioselectivity to separate the L and D forms of polar metabolites. For example, the commercially available macrocyclic glycopeptide-based column, Astec® CHIROBIOTIC™ R, has been used to separate the enantiomers of 2HG[96] and lactic acid[97]. Although chiral chromatography columns offer high enantioselective resolution, their high cost and the need for specialized technical expertise limit their widespread adoption in many laboratory settings. In addition, despite technological advancements in MS that have improved sensitivity, the reliable detection and quantification of low abundance metabolites, including 2HG, remains an ongoing analytical challenge. This sensitivity challenge is further amplified for molecules with low ionization efficiencies in the negative mode (*e.g.*, 2HG), not least because (1) proton loss is energetically less favorable than protonation in many LC solvents, and (2) common components in biological matrices (*e.g.*, phosphates) compete for charge, leading to ion suppression. As such, investigators often use derivatization by chemically modifying analytes to enhance their ionization efficiencies and, therefore, increase the lower limit of their detection.

Chiral derivatization involves chemically modifying enantiomers (*e.g.*, L/D2HG) with a chiral reagent to form diastereomers, the chromatographic separation of which can be achieved using relatively straightforward conventional achiral chromatography. Early work by Kamerling and colleagues described a derivatization approach to measure urinary hydroxydicarboxylic acids stereoselectively (*e.g.*, L/D2HG) by gas chromatography coupled to MS, involving esterification with *R*-(–)-2-butanolic HCl and subsequent acetylation of the hydroxyl group with acetic anhydride[98]. This approach was later used by the laboratory of Craig Thompson in their seminal work on L2HG in hypoxia and beyond[22,99]. In addition, Struys and colleagues derivatized urine samples with (+)-*O,O'*-diacetyl-L-tartaric anhydride (DATAN) followed by reverse-phase chromatographic separation of L2HG and D2HG and MS/MS analysis[100]. In the same study, the authors reported a detection limit of 20 pmol for a urine sample volume of 20 µL. We and others have since used modified versions of this approach to measure DATAN-derivatized L2HG and D2HG by LC–MS in numerous biological matrices[21,24,101-103]. For a detailed outline of this method, the reader is referred to our published protocol in Ref.[104].

In 2005, Cheng and colleagues developed an improved method for the detection of 2HG enantiomers *via* derivatization with the chiral reagent *N*-(p-toluenesulfonyl)-L-phenylalanyl chloride (TSPC), followed by reverse-phase LC–MS analysis[105]. Remarkably, derivatization with TSPC led to an approximately ~300-fold enhancement in the detection sensitivity of both 2HG enantiomers compared to their underivatized forms, whereas derivatization with DATAN achieved only a ~3-fold increase. The authors reported limits of detection of 1.2 fmol for TSPC-D2HG and 1.0 fmol for TSPC-L2HG. It is worth noting, however, that chromatographic separation of TSPC-derivatized L2HG and D2HG using columns different from those described in the original publication requires extensive optimization of chromatographic gradients. Indeed, using a collection of C18 columns available in our laboratory, we were only able to achieve baseline separation of the L and D forms of TSPC-2HG by connecting two sub-2 µm C18 columns in series (Vigder and Cordwell, University of Sydney, unpublished). This chromatographic challenge can be addressed using ion mobility spectrometry (IMS), an orthogonal separation technique that resolves gas-phase ions according to their drift time through a neutral buffer gas, which reflects the ion collision cross section and is influenced by its size, shape, and charge. For example, Fukui and colleagues showed that field asymmetric waveform IMS (FAIMS)/MS enabled the separation of derivatized L2HG and D2HG in less than a second[106]. Possibly useful for laboratories with

limited LC–MS expertise and/or access, Ohtawa and colleagues used the fluorescent derivatization reagent, 4-nitro-7-piperazino-2,1,3-benzoxadiazole, to derivatize lactonized 2HG and subsequently measure L2HG and D2HG by two-dimensional liquid chromatography coupled with fluorescence detection at excitation and emission wavelengths of 491 and 547 nm, respectively[107].

Irrespective of the derivatization reagent or detection method employed, it is critical to assess the derivatization yield for each biological matrix under study. The efficiency of the derivatization can vary significantly depending on the chemical environment of the sample, which may influence both reaction kinetics and completeness. Factors such as matrix complexity, pH, ionic strength, and the presence of interfering substances (*e.g.*, salts, proteins, lipids) can all impact derivatization efficiency. Importantly, the biochemical composition of a sample can vary markedly between non-diseased and diseased states, potentially leading to differences in derivatization yield. For example, disease-associated changes in metabolite concentrations, protein content, oxidative stress, or enzyme activity may influence the availability or reactivity of target functional groups. Therefore, derivatization conditions optimized in one biological context may not directly translate to another without careful validation. That said, rigorous evaluation of derivatization efficiency is essential to ensure quantitative accuracy, particularly when comparing metabolite levels across disease conditions and/or organs.

Beyond bulk quantification, understanding the spatial distribution of 2HG within tissues is critical for linking metabolite abundance to histopathological features and cellular heterogeneity. Lan and colleagues developed a method using matrix-assisted laser desorption/ionization (MALDI) MS imaging to study the localization of 2HG in human glioma tissues[108]. However, because MALDI lacks chromatographic separation prior to MS analysis, it does not inherently provide enantioselectivity unless coupled with IMS.

1.6.2.2 Biosensors

Genetically encoded biosensors are a powerful means to measure metabolites (reviewed in Ref.[109]). In 2021, Kang and colleagues identified LhgR, an allosteric transcription factor that regulates L2HG catabolism in *Pseudomonas putida* strain W619[110]. Mechanistically, LhgR functions as a transcriptional repressor of the gene encoding the bacterial enzyme L2HG oxidase (LhgO)[110]. Binding of L2HG to LhgR inhibits its interaction with the *lhgO* promoter, thereby

relieving transcriptional repression[110]. As such, the authors used LhgR as a biorecognition element in an L2HG-sensing fluorescent reporter (LHGFR) based on fluorescent resonance energy transfer (FRET)[110]. In the same paper, the authors constructed LHGFR by fusing the fluorescent proteins, monomeric teal fluorescent protein (mTFP) and Venus, to the *N*-terminus of LhgR. L2HG binding to LHGFR reduced the emission peak of mTFP at 492 nm and increased the emission peak of Venus at 526 nm, thereby increasing the Venus-to-mTFP emission ratio with a dissociation constant (K_d) of approximately 2.7 μM. Notably, this emission ratio was unchanged by D2HG, as well as a range of other similarly structured metabolites (*e.g.*, lactate and succinate), highlighting biosensor selectivity for L2HG. Nevertheless, LHGFR does not offer a high enough spatial resolution to distinguish the distribution of L2HG within different intracellular compartments.

To address the low spatial resolution of LHGFR, the same group recently fused circularly permuted yellow fluorescent protein (cpYFP) and LhgR to develop single fluorescent protein-based L2HG–sensing fluorescent reporter with high detection range ($sfLHGR_H$), offering improved spatiotemporal sensitivity compared to LHGFR (apparent K_d of approximately 180 μM and a lower detection limit of 0.56 μM)[19]. Using $sfLHGR_H$, the authors validated that hypoxia and α-keto-β-methylvaleric acid both increased L2HG in HEK293FT cells in a manner dependent on LDHA and MDH2. In the same study, the authors developed derivatives of $sfLHGR_H$ that localize in different intracellular compartments by fusing it with sequences for nuclear exclusion, mitochondrial localization, and nuclear localization. Using this approach, the authors demonstrated that exogenously added L2HG accumulates in the cytosol and nucleus alike in HEK293FT cells, but to a markedly lesser extent in the mitochondria. Moreover, over-expression of mitochondrial malic enzyme 2 increased L2HG in mitochondria, but not in the cytosol. In addition to $sfLHGR_H$, the authors developed a more sensitive L2HG probe ($sfLHGR_L$) for *in vivo* applications, which exhibited a lower limit of detection of 0.14 μM.

In addition to the biosensors mentioned above, Hou and colleagues developed the enzymatic assay-based L2HG-sensing fluorescence reporter (EaLHGFR) by coupling the resazurin fluorescence system with an enzyme exhibiting high specificity and catalytic activity toward L2HG dehydrogenation in *Azoarcus olearius* BH72[111]. Although EaLHGFR showed a lower limit of detection than LHGFR, $sfLHGR_H$, and $sfLHGR_L$, its detection range was relatively small (0.042–5 μM)[111].

Overall, using these biosensors for 2HG quantification is crucial for understanding its intracellular distribution under different (patho)physiological conditions, as they allow real-time, non-destructive monitoring of compartment-specific fluctuations in live cells that would otherwise be obscured by conventional extraction-based methods prone to metabolite redistribution or degradation.

1.6.2.3 Enzymatic assays

Numerous enzymatic assays have been developed and used to measure L2HG and D2HG. For example, Balss *et al.*[112] developed a rapid, inexpensive, and sensitive enzymatic assay for D2HG quantification based on D2HGDH-catalyzed oxidation of D2HG to αKG with stoichiometric NADH generation, achieving detection limits sufficient to measure basal D2HG levels in tumor tissue and serum independently of IDH mutation status. In addition, we previously quantified L2HG in tissue homogenates using a coupled enzymatic assay in which exogenously added purified recombinant L2HGDH drives oxidation of L2HG to αKG, coupled to a peroxidase-linked conversion of 10-acetyl-3,7-dihydroxyphenoxazine to fluorescent resorufin, with signal intensity proportional to L2HG abundance and specificity ensured by subtraction of L2HGDH-independent background[25]. In principle, stereochemical selectivity in these enzymatic assays is conferred by supplementation with the L- or D-specific 2HGDH enzyme; however, this approach is limited by dependence on enzyme purity and activity, potential interference from endogenous metabolites, and lower throughput and multiplexing capacity relative to MS-based methods.

In addition to enabling quantification of 2HG, these enzymatic assays can also be used to directly measure 2HGDH activity. Because 2HGDH enzymes are evolutionarily conserved, such activity assays often employ purified recombinant enzymes from diverse species, including human, *Drosophila*, and bacterial homologs. For example, Yang *et al.*[113] quantified *Drosophila melanogaster* L2HGDH activity by spectrophotometrically monitoring reduction of 2,6-dichloroindophenol. In addition, activity of the *E. coli* L2HGDH homolog, YgaF, has been assayed using ortho-phenylenediamine–based detection of αKG formation to derive kinetic parameters for L2HG oxidation[114].

1.7 Gaps in knowledge and future work

Despite rapid progress in defining the biochemical roles of 2HG, substantial gaps remain in our understanding of how 2HG is generated, compartmentalized, and interpreted by cells under physiological and pathological conditions. A key unresolved issue concerns the relative contribution of distinct enzymatic sources to the total D/L2HG pools across tissues, redox states, and microenvironments. More broadly, the possibility that additional hydroxyacid–oxoacid transhydrogenases (enzymes capable of promiscuous reduction of α-ketoacids) contribute meaningfully to 2HG production has not been systematically explored. Similarly, it remains unknown whether 2HGDH-independent clearance pathways exist for either enantiomer, whether 2HG can be oxidized to αKG non-enzymatically, and whether there exist racemases capable of interconverting between the L and D forms of 2HG. Resolving these questions will be essential for constructing a quantitative and context-specific model of 2HG homeostasis.

Another major frontier lies in understanding 2HG transport and compartmentalization. The identity of dedicated or promiscuous 2HG transporters, including whether uptake occurs *via* known organic acid transporters, remains largely unclear. Moreover, the extent to which 2HG can "leak" or be actively shuttled between subcellular compartments has important implications for function, not least because the biological consequences of 2HG are likely to be compartment-specific, dictated by differential exposure to dioxygenases, kinases, chromatin regulators, and RNA-binding proteins. This raises the possibility that mitochondrial, nuclear, and cytosolic pools of 2HG exert distinct and even opposing effects, an idea that has not yet been tested rigorously. This concept is well supported by emerging evidence for compartmentalized signaling and function of structurally related metabolites, such as αKG[75].

Finally, while individual protein targets and pathways have been identified, the field lacks a systematic, quantitative map of 2HG–target interactions and their affinities across different (patho)biological contexts. Emerging structure-sensitive proteomics approaches, such as peptide-centric local stability assays, provide a promising avenue to define context-dependent 2HG interactomes. In parallel, the recent discovery of 2HGylation as a covalent, chiral-specific PTM highlights an additional, largely unexplored layer of regulation. Comprehensive mapping of 2HGylation sites, elucidation of their enzymatic or non-enzymatic origins, and functional interrogation of their consequences will require further methodological innovation. Taken together,

these efforts will be critical for moving beyond descriptive associations and toward a mechanistic understanding of how 2HG integrates metabolism, signaling, and gene regulation in health and disease.

1.8 Conclusions

In conclusion, the literature reviewed here establishes 2HG as a stereochemically defined metabolite whose biological roles are shaped by its enantiomeric identity, metabolic origin, intracellular compartmentalization, and concentration. Early chemical and enzymological observations laid the foundation for recognizing that L2HG and D2HG are generated and cleared by distinct pathways, a concept that has been refined by more recent work demonstrating context-dependent production through enzyme promiscuity, neomorphic activity of mutIDH, and additional IDH-independent routes. Mechanistic studies have revealed that 2HG influences cellular physiology through multiple, non-mutually exclusive modes of action, including competitive inhibition of αKG–dependent dioxygenases, direct noncovalent protein interactions, and covalent protein modification, with outcomes that vary across tissues and disease states. Methodological advances in LC–MS, biosensors, and enzymatic assays have greatly expanded the capacity to interrogate 2HG (patho)biology, while simultaneously highlighting limitations related to stereoselectivity, sensitivity, and spatial resolution. Collectively, this review emphasizes that a comprehensive understanding of 2HG (patho)biology requires an integrative outlook that accounts for stereochemistry, metabolic context, and subcellular distribution, thereby providing a conceptual framework for experimental studies presented in the subsequent chapters of this thesis.

1.9 Hypotheses and aims

This thesis is founded on the overarching hypothesis that L2HG functions as an active regulator of cellular metabolism and stress adaptation, rather than representing a passive byproduct of metabolic errors and/or altered redox state. Importantly, this work integrates both hypothesis-driven experimentation and discovery-driven, hypothesis-generating approaches, with distinct components of the thesis deliberately designed to move between targeted testing of predefined mechanisms and unbiased multi-omics analyses that generate new biological hypotheses.

The initial, hypothesis-driven focus of this work was on neutral lipid metabolism, based on emerging evidence that L2HG alters mitochondrial redox balance and energy metabolism (see Section 1.3). Accordingly, the first major aim of the thesis was to determine whether L2HG alters triglyceride homeostasis through effects on lipid partitioning and fatty acid oxidation. As detailed in Chapter 2, this hypothesis was interrogated using integrated multi-omics approaches, including lipidomics, transcriptomics, metabolomics, and proteomics analyses, followed by targeted validation and mechanistic studies across multiple cell types and animal models.

The focus of Chapter 3 did not stem from a predefined mechanistic hypothesis but emerged from hypothesis-generating, discovery-based lipidomics findings reported in Chapter 2. Unbiased lipidomics profiling revealed a consistent downregulation of multiple phosphatidylethanolamine species in OL2HG-treated cells, prompting further investigation. Based on these observations, a subsequent aim of the thesis was to systematically characterize the relationship between L2HG and phosphatidylethanolamine metabolism. Given that neutral lipids and glycerophospholipids share key precursor pools, including glycerol-3-phosphate, diacylglycerol, and fatty acyl-CoAs (see Section 3.1), Chapter 3 was designed to define whether phosphatidylethanolamine represents a sensitive node within a broader lipid-partitioning network regulated by L2HG.

Finally, recognizing that metabolic and proteomic perturbations rarely operate through isolated linear pathways, a further aim of this thesis was to determine whether L2HG exerts broader systems-level effects that can be revealed through network-based analysis of unbiased proteomics data. Rather than testing a single protein-centric hypothesis, Chapter 4 applies network medicine principles[115] to discovery-driven proteomics from baseline-perfused and ischemic hearts to identify novel nodal proteins and pathways associated with L2HG metabolism.

1.10 References

1 Ritthausen, H. Ueber die Glutansäure, das Zersetzungsproduct der Glutaminsäure durch salpetrige Säure. *Journal für Praktische Chemie* **103**, 239–242 (1868).

2 Ritthausen, H. Ueber das Drehungsvermögen von Glutan- und Aepfelsäure. *Journal für Praktische Chemie* **5**, 354–355 (1872).

3 Thunberg, T. Zur Kenntnis des intermediären Stoffwechsels und der dabei wirksamen Enzyme. *Skandinavisches Archiv Für Physiologie* **40**, 1–91 (1920).

4 Wishart, G. M. On the Reduction of Methylene Blue by Tissue Extracts. *Biochemical Journal* **17**, 103–114 (1923).

5 Weil-Malherbe, H. The oxidation of *l*(-)α-hydroxyglutaric acid in animal tissues. *Biochemical Journal* **31**, 2080–2094 (1937).

6 Tubbs, P. K. & Greville, G. D. The oxidation of D-alpha-hydroxy acids in animal tissues. *Biochemical Journal* **81**, 104–114 (1961).

7 Achouri, Y. *et al.* Identification of a dehydrogenase acting on D-2-hydroxyglutarate. *Biochemical Journal* **381**, 35–42 (2004).

8 Rzem, R. *et al.* A gene encoding a putative FAD-dependent L-2-hydroxyglutarate dehydrogenase is mutated in L-2-hydroxyglutaric aciduria. *Proceedings of the National Academy of Sciences of the United States of America* **101**, 16849–16854 (2004).

9 Kranendijk, M., Struys, E. A., Salomons, G. S., Van der Knaap, M. S. & Jakobs, C. Progress in understanding 2-hydroxyglutaric acidurias. *Journal of Inherited Metabolic Disease* **35**, 571–587 (2012).

10 Chalmers, R. A. *et al.* D-2-hydroxyglutaric aciduria: case report and biochemical studies. *Journal of Inherited Metabolic Disease* **3**, 11–15 (1980).

11 Duran, M., Kamerling, J. P., Bakker, H. D., van Gennip, A. H. & Wadman, S. K. L-2-Hydroxyglutaric aciduria: an inborn error of metabolism? *Journal of Inherited Metabolic Disease* **3**, 109–112 (1980).

12 Muntau, A. C. *et al.* Combined D-2- and L-2-hydroxyglutaric aciduria with neonatal onset encephalopathy: a third biochemical variant of 2-hydroxyglutaric aciduria? *Neuropediatrics* **31**, 137–140 (2000).

13 Struys, E. A. *et al.* Mutations in the D-2-hydroxyglutarate dehydrogenase gene cause D-2-hydroxyglutaric aciduria. *The American Journal of Human Genetics* **76**, 358–360 (2005).

14 Steenweg, M. E. *et al.* An overview of L-2-hydroxyglutarate dehydrogenase gene (L2HGDH) variants: a genotype-phenotype study. *Human Mutation* **31**, 380–390 (2010).

15 Kranendijk, M. *et al.* Evidence for genetic heterogeneity in D-2-hydroxyglutaric aciduria. *Human Mutation* **31**, 279–283 (2010).

16 Kranendijk, M. *et al.* IDH2 mutations in patients with D-2-hydroxyglutaric aciduria. *Science* **330**, 336 (2010).

17 Nota, B. *et al.* Deficiency in SLC25A1, encoding the mitochondrial citrate carrier, causes combined D-2- and L-2-hydroxyglutaric aciduria. *The American Journal of Human Genetics* **92**, 627–631 (2013).

18 Edvardson, S. *et al.* Agenesis of corpus callosum and optic nerve hypoplasia due to mutations in SLC25A1 encoding the mitochondrial citrate transporter. *Journal of Medical Genetics* **50**, 240–245 (2013).

19 Kang, Z. *et al.* An Ultrasensitive Biosensor for Probing Subcellular Distribution and Mitochondrial Transport of l-2-Hydroxyglutarate. *Advanced Science* **11**, e2404119 (2024).

20 Khersonsky, O. & Tawfik, D. S. Enzyme promiscuity: a mechanistic and evolutionary perspective. *Annual Review of Biochemistry* **79**, 471–505 (2010).

21 Oldham, W. M., Clish, C. B., Yang, Y. & Loscalzo, J. Hypoxia-Mediated Increases in L-2-hydroxyglutarate Coordinate the Metabolic Response to Reductive Stress. *Cell Metabolism* **22**, 291–303 (2015).

22 Intlekofer, A. M. *et al.* Hypoxia Induces Production of L-2-Hydroxyglutarate. *Cell Metabolism* **22**, 304–311 (2015).

23 Nadtochiy, S. M. *et al.* Acidic pH Is a Metabolic Switch for 2-Hydroxyglutarate Generation and Signaling. *Journal of Biological Chemistry* **291**, 20188–20197 (2016).

24 Intlekofer, A. M. *et al.* L-2-Hydroxyglutarate production arises from noncanonical enzyme function at acidic pH. *Nature Chemical Biology* **13**, 494–500 (2017).

25 He, H. *et al.* L-2-Hydroxyglutarate Protects Against Cardiac Injury via Metabolic Remodeling. *Circulation Research* **131**, 562–579 (2022).

26 Yan, H. *et al.* IDH1 and IDH2 mutations in gliomas. *The New England Journal of Medicine* **360**, 765–773 (2009).

27 Dang, L. & Su, S. M. Isocitrate Dehydrogenase Mutation and (R)-2-Hydroxyglutarate: From Basic Discovery to Therapeutics Development. *Annual Review of Biochemistry* **86**, 305–331 (2017).

28 Ward, P. S. *et al.* Identification of additional IDH mutations associated with oncometabolite R(−)-2-hydroxyglutarate production. *Oncogene* **31**, 2491–2498 (2012).

29 Dang, L. *et al.* Cancer-associated IDH1 mutations produce 2-hydroxyglutarate. *Nature* **462**, 739–744 (2009).

30 Zhao, G. & Winkler, M. E. A novel alpha-ketoglutarate reductase activity of the serA-encoded 3-phosphoglycerate dehydrogenase of Escherichia coli K-12 and its possible implications for human 2-hydroxyglutaric aciduria. *Journal of Bacteriology* **178**, 232–239 (1996).

31 Kopchick, J. J. & Hartline, R. A. alpha-Hydroxyglutarate as an intermediate in the catabolism of alpha-aminoadipate by Pseudomonas putida. *Journal of Biological Chemistry* **254**, 3259–3263 (1979).

32 Wegener, W. S., Reeves, H. C. & Ajl, S. J. Propionate metabolism. 3. Studies on the significance of the alpha-hydroxyglutarate pathway. *Archives of Biochemistry and Biophysics* **123**, 62–65 (1968).

33 Fan, J. *et al.* Human phosphoglycerate dehydrogenase produces the oncometabolite D-2-hydroxyglutarate. *ACS Chemical Biology* **10**, 510–516 (2015).

34 Engqvist, M. K., Eßer, C., Maier, A., Lercher, M. J. & Maurino, V. G. Mitochondrial 2-hydroxyglutarate metabolism. *Mitochondrion* **19 Pt B**, 275–281 (2014).

35 Kaufman, E. E., Nelson, T., Fales, H. M. & Levin, D. M. Isolation and characterization of a hydroxyacid-oxoacid transhydrogenase from rat kidney mitochondria. *Journal of Biological Chemistry* **263**, 16872–16879 (1988).

36 Diekmann, Y. & Pereira-Leal, J. B. Evolution of intracellular compartmentalization. *Biochemical Journal* **449**, 319–331 (2013).

37 Chowdhury, R. *et al.* The oncometabolite 2-hydroxyglutarate inhibits histone lysine demethylases. *EMBO Reports* **12**, 463–469 (2011).

38 Hausinger, R. P. FeII/alpha-ketoglutarate-dependent hydroxylases and related enzymes. *Critical Reviews in Biochemistry and Molecular Biology* **39**, 21–68 (2004).

39 Gray, Z. H., Honer, M. A., Ghatalia, P., Shi, Y. & Whetstine, J. R. 20 years of histone lysine demethylases: From discovery to the clinic and beyond. *Cell* **188**, 1747–1783 (2025).

40 Tsukada, Y. *et al.* Histone demethylation by a family of JmjC domain-containing proteins. *Nature* **439**, 811–816 (2006).

41 Venneti, S. *et al.* Histone 3 lysine 9 trimethylation is differentially associated with isocitrate dehydrogenase mutations in oligodendrogliomas and high-grade astrocytomas. *Journal of Neuropathology and Experimental Neurology* **72**, 298–306 (2013).

42 Gu, W. *et al.* L-2-hydroxyglutarate impairs neuronal differentiation through epigenetic activation of MYC expression. *bioRxiv* (2025). https://doi.org/10.1101/2025.04.16.649033

43 Rasmussen, K. D. & Helin, K. Role of TET enzymes in DNA methylation, development, and cancer. *Genes & Development* **30**, 733–750 (2016).

44 Zhang, X., Zhang, Y., Wang, C. & Wang, X. TET (Ten-eleven translocation) family proteins: structure, biological functions and applications. *Signal Transduction and Targeted Therapy* **8**, 297 (2023).

45 López-Moyado, I. F. *et al.* Paradoxical association of TET loss of function with genome-wide DNA hypomethylation. *Proceedings of the National Academy of Sciences of the United States of America* **116**, 16933–16942 (2019).

46 Kusi, M. *et al.* 2-Hydroxyglutarate destabilizes chromatin regulatory landscape and lineage fidelity to promote cellular heterogeneity. *Cell Reports* **38**, 110220 (2022).

47 Xu, W. *et al.* Oncometabolite 2-hydroxyglutarate is a competitive inhibitor of α-ketoglutarate-dependent dioxygenases. *Cancer Cell* **19**, 17–30 (2011).

48 Figueroa, M. E. *et al.* Leukemic IDH1 and IDH2 mutations result in a hypermethylation phenotype, disrupt TET2 function, and impair hematopoietic differentiation. *Cancer Cell* **18**, 553–567 (2010).

49 Zhao, S. *et al.* Glioma-derived mutations in IDH1 dominantly inhibit IDH1 catalytic activity and induce HIF-1alpha. *Science* **324**, 261–265 (2009).

50 Williams, N. C. *et al.* Signaling metabolite L-2-hydroxyglutarate activates the transcription factor HIF-1α in lipopolysaccharide-activated macrophages. *Journal of Biological Chemistry* **298**, 101501 (2022).

51 Koivunen, P. *et al.* Transformation by the (R)-enantiomer of 2-hydroxyglutarate linked to EGLN activation. *Nature* **483**, 484–488 (2012).

52 Fedeles, B. I., Singh, V., Delaney, J. C., Li, D. & Essigmann, J. M. The AlkB Family of Fe(II)/α-Ketoglutarate-dependent Dioxygenases: Repairing Nucleic Acid Alkylation Damage and Beyond. *Journal of Biological Chemistry* **290**, 20734–20742 (2015).

53 Wang, P. *et al.* Oncometabolite D-2-Hydroxyglutarate Inhibits ALKBH DNA Repair Enzymes and Sensitizes IDH Mutant Cells to Alkylating Agents. *Cell Reports* **13**, 2353–2361 (2015).

54 Chen, F. *et al.* Oncometabolites d- and l-2-Hydroxyglutarate Inhibit the AlkB Family DNA Repair Enzymes under Physiological Conditions. *Chemical Research in Toxicology* **30**, 1102–1110 (2017).

55 Sasaki, M. *et al.* D-2-hydroxyglutarate produced by mutant IDH1 perturbs collagen maturation and basement membrane function. *Genes & Development* **26**, 2038–2049 (2012).

56 Hornisch, M. & Piazza, I. Regulation of gene expression through protein-metabolite interactions. *npj Metabolic Health and Disease* **3**, 7 (2025).

57 Piazza, I. *et al.* A Map of Protein-Metabolite Interactions Reveals Principles of Chemical Communication. *Cell* **172**, 358–372.e323 (2018).

58 Hicks, K. G. *et al.* Protein-metabolite interactomics of carbohydrate metabolism reveal regulation of lactate dehydrogenase. *Science* **379**, 996–1003 (2023).

59 Li, K. *et al.* A peptide-centric local stability assay enables proteome-scale identification of the protein targets and binding regions of diverse ligands. *Nature Methods* **22**, 278–282 (2025).

60 Choudhary, C., Weinert, B. T., Nishida, Y., Verdin, E. & Mann, M. The growing landscape of lysine acetylation links metabolism and cell signalling. *Nature Reviews Molecular Cell Biology* **15**, 536–550 (2014).

61 Kim, S. C. *et al.* Substrate and functional diversity of lysine acetylation revealed by a proteomics survey. *Molecular Cell* **23**, 607–618 (2006).

62 Zhang, Z. *et al.* Identification of lysine succinylation as a new post-translational modification. *Nature Chemical Biology* **7**, 58–63 (2011).

63 Weinert, B. T. *et al.* Lysine succinylation is a frequently occurring modification in prokaryotes and eukaryotes and extensively overlaps with acetylation. *Cell Reports* **4**, 842–851 (2013).

64 Zou, L. *et al.* Lysine Malonylation and Its Links to Metabolism and Diseases. *Aging and Disease* **14**, 84–98 (2023).

65 Zhang, D. *et al.* Metabolic regulation of gene expression by histone lactylation. *Nature* **574**, 575–580 (2019).

66 Zhang, Z. *et al.* Discovery of Chirally-dependent Protein O-2-Hydroxyglutarylation by D2HG and L2HG. *bioRxiv* (2025). https://doi.org/10.1101/2025.01.24.634716

67 Notarangelo, G. *et al.* Oncometabolite d-2HG alters T cell metabolism to impair CD8(+) T cell function. *Science* **377**, 1519–1529 (2022).

68 Huttlin, E. L. *et al.* The BioPlex Network: A Systematic Exploration of the Human Interactome. *Cell* **162**, 425–440 (2015).

69 Samokhin, A. O. *et al.* NEDD9 targets COL3A1 to promote endothelial fibrosis and pulmonary arterial hypertension. *Science Translational Medicine* **10**, eaap7294 (2018).

70 Maron, B. A. *et al.* Individualized interactomes for network-based precision medicine in hypertrophic cardiomyopathy with implications for other clinical pathophenotypes. *Nature Communications* **12**, 873 (2021).

71 Wang, R. S. *et al.* Individualized Interactomes from Pulmonary Arterial Hypertension Cell Biopsies Predict Therapeutic Response. *medRxiv* (2025). https://doi.org/10.1101/2025.11.13.25340200

72 Wang, X. *et al.* SLC1A1-mediated cellular and mitochondrial influx of R-2-hydroxyglutarate in vascular endothelial cells promotes tumor angiogenesis in IDH1-mutant solid tumors. *Cell Research* **32**, 638–658 (2022).

73 Pizzagalli, M. D., Bensimon, A. & Superti-Furga, G. A guide to plasma membrane solute carrier proteins. *The FEBS Journal* **288**, 2784–2835 (2021).

74 Fets, L. *et al.* MCT2 mediates concentration-dependent inhibition of glutamine metabolism by MOG. *Nature Chemical Biology* **14**, 1032–1042 (2018).

75 Parker, S. J. *et al.* Spontaneous hydrolysis and spurious metabolic properties of α-ketoglutarate esters. *Nature Communications* **12**, 4905 (2021).

76 Swain, A. *et al.* Comparative evaluation of itaconate and its derivatives reveals divergent inflammasome and type I interferon regulation in macrophages. *Nature Metabolism* **2**, 594–602 (2020).

77 Hinson, J. A. & Neal, R. A. An examination of octanol and octanal metabolism to octanoic acid by horse liver alcohol dehydrogenase. *Biochimica et Biophysica Acta* **384**, 1–11 (1975).

78 Rizzo, W. B., Craft, D. A., Dammann, A. L. & Phillips, M. W. Fatty alcohol metabolism in cultured human fibroblasts. Evidence for a fatty alcohol cycle. *Journal of Biological Chemistry* **262**, 17412–17419 (1987).

79 Schwabe, A. D., Bennett, L. R. & Bowman, L. P. OCTANOIC ACID ABSORPTION AND OXIDATION IN HUMANS. *Journal of Applied Physiology* **19**, 335–337 (1964).

80 van de Casteele, M. *et al.* Oxidative breakdown of octanoic acid is maintained in patients with cirrhosis despite advanced disease. *Neurogastroenterology & Motility* **15**, 113–120 (2003).

81 McGarry, J. D. & Foster, D. W. The regulation of ketogenesis from octanoic acid. The role of the tricarboxylic acid cycle and fatty acid synthesis. *Journal of Biological Chemistry* **246**, 1149–1159 (1971).

82 Ingólfsson, H. I. & Andersen, O. S. Alcohol's effects on lipid bilayer properties. *Biophysical Journal* **101**, 847–855 (2011).

83 Pappas, C. A., Rioult, M. G. & Ransom, B. R. Octanol, a gap junction uncoupling agent, changes intracellular [H+] in rat astrocytes. *Glia* **16**, 7–15 (1996).

84 Barhoumi, R., Bailey, H. R., Hutchinson, R. W., Bowen, J. A. & Burghardt, R. C. Enhancement of melphalan toxicity by octanol in ovarian adenocarcinoma cell lines:

effects of altered cell-cell communication, glutathione levels, and plasma membrane fluidity. *Fundamental and Applied Toxicology* **25**, 70–79 (1995).

85 Talaverón, R. *et al.* The Gap Junction Inhibitor Octanol Decreases Proliferation and Increases Glial Differentiation of Postnatal Neural Progenitor Cells. *International Journal of Molecular Sciences* **25** (2024).

86 Kim, Y. J., Elliott, A. C., Moon, S. J., Lee, S. I. & Seo, J. T. Octanol blocks fluid secretion by inhibition of capacitative calcium entry in rat mandibular salivary acinar cells. *Cell Calcium* **25**, 77–84 (1999).

87 Kurata, Y., Marszalec, W., Yeh, J. Z. & Narahashi, T. Agonist and potentiation actions of n-octanol on gamma-aminobutyric acid type A receptors. *Molecular Pharmacology* **55**, 1011–1019 (1999).

88 Losman, J. A. *et al.* (R)-2-hydroxyglutarate is sufficient to promote leukemogenesis and its effects are reversible. *Science* **339**, 1621–1625 (2013).

89 Gelman, S. J. *et al.* Evidence that 2-hydroxyglutarate is not readily metabolized in colorectal carcinoma cells. *Cancer Metabolism* **3**, 13 (2015).

90 Xiao, W. *et al.* Branched-chain α-ketoacids aerobically activate HIF1α signalling in vascular cells. *Nature Metabolism* **6**, 2138–2156 (2024).

91 Zhao, J. *et al.* Metabolic remodelling during early mouse embryo development. *Nature Metabolism* **3**, 1372–1384 (2021).

92 Rzem, R. *et al.* A mouse model of L-2-hydroxyglutaric aciduria, a disorder of metabolite repair. *PLOS ONE* **10**, e0119540 (2015).

93 Ma, S. *et al.* L2hgdh Deficiency Accumulates l-2-Hydroxyglutarate with Progressive Leukoencephalopathy and Neurodegeneration. *Molecular and Cellular Biology* **37** (2017).

94 Buszewski, B. & Noga, S. Hydrophilic interaction liquid chromatography (HILIC)--a powerful separation technique. *Analytical and Bioanalytical Chemistry* **402**, 231–247 (2012).

95 Simon, G. A. & Wierenga, A. Quantitation of plasma and urine 3-hydroxyglutaric acid, after separation from 2-hydroxyglutaric acid and other compounds of similar ion transition, by liquid chromatography-tandem mass spectrometry for the confirmation of glutaric aciduria type 1. *Journal of Chromatography B: Analytical Technologies in the Biomedical and Life Sciences* **1097-1098**, 101–110 (2018).

96 Wöhlgemuth, R., Rudolf Köhling, R. & Cramer, H. *Chiral LC-MS/MS of D- and L-2-Hydroxyglutaric Acid Biomarkers*, <https://theanalyticalscientist.com/media/qk5kt3tk/chiral_lcms_2-ohg_t213003cleaned.pdf>

97 Henry, H., Marmy Conus, N., Steenhout, P., Béguin, A. & Boulat, O. Sensitive determination of D-lactic acid and L-lactic acid in urine by high-performance liquid chromatography-tandem mass spectrometry. *Biomedical Chromatography* **26**, 425–428 (2012).

98 Kamerling, J. P. *et al.* Determination of the absolute configuration of some biologically important urinary 2-hydroxydicarboxylic acids by capillary gas--liquid chromatography. *Journal of Chromatography B: Biomedical Sciences and Applications* **222**, 276–283 (1981).

99 Ward, P. S. *et al.* The common feature of leukemia-associated IDH1 and IDH2 mutations is a neomorphic enzyme activity converting alpha-ketoglutarate to 2-hydroxyglutarate. *Cancer Cell* **17**, 225–234 (2010).

100 Struys, E. A., Jansen, E. E., Verhoeven, N. M. & Jakobs, C. Measurement of urinary D- and L-2-hydroxyglutarate enantiomers by stable-isotope-dilution liquid chromatography-tandem mass spectrometry after derivatization with diacetyl-L-tartaric anhydride. *Clinical Chemistry* **50**, 1391–1395 (2004).

101 Li, X., Bo, Y., Le, L. & Yang, F. Simultaneous Determination of D and L Enantiomers of 2-Hydroxyglutarate by UHPLC-MS/MS Method in Human Biological Fluids and its Clinical Application. *Journal of Chromatography Science* **63** (2025).

102 Suijker, J. *et al.* Inhibition of mutant IDH1 decreases D-2-HG levels without affecting tumorigenic properties of chondrosarcoma cell lines. *Oncotarget* **6**, 12505–12519 (2015).

103 Andrade, J. *et al.* Control of endothelial quiescence by FOXO-regulated metabolites. *Nature Cell Biology* **23**, 413–423 (2021).

104 Oldham, W. M. & Loscalzo, J. Quantification of 2-Hydroxyglutarate Enantiomers by Liquid Chromatography-mass Spectrometry. *Bio-protocol* **6** (2016).

105 Cheng, Q. Y. *et al.* Sensitive Determination of Onco-metabolites of D- and L-2-hydroxyglutarate Enantiomers by Chiral Derivatization Combined with Liquid Chromatography/Mass Spectrometry Analysis. *Science Reports* **5**, 15217 (2015).

106 Fukui, S. *et al.* Rapid chiral discrimination of oncometabolite dl-2-hydroxyglutaric acid using derivatization and field asymmetric waveform ion mobility spectrometry/mass spectrometry. *Journal of Separation Science* **44**, 3489–3496 (2021).

107 Ohtawa, T. & Tsunoda, M. An on-line heart-cutting two-dimensional liquid chromatography method for intracellular 2-hydroxyglutarate enantiomers. *Analytical Methods* **15**, 2833–2838 (2023).

108 Lan, C. *et al.* Absolute quantification of 2-hydroxyglutarate on tissue by matrix-assisted laser desorption/ionization mass spectrometry imaging for rapid and precise identification of isocitrate dehydrogenase mutations in human glioma. *International Journal of Cancer* **149**, 2091–2098 (2021).

109 Liu, D., Evans, T. & Zhang, F. Applications and advances of metabolite biosensors for metabolic engineering. *Metabolic Engineering* **31**, 35–43 (2015).

110 Kang, Z. *et al.* An L-2-hydroxyglutarate biosensor based on specific transcriptional regulator LhgR. *Nature Communications* **12**, 3619 (2021).

111 Hou, S. *et al.* An enzymic l-2-hydroxyglutarate biosensor based on l-2-hydroxyglutarate dehydrogenase from Azoarcus olearius. *Biosensors and Bioelectronics* **243**, 115740 (2024).

112 Balss, J. *et al.* Enzymatic assay for quantitative analysis of (D)-2-hydroxyglutarate. *Acta Neuropathologica* **124**, 883–891 (2012).

113 Yang, J., Chen, X., Jin, S. & Ding, J. Structure and biochemical characterization of l-2-hydroxyglutarate dehydrogenase and its role in the pathogenesis of l-2-hydroxyglutaric aciduria. *Journal of Biological Chemistry* **300**, 105491 (2024).

114 Kalliri, E., Mulrooney, S. B. & Hausinger, R. P. Identification of Escherichia coli YgaF as an L-2-hydroxyglutarate oxidase. *Journal of Bacteriology* **190**, 3793–3798 (2008).

115 Vigder, N., Cordwell, S. J., & Loscalzo, J. *Network medicine: A new paradigm for cardiovascular disease research and beyond*. In C. Banfi (Ed.), *Cardiovascular Proteomics Techniques* (Chap. 16). John Wiley & Sons (2026). https://doi.org/10.1002/9781394211166.ch16

Chapter 2

A Novel Role for L-2-Hydroxyglutarate in Triglyceride and Fatty Acid Metabolism and Lipid Droplet (Patho)biology

2.1 Introduction

Lipids constitute a central and versatile class of biomolecules that support cell structure, energy homeostasis, and signal transduction across virtually all mammalian tissues. In primary, non-transformed human cells, lipid metabolism operates within a tightly regulated physiological framework, integrating substrate availability, hormonal cues, redox state, and mitochondrial function to maintain cellular homeostasis[1,2]. Dysregulation of these processes contributes to a broad spectrum of cardiometabolic disorders[3,4]; however, even under basal conditions, lipid metabolic pathways exhibit remarkable plasticity and inter-organ coordination[5,6].

Cellular lipids comprise several major classes that differ in structure, biosynthesis, and biological function. These include glycerolipids, such as triglycerides (TGs) and diacylglycerols (DAGs), which primarily serve in energy storage and signaling[1,7]; glycerophospholipids, including phosphatidylcholine (PC), phosphatidylethanolamine (PE), phosphatidylserine (PS), phosphatidylglycerol (PG), and phosphatidylinositol (PI), which are essential structural components of membranes and platforms for signal transduction[8]; and sphingolipids, such as ceramides and sphingomyelins, which contribute to membrane organization and act as bioactive signaling molecules[9]. Additional lipid classes, including sterols and sterol esters, further expand the functional lipid repertoire by regulating membrane fluidity, intracellular trafficking, and hormone synthesis[10]. These lipid classes form an interconnected metabolic network, with shared intermediates and coordinated regulation that allow cells to balance structural integrity, signaling, and energy homeostasis.

Given current understanding that L-2-hydroxyglutarate (L2HG) perturbs carbohydrate metabolism (see Section 1.3) and considering the extensive metabolic interplay between carbohydrate and fatty acid metabolism[11], we hypothesized that L2HG also influences TG and fatty acid metabolism. To establish the relevant background for the current chapter, the following sections examine TG and fatty acid (patho)biology in greater detail.

2.1.1 TG metabolism

Glycerolipids – and, in particular, TGs – serve as a dominant form of energy storage in humans, buffering fluctuations in nutrient availability and metabolic demand[1,2,7]. TGs are synthesized

through the esterification of fatty acyl chains onto a glycerol backbone *via* acyl-CoA (which are generated from free fatty acids and coenzyme A by acyl-CoA synthetases), a process that links carbohydrate metabolism, fatty acid availability, and cellular energy status. TGs, composed of three fatty acids esterified to glycerol, represent the terminal storage form of this pathway. In most primary human cells, with the exception of enterocytes, TG synthesis proceeds predominantly through the glycerol-3-phosphate (G3P) pathway in the mitochondria or endoplasmic reticulum (ER), with G3P derived from glycolysis or from glycerol phosphorylation, depending on cell type and enzymatic capacity[12,13].

The stepwise acylation reactions of G3P by *sn*-1-G3P acyltransferases (GPAT1–4) and 1-acylglycerol-3-phosphate acyltransferases (AGPAT1–3) yield lysophosphatidic acid (LPA) and phosphatidic acid (PA), respectively. Dephosphorylation of PA by lipins (LPIN1–3; also known as PA phosphatases, PAPs) yields DAG which are further acylated by DAG acyltransferases (DGAT1–2) to form TG. This pathway of TG synthesis intersects directly with phospholipid biosynthesis, as PA is the shared precursor for PI, PG, and cardiolipin, while DAG is the shared precursor for PS, PC, and PE. In addition to this canonical TG pathway, alternative routes exist and can contribute under specific metabolic contexts. These include the acylation of dihydroxyacetone phosphate (DHAP) by DHAP acyltransferase (DHAPAT) in peroxisomes followed by reduction to LPA[14,15], as well as the acylation of *sn*-2-monoacylglycerol (MAG) in the endoplasmic reticulum *via* monoacylglycerol acyltransferases (MGAT1–2)[16].

2.1.2 Lipid droplets as dynamic metabolic organelles

TGs are stored intracellularly within lipid droplets (LDs), which are specialized organelles composed of a neutral lipid core surrounded by a phospholipid monolayer and containing a distinct proteome. LDs also store cholesteryl esters (CEs), the esterified form of cholesterol which, together with TGs, constitute the predominant neutral lipid classes within cells. Once considered inert lipid depots, LDs are now recognized as highly dynamic structures that coordinate lipid storage, mobilization, and inter-organelle communication[17,18]. In primary human cells, LDs respond rapidly to changes in nutrient supply, hormonal signaling, and energetic demand, expanding or contracting through tightly controlled enzymatic processes[17,18].

LD biogenesis originates at the ER, where newly synthesized neutral lipids accumulate between the ER membrane leaflets before budding into the cytosol. The size, number, and composition of LDs vary substantially across cell types[19]. Adipocytes contain large unilocular droplets optimized for long-term energy storage, whereas non-adipose cells harbor smaller, more transient LDs that serve as short-term buffers against fatty acid excess and lipotoxic stress[17,18,20]. Importantly, LDs play a protective role in primary cells by sequestering excess fatty acids that would otherwise disrupt membrane integrity, induce oxidative stress, or impair mitochondrial function – a phenomenon collectively referred to as lipotoxicity[5,21,22]. The regulated packaging of fatty acids into TGs within LDs therefore represents not merely energy storage, but a broader cellular defense mechanism. Conversely, impaired LD homeostasis can expose cells to cytotoxic lipid intermediates, highlighting the necessity of balanced TG and fatty acid metabolism.

2.1.3 Mobilization of TGs

The mobilization of stored TGs requires enzymatic hydrolysis. Intracellular TG breakdown occurs through two principal pathways: neutral lipolysis at the surface of cytosolic LDs and acid lipolysis within lysosomes following autophagic delivery of LDs through a process referred to as lipophagy[23,24]. Neutral lipolysis proceeds through a conserved, stepwise enzymatic cascade involving adipose triglyceride lipase (ATGL; encoded by *PNPLA2*), hormone-sensitive lipase (HSL; encoded by *LIPE*), and MAG lipase (MGL; encoded by *MGLL*), which sequentially hydrolyze TGs to DAGs, MAG, and free fatty acids, respectively. By contrast, acid lipolysis is mediated by lysosomal acid lipase (LAL; encoded by *LIPA*), which hydrolyzes TGs and other neutral lipids (including cholesteryl esters) delivered to lysosomes through autophagic or endocytic routes. Taken together, these pathways ensure controlled liberation of fatty acids from intracellular lipid stores across diverse cell types.

Among neutral lipases, ATGL functions as the primary rate-limiting enzyme for TG hydrolysis and is activated by its obligate co-activator 1-acylglycerol-3-phosphate *O*-acyltransferase (ABHD5, also known as comparative gene identification 58, CGI-58). ATGL deficiency induced by loss-of-function *PNPLA2* mutations results in profound TG accumulation and is the cause of neutral lipid storage disease with myopathy in humans[25] and cardiomyopathy and death in mice at 3–4 months old[26], whereas HSL deficiency induced by loss-of-function mutations in *LIPE* are

characterized by relatively more mild forms of dyslipidaemia, hepatic steatosis, type 2 diabetes and partial lipodystrophy[27,28]. MGL completes the final hydrolytic step, ensuring efficient release of free fatty acids. Lipase activity is further regulated by post-translational modifications (PTMs), including phosphorylation[29-32], as well as by interactions with LD–associated proteins, forming a highly coordinated lipolytic protein network referred to as the "lipolysome"[33]. A central component of this regulatory network is the perilipin (PLIN) family of LD–associated proteins, which act as gatekeepers of lipolysis by controlling lipase access to the LD surface[7,34]. Under basal conditions, PLINs shield stored TGs from constitutive hydrolysis, whereas upon appropriate signaling they undergo conformational changes and PTMs that permit recruitment and activation of lipolytic enzymes. For example, Granneman and colleagues demonstrated that PLIN1 suppresses basal lipolysis by binding and sequestering ABHD5 away from ATGL, whereas phosphorylation of PLIN1 at Ser492 or Ser517 releases ABHD5 to interact with ATGL, an interaction that occurs predominantly on PLIN-containing LD[35]. Importantly, distinct PLIN isoforms exhibit tissue-specific expression and functional specialization, thereby enabling fine-tuned regulation of TG mobilization across different cellular contexts. For a more detailed review of PLIN (patho)biology, the reader is referred to Refs.[17,18,36-38].

Following release, fatty acids may be re-esterified, incorporated into signaling lipids, or directed toward mitochondrial oxidation depending on cellular context and energetic demand. In tissues with high oxidative capacity, such as heart and skeletal muscle, lipolysis-derived fatty acids provide a major substrate pool for mitochondrial β-oxidation. Indeed, cardiac and skeletal muscle energy metabolism cannot be explained by glucose oxidation alone and instead is largely supported by fatty acids, which are taken up from plasma, transiently esterified into intracellular TG pools, and subsequently released by lipolysis to fuel mitochondrial oxidation during rest and exercise[39]. The functional integration of lipolysis with downstream fatty acid utilization emphasizes that TG mobilization is not merely a fuel-releasing process, but a central regulatory node in cellular metabolism.

2.1.4 Fatty acid oxidation

Mitochondrial fatty acid β-oxidation (FAO) constitutes the principal pathway for the degradation of fatty acids and is essential for maintaining whole-body and cellular energy homeostasis,

particularly under conditions of limited glucose availability such as fasting or sustained energy demand. Fatty acids serve as a major oxidative substrate in organs with high and continuous energetic requirements, including heart, skeletal muscle, kidney, and liver, wherein FAO remains a substantial energy source even when glucose is abundant. In this process, fatty acids are activated in the cytosol to fatty acyl-CoA esters by acyl-CoA synthetases (of which there are 26 in mammals[40]) and subsequently imported into mitochondria, where they undergo stepwise β-oxidation to generate acetyl-CoA, NADH, and $FADH_2$, thereby fueling the TCA cycle, ketogenesis, and oxidative phosphorylation.

Since the inner mitochondrial membrane is impermeable to long-chain acyl-CoAs, mitochondrial FAO of long-chain fatty acids requires the carnitine shuttle[41]. This transport system consists of carnitine palmitoyltransferase 1 (CPT1), which converts acyl-CoAs to acylcarnitines at the outer mitochondrial membrane; carnitine–acylcarnitine translocase (CACT), which exchanges acylcarnitines for free carnitine across the inner membrane; and carnitine palmitoyltransferase 2 (CPT2), which reconverts acylcarnitines to acyl-CoAs in the mitochondrial matrix. In contrast, medium- and short-chain fatty acids can enter mitochondria independently of the carnitine cycle. Once inside the matrix, fatty acyl-CoAs are degraded through a cyclic sequence of four reactions – dehydrogenation, hydration, dehydrogenation, and thiolysis – each cycle shortening the acyl chain by two carbons and producing acetyl-CoA which can subsequently feed into, for example, the TCA cycle or ketogenesis[42].

FAO is mediated by a coordinated set of chain-length–specific enzymes that together enable the complete oxidation of long-, medium-, and short-chain fatty acids. Very long-chain acyl-CoAs are initially processed by membrane-associated enzymes such as very-long-chain acyl-CoA dehydrogenase and the mitochondrial trifunctional protein, whereas medium- and short-chain intermediates are subsequently handled by matrix-localized enzymes including medium-chain and short-chain acyl-CoA dehydrogenases and their associated hydratases, dehydrogenases, and thiolases. The electron equivalents generated during FAO are transferred *via* electron-transfer flavoprotein to the respiratory chain, thereby linking fatty acid catabolism to ATP production. The physiological importance of this pathway is underscored by the severe metabolic, cardiac, and muscular phenotypes observed in inherited FAO disorders[43], highlighting FAO as a central determinant of metabolic flexibility and energy balance in mammalian systems.

2.1.5 Integration of TG storage and FAO

A defining feature of lipid metabolism in primary human cells is the continuous interplay between TG synthesis, storage, mobilization, and oxidation. Rather than representing opposing processes, TG storage and FAO function as complementary components of a unified metabolic system that stabilizes intracellular fatty acid availability. This integration allows cells to buffer fluctuations in nutrient supply while maintaining mitochondrial efficiency and limiting lipotoxic stress. Emerging evidence suggests that the spatial organization of LDs relative to mitochondria further facilitates this coordination, enabling efficient channeling of fatty acids toward oxidation when demand increases. For example, LDs and mitochondria engage in both dynamic transient and stable anchored interactions, mediated by proteins such as PLIN1 and PLIN5[44,45]. Furthermore, Talati *et al.*[46] demonstrated that the liver contains a distinct population of mitochondria (referred to as peridroplet mitochondria) that are physically tethered to LD and are functionally specialized for higher FAO flux compared with cytoplasmic mitochondria through increased CPT1 activity during *ad libitum* feeding. In the same study, the authors showed that FAO in peridroplet mitochondria is selectively impaired in high-fat diet–induced non-alcoholic fatty liver disease (NAFLD), indicating that disruption of this TG–lipolysis–FAO interface contributes to hepatic steatosis and metabolic disease. Such physical and functional coupling between LDs and mitochondria underscores the concept that LDs are active participants in cellular energy metabolism rather than passive storage sites[47].

2.1.6 Classification and nomenclature of lipids

Lipid metabolic intermediates and end-products do not represent single molecular entities but rather classes of molecules that encompass diverse molecular species, distinguished by acyl chain length, degree of saturation, and backbone composition. For example, acylation of G3P with oleoyl-CoA yields PA with an 18-carbon fatty acid chain containing one double bond, while acylation with palmitoyl-CoA yields PA with a 16-carbon saturated fatty acid chain (denoted in LIPID MAPS [lipidmaps.org[48]] notation as PA(18:1) and PA(16:0), respectively). In LIPID MAPS notation for lipids containing more than one fatty acyl chain, an underscore denotes that the overall acyl composition is known without assignment of sn-positions on the glycerol backbone, whereas a slash indicates positional resolution of the acyl chains. For example, TG(18:1_16:0_16:1)

specifies the acyl composition only, while TG(18:1/16:0/16:1) denotes defined sn-1, sn-2, and sn-3 positioning. Because the specific acyl chain composition of a given lipid species can confer distinct biochemical functions, cellular origins, and metabolic fates, it is essential to resolve individual molecular species rather than lipid classes alone. Accordingly, liquid chromatography tandem mass spectrometry (LC–MS/MS)-based lipidomics represents the gold-standard analytical approach[49], as classical colorimetric assays and thin-layer chromatography lack the molecular resolution required to discriminate among species within a single lipid class, resulting in substantial loss of biologically relevant information. Notably, however, the LC–MS/MS approach used herein does not always permit unambiguous assignment of sn-positions on the glycerol backbone.

Collectively, the work summarized above establishes TG and fatty acid metabolism as highly dynamic, tightly regulated processes that are intimately integrated with central carbon metabolism, mitochondrial function, and redox state. Given the extensive biochemical overlap between carbohydrate utilization, lipid synthesis, lipid storage, and FAO – and considering prior evidence demonstrating that L2HG perturbs glycolysis, mitochondrial metabolism, and redox balance (see Section 1.3) – it is plausible that L2HG exerts broader effects on lipid metabolic networks. In particular, pathways governing glycerolipid synthesis, LD dynamics, lipolysis, and FAO share substrates, cofactors, and regulatory nodes with glycolytic and mitochondrial processes previously shown to be sensitive to L2HG. For example, L2HG stabilizes HIF-1α protein (see Section 1.3), the downstream outcome of which may be differential regulation of lipid-related genes. These considerations provide a strong biological rationale to interrogate whether accumulation of 2HG, and predominantly the L enantiomer, reshapes the cellular lipidome, with a specific focus on TG composition and turnover. Accordingly, the central hypothesis of this work is that L2HG alters TG and fatty acid metabolism by reprogramming the balance between lipid synthesis, storage, and oxidation.

2.2 Methods and materials

2.2.1 Chemicals and reagents

LC–MS grade water (cat. no. LC365), methanol (cat. no. 34966), and acetonitrile (cat. no. LC015), were purchased from Honewell. LC–MS-grade chloroform (cat. no. AC364320010), isopropanol

(cat. no. A461), and iodoacetamide (cat. no. 122270050) were purchased from Fisher Scientific. d_8-valine (cat. no. DLM-311), $^{13}C_5$-glutamine (cat. no. CLM-1822), and $^{13}C_{18}$-oleic acid (cat. no. 490431) were purchased from Cambridge Isotope Laboratories. $^{14}C_1$-palmitic acid (cat. no. NEC075H050UC) was purchased from Revvity. LC–MS vials (cat. no. 5182-0716) with 250 µL inserts (cat. no. 5183-2085) were purchased from Agilent. Butylated hydroxytoluene (cat. no. B1378), ammonium carbonate (cat. no. 379999), medronic acid (cat. no. 64255), ammonium formate (cat. no. 70221), unmodified L2HG (cat. no. 90790), dithiothreitol (cat. no. D0632), sodium dodecyl sulfate (SDS; cat. no. 151213) and oleic acid (cat. no O1008) were purchased from Sigma. EquiSPLASH™ (cat. no. 330731) and Carnitine SPLASH™ (cat. no. 330379) were purchased from Avanti Polar Lipids. Octyl-L2HG (OL2HG, cat. no. 16367), octyl-D2HG (OD2HG, cat. no. 16366), octyl-α-ketoglutarate (OαKG, cat. no. 11970), carnitine (cat. no. 21489), BSA–palmitate complex (cat. no. 29558), etomoxir (cat. no. 11969), PF-06424439 (cat. no. 17680), and A-922500 (cat. no. 10012708) were purchased from Cayman Chemical.

2.2.2 Cell culture and treatments

Primary human cardiac myocytes (HCM) isolated from the ventricles of an adult heart (cat. no. C-12810, PromoCell) were cultured in complete myocyte growth medium (cat. no. C-22070, PromoCell). Primary human pulmonary artery endothelial cells (HPAEC; cat. no. CC-2530, Lonza) were cultured in endothelial basal medium (cat. no. CC-3156, Lonza) with supplements (cat. no. CC-4176, Lonza). Primary human ventricular cardiac fibroblasts (HCF; cat. no. CC-2904, Lonza) were cultured in fibroblast growth medium (cat. no. CC-3131, Lonza) with supplements (cat. no. CC-45525, Lonza). Primary human pulmonary arterial smooth muscle cells (PASMC; cat. no. CC-2581, Lonza) and human coronary artery smooth muscle cells (CASMC; cat. no. CC-2583, Lonza) were cultured in SmBM® Basal Medium (cat. no. CC-3181, Lonza) and SmGM®-2 SingleQuots® supplements (cat. no. CC-4149, Lonza). HepG2 cells (cat. no. HB-8065, ATCC) were purchased from ATCC and cultured in DMEM containing 10% (v/v) fetal bovine serum (FBS). Passages 4–7 were used for all primary cell types, with the exception of HCMs, which were used between passage 5 and 9. The cells used in this study were obtained from commercial sources and were marketed by the suppliers as originating from non-diseased donors.

All cells were maintained at 37 °C in an incubator with 95% humidity and 5% CO_2. Medium was refreshed every other day for cell growth. For treatments, cells were refreshed with new media supplemented with the appropriate treatment for 24 h at the following concentrations, unless otherwise indicated in the main text or Figure legends: OL2HG (500 μM), OD2HG (500 μM), octyl acetate (0.25–1 mM), unmodified L2HG (0.5–2 mM), A-922500 (10 μM), PF-06424439 (10 μM). For hypoxic experiments, HCMs were exposed to 0.5% (v/v) O_2 for 24 h using a modular hypoxia chamber. For controls, an equal volume of sterile dimethylsulfoxide (DMSO, cat. no. D2650, Sigma) was used, except where otherwise indicated where ultrapure DNase/RNase-free distilled water (cat. no. 10977015, Thermo Fisher) was used as an additional control.

2.2.3 Lipogenesis, lipolysis, and acylcarnitine flux experiments

Stable-isotope tracing was used to quantify flux through TG synthesis and fatty acid handling using two complementary experimental designs. In both approaches, oleic acid uniformly labeled with heavy carbon ($^{13}C_{18}$-oleate) was supplied at 50 μM, and lipid species were quantified by LC–MS-based on isotopologue composition, as described in Section 2.2.5, with emphasis on TG containing three labeled oleate chains (TG[3 × $^{13}C_{18}$-oleate]) and labeled $^{13}C_{18}$-oleoylcarnitine. For all experiments, cells were plated in 12-well plates at 150,000 cells / well, with the exception of HCMs which were used at 75,000 cells / well.

The first approach was designed to assess labeling/appearance kinetics. Cells were pre-treated with vehicle (DMSO) or OL2HG (500 μM) for 24 h, after which complete medium was refreshed containing only $^{13}C_{18}$-oleate (50 μM). Cells were harvested at variable time points between 1 and 24 h following tracer addition. Lipogenic flux from extracellular oleate into TG stores was inferred from the time-dependent appearance of TG[3 × $^{13}C_{18}$-oleate], while fatty acid activation/handling toward mitochondrial import was assessed from the appearance of $^{13}C_{18}$-oleoylcarnitine.

In the second approach, a classic pulse–chase design was implemented. Cells were first pulsed with complete medium containing $^{13}C_{18}$-oleate (50 μM) for 24 h to pre-label intracellular lipid pools. Media were then replaced with fresh medium containing equimolar unlabeled oleate ($^{12}C_{18}$-oleate) together with either DMSO or OL2HG (500 μM), and cells were harvested across a 0–24 h chase. Turnover/clearance of pre-labeled lipid pools was quantified using LC–MS, as described in Section 2.2.5, from the clearance kinetics of TG[3 × $^{13}C_{18}$-oleate] and $^{13}C_{18}$-oleoylcarnitine,

whereas concurrent synthesis and/or recycling under chase conditions was assessed from the appearance of newly synthesized TG[3 × $^{12}C_{18}$-oleate] and $^{13}C_{18}$-oleoylcarnitine over time.

2.2.4 RNA sequencing

HCMs and PAECs were plated in 6-well plates at 150,000 cells / well or 250,000 cells / well, respectively, and allowed to adhere overnight. Cells were then treated with vehicle (DMSO) or OL2HG (500 μM) for 24 h (n = 4 replicates *per* condition). Following treatment, cells were washed twice with LC–MS-grade water and total RNA was isolated using the miRNeasy kit (cat. no. 217604, Qiagen) according to the manufacturer's instructions. RNA concentration and purity were assessed by UV spectrophotometry using a NanoDrop (cat. no. 3400518, Thermo Scientific). RNA samples were shipped to Innomics Inc. (Cambridge, MA, USA) for library preparation, sequencing, and primary data processing. Processed expression data were returned as transcript-*per*-million (TPM) matrices and were subsequently aggregated at the gene level, as multiple transcript entries *per* gene were present, prior to downstream targeted analyses of genes of interest.

2.2.5 Semi-targeted metabolomics, non-targeted lipidomics, and stable-isotope–based fluxomics

All solvents outlined below are LC–MS-grade.

2.2.5.1 Sample preparation

For metabolomic analyses, cells were plated in 6-well plates at a concentration of 2.5 x 10^5 cells / well with the exception of HCM, which were plated at 1 x 10^5 cells / well. For lipidomic analyses, cells were plated in 12-well plates at a concentration of 1.25 x 10^5 cells / well with the exception of HCM, which were plated at 5 x 10^4 cells / well. Cells were treated as described in the main text and Figure legends, washed twice with LC–MS-grade water, flash-frozen by placing the plate on liquid N_2, and stored at -80 °C until LC–MS analysis as described below.

Metabolites were extracted from frozen cells or plasma/medium (50 μL) by adding 200 μL of extraction buffer [50/30/20 (v/v/v) methanol/acetonitrile/water containing 1 μM d_8-valine and1 μM $^{13}C_5$-glutamine] to each well of the plate on ice. After ~10 min, lysates were scraped, collected, and centrifuged (17,000 x *g*, 10 min, 4 °C). The supernatant (180 μL) was concentrated to dryness

at 45 °C using a refrigerated CentriVap vacuum concentrator equipped with a cold trap (Labconco). Dried extracts were kept at -80 °C. Immediately before LC–MS analysis, extracts were reconstituted in 50 µL of water, centrifuged (17,000 x *g*, 10 min, 4 °C), and 35 µL of the supernatant transferred to glass LC–MS vials for analysis. For each experimental batch, an additional 10 µL of the supernatant from each sample were pooled, centrifuged (17,000 x *g*, 10 min, 4 °C), and transferred to glass LC–MS vials for quality control purposes.

To extract lipids from frozen cells or plasma (50 µL), 200 µL of 1/1 (v/v) methanol/water were added to each well of the plate. After ~10 min, lysates were scraped and collected. To each lysate, 50 µL of butylated hydroxytoluene (1 mg/mL in methanol), 5 µL of an internal standard mixture [1/1/38 (v/v/v) EquiSPLASH™/Carnitine SPLASH™ /methanol), and 200 µL of chloroform were added. The mixtures were mixed vigorously for 30 s, centrifuged (17,000 x *g*, 10 min, 4 °C), and 180 µL of the bottom chloroform layer were collected and concentrated to dryness under a gentle stream of N_2 gas. Dried extracts were kept at -80 °C. Immediately before LC–MS analysis, extracts were reconstituted in 100 µL of 1/1 (v/v) chloroform/methanol, centrifuged (17,000 x *g*, 10 min, 4 °C), and 80 µL of the supernatant were transferred to amber glass LC–MS vials for positive and negative acquisition, as described below. For each experimental batch, an additional 10 µL of the supernatant from each sample were pooled, centrifuged (17,000 x *g*, 10 min, 4 °C), and transferred to glass LC–MS vials for quality control purposes.

2.2.5.2 LC–MS data acquisition and analysis

LC–MS analyses were performed using a Vanquish ultra-high-performance liquid chromatography (UHPLC) system connected to a Q Exactive Orbitrap mass spectrometer with a heated electrospray ionization (HESI)-II source (Thermo Fisher Scientific). Samples were stored in the autosampler at 5 °C prior to injection. For metabolomics, the following chromatographic parameters were used: solvent A, 20 mM ammonium carbonate in water containing 5 µM medronic acid, pH corrected to 9.2 with ammonium hydroxide; solvent B, acetonitrile; injection volume, 2 µL; oven temperature, 25 °C; flow rate, 0.1 mL/min. Compounds were separated using a SeQuant zwitterionic polymer-based hydrophilic interaction liquid chromatography (ZIC-pHILIC) column (5 µm, 150 × 2.1 mm; Merck) with a guard column and a linear gradient of solvent B as follows: 0 min, 80%; 20 min, 20%; 20.5 min, 8%; 24 min, 8%; 24.5 min; 80%; 35 min, 80%. MS scan parameters were as

follows: scan type, full MS; scan range, 60-900 Th; fragmentation, none; resolution, 70,000; microscans, 1; lock masses, off; automatic gain control (AGC) target, 1 x 10^6; maximum injection time, 80 ms. The MS was operated in polarity switching mode. HESI source parameters were as follows: sheath gas flow rate, 40, auxiliary gas flow rate, 15; sweep gas flow rate, 1; spray voltage, 1 kV; capillary temperature, 320 °C; S-lens radio frequency level, 50; auxiliary gas heater temperature, 350 °C. Semi-targeted peak identification was performed using the Thermo TraceFinder General LC software (Thermo Fisher Scientific), using an in-house library of ~150 metabolites with known retention times, as assessed and optimized previously with authentic standards using the same method parameters.

For lipidomics, the following chromatographic parameters were used: solvent A, 10 mM ammonium formate in 60/40 (v/v) acetonitrile/water; solvent B, 10 mM ammonium formate in 90/10 (v/v) isopropanol/acetonitrile; injection volume, 5 µL; oven temperature, 55 °C; flow rate, 0.3 mL/min. Compounds were separated using an ACQUITY UPLC charged surface hybrid (CSH) C18 column (1.7 µm, 100 × 2.1 mm; Waters) with a guard column and a linear gradient of solvent B as follows: 0 min, 0%; 6 min, 40%; 30 min, 100%; 34 min, 100%; 36 min; 0%; 40 min, 0%. Data were acquired using data-dependent MS^2 acquisition. MS^1 scan parameters were as follows: scan type, full MS; scan range, 200-1200 Th; fragmentation, none; resolution, 70,000; microscans, 1; lock masses, off; AGC target, 1 x 10^6; maximum injection time, 250 ms. MS^2 scan parameters were as follows: scan type, AIF; scan range, 200-1200 Th; fragmentation, collision energy, 30; resolution, 17,500; microscans, 1; lock masses, off; AGC target, 1 x 10^5; maximum injection time, 120 ms; loop count, 5; TopN, 5; isolation window, 1.0 m/z; first fixed mass, 50 m/z. Data dependent (dd) settings were as follows: maximum AGC target, 5 x 10^3; intensity threshold, 4.2 x 10^4; apex trigger, off; charge exclusion, off; peptide match, off; exclude isotopes, off; dynamic exclusion, 20 s. Positive and negative acquisition modes were used separately. HESI source parameters were as follows: sheath gas flow rate, 40 for negative mode and 50 for positive mode, auxiliary gas flow rate, 15 for negative mode and 7 for positive mode; sweep gas flow rate, 1 for negative mode and 5 for positive mode; spray voltage, 3 kV; capillary temperature, 320 °C for negative mode and 300 °C for positive mode; S-lens RF level, 70; auxiliary gas heater temperature, 350 °C for negative mode and 300 °C for positive mode. Non-targeted lipidomic analysis was performed using LipidMatch (Innovative Omics) with blank filtering. Only the features with the highest confident

identifications (*i.e.,* confirmed by MS^2) were used for subsequent statistical analyses. For stable isotope flux experiments with $^{13}C_{18}$-oleate, peaks of interest were integrated manually using the software Freestyle (Thermo Fisher Scientific).

For both metabolomics and lipidomics, peak intensities for each feature were normalized to the total metabolite pool (sum of integrated peak intensities across all identified semi-targeted features) or total lipid pool (sum of integrated peak intensities across all MS^2-confirmed lipid features), respectively. Pool-normalization was selected because the global metabolome and lipidome were stable across treatment conditions while only a defined subset of species was altered, allowing the total-pool sum to serve as an internal biomass reference that controls for inter-sample differences in extracted material. Cell viability and morphology were monitored visually at harvest in all experiments; OL2HG treatment (500 μM, 24 h) did not produce detectable changes in adherence, morphology, or cell number across the primary cell types used. In experiments where treatments were anticipated to affect viability, protein-content normalization was applied *a priori*.

2.2.6 LC–MS-based proteomics

2.2.6.1 Cell lysis, protein reduction, and protein alkylation

HCMs were plated in 6-well plates at a density of 150,000 cells *per* well and allowed to adhere overnight. Cells were treated for 24 h with one of four conditions: vehicle control (DNase/RNase-free water + DMSO), L2HG (500 μM, prepared in DNase/RNase-free water), octyl acetate (OA; 500 μM, prepared in DMSO), or OL2HG (500 μM, prepared in DMSO). Following treatment, cells were washed twice with LC–MS-grade water, snap-frozen in liquid N_2, and stored at −80 °C until proteomic sample preparation. Cell lysis was performed using 100 μL of 8 M urea in 200 mM EPPS buffer (pH 8.5, corrected with ammonium hydroxide) supplemented with Pierce™ protease inhibitors (cat. no. A32955, Thermo Fisher). Cells were lysed by syringe lysis and sonication. Protein concentration was determined by bicinchoninic acid (BCA) assay. Samples were reduced with dithiothreitol (10 mM, 30 min, room temperature) and alkylated with iodoacetamide (20 mM, 1 h, room temperature, protected from light). Samples were then standardized to 50 μg total protein (final volume, 109 μL) prior to downstream processing.

2.2.6.2 Tissue homogenization, protein reduction, and protein alkylation

For proteomics analysis of baseline-perfused, fatty acid-deprived hearts, whole hearts were homogenized in 500 µL of 6 M urea, 2 M thiourea containing 1 µM pepstatin A (cat. no. P5318, Sigma), 1 µM leupeptin (cat. no. L5793, Sigma), 1 µM aprotinin, and 10 mM dithiothreitol using a hand-held homogenizer (Omni, Kennesaw GA). The homogenate was subsequently transferred to bead-beating tubes preloaded with 100 µL of 10% (w/v) SDS and acid-washed glass beads (cat. no. G4649, Sigma) and further disrupted using a bead-beating homogenizer (cat. no. P002511-PEVT0-A.0-BER, Precellys Evolution Touch), yielding a final volume of 600 µL and a final SDS concentration of 1.67% (w/v). Samples were then incubated at room temperature for 30 min to allow for protein reduction, followed by alkylation using 20 mM iodoacetamide for 1 h in the dark.

2.2.6.3 Protein extraction, digestion, and cleanup

Proteins were precipitated by chloroform–methanol extraction through sequential addition of chloroform (250 µL), methanol (250 µL), and water (125 µL), followed by vigorous mixing for 5 s and centrifugation (8,000 × *g*, 5 min, 4 °C) to pellet proteins. Pellets were resuspended in 100 µL of 200 mM EPPS (pH 8.5) using tip-probe sonication and digested overnight at 37 °C with shaking at 600 r.p.m. and digested using a Trypsin/Lys-C protease mix at a 25:1 protein-to-protease ratio. Digestion was quenched by acidification to ~1% trifluoroacetic acid (TFA; cat. no. 85183, Thermo Fisher Scientific), followed by centrifugation (14,000 × *g*, 15 min, room temperature).

Peptides were desalted by reversed-phase solid-phase extraction using Oasis hydrophilic-lipophilic balance (HLB) cartridges (cat. no. 186000383, Waters). Cartridges were washed and equilibrated sequentially with 200 µL methanol, 200 µL acetonitrile, 200 µL 70:30 (v/v) acetonitrile:water containing 0.1% (v/v) TFA, and three washes with 200 µL 0.1% (v/v) TFA. Samples were loaded onto cartridges, with eluate reloaded twice to enhance peptide binding, washed three times with 200 µL 0.1% (v/v) TFA, and eluted with 200 µL 70:30 (v/v) acetonitrile:water containing 0.1% (v/v) TFA. Desalted peptides were dried to completeness under vacuum using a refrigerated CentriVap concentrator equipped with a cold trap (Labconco).

2.2.6.4 Tandem mass tag (TMT) labeling

TMT labeling was performed as described previously[50,51], with minor modifications. Dried peptides were reconstituted in 200 mM EPPS (pH 8.5; NaOH-adjusted) and aliquoted for labeling. Peptides (25 µg *per* channel) were labeled with TMTpro 16-plex reagents (cat. no. A44521, Thermo Fisher Scientific) at a peptide-to-label ratio of 1:2.5 (w/w) and incubated for 1 h at room temperature. Labeling efficiency and relative channel intensities were assessed by LC–MS/MS as described below using a pooled test mixture. Following normalization based on reporter ion intensities, labeling reactions were quenched with hydroxylamine (5% (v/v) stock; final concentration, 0.3% (v/v)). Labeled samples were pooled according to corrected ratios, diluted with 200 mM EPPS (pH 8.5) to reduce acetonitrile content to 7.5% (v/v), acidified to 1% (v/v) TFA, and desalted as described above.

2.2.6.5 Off-line basic pH reversed-phase (BPRP) fractionation

We fractionated the pooled TMT-labeled peptides *via* BPRP HPLC with an Agilent 1260 pump. Peptides were subjected to a 560 min linear gradient from 5% to 35% acetonitrile in 10 mM ammonium bicarbonate pH 8 at a flow rate of 0.25 mL/min over an Agilent 300Extend C18 column (3.5 µm particles, 2.1 mm ID and 25 cm long). The peptide mixture was fractionated into a total of 96 fractions, which were consolidated into 24 super-fractions and subjected to FAIMS-MS/MS. These fractions were subsequently acidified with 1% formic acid and vacuum centrifuged to near dryness. Each fraction was also desalted as described above, dried *via* vacuum centrifugation, and reconstituted in 5% acetonitrile, 5% formic acid for LC–MS/MS.

2.2.6.6 Data collection

Mass spectrometric data were collected on an Orbitrap Eclipse mass spectrometer coupled to a Vanquish Neo UHPLC. Approximately 1µg of peptide was separated at a flow rate of 450 nL/min on a 100 µm capillary column that was packed with 35 cm of Accucore 150 resin (2.6 µm, 150Å; Thermo Fisher Scientific). The scan sequence began with an MS1 spectrum (Orbitrap analysis, resolution 60,000, 350-1350 Th, AGC) target is set to 100%, maximum injection time set to "auto"). Data were acquired over 90 minutes *per* fraction. The high resolution MS2 stage consisted of fragmentation by higher energy collisional dissociation (HCD, normalized collision energy

36%) and analysis using the Orbitrap (AGC 200%, maximum injection time 120ms, isolation window 0.6 Th, resolution 30,000 Turbo TMT). Data were acquired using the FAIMSpro interface with the dispersion voltage (DV) set to 5,000 V, the compensation voltages (CVs) were set at -30 V, -50 V, and -70 V. The TopSpeed parameter was set at 1 s per CV[52].

2.2.6.7 Data analysis

Mass spectra were processed using a Comet-based in-house software pipeline. Spectra were converted to mzXML *via* MSconvert[53]. Database searching included all entries from the human UniProt reference database (downloaded: January 2024). The database was concatenated with one composed of all protein sequences for that database in the reversed order to determine false discovery. Searches were performed using a 50 ppm precursor ion tolerance for total protein level profiling. The product ion tolerance was set to 0.03 Da. These wide mass tolerance windows were chosen to maximize sensitivity in conjunction with Comet searches and linear discriminant analysis[54,55]. TMTpro labels on lysine residues and peptide *N*-termini +304.207 Da), as well as carbamidomethylation of cysteine residues (+57.021 Da) were set as static modifications, while oxidation of methionine residues (+15.995 Da) was set as a variable modification. Peptide-spectrum matches (PSMs) were adjusted to a 1% false discovery rate (FDR)[56,57]. PSM filtering was performed using a linear discriminant analysis, as described previously[55], and then assembled further to a final protein-level FDR of 1%[57]. Proteins were quantified by summing reporter ion counts across all matching PSMs, as described previously[58]. Reporter ion intensities were adjusted to correct for the isotopic impurities of the different TMTpro reagents according to manufacturer specifications. The signal-to-noise (*S/N*) measurements of peptides assigned to each protein were summed and these values were normalized so that the sum of the signal for all proteins in each channel was equivalent to account for equal protein loading. Finally, each protein abundance measurement was scaled, such that the summed *S/N* for that protein across all channels equals 100, thereby generating a relative abundance measurement.

2.2.7 Gene silencing by small interfering RNA (siRNA)

ON-TARGETplus siRNAs targeting human *HIF-1α* (cat. no. L-004018-00-0005), *SREBF1* (cat. no. L-006891-00-0005), and non-targeting control (cat. no. D-001810-10-05) were purchased from Dharmacon. HCMs were transfected with 5 pmol of each siRNA using Lipofectamine

RNAiMAX transfection reagent (cat. no. 13778-150, Life Technologies). After transfection for 24 h, the cell medium was refreshed, and cells were then treated with OL2HG or DMSO as indicated.

2.2.8 Immunoblotting

Cells were lysed by sonication in RIPA lysis and extraction buffer (cat. no. 89900, Thermo Fisher Scientific) supplemented with Halt Protease Inhibitor Cocktail (cat. no. 78430, Thermo Fisher Scientific). Ten micrograms of total protein was loaded and separated on 4–15% pre-cast SDS–PAGE gels (cat. no. 4561086, Bio-Rad) using running buffer (cat. no. 161-0772, Bio-Rad) and then transferred to PVDF membranes using a semi-dry Turbo transfer system (cat. no. 170-4272, Bio-Rad). Protein blots were blocked with 5% (w/v) blotting grade milk (cat. no. 1706404XTU) prepared in Tris Buffered Saline with Tween (TBST, cat. no. 1706435 and 161-0781. Bio-Rad) and then incubated with specific primary antibodies (**Table 2.1**) overnight at 4 °C. HRP-linked secondary mouse or rabbit antibody (cat. no. 7076S and 7074S, Cell Signalling Technology; 1:2,000 dilution) and Immobilon detection reagents (cat. no. WBLUF0100, Sigma) were used to visualize protein blots. Images were captured using a ChemiDoc Touch Imaging system and quantitated by Image Lab software v.5.2 (Bio-Rad). Detailed information of all antibodies and their dilutions is included in **Table 2.1**.

Table 2.1. Antibodies used in this study and their sources and dilutions.

Antibody	CAT #	Vendor	Dilution, v/v
PLIN2	15294-1-AP	Proteintech	1:2000
PLIN3	10694-1-AP	Proteintech	1:2000
PLIN5	26951-1-AP	Proteintech	1:2000
HIF-1α	610958	BD Biosciences	1:500
β-actin	sc-47778 HRP	Santa Cruz	1:1000
SREBP1	95879S	Cell Signaling Technologies	1:1000
SREBP2	25940T	Cell Signaling Technologies	1:1000
VLDLR	19493-1-AP	Proteintech	1:1000
CPT1A	12252T	Sigma	1:1000

2.2.9 BODIPY staining

HCMs were seeded in 4- or 8-well chamber slides at 50,000 or 25,000 cells *per* well, respectively, and allowed to adhere overnight in a humidified incubator (37 °C, 95% humidity, 5% CO_2). Cells were treated with vehicle (DMSO) or OL2HG (500 μM) for 24 h, washed once with 1 mL serum-free myocyte growth medium (PromoCell, cat. no. C-22070), and stained with 4,4-Difluoro-1,3,5,7,8-Pentamethyl-4-Bora-3a,4a-Diaza-*s*-Indacene (BODIPY 493/503, 1 μg/mL; cat. no. D3922, Thermo Fisher Scientific) prepared by dilution from a 2 mM DMSO stock into serum-free myocyte growth medium. Staining was performed at 37 °C in a humidified incubator (37 °C, 95% humidity, 5% CO_2) for 30 min. Following staining, cells were washed once with Dulbecco's phosphate-buffered saline (DPBS; cat. no. D8537, Sigma) and refreshed with 500 μL DPBS containing 1 μg/mL Hoechst (cat. no. 62249, Invitrogen). Data were acquired on a Zeiss confocal microscope, and BODIPY was quantified using an in-house code.

2.2.10 Flow cytometry

PAECs were seeded in 12-well plates at 125,000 cells per well and allowed to adhere overnight in a humidified incubator (37 °C, 95% humidity, 5% CO_2). Cells were treated with vehicle (DMSO) or OL2HG (500 μM) for 24 h, washed once with 1 mL serum-free endothelial basal medium (cat. no. CC-3156, Lonza), and stained with BODIPY 493/503 (1 μg/mL) prepared by dilution from a 2 mM DMSO stock into serum-free endothelial basal medium. Staining was performed at 37 °C in a humidified incubator for 30 min.

Following staining, cells were washed once with DPBS, detached using trypsin (cat. no. 25200-056, Gibco), centrifuged (2,000 × *g*, 5 min, 4 °C), and resuspended in 100 μL DPBS in a 96-well plate. Immediately prior to acquisition, cells were stained with 100 μL of 2 μg/mL DAPI stock (4′,6-diamidino-2-phenylindole; cat. no. D9542, Sigma). Data were acquired on a CytoFLEX flow cytometer (Beckman Coulter), and BODIPY was quantified as mean FITC-A fluorescence intensity using CytExpert 2.0 software. To exclude nonviable cells, BODIPY quantification was performed exclusively in DAPI-negative cells.

2.2.11 Very low-density lipoprotein uptake

Purified human very low density lipoprotein (VLDL) labeled with 1,1'-dioctadecyl- 3,3,3',3'-tetramethylindocarbocyanine perchlorate (DiI-VLDL, cat. no. 770130-9, Kalen Biomedical) was diluted aseptically in complete HCM medium to a final concentration of 50 µg/mL immediately prior to use. HCM cells were seeded at 7,500 cells per well in 8-chamber slides and cultured overnight in complete medium.

Cells were treated for 24 h with vehicle control (0.2% DMSO), OL2H (500 µM), oleate (50 µM), or OL2HG (500 µM) plus oleate (50 µM). Following treatment, cells were incubated with DiI-VLDL (50 µg/mL) in serum-free HCM medium for 2 h at 37 °C in the dark under 5% CO_2. Cells were washed three times with warm serum-free medium and counterstained with Hoechst (10 µg/mL) for 15 min in DPBS. Live-cell imaging was performed at 37 °C.

Fluorescence images were acquired using a Zeiss LSM 800 confocal microscope (excitation 549 nm, emission 565 nm) with identical acquisition settings for all samples. Quantification was performed using Zen Blue software. Data are presented as mean fluorescence intensity (MFI) per field normalized to cell. Data are from independent biological replicates (n = 2).

2.2.12 Palmitate oxidation

Palmitate oxidation was quantified by measuring the production of radiolabeled CO_2 from [^{14}C]-palmitate, as adapted from Huynh *et al*[59]. HCMs and PAECs were seeded in 24-well plates (25,000 and 50,000 cells *per* well, respectively) and allowed to adhere overnight. Cells were treated with either vehicle control (DMSO) or 500 µM OL2HG for 24 h before assessment of palmitate oxidation. For palmitate oxidation, [^{14}C]-palmitate (cat. no. NEC075H050UC) was added to 5 mM cold palmitate (cat. no. 29558) (exact reagent volumes were back-calculated for each experiment based on the number of wells used). This palmitate mixture was incubated at 37 °C for 60 min with gentle shaking to ensure complete complex formation and diluted into serum-free MCDDB 131 medium (cat. no. CM134-050) to final medium concentrations of 200 µM cold palmitate and 0.4 µCi mL^{-1} [^{14}C]-palmitate. Carnitine (cat. no. 21489) was added to this hot BSA–palmitate mixture to a final concentration of 1 mM. Cells were washed twice with DPBS and incubated with the hot palmitate-containing medium for 3 h at 37 °C in an incubator with 95% humidity and 5%

CO_2, with plates sealed using parafilm (cat. no. HS234526B, Sigma). Following incubation, 400 µL of medium was transferred to 1.5 mL tubes containing 200 µL of 1 M perchloric acid, with NaOH-soaked filter paper (cat. no. WHA1004270) mounted in the tube cap (20 µL of 1 N NaOH). After incubation at room temperature for 1 h while shaking at 200 r.p.m, filters containing trapped $^{14}CO_2$ were transferred to scintillation vials filled with 4 mL of Ecoscint H (cat. no. LS-275), mixed vigorously for 10 s, and radioactivity was measured as disintegrations *per* minute (DPM) using a liquid scintillation counter (LS 6500, Beckman Coulter). Non-incubated medium samples were processed in parallel to determine input radioactivity for calculation of specific activity.

All procedures involving radioactive materials were performed in accordance with institutional radiation safety guidelines and approved protocols at Brigham and Women's Hospital and Harvard Medical School (Boston, MA, USA).

2.2.13 Mouse models

2.2.13.1 Animal housing ethics compliance

Animals (aged- and sex-matched, 6-8 month old) were maintained in the Brigham and Women's Hospital animal facility under a 12 h light–dark cycle and controlled humidity (50–60%), with unrestricted access to water and standard chow (PicoDiet 5053, LabDiet; cat. no. 3005740-220). All experimental procedures were conducted in accordance with protocols approved by the Institutional Animal Care and Use Committee of Brigham and Women's Hospital.

2.2.13.2 Baseline characterization

Male (*L2hgdh*$^{+/+}$, n = 5; *L2hgdh*$^{-/-}$, n= 5) and female (*L2hgdh*$^{+/+}$, n = 6; *L2hgdh*$^{-/-}$, n= 5) mice were euthanized by intraperitoneal overdose of ketamine (240–300 mg kg^{-1}) and xylazine (15–30 mg kg^{-1}). Whole blood was immediately collected from the left ventricle into 2 mL tubes preloaded with heparin (10 µL; cat. no. NDC 25021-400-10), centrifuged (1,500 × *g*, 10 min, 4 °C), and plasma was flash-frozen in liquid nitrogen and stored at −80 °C until metabolomic and lipidomic analyses as described above. Hearts and livers were subsequently harvested, clamp-frozen in liquid N_2, and stored at −80 °C until metabolomic and lipidomic analyses, as described above.

2.2.13.3 Langendorff perfusion

Hearts were isolated and perfused in Langendorff mode as described previously[60]. Briefly, mice were anticoagulated by intraperitoneal injection of 100 units of heparin 15 min before experiments and then euthanized with over-dose isoflurane (5% inhalation in isoflurane chamber). The hearts were quickly excised and arrested in ice-cold regular Krebs-Henseleit (KH) buffer containing (in mM) NaCl 118, KCl 5.3, $CaCl_2$ 2.5, $MgSO_4$ 1.2, EDTA 0.5, $NaHCO_3$ 25, glucose 10, prepared freshly and equilibrated with 95% O2 / 5% CO_2, yielding a pH of 7.40, and connected *via* the aorta to the perfusion cannula. Right ventricular drainage was accomplished by incision of the pulmonary artery. The effluent from the thebesian veins was drained by a thin polyethylene tube (PE-10) pierced through the apex of the left ventricle. For baseline perfusion of male hearts (*L2hgdh*$^{+/+}$, n = 11; *L2hgdh*$^{-/-}$, n = 12), isolated hearts were perfused in the Langendorff mode at a constant coronary perfusion pressure of 80 mmHg at 37 °C with regular KH buffer for 30 min to equilibrate followed by an additional 30 min of base-line perfusion. For low-flow ischemia (LFI) of male (*L2hgdh*$^{+/+}$, n = 8; *L2hgdh*$^{-/-}$, n= 5) and female (*L2hgdh*$^{+/+}$, n = 8; *L2hgdh*$^{-/-}$, n= 11) hearts, hearts were perfused as *per* the baseline-perfusion protocol, with the addition of 90 min perfusion at 10 mmHg. These perfusion protocols are adapted directly from our previous publication[60].

2.2.13.4 Metabolic cage

Male mice (*L2hgdh*$^{+/+}$, n = 8; *L2hgdh*$^{-/-}$, n = 8) entered the metabolic cage (Promethion Core®) at 23 °C. After acclimating for a whole day, the mice were left undisturbed for two days to record baseline metabolic and behavioral activity. The food was then removed from the cages, and the mice were fasted overnight before the food was replaced. EchoMRIs were completed before entry and after exit from the Promethion to determine body composition.

2.2.14 Statistics

All statistical analyses were performed using GraphPad Prism (version 9.0), unless otherwise indicated. Data normality was assessed using the Shapiro–Wilk test. For datasets that satisfied normality assumptions, statistical significance among three or more groups was evaluated using one-way analysis of variance (ANOVA), followed by either Tukey's or Dunnett's *post hoc*

multiple-comparison test, as appropriate. Comparisons between two independent groups were performed using an unpaired two-tailed Student's *t*-test.

For datasets that did not meet normality assumptions, statistical significance among three or more groups was assessed using the Kruskal–Wallis test, followed by Dunn's *post hoc* test, while comparisons between two experimental conditions were conducted using the non-parametric Mann–Whitney *U* test. Data collection and analysis were performed blinded to experimental conditions whenever feasible. All data are presented as mean ± standard error of mean (SEM).

2.3 Results

2.3.1 2HG enantiomers differentially increase TGs, free fatty acids, and LDs in primary human cells

As an initial step, we sought to verify that exogenously supplied OL2HG is taken up by cells and leads to a measurable increase in intracellular 2HG levels, thereby establishing an appropriate *in vitro* model to study the cellular effects of L2HG and D2HG (see Section 1.6.1). Using LC–MS for detection, total O2HG was virtually undetected in DMSO-treated HCMs, and significantly higher concentrations were detected in cells treated with OL2HG or OD2HG (**Fig. 2.1A**). In addition, when compared to controls, significantly higher concentrations of total, unmodified 2HG were detected in cells treated with OL2HG and, to a significantly greater extent, OD2HG (**Fig. 2.1B**).

We next assessed whether OL2HG alters the cellular lipidome using high-throughput, discovery-driven LC–MS/MS-based lipidomics. We used LipidMatch for analysis, an automated, rule-based lipid identification workflow that annotates lipids from untargeted high-resolution LC–MS/MS data by matching experimental precursor and fragment ions to extensive *in silico* fragmentation libraries. Rather than relying solely on spectral similarity scores, LipidMatch requires lipid class–specific diagnostic fragments for identification and ranks candidate annotations for each feature based on the summed intensity of matched fragments, thereby avoiding over-reporting of structural detail. This approach enables accurate lipid annotation at the level supported by the data while accommodating co-eluting isomeric species common in complex lipidomic datasets. Lipidomics analysis using LipidMatch identified and quantified a total of 626 highly confident (*i.e.,* validated

by MS/MS) lipid species (**Supplementary Data S2.1**). OL2HG treatment altered the abundance of numerous lipid species spanning several lipid classes (**Fig. 2.1C**). Among these, the most unambiguous and directionally consistent changes were observed in TGs (blue) and PEs (purple), which were uniformly upregulated and downregulated, respectively (**Fig. 2.1C**). Furthermore, cells treated with OL2HG exhibited significantly higher concentrations of total TGs than control cells, whereas OD2HG increased total TGs to a significantly lesser extent (**Fig. 2.1D**). Moreover, OL2HG and OD2HG significantly increased total intracellular DAG concentrations when compared to controls (**Fig. 2.1E**). Since the (patho)biological properties of TGs are influenced strongly by the composition of their fatty acyl chains (*i.e.,* carbon number and degree of saturation), we examined whether OL2HG-mediated TG accumulation was selective for specific TG species. Although the magnitude of upregulation varied across species, OL2HG increased all detectable TG and DAG species (**Fig. 2.1F-G**).

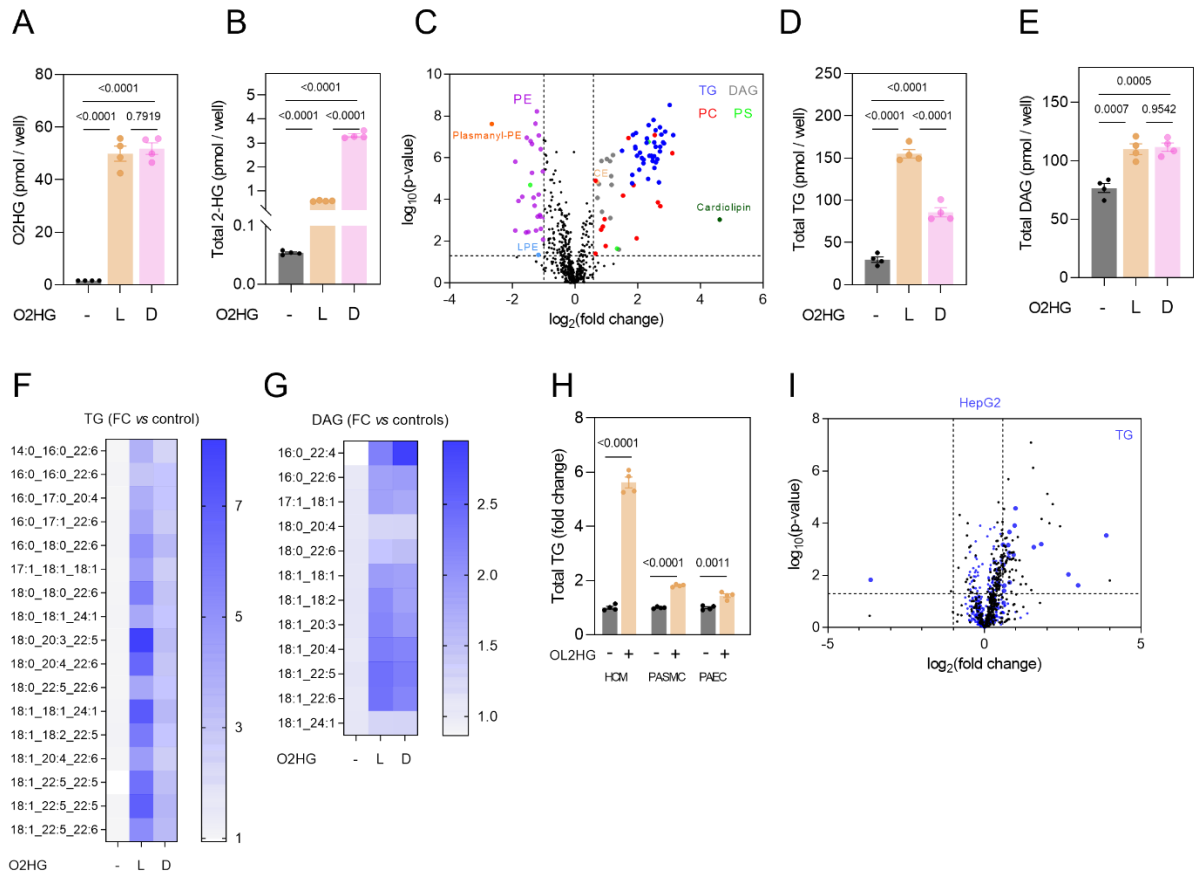

Figure 2.1. Effects of O(L/D)2HG on the lipidome of primary human cells. A and **B**, Total intracellular O2HG and 2HG in HCMs treated with DMSO (n=4), OL2HG (n=4), or OD2HG (n=4) for 24 h. **C**, Lipidomics analysis of HCMs treated with OL2HG or DMSO (n=4). **D** and **E**, Total intracellular TG and DAG in HCMs treated with DMSO (n=4), OL2HG (n=4), or OD2HG (n=4) for 24 h. **F** and **G**, Expression of individual TGs and DAGs in HCMs treated with DMSO (n=4), OL2HG (n=4), or OD2HG (n=4) for 24 h. **H**, Total intracellular TG in HCMs, PASMCs, and PAECs following treatment with DMSO (n=4) or OL2HG (n=4) for 24 h. **I**, Lipidomics analysis of HepG2 cells following treatment with OL2HG (n=4) or DMSO (n=4). Data are presented as mean ± SEM. Data were tested for normality by Shapiro–Wilk test. Normal data were analyzed by ordinary one-way ANOVA (>2 groups) or unpaired *t*-test (pairwise). Non-normal data were analyzed by the Kruskal-Wallis test (> 2 groups) or Mann–Whitney test (pairwise).

To determine whether OL2HG-induced TG accumulation depends on cell type, we assessed additional primary human cell types and expressed TG abundance as percent change relative to DMSO-treated controls. OL2HG increased total intracellular TGs in PASMCs and PAECs (**Fig. 2.1H**). Given that investigators often study OL2HG in the context of cancer[61-63], we examined whether OL2HG increases TG abundance in HepG2 cells, a human liver cancer cell line. Although not all TG species (blue) were differentially regulated, numerous TG species were significantly upregulated (**Fig. 2.1I**). The magnitude and consistency of TG upregulation were more apparent in the primary human cells that we tested; however, the HepG2 data suggest that OL2HG may also influence lipid metabolism in cancer cells, raising the possibility that OL2HG contributes to oncometabolic remodeling by regulating TG metabolism.

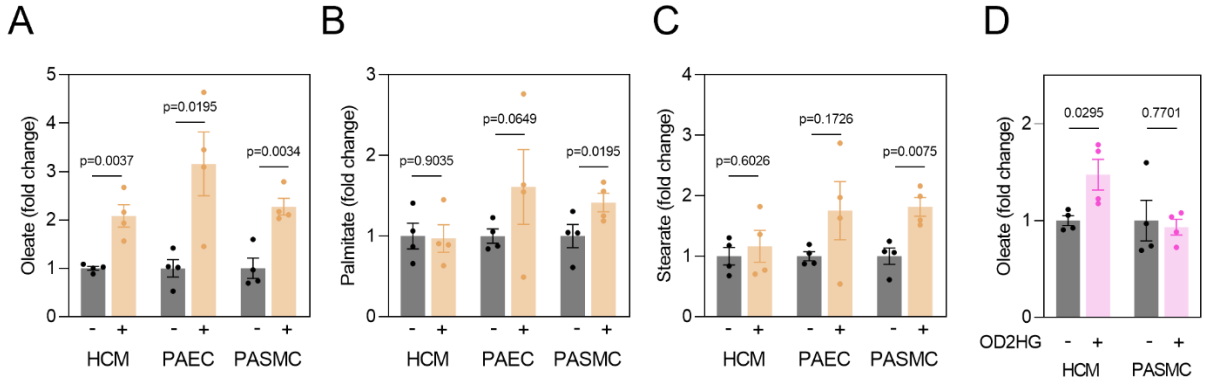

Figure 2.2. Effect of OL2HG and OD2HG on free fatty acids in primary human cells. A–**C**, Expression of intracellular oleate, palmitate, and stearate in HCMs, PAECs, and PASMCs following treatment with OL2HG (n=4) or DMSO (n=4) for 24 h. **D**, Expression of intracellular oleate in HCMs and PASMCs following treatment with OD2HG (n=4) or DMSO (n=4) for 24 h. Data are presented as mean ± SEM. Data were tested for normality by Shapiro–Wilk test. Normal data were analyzed by unpaired *t*-test. Non-normal data were analyzed by the Mann–Whitney test.

We then asked whether OL2HG modulates intracellular free fatty acids. OL2HG increased intracellular oleate bioavailability significantly in HCMs, PAECs, and PASMCs (**Fig. 2.2A-C**). OL2HG also increased palmitate in a cell-type-specific manner (HCM, p=0.9035; PAEC**,** 61.0 ± 46.5 %, p=0.0649; PASMC, 41.6 ± 11.6 %, p=0.0195), as well as stearate (HCM, p=0.6026; PAEC**,** p=0.1726; PASMC, 81.7 ± 15.5 %, p=0.0075). Furthermore, OD2HG increased intracellular oleate in HCMs (**Fig. 2.2D**), although the magnitude of this increase was substantially lower than that induced by OL2HG (**Fig. 2.2A**). OD2HG did not increase oleate in PASMCs (**Fig. 2.2D**). Taken together, these findings show that, among all detectable and examined free fatty acids, oleate was the only species consistently upregulated by OL2HG across all cell types examined.

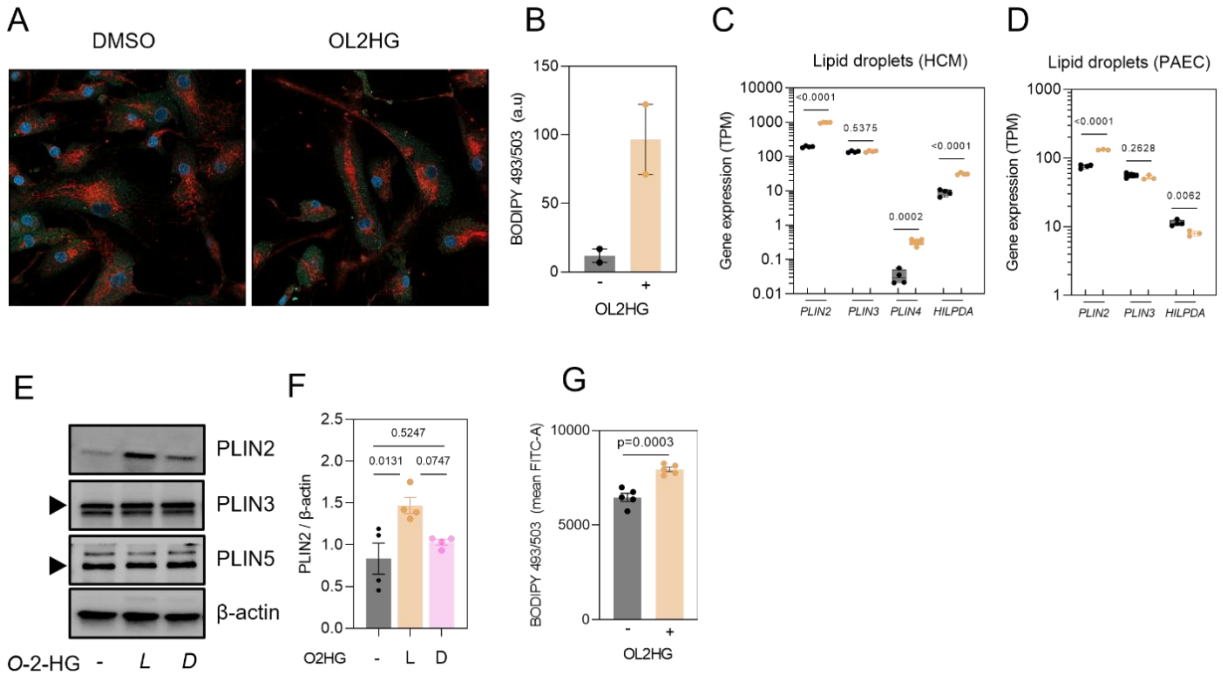

Figure 2.3. OL2HG increases intracellular lipid droplets in primary cells. A, Representative images of BODIPY 493/503- (green) and MitoTracker-stained (red) HCMs following treatment with DMSO (n=2) or OL2HG (n=2) for 24 h. Images were viewed under 63X magnification using a confocal microscope. **B**, Quantification of BODIPY 493/503 fluorescence intensity normalized to cell number and expressed as arbitrary units (a.u). **C** and **D**, Expression of lipid droplet-associated genes in HCMs and PAECs following treatment with DMSO (n=4) or OL2HG (n=3–4) for 24 h. Data are expressed as transcripts per million (TPM). **E**, Representative immunoblot and quantification of different perilipin (PLIN) proteins in HCMs treated with DMSO (n=4), OL2HG (n=4), or OD2HG (n=4) for 24 h. **G**, Mean BODIPY 493/503 fluorescence signal in PAECs treated with DMSO (n=5) or OL2HG (n=5) for 24 h, as assessed by flow cytometry. Data are presented as mean ± SEM. Data were tested for normality by Shapiro–Wilk test. Normal data were analyzed by ordinary one-way ANOVA (>2 groups) or unpaired *t*-test (pairwise). Non-normal pairwise data were analyzed by the Kruskal-Wallis test (> 2 groups) or Mann–Whitney test (pairwise).

Given that intracellular TGs are stored primarily within LDs, we next assessed whether OL2HG influences LD abundance. To this end, we used BODIPY 493/503, a lipophilic fluorescent dye that stains neutral lipids, making it a commonly used probe for assessing LDs. HCMs treated with OL2HG exhibited increased BODIPY 493/503 fluorescence, as assessed by confocal microscopy (**Fig. 2.3A-B**). Moreover, transcripts encoding several perilipin family members (*i.e.*, LD–coating proteins) were significantly upregulated by OL2HG, with the PLIN2 isoform increased in both HCMs and PAECs (**Fig. 2.3C-D**). OL2HG, but not OD2HG, increased protein abundance of PLIN2 in HCMs, while expression of PLIN3 and PLIN5 remained unchanged (**Fig. 2.3E-F**). In agreement with the confocal microscopy data, OL2HG significantly increased intracellular BODIPY signal in PAECs, as measured by flow cytometry (**Fig. 2.3G**).

Since OL2HG contains an octyl moiety that may confer L2HG-independent effects (see Section 1.6.1.1), we next tested whether unmodified L2HG also increases intracellular TGs. PAECs required a ~two-fold higher concentration of L2HG than OL2HG to achieve similar intracellular accumulation of total 2HG (*i.e.,* L2HG/OL2HG at 0.5/0.25 mM yielded ~3–5-fold increases, 1.0/0.5 mM yielded ~5–8-fold increases, and 2.0/1.0 mM yielded ~10–20-fold increases, respectively) (**Fig. 2.4A**). Consistent with this difference in potency, when cells were treated with unmodified L2HG at twice the concentration of OL2HG (1 mM *vs.* 500 µM), both metabolites increased total intracellular TG and CE to comparable extents (**Fig. 2.4B-C**).

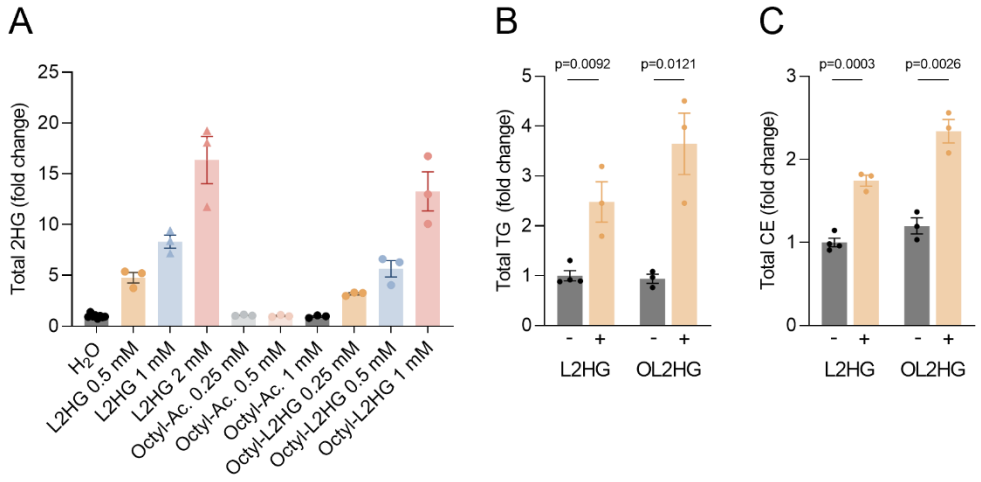

Figure 2.4. Unmodified L2HG increases intracellular TGs and CEs. A, Total 2HG in PAECs treated with different concentrations of unmodified L2HG (n=3), octyl acetate (Octyl-Ac.; n=3), and OL2HG (n=3) for 24 h. **B** and **C**, Total intracellular TG and CE in PAECs treated with DMSO (n=4), L2HG (1 mM; n=3), or OL2HG (500 µM; n=3) for 24 h. Data are presented as mean ± SEM. Data were tested for normality by Shapiro–Wilk test. Normal data were analyzed by unpaired *t*-test. Non-normal pairwise data were analyzed by the Mann–Whitney test.

2.3.2 L2HG increases lipogenic flux and decreases lipolytic flux

Having established that OL2HG increases intracellular BODIPY fluorescence, we next sought to determine whether this effect requires DGAT-mediated TG synthesis. Inhibition of DGAT1/2 with selective pharmacological inhibitors (*i.e.*, A-922500[64] and PF-06424439[65], respectively) completely abrogated the OL2HG-induced increase in BODIPY fluorescence signal (**Fig. 2.5A-B**), indicating that LD expansion in response to OL2HG is DGAT dependent.

To assess whether OL2HG enhances lipogenic flux, we pre-treated cells with or without OL2HG for 24 h and then exposed them to $^{13}C_{18}$-oleate for variable pulse durations (1–24 h), followed by detection of TGs containing three $^{13}C_{18}$-oleate acyl chains [*i.e.*, TG(3 × $^{13}C_{18}$-oleate) or $^{13}C_{54}$-trioleylglycerol] by LC–MS (**Fig. 2.5C**). Using this approach, we assessed the effects of OL2HG pre-treatment on TG biosynthetic flux. In HCMs, OL2HG increased the signal intensity of TG(3×$^{13}C_{18}$-oleate) significantly across all time points (**Fig. 2.5D**), demonstrating accelerated incorporation of exogenous oleate into newly synthesized TG. By assessing the rate of appearance of TG(3×$^{13}C_{18}$-oleate) (*i.e.,* the first derivative / slope of its signal intensity curve shown in **Fig. 2.5D**), we observed that the increase in lipogenic flux was most pronounced during the first six hours, whereas labeling flux between 6 and 24 h was substantially reduced (**Fig. 2.5E**), consistent with the system reaching isotopic steady state.

We next evaluated whether these effects were conserved across primary human cell types. In PAECs, OL2HG increased the signal intensity of TG(3×$^{13}C_{18}$-oleate) during the first 1 h and, again, between 6 and 24 h (**Fig. 2.5F-G**). In contrast, in HCFs, OL2HG enhanced TG(3×$^{13}C_{18}$-oleate) intensity primarily in the 3–6-h interval, while producing a modest decrease in flux during the first hour (**Fig. 2.5H-I**). These distinct temporal signatures highlight cell-type specificity in the kinetics of OL2HG-mediated elevations in lipogenesis. Despite these kinetic differences, OL2HG consistently increased TG biogenic flux across all cell types examined, demonstrating a conserved lipogenic effect with cell-specific temporal dynamics.

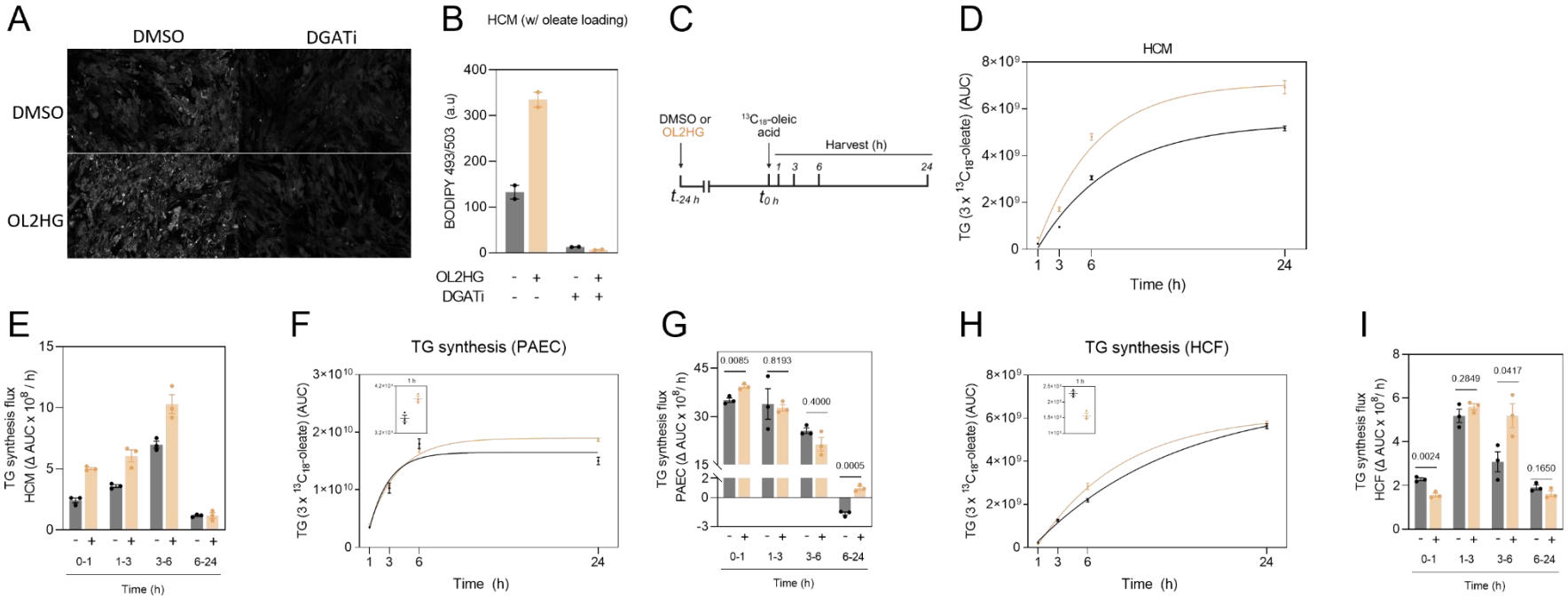

Figure 2.5. OL2HG increases lipogenic flux in numerous cell types. A, Representative images of BODIPY 493/503-stained (white) HCMs following treatment with DMSO (n=2) or OL2HG (n=2) in the presence or absence of inhibition of DGAT1/2 with selective pharmacological inhibitors (10 µM A-922500 and 10 µM PF-06424439) for 24 h. Images were viewed under 20X magnification using a confocal microscope. **B**, Quantification of BODIPY 493/503 fluorescence intensity normalized to cell number and expressed as arbitrary units (a.u). **C**, Experimental design of cells pre-treated with DMSO or OL2HG for 24 h, followed by removal of OL2HG and introduction of $^{13}C_{18}$-oleic acid for 1–24 h. **D**, **F** and **H**, Signal intensity of newly synthesized TGs containing three $^{13}C_{18}$-oleate acyl chains [*i.e.,* TG(3 x $^{13}C_{18}$-oleate) or $^{13}C_{54}$-trioleylglycerol] in HCMs, PAECs, and HCFs following pre-treatment with DMSO (n=3) or OL2HG (n=3) for 24 h and subsequent exposure to $^{13}C_{18}$-oleic acid for 1–24 h. **E**, **G**, and **I**, TG synthesis flux in DMSO- or OL2HG-treated HCMs, PAECs, and HCFs. Data are presented as mean ± SEM. Data were tested for normality by Shapiro–Wilk test. Normal data were analyzed by unpaired *t*-test. Non-normal data were analyzed by the Mann–Whitney test.

To examine whether OL2HG regulates TG catabolism, we performed a pulse–chase isotope–labeling experiment using a modified design distinct from the *de novo* labeling studies described above. Cells were first pre-labeled with $^{13}C_{18}$-oleate for 24 h to generate a pre-existing pool of TG(3x$^{13}C_{18}$-oleate). During the chase period, the medium was replaced with ^{12}C-oleate, and cells were exposed to OL2HG or DMSO control for variable time points (1–24 h) (**Fig. 2.6A**), enabling quantification of both the disappearance of TG(3x$^{13}C_{18}$-oleate) (reflecting lipolysis) and the synthesis of newly formed TG(3x$^{12}C_{18}$-oleate) (reflecting lipogenesis).

Consistent with our lipogenic flux analyses in Fig. 2.5, HCMs and HCFs treated with OL2HG had significantly higher TG(3x$^{12}C_{18}$-oleate) after 24 h of OL2HG exposure (**Fig. 2.6B-C**), indicating an overall enhancement in TG production from exogenous oleate. However, TG(3x$^{12}C_{18}$-oleate) signal intensities remained unchanged during the first six hours of treatment (**Fig. 2.6B-C**). This temporal pattern suggests that OL2HG exerts its effects on TG synthesis through relatively longer-term mechanisms (*i.e.*, > 6 h) rather than through direct, rapid ligand-like actions, which would be expected to alter TG(3x$^{12}C_{18}$-oleate) abundance even with relatively shorter OL2HG exposure.

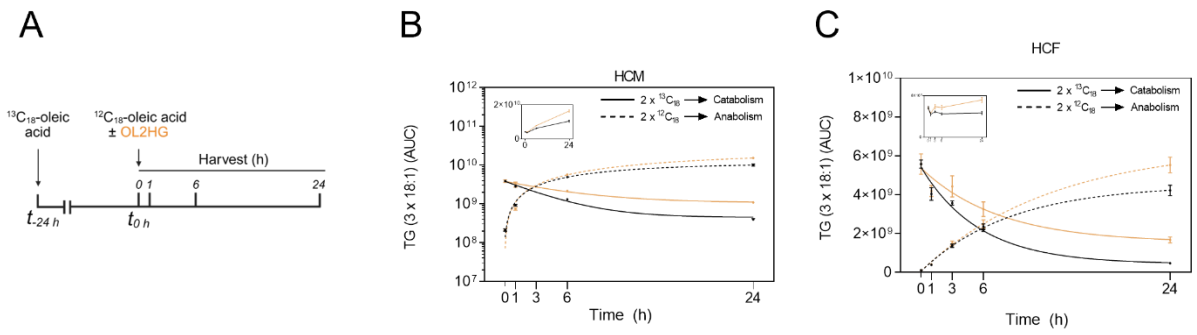

Figure 2.6. OL2HG decreases lipolytic flux in numerous cell types. A, Experimental design of cells pre-treated with $^{13}C_{18}$-oleic acid for 24 h followed by replacement with equimolar $^{12}C_{18}$-oleic acid in the presence or absence of OL2HG for 1–24 h. **B** and **C**, Signal intensity of pre-labeled TG(3 x $^{13}C_{18}$-oleate) and newly synthesized TG(3 x $^{12}C_{18}$-oleate) in HCMs and HCFs. Data are presented as mean ± SEM. Data were tested for normality by Shapiro–Wilk test. Normal data were analyzed by unpaired *t*-test. Non-normal data were analyzed by the Mann–Whitney test.

In contrast, when compared to controls, cells treated with OL2HG had significantly higher intensities of pre-labeled TG(3x$^{13}C_{18}$-oleate) after as early as 6 h in HCMs and 3 h in HCFs (**Fig. 2.6B-C**), indicating decreased clearance of pre-labeled TG(3x$^{13}C_{18}$-oleate) during the chase period. Together, these data reveal that OL2HG promotes the synthesis of new TGs while

simultaneously decreasing the degradation of existing ones. Importantly, the different time scales required for these effects suggest that OL2HG-induced stimulation of TG synthesis and inhibition of TG clearance may be mediated through distinct mechanisms: shorter OL2HG exposures inhibited TG clearance, whereas longer exposures were required to increase TG synthesis.

We next examined whether OL2HG alters transcriptional programs associated with canonical TG metabolic pathways. For this purpose, we analyzed RNA-seq datasets generated from OL2HG-treated HCMs and PAECs (**Supplementary Data S2.2-2.3**), focusing on genes involved in TG synthesis, TG catabolism, and *de novo* lipogenesis. For this analysis, gene expression values were converted from raw counts to transcripts *per* million (TPM), enabling direct pairwise comparison of selected genes involved in a targeted manner and permitting the use of straightforward statistical tests (*e.g.,* t-test), rather than a discovery-driven, untargeted transcriptomic analysis. In HCMs, OL2HG increased the expression of *GPAT3*, *DGAT2*, *ACACA*, *SCD*, *ELOVL6* significantly (**Fig. 2.7A–B**), while decreasing the expression of *ELOVL1* and *LIPE* significantly (**Fig. 2.7B–C**).

In PAECs, OL2HG significantly increased the expression of *LPIN2*, *DGAT1*, and *ELOVL4* (**Fig. 2.7D–E**), while decreasing the expression of *GPAT2*, *ACLY*, *SCD*, and *ELOVL6* significantly (**Fig. 2.7D–E**). None of the canonical TG catabolic genes, including *PNPLA2/3*, *CES1*, *LIPE*, and *MGL,* were differentially regulated by OL2HG in PAECs (**Fig. 2.7F**).

Although we detected some OL2HG-associated changes in individual lipid-related transcripts in a cell type-specific manner, these differences were not consistent across both cell types and did not reveal any obvious or unambiguous patterns within the canonical pathways governing TG synthesis, TG breakdown, or *de novo* lipogenesis. Together, these data indicate that OL2HG-mediated alterations in TG biogenesis and turnover are not accompanied by coordinated transcriptional remodeling of established lipid metabolic pathways alone.

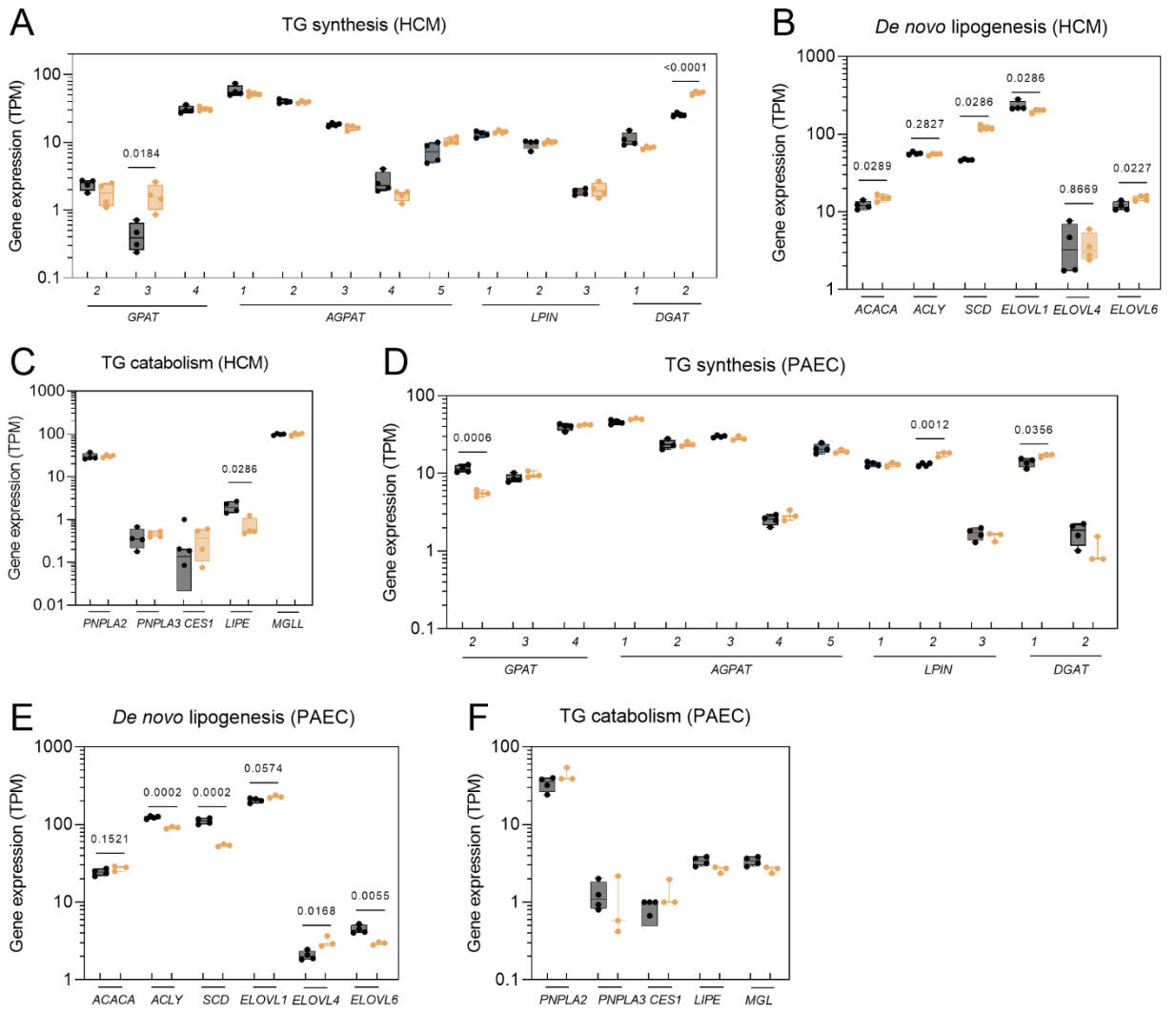

Figure 2.7. Effects of OL2HG on gene expression of TG synthesis-, lipogenesis-, and TG catabolism-related genes. A–**F**, Expression of genes related to TG synthesis, de novo lipogenesis, and TG catabolism in HCMs and PAECs following treatment with DMSO (n=4) or OL2HG (n=3–4) for 24 h. Data are expressed as transcripts *per* million (TPM). Data are presented as mean ± SEM. Data were tested for normality by Shapiro–Wilk test. Normal data were analyzed by unpaired *t*-test. Non-normal data were analyzed by the Mann–Whitney test.

2.3.3 HIF-1α contributes to, but is not required for, OL2HG-induced alterations in LD expansion and TG metabolism

To determine whether OL2HG-induced remodeling of TG metabolism is mediated by competitive inhibition of αKG-dependent enzymes, we assessed whether co-treatment with an octyl ester form of αKG (OαKG) affects TG synthesis and clearance fluxes using the pulse–chase experimental design as shown in **Fig. 2.6A**. While OL2HG treatment alone significantly increased the signal intensity of TG($3x^{12}C_{18}$-oleate), cells treated with OαKG in the absence or presence of OL2HG had levels comparable to controls (**Fig. 2.8A**). These findings indicate that the OL2HG-induced increase in lipogenesis is, at least in part, dependent on perturbation of αKG-dependent enzymatic pathways. In contrast, cells co-treated with OαKG exhibited significantly higher TG($3x^{13}C_{18}$-oleate) at the end of the 24 h chase period, when compared to OL2HG or OαKG treatments alone (**Fig. 2.8B**). Thus, OαKG attenuated the OL2HG-induced increase in TG synthesis, while enhancing the OL2HG-induced inhibition of TG clearance, indicating that OL2HG likely regulates TG synthesis and turnover through mechanistically distinct pathways. Despite these divergent effects on individual flux components, the OL2HG-induced increase in total trioleylglycerol [*i.e.*, TG($3x^{12}C_{18}$-oleate) + TG($3x^{13}C_{18}$-oleate)] was completely prevented by OαKG (**Fig. 2.8C**).

Given that L2HG inhibits the αKG-dependent enzyme PHD2 to stabilize HIF-1α, we next assessed whether OL2HG-mediated regulation of LDs and TG metabolism depends on HIF-1α. We first tested whether OL2HG increases HIF-1α protein abundance in our model systems. In HCMs, OL2HG increased HIF-1α protein expression, as assessed by immunoblotting (**Fig. 2.9A–B**). Similarly, in CASMCs, OL2HG increased HIF-1α protein expression, whereas OD2HG decreased it under the same experimental conditions (**Fig. 2.9C–D**).

To determine whether OL2HG-stabilized HIF-1α is transcriptionally active, we examined the expression of canonical HIF-1α target genes in HCMs. RNA-seq analysis showed that OL2HG significantly increased transcripts encoding glycolytic and hypoxia-responsive genes (**Fig. 2.9E**), consistent with activation of a HIF-1α–dependent transcriptional program.

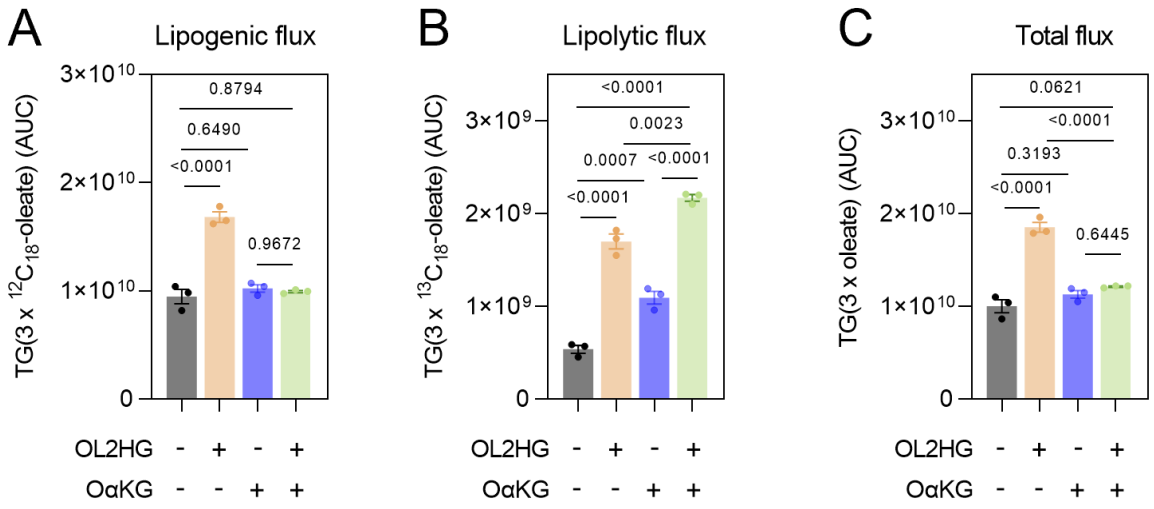

Figure 2.8. OL2HG-induced increase in lipogenic flux is reversed by OαKG. A–C, Intensities of newly synthesized TG(3 x $^{12}C_{18}$-oleate), pre-labeled TG(3 x $^{13}C_{18}$-oleate), and total TG(3 x oleate) in HCMs pre-labeled with $^{13}C_{18}$-oleic acid for 24 h, followed by replacement with $^{12}C_{18}$-oleic acid in the presence (n=3) or absence (n=3) of OL2HG and/or OαKG for 24 h. Data are presented as mean ± SEM. Data were tested for normality by Shapiro–Wilk test. Normal data were analyzed by unpaired *t*-test. Non-normal data were analyzed by the Mann–Whitney test. Normal data were analyzed by ordinary one-way ANOVA. Non-normal data were analyzed by the Kruskal-Wallis test.

We next tested whether OL2HG-mediated upregulation of PLIN2 protein, as a measure of LD and TG accumulation, requires HIF-1α. We used siRNA to genetically knock-down HIF-1α in HCMs and confirmed efficient knock-down by the absence of detectable HIF-1α protein in siHIF-1α–treated cells (**Fig. 2.9F–G**). HIF-1α knock-down modestly attenuated the upregulation of PLIN2 protein by OL2HG, although its expression remained significantly higher than in control cells (**Fig. 2.9F,H**). These findings indicate that HIF-1α contributes to, but does not fully account for, OL2HG-mediated PLIN2 protein upregulation.

Finally, because OL2HG functions as a pseudohypoxic stimulant and stabilizes HIF-1α, we tested whether hypoxia-induced HIF-1α stabilization alone is sufficient to accumulate TGs, as observed with OL2HG treatment. We exposed HCMs to hypoxia (0.5% O_2, 24 h) as an alternative means of stabilizing HIF-1α protein. Unlike OL2HG, hypoxia decreased intracellular TG levels relative to normoxic cells (**Fig. 2.9I**). These findings show that hypoxia-driven HIF-1α stabilization does not mirror the lipogenic effect of OL2HG, indicating that OL2HG-mediated TG accumulation likely involves additional, HIF-1α–independent, mechanisms.

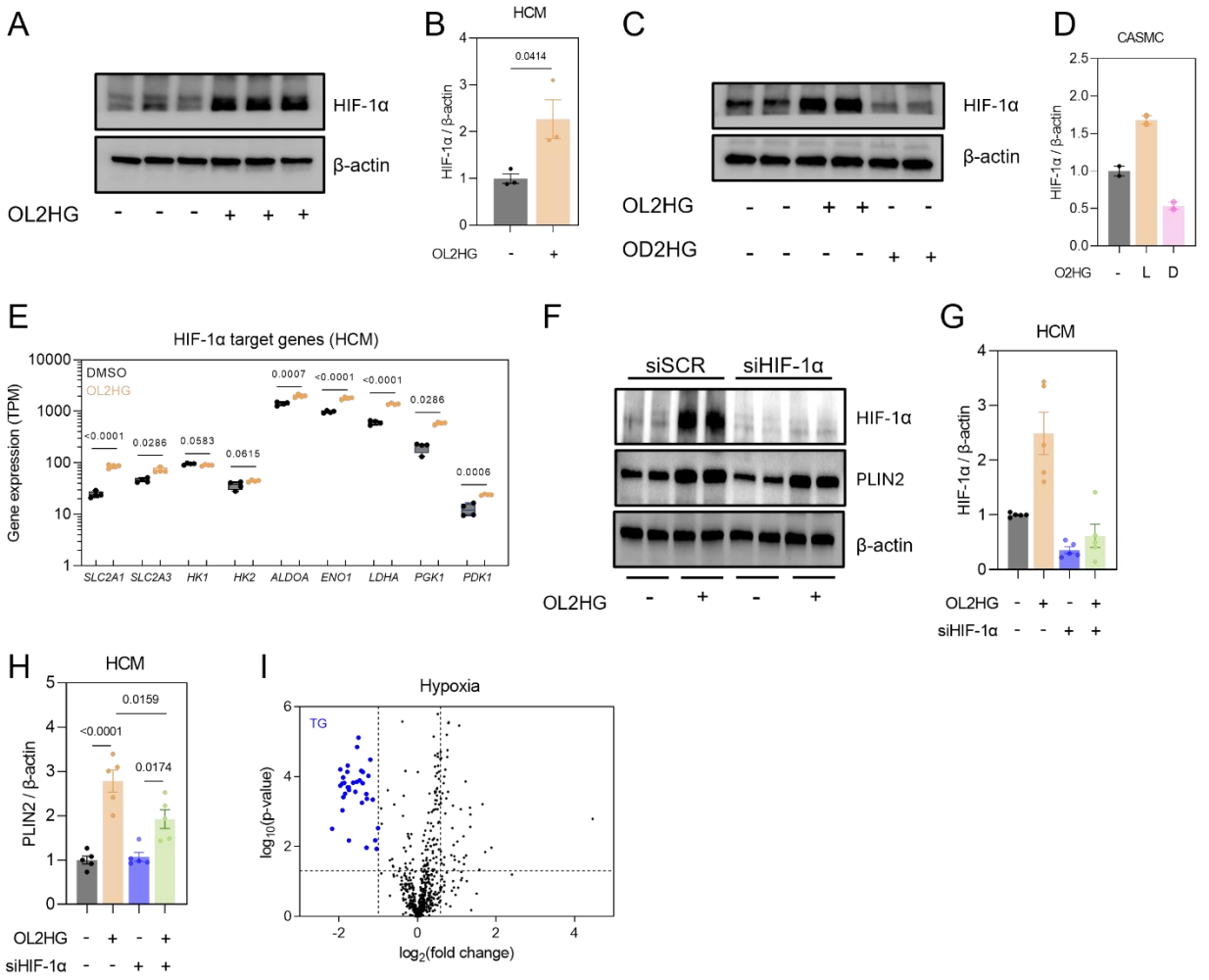

Figure 2.9. OL2HG-mediated HIF-1α stabilization contributes to, but is not required for, lipid droplet accumulation. A and **B**, Representative immunoblot and quantification of HIF-1α in HCMs treated with DMSO (n=3) or OL2HG (n=3) for 24 h. **C** and **D**, Representative immunoblot and quantification of HIF-1α in CASMCs treated with DMSO (n=2), OL2HG (n=2), or OD2HG (n=2) for 24 h. **E**, Expression of HIF-1α target genes in HCMs following treatment with DMSO (n=4) or OL2HG (n=4) for 24 h. Data are expressed as transcripts *per* million (TPM). **F**–**H**, Representative immunoblot and quantification of HIF-1α and PLIN2 in siSCR- or siHIF-1α-treated cells following treatment with DMSO (n=5) or OL2HG (n=5) for 24 h. **I,** Lipidomic analysis of HCMs cells following treatment with (n=4) or without (n=4) hypoxia. Data are presented as mean ± SEM. Data were tested for normality by Shapiro–Wilk test. Normal data were analyzed by ordinary one-way ANOVA (>2 groups) or unpaired *t*-test (pairwise). Non-normal data were analyzed by the Kruskal-Wallis test (> 2 groups) or Mann–Whitney test (pairwise).

2.3.4 OL2HG-induced PLIN2 upregulation is independent of SREBP1

We next determined whether OL2HG regulates expression of the lipid-metabolism–related transcription factor SREBP1 (sterol regulatory element-binding protein 1). In HCMs, OL2HG increased SREBP1 protein abundance, but not SREBP2, as shown by immunoblotting (**Fig. 2.10A–B**). OL2HG did not alter *SREBF1* or *SREBF2* transcript levels (**Fig. 2.10C**), the genes encoding SREBP1 and SREBP2, indicating that OL2HG likely regulates SREBP1 protein abundance through changes in turnover and/or stability rather than transcription. In HCMs, OL2HG increased SREBP1 protein expression in an enantiospecific manner, with OD2HG exerting only a modest effect (**Fig. 2.10D**), mirroring the differential induction of TG accumulation by the two enantiomers (**Fig. 2.1D**). To determine whether OL2HG-induced SREBP1 upregulation occurs across primary human cell types, we examined SREBP1 and SREBP2 protein expression in PAECs and CASMCs. In both cell types, OL2HG increased SREBP1 protein abundance, whereas OD2HG had minimal or no effect in CASMCs (**Fig. 2.10E–H**). We next tested whether HIF-1α regulates OL2HG-mediated SREBP1 stabilization. To do so, we knocked down HIF-1α in HCMs using siRNA and then assessed SREBP1 protein abundance by immunoblotting. OL2HG increased SREBP1 in HIF-1α-deficient cells (**Fig. 2.10I–J**). These findings show that HIF-1α is not required for OL2HG-driven SREBP1 stabilization.

SREBP1 is synthesized as an inactive, endoplasmic reticulum–bound precursor and undergoes proteolytic activation in the Golgi, releasing the *N*-terminal fragment that translocates to the nucleus to drive target gene transcription. Of note, the SREBP1 band detected by immunoblotting corresponds to the non-cleaved, endoplasmic reticulum–resident precursor (~125 kDa), rather than the transcriptionally active nuclear fragment (60–80 kDa). To test whether OL2HG-induced accumulation of SREBP1 precursor leads to its transcriptional activity, we examined the expression of established SREBP1 target genes using our RNA-seq dataset. Although OL2HG increased *SCD* transcript levels significantly, OL2HG did not increase expression of the canonical SREBP1 target genes *FASN*, *ACACA*, or *ACLY* (**Fig. 2.10K**). These findings indicate that OL2HG increases the precursor, non-transcriptionally active form of SREBP1, without necessarily increasing its canonical transcriptional activity.

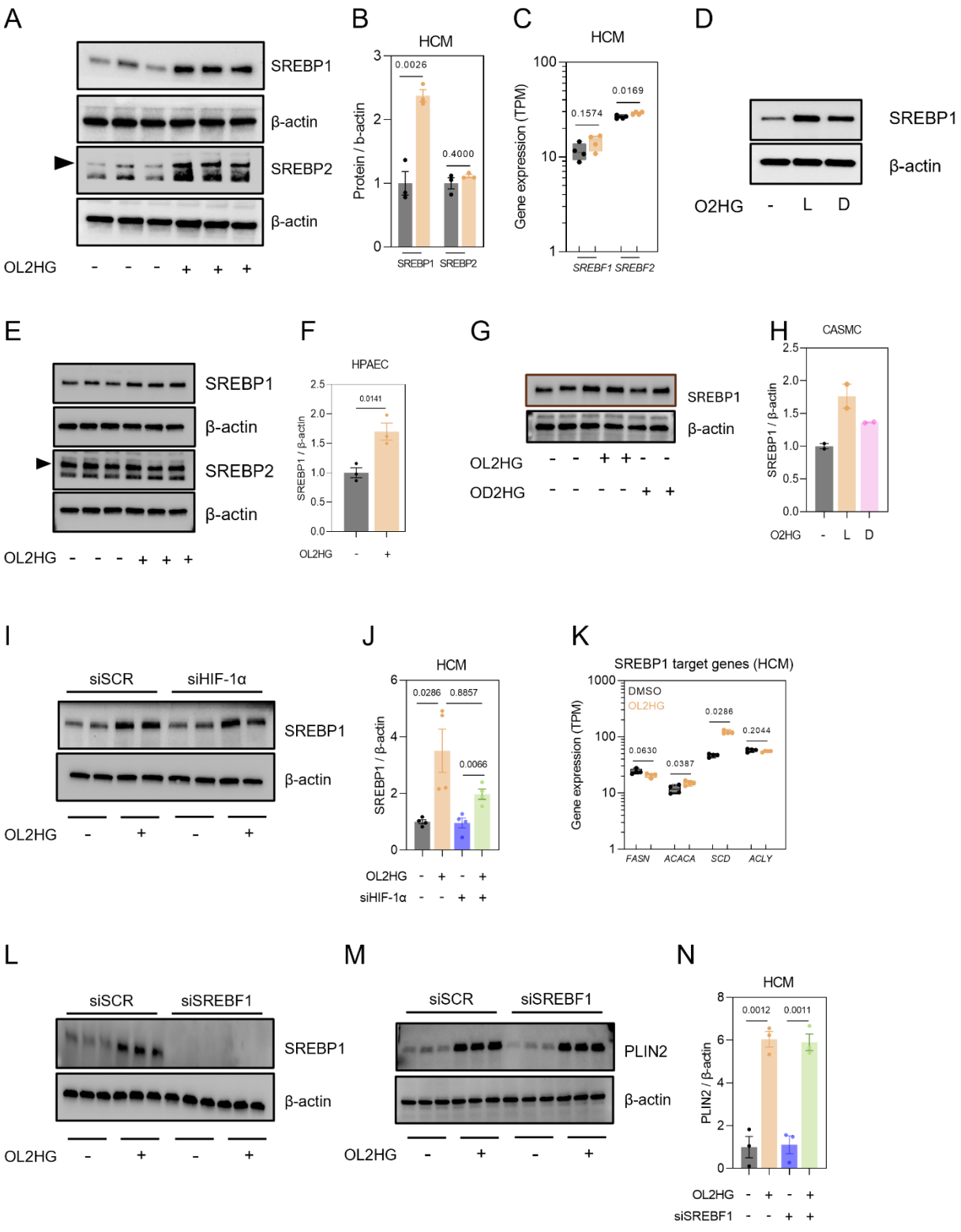
A
SREBP1
β-actin
SREBP2
β-actin
OL2HG - - - + + +
B
HCM
Protein / b-actin
0.0026
0.4000
SREBP1 SREBP2
C
HCM
Gene expression (TPM)
0.1574
0.0169
SREBF1 SREBF2
D
SREBP1
β-actin
O2HG - L D
E
SREBP1
β-actin
SREBP2
β-actin
OL2HG - - - + + +
F
HPAEC
SREBP1 / β-actin
0.0141
OL2HG - +
G
SREBP1
β-actin
OL2HG - - + + - -
OD2HG - - - - + +
H
CASMC
SREBP1 / β-actin
O2HG - L D
I
siSCR siHIF-1α
SREBP1
β-actin
OL2HG - + - +
J
HCM
SREBP1 / β-actin
0.0286 0.8857 0.0066
OL2HG - + - +
siHIF-1α - - + +
K
SREBP1 target genes (HCM)
Gene expression (TPM)
DMSO
OL2HG
0.0630 0.0387 0.0286 0.2044
FASN ACACA SCD ACLY
L
siSCR siSREBF1
SREBP1
β-actin
OL2HG - + - +
M
siSCR siSREBF1
PLIN2
β-actin
OL2HG - + - +
N
HCM
PLIN2 / β-actin
0.0012 0.0011
OL2HG - + - +
siSREBF1 - - + +

Figure 2.10. OL2HG-induced SREBP1 stabilization is not required for lipid droplet accumulation. A and **B**, Representative immunoblot and quantification of SREBP1 and SREB2 in HCMs treated with DMSO (n=3) or OL2HG (n=3) for 24 h. **C**, Expression of *SREBF1* and *SREBF2* in HCMs treated with DMSO (n=4) or OL2HG (n=4) for 24 h. **D**, Representative immunoblot of SREBP1 in HCMs treated with DMSO, OL2HG, or OD2HG. **E** and **F**, Representative immunoblot and quantification of SREBP1 and SREBP2 in PAECs treated with DMSO (n=3) or OL2HG (n=3). **G** and **H**, Representative immunoblot and quantification of SREBP1 in CASMCs treated with DMSO (n=2), OL2HG (n=2), or OD2HG (n=2) for 24 h. **I** and **J**, Representative immunoblot and quantification of SREBP1 in siSCR and siHIF-1α-treated HCMs following treatment with DMSO (n=4) or OL2HG (n=4) for 24 h. **K**, Expression of SREBP1 target genes in HCMs following treatment with DMSO (n=4) or OL2HG (n=4) for 24 h. Data are expressed as transcripts *per* million (TPM). **L**, Immunoblot of SREBP1 in siSCR- or siSREBF1-treated cells following treatment with DMSO (n=3) or OL2HG (n=3). **M** and **N**, Representative immunoblot and quantification of PLIN2 in siSCR- or siSREBF1-treated cells following treatment with DMSO (n=3) or OL2HG (n=3) for 24 h. Data are presented as mean ± SEM. Data were tested for normality by Shapiro–Wilk test. Normal data were analyzed by ordinary one-way ANOVA (>2 groups) or unpaired *t*-test (pairwise). Non-normal data were analyzed by the Kruskal-Wallis test (> 2 groups) or Mann–Whitney test (pairwise).

We next tested whether SREBP1 is required for OL2HG-mediated induction of PLIN2 expression, as a measure of LD and TG accumulation. We used siRNA to knock down *SREBF1*, the gene encoding SREBP1, in HCMs. We confirmed efficient silencing by the absence of detectable SREBP1 protein in si*SREBF1*-treated cells (**Fig. 2.10L**). PLIN2 protein abundance was significantly increased by OL2HG in the presence or absence of si*SREBF1* (**Fig. 2.10M–N**). These findings show that OL2HG-mediated PLIN2 upregulation occurs independently of *SREBF1* gene and SREBP1 protein expression.

2.3.5 OL2HG upregulates VLDL receptor expression and VLDL uptake

We next performed untargeted, TMTpro label-based proteomics using LC–MS/MS to identify potential mechanisms underpinning OL2HG-induced TG accumulation in HCMs. LC–MS/MS identified and quantified 7,260 proteins (see Section 2.2.6.7 for data analysis approach) and significance was defined as a +/- fold change of 1.5 at $p<0.05$ (**Supplementary Data S2.4**). We shortlisted significantly regulated features to proteins annotated in KEGG pathways containing the terms “lipid,” “cholesterol,” “fatty acid,” or “triglyceride” (**Fig. 2.11A**). This shortlisting reflects a targeted screening approach focused on lipid metabolism, rather than a fully discovery-driven analysis of the entire proteome; principal component analysis (PCA) and pathway-enrichment analysis of the full proteomic dataset are provided in **Supplementary Data S2.4**. Among these

lipid-associated gene products, PLIN2 ranked as one of the most significantly upregulated proteins (**Fig. 2.11A**), validating our prior immunoblot findings demonstrating increased PLIN2 protein abundance following OL2HG treatment (**Fig. 2.3E**). Notably, VLDLR (very low-density lipoprotein receptor) emerged among the most robustly upregulated lipid-associated proteins (**Fig. 2.11A**). Given its direct role in TG-rich lipoprotein uptake and TG metabolism, we selected VLDLR for further investigation. Using immunoblotting, we confirmed that OL2HG increased the protein abundance of VLDLR when compared to control (**Fig. 2.11B–C**). Further, *VLDLR* transcript levels were also increased significantly in both HCMs and PAECs, based on RNA-seq analysis (**Fig. 2.11D–E**). To determine whether increased VLDLR expression was associated with enhanced VLDL uptake, we incubated HCMs with purified human VLDL labeled with the fluorescent dye, 1,1'-dioctadecyl- 3,3,3',3'-tetramethylindocarbocyanine perchlorate (DiI–VLDL), in the absence or presence of oleate pre-loading. OL2HG increased DiI–VLDL fluorescence significantly under both conditions (**Fig. 2.11F–G**), indicating that OL2HG enhances cellular VLDL uptake.

2.3.6 OL2HG inhibits palmitate oxidation, alters carbon flux through oleoylcarnitine, and regulates expression of short chain acylcarnitines

Given that TGs serve as a major storage pool for fatty acids and that lipolysis liberates free fatty acids for ATP production *via* mitochondrial β-oxidation, we next determined whether OL2HG regulates FAO. We first quantified FAO using the classical radiolabeled $^{14}C_1$-palmitate oxidation assay with detection by scintillation counting. These experiments were conducted in glucose-deficient media to increase the cells' dependency on FAO. In oleate pre-loaded HCMs, OL2HG decreased palmitate oxidation significantly when compared with control cells (**Fig. 2.12A**). In PAECs, OL2HG decreased palmitate oxidation when compared to control in the absence or presence of oleate preloading (**Fig. 2.12B**).

To assess biochemical flux underlying these changes in FAO, we next performed stable-isotope tracing using $^{13}C_{18}$-oleate coupled to LC–MS to quantify the appearance and clearance of $^{13}C_{18}$-oleoylcarnitine, a key mitochondrial β-oxidation intermediate. We implemented two complementary isotope-tracing strategies to distinguish between the effects of longer-term *versus* shorter-term OL2HG exposure. In the first approach, we pre-treated cells with or without OL2HG

for 24 h and then exposed them to $^{13}C_{18}$-oleate for variable pulse durations, thereby assessing the effects of relatively longer OL2HG exposure (*i.e.,* 24 h) on subsequent FAO flux (**Fig. 2.12C**). Following cellular uptake, $^{13}C_{18}$-oleate undergoes conversion to $^{13}C_{18}$-oleoylcarnitine as part of mitochondrial fatty acid import and β-oxidation (**Fig. 2.12D**). In HCMs, OL2HG decreased the signal intensity of $^{13}C_{18}$-oleoylcarnitine significantly across all measured time points (**Fig. 2.12E**). In PAECs and HCFs, OL2HG produced the same directional effect, albeit with cell-type-specific temporal signatures (**Fig. 2.12F–G**).

In the second approach, we reversed the labeling logic to assess the effects of variable OL2HG exposures on pre-existing FAO intermediates. For this purpose, we pre-labeled cells with $^{13}C_{18}$-oleate for 24 h to enrich the intracellular $^{13}C_{18}$-oleoylcarnitine pool, and during the chase phase introduced unlabeled oleate in the presence or absence of OL2HG for 1–24 h (**Fig. 2.12H**). This design allowed us to isolate the relatively shorter-term effects of OL2HG, in direct contrast to the first experiment, which captured longer-term OL2HG programming of FAO pathways. In both HCMs and HCFs, OL2HG did not markedly alter the clearance of pre-labeled $^{13}C_{18}$-oleoylcarnitine (**Fig. 2.12I–J**). However, OL2HG increased the signal intensity of newly formed unlabeled $^{12}C_{18}$-oleoylcarnitine at early time points (1 h in HCMs and 1–6 h in HCFs), while decreasing it at later time points (3–24 h in HCMs and 24 h in HCFs) (**Fig. 2.12I–J**).Taken together, these dual isotope-tracing strategies demonstrate that OL2HG suppresses FAO through both chronic and acute mechanisms, while its effects on carbon flux through the oleoylcarnitine pool depend strongly on temporal dynamics and cell-type context.

Given our observations that OL2HG regulated palmitate oxidation and carbon flux through oleoylcarnitine, we next asked whether OL2HG also alters the intracellular expression of shorter chain acylcarnitines, as assessed by LC–MS. In HCMs, HCFs, and PASMCs, but not in PAECs, OL2HG significantly increased intracellular free carnitine (**Fig. 2.13A**). In contrast, OL2HG decreased intracellular acetylcarnitine and butyrylcarnitine across all four cell types examined, with the exception of acetylcarnitine in PASMCs (**Fig. 2.13B–C**).

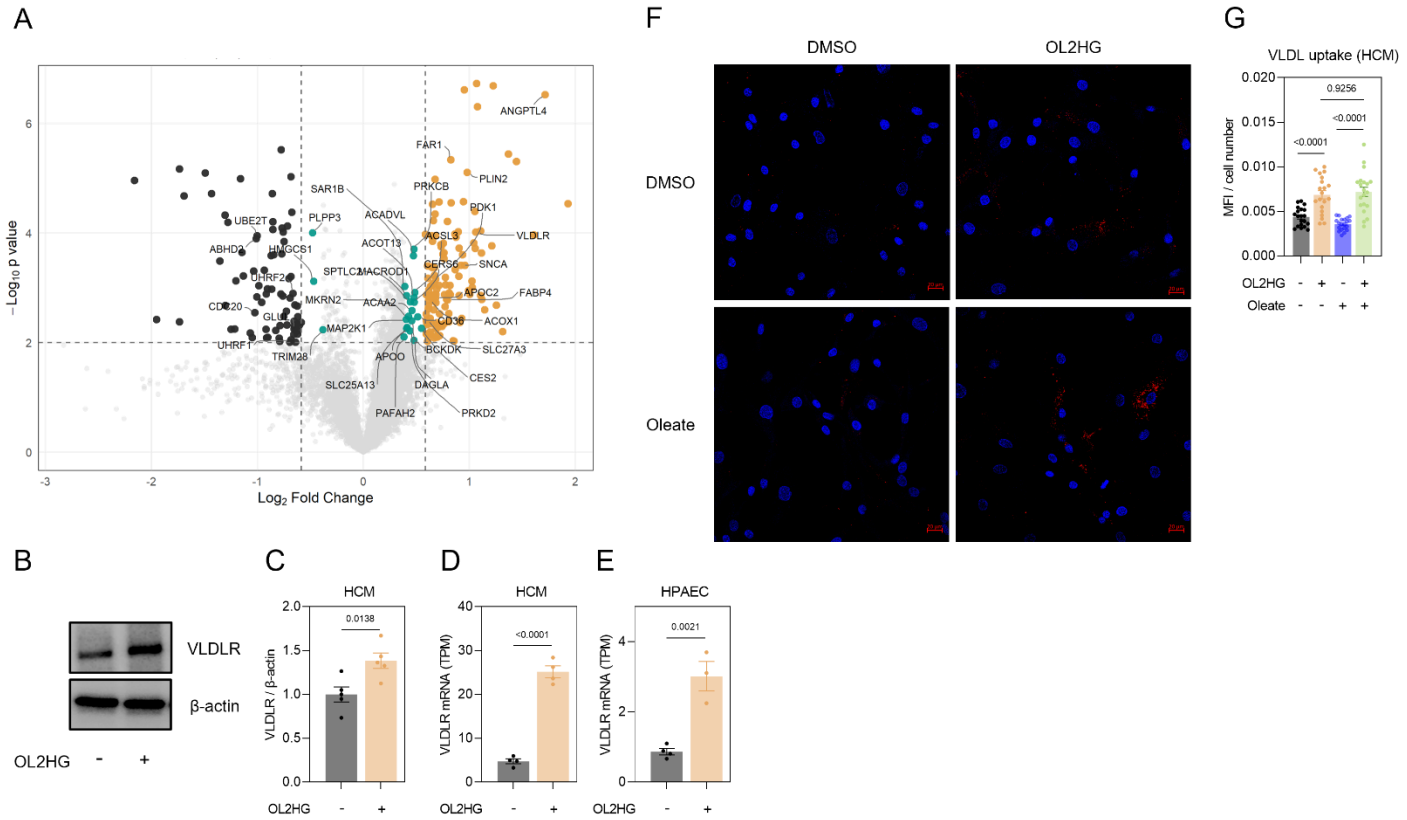

Figure 2.11. OL2HG increases VLDLR expression and VLDL uptake in primary cells. **A**, TMTpro-based proteomics of HCMs treated with DMSO (n=4) or OL2HG (n=4) for 24 h. Significance threshold set to $p<0.05$ and $|\text{fold change}|>1.5$. Color-coded significant features shortlisted to proteins annotated in KEGG pathways containing the terms "lipid," "cholesterol," "fatty acid," or "triglyceride". **B** and **C**, Representative immunoblot and quantification of VLDLR in HCMs treated with DMSO (n=5) or OL2HG (n=5) for 24 h. **D** and **E**, Expression of *VLDLR* in HCMs and PAECs following treatment with DMSO (n=4) or OL2HG (n=3-4) for 24 h. Data are expressed as transcripts *per* million (TPM). **F** and **G**, Representative confocal images and quantification of HCMs pre-loaded with or without oleic acid for 24 h and subsequently treated with DMSO or OL2HG for 24 h. Cells were stained with 1,1'-dioctadecyl- 3,3,3',3'-tetramethylindocarbocyanine perchlorate (DiI–VLDL) (red) and 4′,6-diamidino-2-phenylindole (DAPI) (blue). Data are expressed as mean fluorescence intensity (MFI) normalized to cell number. Data are presented as mean ± SEM. Data were tested for normality by Shapiro–Wilk test. Normal data were analyzed by ordinary one-way ANOVA (>2 groups) or unpaired *t*-test (pairwise). Non-normal data were analyzed by the Kruskal-Wallis test (> 2 groups) or Mann–Whitney test (pairwise).

To test whether a functional relationship links long-chain and short-chain acylcarnitine metabolism, we treated HCMs with OL2HG in the presence or absence of etomoxir, a widely used inhibitor of the mitochondrial long-chain acylcarnitine transporter CPT1. Etomoxir decreased the expression of intracellular butyrylcarnitine and propionylcarnitine significantly, and this decrease was potentiated by OL2HG (**Fig. 2.13D**). To determine whether OL2HG-induced changes in intracellular short-chain acylcarnitines associated with altered extracellular concentrations, we measured extracellular carnitine and butyrylcarnitine expression in HCMs and HCFs. In both cell types, OL2HG decreased extracellular carnitine and butyrylcarnitine significantly (**Fig. 2.13E–F**). These data indicate that OL2HG alters both intracellular and extracellular short chain acylcarnitine homeostasis across human cell types. Importantly, to exclude a confounding effect from the octyl moiety of OL2HG, we confirmed that unmodified L2HG also decreased intracellular butyrylcarnitine expression in PAECs (**Fig. 2.13G**).

We next examined whether the inhibition of palmitate oxidation and the differential regulation of acylcarnitines by OL2HG are associated with transcriptional changes in genes governing the carnitine shuttle and FAO. We focused this analysis on PAECs, as OL2HG inhibited palmitate oxidation in these cells both in the presence and absence of oleate pre-loading, whereas in HCMs OL2HG inhibited palmitate oxidation only under oleate pre-loading conditions. Using RNA-seq data, we found that OL2HG significantly decreased expression of *SLC22A5*, *EHHADH*, *HADH*, *ACAT1*, and *ACAT2*, while significantly increasing expression of *CRAT*, *CROT*, *CPT1A*, *CPT1B*, and *ACADVL* (**Fig. 2.14A–B**). Consistent with transcriptional upregulation, OL2HG also increased CPT1A protein expression, as assessed by immunoblotting (**Fig. 2.14C–D**). Notably, this increase in CPT1A occurred despite the observed inhibition of palmitate oxidation, suggesting, that CPT1A upregulation likely reflects a compensatory response to OL2HG-mediated suppression of FAO. Cross-reference to the TMTpro proteomics screen in HCMs (**Supplementary Data S2.4**) further confirmed protein-level upregulation of CPT1A and ACADVL; other RNA-sequencing hits did not show concordant protein-level changes, consistent with the temporal and abundance-related decoupling commonly observed between transcript and protein responses.

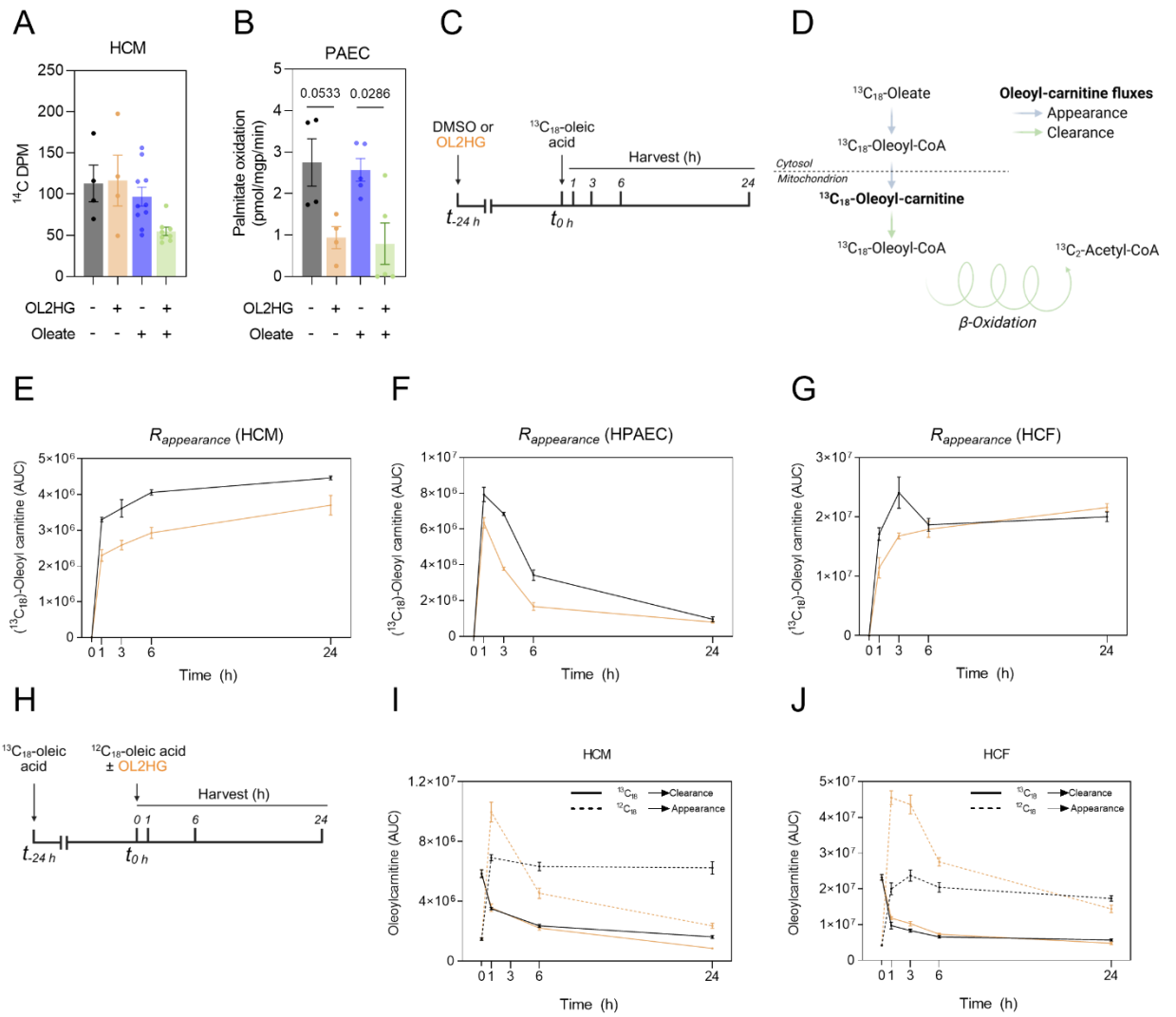

Figure 2.12. OL2HG decreases palmitate oxidation and alters carbon flux through oleoylcarnitine. A and **B**, Palmitate oxidation of HCMs and PAECs pre-loaded with or without oleic acid for 24 h and subsequently treated with DMSO or OL2HG for 24 h. Data are expressed as ^{14}C disintegrations per min (DPM, **A**) or pmol palmitate oxidized *per* mg protein (mgp) *per* min (**B**). **C**, Experimental design of cells pre-treated with DMSO or OL2HG for 24 h followed by ^{13}C$_{18}$-oleic acid for 1–24 h. **D**, Schematic representation of carbon flux from ^{13}C$_{18}$-oleate to ^{13}C$_{18}$-oleoylcarnitine. **E**–**G**, Signal intensity of newly formed ^{13}C$_{18}$-oleoylcarnitine in HCMs, PAECs, and HCFs using the experimental design in Panel **C**. **H**, Experimental design of cells pretreated with ^{13}C$_{18}$-oleic acid for 24 followed by replacement with equimolar ^{12}C$_{18}$-oleic acid in the presence or absence of OL2HG for 1–24 h. **I** and **J**, Signal intensity of pre-labeled ^{13}C$_{18}$-oleoylcarnitine and newly formed ^{12}C$_{18}$-oleoylcarnitine in HCMs and HCFs using the experimental design in Panel **H**. Data are presented as mean ± SEM. Data were tested for normality by Shapiro–Wilk test. Normal data were analyzed by ordinary one-way ANOVA (>2 groups) or unpaired *t*-test (pairwise). Non-normal data were analyzed by the Kruskal-Wallis test (> 2 groups) or Mann–Whitney test (pairwise).

2.3.7 *L2hgdh*$^{-/-}$ mice exhibit hypertriglyceridemia and sex-dependent differential expression of acylcarnitines

We next asked whether the OL2HG-induced alterations in TG metabolism and lipid-droplet abundance observed in primary human cells could be recapitulated *in vivo*. To address this question, we used a mouse model in which *L2hgdh*, the gene encoding the only known enzyme capable of catabolizing L2HG, is homozygously disrupted by a gene-trap insertion. These *L2hgdh*$^{-/-}$ mice develop L2HG aciduria, characterized by systemic accumulation of L2HG but not D2HG[66]. As expected, we confirmed that total circulating 2HG concentrations were elevated significantly in both male and female *L2hgdh*$^{-/-}$ mice relative to wild-type controls (**Fig. 2.15A**).

Consistent with our *in vitro* findings showing that OL2HG increases intracellular TGs across multiple primary human cell types, *L2hgdh*$^{-/-}$ mice exhibited significantly higher circulating TGs in both sexes (**Fig. 2.15B**). By contrast, circulating CEs were significantly decreased in female *L2hgdh*$^{-/-}$ mice while remaining unchanged in males, indicating a sex-specific effect on CE metabolism (**Fig. 2.15C**).

Given our *in vitro* observations that OL2HG inhibited palmitate oxidation and altered carbon flux through oleoylcarnitine, we next examined the abundances of circulating long-chain acylcarnitines, using LC–MS/MS for detection. Palmitoylcarnitine [Car(16:0)] and oleoylcarnitine [Car(18:1)] were significantly decreased in female *L2hgdh*$^{-/-}$ mice, but unchanged in males, again demonstrating sex-dependent effects (**Fig. 2.15D–E**).

To evaluate systemic metabolic alterations in an unbiased manner, we performed LC–MS-based plasma metabolomics. We quantified 116 metabolites from our in-house library of metabolites with known retention times (**Supplementary Data S2.5**). Apart from 2HG, the differentially expressed metabolites were distinct between males and females. (**Fig. 2.15F–G**), supporting sex-specific metabolic remodeling in response to L2HG accumulation *in vivo*. Of particular interest, butyrylcarnitine [Car(4:0)] was decreased significantly in *L2hgdh*$^{-/-}$ male mice but remained unchanged in females (**Fig. 2.15F–H**). These findings show that loss of *L2hgdh*, and subsequent systemic L2HG elevation, induce hypertriglyceridemia in both sexes, while producing sex-dependent alterations in the expression patterns of CEs and acylcarnitines.

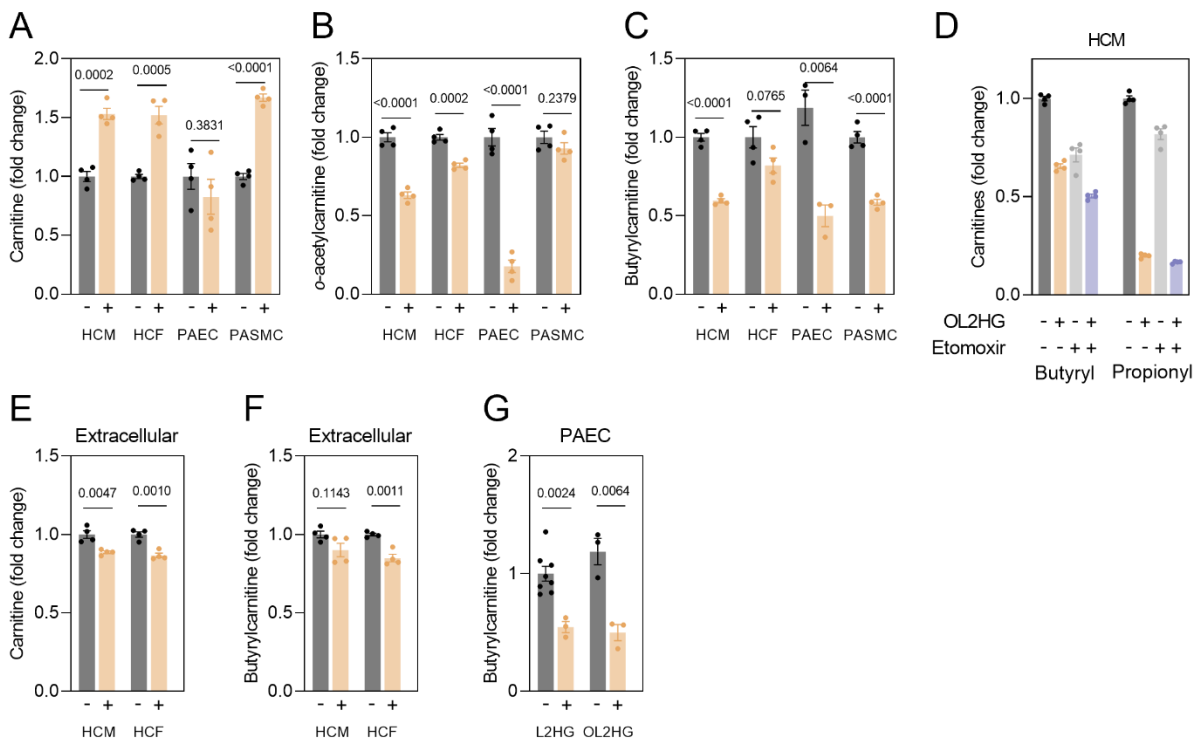

Figure 2.13. OL2HG alters the bioavailability of short chain fatty acids in primary human cells. A–**C**, Intracellular expression of carnitine, *O*-acetylcarnitine, and butyrylcarnitine in HCMs, HCFs, PAECs, and PASMCs following treatment with DMSO (n=3-4) or OL2HG (n=3-4) for 24 h. **D**, Intracellular expression of butyrylcarnitine and propionylcarnitine in HCMs following treatment with DMSO or OL2HG in the presence or absence of etomoxir. **E** and **F**, extracellular expression of carnitine and butyrylcarnitine in HCMs and HCFs following treatment with DMSO (n=4) or OL2HG (n=4) for 24 h. **G**, Intracellular expression of butyrylcarnitine in PAECs following treatment with unmodified L2HG (1 mM) or OL2HG (500 μM) for 24 h. Data are presented as mean ± SEM. Data were tested for normality by Shapiro–Wilk test. Normal data were analyzed by ordinary one-way ANOVA (>2 groups) or unpaired *t*-test (pairwise). Non-normal data were analyzed by the Kruskal-Wallis test (> 2 groups) or Mann–Whitney test (pairwise).

Next, we sought to examine whether L2HG regulates circulating TGs with specificity for particular acyl chain compositions. Because TGs store fatty acids of distinct chain lengths and saturation states (*i.e.*, features that impart unique biochemical and signaling properties, *e.g.*, palmitate as a readily oxidized substrate and arachidonic acid as a bioactive signaling lipid), we asked whether L2HG associates preferentially with specific TG species. To address this question, we computed the Pearson correlation coefficient between circulating total 2HG and each individual TG species. TGs containing relatively shorter acyl chains (~50 total carbons) showed markedly stronger positive correlations with circulating 2HG, whereas TGs containing longer chains (~60–65 carbons) displayed weak or absent correlations (**Fig. 2.16A**). Indeed, we observed a statistically

significant negative relationship between the number of carbons in a TG species and its correlation with circulating 2HG (**Fig. 2.16A**), indicating that L2HG associates preferentially with lower-carbon TGs and suggesting that the synthesis of longer fatty acyl chain TGs may be inhibited by systemic L2HG accumulation.

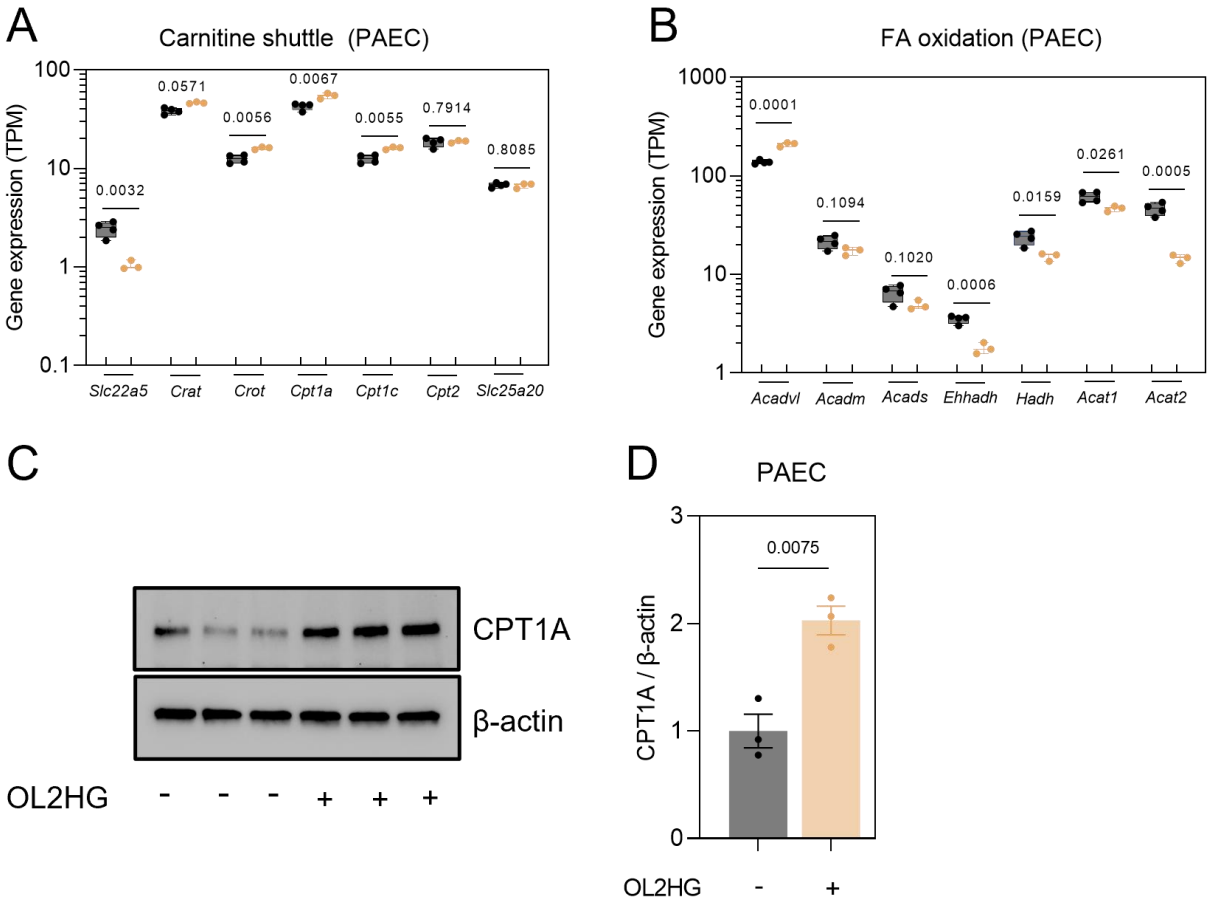

Figure 2.14. OL2HG alters expression of genes related to fatty acid oxidation. A and **B**, Expression of genes involved in the carnitine shuttle and fatty acid oxidation pathway in PAECs following treatment with DMSO (n=4) or OL2HG (n=3) for 24 h. Data are expressed as transcripts *per* million (TPM). **C** and **D**, Representative immunoblot and quantification of CPT1A in PAECs following treatment with DMSO (n=3) or OL2HG (n=3) for 24 h. Data are presented as mean ± SEM. Data were tested for normality by Shapiro–Wilk test. Normal data were analyzed by unpaired *t*-test (pairwise). Non-normal data were analyzed by the Mann–Whitney test.

We next assessed whether TG species correlate with each other according to structural similarity. Indeed, TGs with the same or similar total carbon numbers correlated more strongly with one another than with relatively smaller / larger species (**Fig. 2.16B**). Importantly, we observed these same trends in an independent human plasma metabolomics dataset (accessed from Metabolomics Workbench Project ID PR001024) (**Fig. 2.16C–D**), indicating that the relationship between 2HG and TG species composition is conserved across species and not restricted to our mouse model. Furthermore, when we stratified TGs into three subcategories based on total acyl-chain carbon number (50–55, 56–60, and 61–66 carbons), circulating TGs were significantly increased in *L2hgdh*$^{-/-}$ mice of both sexes in the 50–55 and 56–60 carbon groups (**Fig. 2.16E**). However, in the 61–66 carbon group, TGs were elevated only in female *L2hgdh*$^{-/-}$ mice, with no significant change observed in males (**Fig. 2.16E**).

2.3.8 Male *L2hgdh*$^{-/-}$ hearts exhibit accelerated TG utilization during *ex vivo* fatty acid deprivation

Given the hypertriglyceridemia observed in *L2hgdh*$^{-/-}$ mice, we next tested whether cardiac and hepatic TG abundance is altered under baseline conditions. Total TG content in both tissues was unchanged between *L2hgdh*$^{-/-}$ and wild-type mice (**Fig. 2.17A**). To determine whether TGs are differentially regulated in *L2hgdh*$^{-/-}$ hearts under metabolic stress, we perfused isolated hearts *ex vivo* from male mice using the Langendorff system. Hearts were equilibrated for 30 min at 80 mmHg, followed by 30 min of baseline perfusion in the absence of exogenous free fatty acids (FFAs) in the perfusate (**Fig. 2.17B**). In this way, hearts were forced to rely primarily on glucose oxidation and/or existing TG pools rather than an exogenous supply of preferred *in vivo* substrate, fatty acids. We first confirmed that L2HG, but not D2HG, was markedly elevated in knockout hearts (**Fig. 2.17C**). Unbiased, discovery-driven LC–MS/MS lipidomics revealed that *L2hgdh*$^{-/-}$ hearts exhibited broad downregulation of TG species, resulting in significantly lower total cardiac TG content relative to wild-type controls (**Fig. 2.17D–E**). This reduction occurred across TGs of all acyl-chain carbon categories, indicating that the effect was not dependent on specific fatty acid compositions (**Fig. 2.17F**). Since freshly excised hearts displayed comparable TG abundance between genotypes (**Fig. 2.17A**), the decrease in TGs after *ex vivo* fatty acid deprivation suggests preferential utilization and/or accelerated clearance of pre-existing TG stores in *L2hgdh*$^{-/-}$ hearts.

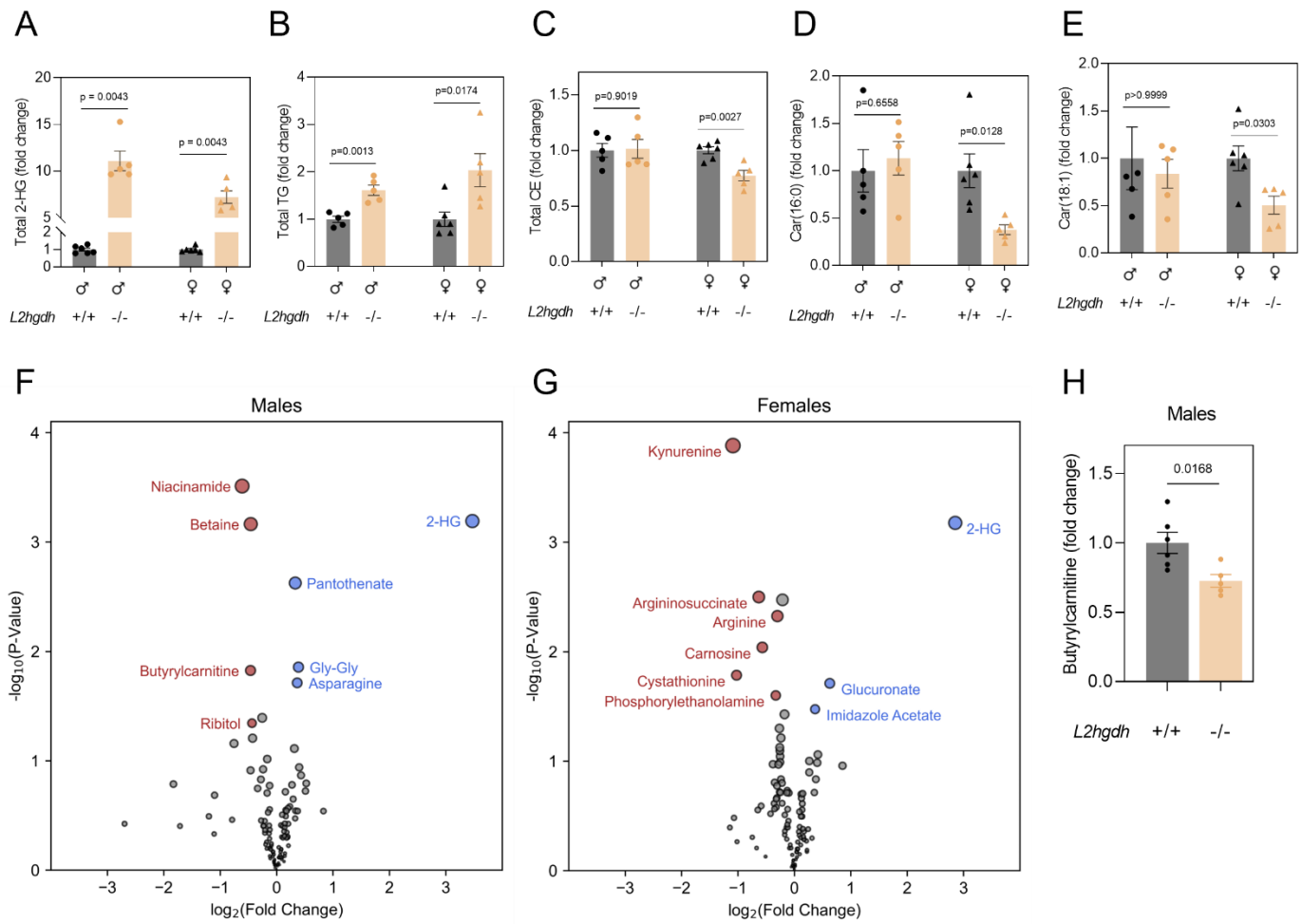

Figure 2.15. *L2hgdh*$^{-/-}$ mice exhibit hypertriglyceridemia and sex-dependent differential expression of acylcarnitines. A–E, Expression of total 2HG, total TG, total CE, palmitoylcarnitine [Car(16:0)], and oleoylcarnitine [Car(18:1)] in plasma of *L2hgdh*$^{+/+}$ (male, n=5; female, n=6) and *L2hgdh*$^{-/-}$ mice (male, n=5; female, n=5). Data are expressed as fold changes relative to *L2hgdh*$^{+/+}$ in the corresponding sex. **F** and **G**, Differential expression of metabolites in plasma of *L2hgdh*$^{+/+}$ (male, n=5; female, n=6) and *L2hgdh*$^{-/-}$ mice (male, n=5; female, n=5). Threshold for significance was set to $p<0.05$ and $|FC|>1.5$. **H**, Expression of plasma butyrylcarnitine in male *L2hgdh*$^{+/+}$ (n=5) and *L2hgdh*$^{-/-}$ (n=5) mice. Data are presented as mean ± SEM. Data were tested for normality by Shapiro–Wilk test. Normal data were analyzed by unpaired *t*-test. Non-normal data were analyzed by the Mann–Whitney test.

To identify a potential mechanism underlying this increased TG clearance flux, we performed TMTpro-based quantitative proteomics (this dataset, including statistical significance thresholds, is summarized in Chapter 4). *L2hgdh*$^{-/-}$ hearts showed significant downregulation of the lipid-droplet–coating proteins PLIN2, PLIN3, and PLIN5 (**Fig. 2.17F–H**), all of which regulate TG storage and protect against lipolysis. Consistent with these findings, pathway-enrichment analysis of differentially expressed proteins demonstrated significant enrichment of TG-related metabolic processes (**Fig. 2.17I**).

2.3.9 Sex-dependent lipidomic differences in *L2hgdh*$^{-/-}$ mice following myocardial ischemia

Given our prior findings that cardiac L2HG accumulates during myocardial ischemia and confers cardioprotection[60], we next examined whether *L2hgdh* deletion influences lipid metabolism during ischemic stress. We perfused isolated hearts as described above (*i.e.*, 30 min equilibration at 80 mmHg followed by 30 min of baseline perfusion), this time introducing an additional 90 min of LFI (10 mmHg) (**Fig. 2.18A**). Since baseline perfusion experiments were performed in males alone, but our earlier plasma analyses demonstrated sex-dependent differences in lipid regulation (**Fig. 2.15**), we conducted LFI experiments in both male and female mice. The rationale to include both sexes is supported further by the fact that females are at lower risk of clinical coronary artery disease (myocardial infarction / angina) than their male counterparts until they reach ~10 years post-menopause at which point the risk is similar.

We first confirmed that myocardial L2HG increased significantly in male hearts following LFI, and that this ischemia-induced accumulation was potentiated in *L2hgdh*$^{-/-}$ mice (**Fig. 2.18B**). Using unbiased LC–MS/MS lipidomics, we found that palmitoylcarnitine [Car(16:0)] and hydroxylinoleoylcarnitine [Car(18:2-OH)] were significantly decreased in ischemic *L2hgdh*$^{-/-}$ hearts relative to wild-type controls, while linoleoylcarnitine [Car(18:2)] displayed a modest, yet non-significant, reduction (**Fig. 2.18C–D**). Notably, all three acylcarnitines accumulated robustly during LFI relative to baseline perfusion (**Fig. 2.18D**).

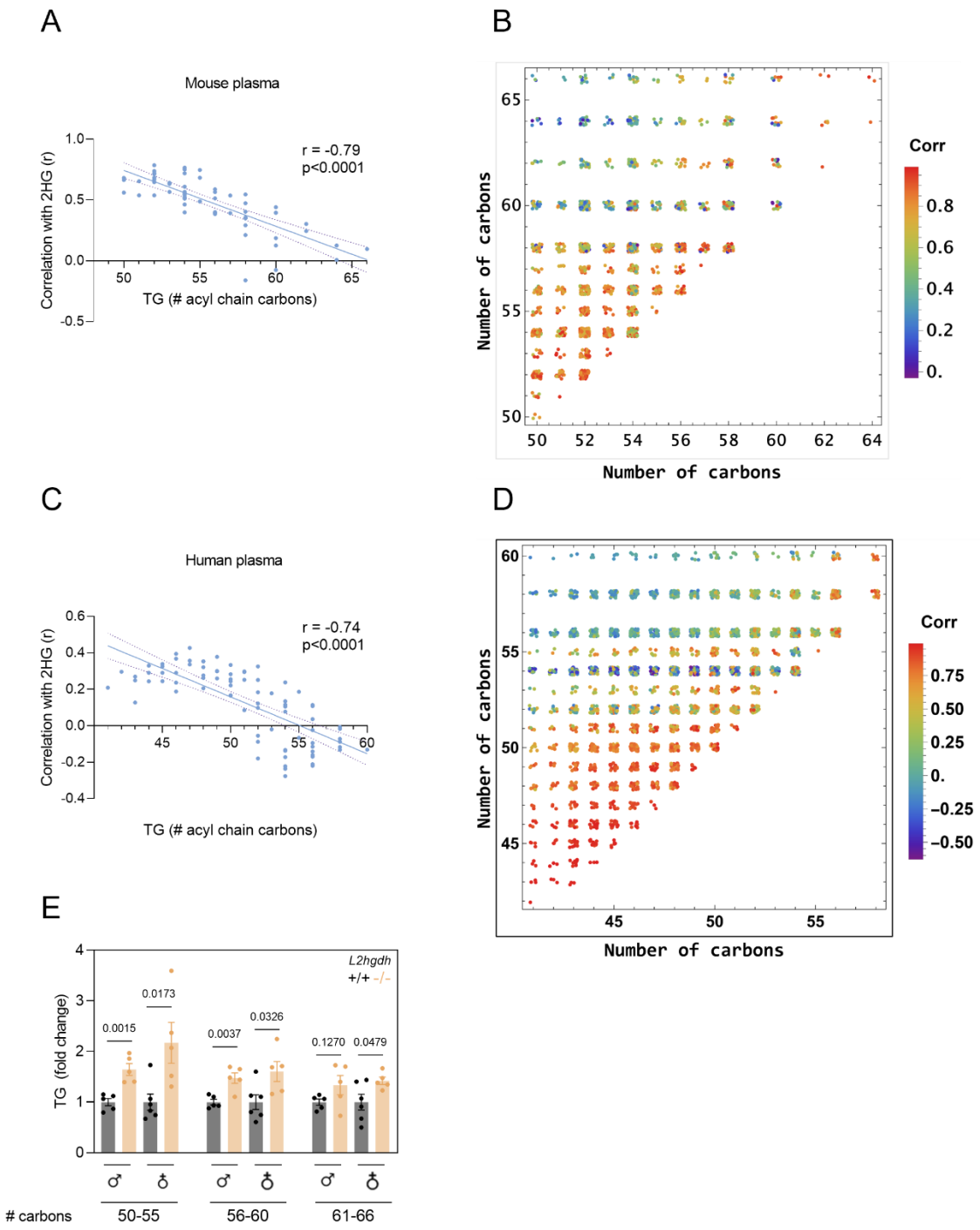

Figure 2.16. Circulating 2HG correlates with TG acyl chain composition in mice and humans. A and **C**, Pearson correlations between each individual TG species and total 2HG in plasma of mouse or humans, as a function of the total number of acyl chain carbons in the TG species. **B** and **D**, Pearson correlations between TG species based on number of acyl chain carbons. **E**, Expression of total TG in plasma of *L2hgdh*$^{+/+}$ (male, n=5; female, n=6) and *L2hgdh*$^{-/-}$ (male, n=5; female, n=5) mice, stratified according to number of total acyl chain carbons. Data are presented as mean ± SEM. Data were tested for normality by Shapiro–Wilk test. Normal data were analyzed by unpaired *t*-test. Non-normal data were analyzed by the Mann–Whitney test.

We next assessed myocardial TG content in hearts subjected to LFI in both male and female mice. Total cardiac TGs were significantly increased in female *L2hgdh*$^{-/-}$ mice following LFI, whereas male mice showed no genotype-dependent differences (**Fig. 2.18E**). Furthermore, stratification by acyl-chain carbon length revealed that all TG subclasses (50–55, 56–60, and 61–66 carbons) were significantly upregulated in ischemic female *L2hgdh*$^{-/-}$ hearts, but remained unchanged in males, indicating a sex-dependent but acyl-chain–composition–independent effect (**Fig. 2.18E**). Collectively, these findings indicate that L2HG partially attenuates the accumulation of long-chain acylcarnitines during myocardial ischemia and promotes TG accumulation during LFI in a sex-dependent manner.

2.3.10 *L2hgdh*$^{-/-}$ mice exhibit altered whole-body metabolism during fasting

To determine whether *L2hgdh* deletion alters whole-body metabolic responses to nutrient stress, we assessed male wildtype and *L2hgdh*$^{-/-}$ mice using a Promethion metabolic cage system during a controlled fasting–refeeding experiment. First, mice were monitored for two days to establish baseline metabolic parameters. Food was removed on the third day, initiating an overnight fast, after which food was returned. EchoMRI analysis showed a modest trend toward an increase in fat mass and total body mass, but not lean mass, in *L2hgdh*$^{-/-}$ mice (**Fig. 2.19A**), consistent with their hypertriglyceridemic phenotype (**Fig. 2.15B**).

Since many metabolic outputs scale with body size, we analyzed all mass-dependent parameters using an ANCOVA model with body mass as the covariate. This statistical approach incorporates mass effect (the influence of body mass on the parameter), group effect (the influence of genotype independent of mass), and interaction effect (whether the effect of genotype depends on body mass). At baseline, none of the measured metabolic parameters showed a significant group effect (**Table 2.2**), indicating that genotype alone did not alter baseline metabolism after accounting for body size. Most parameters also lacked a significant interaction effect, demonstrating that the relationship between body mass and metabolic output was similar in wild-type and *L2hgdh*$^{-/-}$ mice. The sole exception was water intake, where *L2hgdh*$^{-/-}$ mice consumed more water; however, this finding was accompanied by a significant interaction effect (**Table 2.2**), meaning that the genotype difference depended on body mass rather than reflecting a uniform increase across all mice.

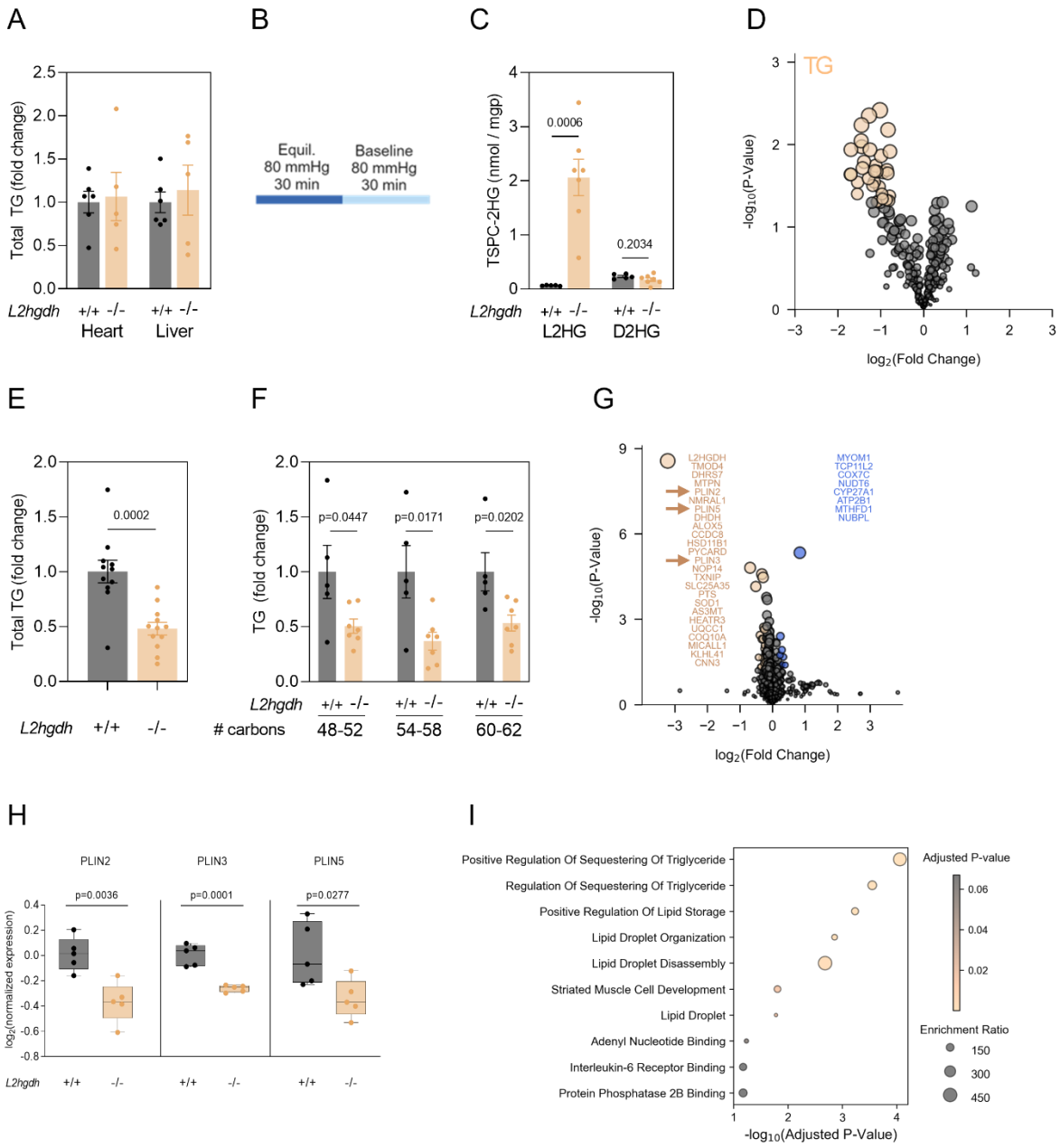

Figure 2.17. L2HG increases cardiac TG utilization during fatty acid deprivation *ex vivo* in males. A, Expression of total TG in freshly excised hearts and livers from male *L2hgdh*$^{+/+}$ (n=6) and *L2hgdh*$^{-/-}$ (n=5) mice. **B**, Schematic representation of fatty acid-deprived baseline perfusion protocol using the Langendorff system. **C**, Quantification of L2HG and D2HG in hearts following 30 min fatty acid-deprived baseline perfusion, using chiral derivatization with *N*-(p-toluenesulfonyl)-L-phenylalanyl chloride (TSPC) for enantioselectivity. **D**–**F**, Differential expression of cardiac TGs following 30 min fatty acid-deprived baseline perfusion. **G**, TMTpro-based proteomics of hearts depicting differential expression in *L2hgdh*$^{-/-}$ hearts following fatty acid-deprived baseline perfusion. Significance threshold set to $p<0.05$ and $|FC|>1.3$. **H**, Expression of perilipin (PLIN) proteins. **I**, Enrichment analysis of differentially regulated proteins. Data are presented as mean ± SEM. Data were tested for normality by Shapiro–Wilk test. Normal data were analyzed by unpaired *t*-test. Non-normal data were analyzed by the Mann–Whitney test.

Consistent with an earlier report[66], *L2hgdh*$^{-/-}$ mice exhibited increased pedestrian locomotion during both light and dark photoperiods and traveled greater total cage distance during the light period under baseline conditions (**Table 2.3**). Under fasting conditions, however, these activity differences were no longer evident (**Table 2.4**), suggesting that fasting suppresses the baseline hyperactivity phenotype. Notably, despite comparable physical activity during fasting, *L2hgdh*$^{-/-}$ mice displayed significantly higher oxygen consumption and a marginal increase in energy expenditure during the light photoperiod, accompanied by a significant decrease in energy balance (**Tables 2.4–5**), indicating a fasting-specific elevation in metabolic rate that is independent of locomotor activity. During refeeding, no metabolic parameters differed between genotypes (**Tables 2.6–7**). Taken together, these findings show that *L2hgdh* deficiency produces a nutrient-state–dependent metabolic phenotype, with genotype-independent baseline metabolism but genotype-dependent increased energy expenditure and reduced energy balance uniquely under fasting conditions.

2.4 Discussion

This chapter identifies a previously unappreciated role for 2HG, particularly L2HG, in the regulation of TG and fatty acid metabolism and LD (patho)biology across primary human cells and *in vivo*. Building from the premise that L2HG perturbs carbohydrate metabolism and mitochondrial redox balance (see Section 1.3), we hypothesized that L2HG may also reprogram lipid metabolism given the extensive biochemical coupling between carbohydrate flux, lipogenesis, lipolysis, and FAO. Our findings support this hypothesis and further reveal that L2HG influences TG homeostasis through a multi-layered mechanism that includes enhanced TG accumulation, LD expansion, altered TG turnover dynamics, and impaired FAO under distinct biological contexts. Importantly, these effects are not restricted to a single cell type and extend beyond *in vitro* models to systemic physiology, where genetic elevation of L2HG in *L2hgdh*$^{-/-}$ mice produces hypertriglyceridemia, sex-dependent remodeling of acylcarnitines, and context-dependent shifts in cardiac TG utilization during nutrient stress and ischemia.

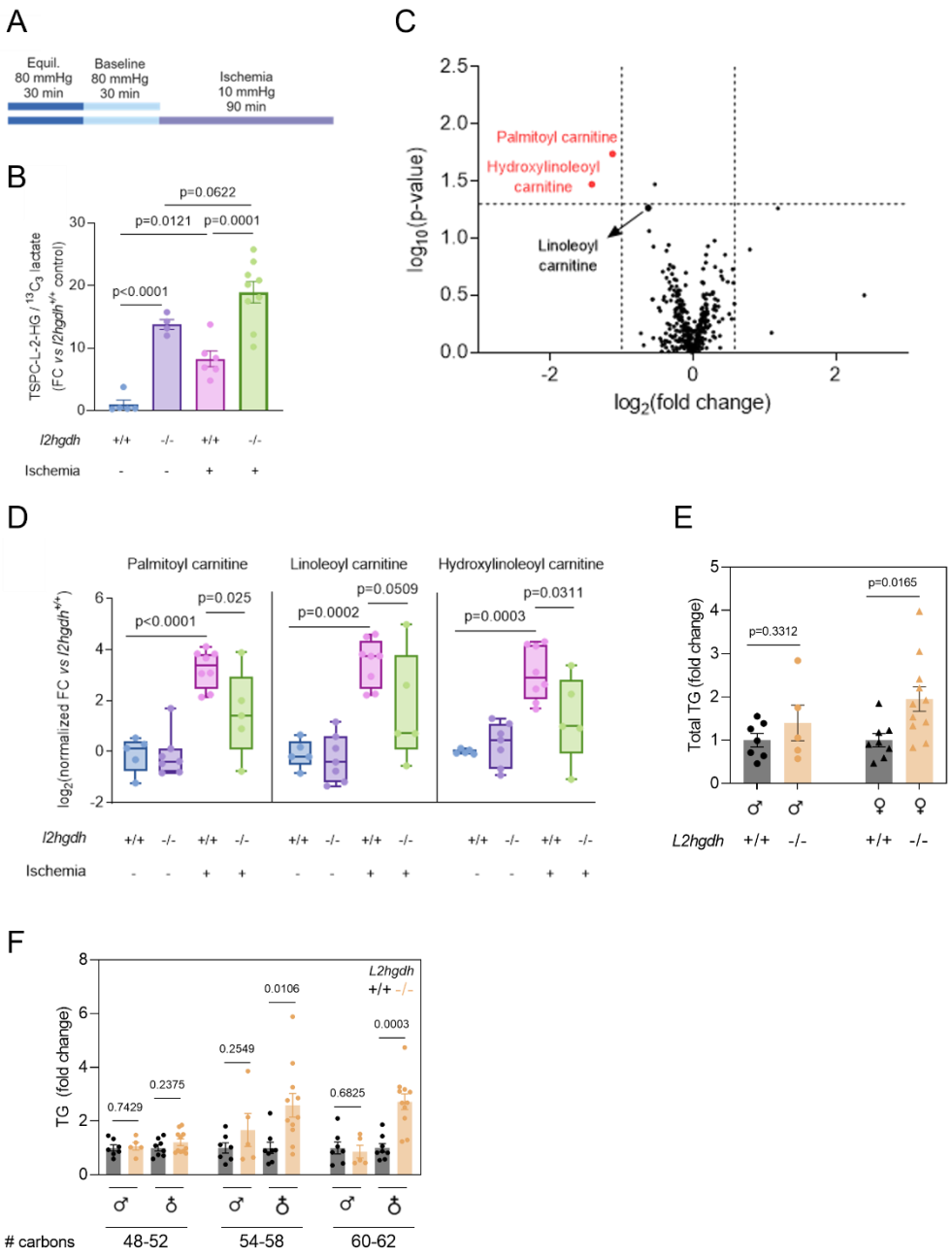

Figure 2.18. L2HG decreases cardiac long chain acylcarnitines in males and increases cardiac TGs in females following low flow ischemia (LFI). A, Schematic representation of fatty acid-deprived baseline perfusion and LFI protocols using the Langendorff system. **B**, Quantification of L2HG in hearts following 30 min fatty acid-deprived baseline perfusion with or without subsequent LFI, using chiral derivatization with *N*-(p-toluenesulfonyl)-L-phenylalanyl chloride (TSPC) for enantioselectivity. **C**–**D**, Differential expression of cardiac long chain acylcarnitines in *L2hgdh*$^{-/-}$ (n=9) *vs. L2hgdh*$^{+/+}$ (n=6) male hearts following LFI. **E**–**F**, Expression of TGs in *L2hgdh*$^{-/-}$ *vs. L2hgdh*$^{+/+}$ hearts following LFI. Data are presented as mean ± SEM. Data were tested for normality by Shapiro–Wilk test. Normal data were analyzed by ordinary one-way ANOVA (>2 groups) or unpaired *t*-test (pairwise). Non-normal data were analyzed by the Kruskal-Wallis test (> 2 groups) or Mann–Whitney test (pairwise).

A necessary prerequisite for mechanistic studies of 2HG biology is a tractable *in vitro* system in which extracellular exposure reliably increases intracellular 2HG (see Section 1.6). We therefore first verified that OL2HG and OD2HG enter cells and elevate intracellular total 2HG, as assessed by LC–MS. Notably, OD2HG increased total 2HG to a greater extent than OL2HG. This observation is consistent with the possibility that the two enantiomers exhibit differential clearance by stereospecific dehydrogenases; however, the finding that total intracellular O2HG levels are comparable following OL2HG and OD2HG treatment suggests that cellular uptake and/or intracellular hydrolysis of the two octyl esters are broadly similar. Although this chapter does not resolve the source of this quantitative difference, it establishes a critical interpretive point for downstream phenotypes: enantiomer-specific lipid effects may reflect both stereochemical signaling differences as well as the magnitude and/or duration of intracellular 2HG exposure. In addition, the subsequent use of unmodified L2HG – titrated to achieve intracellular total 2HG levels comparable to those induced by OL2HG – together with inclusion of octyl acetate as a control, was essential to demonstrate that the observed lipid phenotypes are attributable to L2HG itself rather than to the octyl modification or ester-derived effects (see Section 1.6.1.1). These validation experiments were essential to ensure that all subsequent analyses were interpreted in an appropriate biochemical context, with intracellular 2HG exposure accurately defined and disentangled from potential confounding effects.

Unbiased, discovery-driven LC–MS/MS lipidomics revealed that OL2HG alters multiple lipid classes, with the most coherent and directionally consistent changes occurring in glycerolipids, particularly TGs (as well as PEs, which are the subject of Chapter 3). OL2HG increased the abundance of essentially all detected TG and DAG species in HCMs, and increased total TGs in multiple primary human cell types. While OD2HG also increased TGs, the magnitude was consistently lower, indicating that TG accumulation is either stereoselective for L2HG biology or sensitive to differences in intracellular 2HG abundance between enantiomers. Importantly, the observation that OL2HG increased TGs across several non-diseased primary human cell types (and, to a lesser extent in cancer cells) suggests that the effect is not restricted to a single specialized lipid-handling lineage but instead reflects a more general lipid remodeling program elicited by L2HG.

At the organellar level, OL2HG increased neutral lipid staining by BODIPY 493/503, as assessed by confocal microscopy and flow cytometry. OL2HG also increased PLIN2 protein abundance, as assessed by immunoblotting, supporting the conclusion that elevated TG levels are accompanied by LD expansion. Notably, PLIN2 was the only perilipin consistently upregulated across multiple primary human cell types, consistent with previous work demonstrating that OD2HG increased *PLIN2* gene expression in lipopolysaccharide-treated macrophages and adipocytes[67,68]. These findings may have important implications for the physical organization and/or intracellular localization of L2HG-induced LD and their interactions with other organelles. Interestingly, according to the BioPlex project (see Section 1.5.4), PLIN2 interacts physically with the mitochondrial membrane protein serine/threonine-protein kinase PINK1 in human colon cancer HCT116 cells[69], although whether this interaction mediates LD–mitochondria tethering remains unknown. Importantly, OL2HG-induced upregulation of PLIN2 observed in cultured cells is likely to manifest in a more complex and context-dependent manner *in vivo*, as genetic loss of *PLIN2* in the heart paradoxically leads to increased TG accumulation due to impaired lipophagy[70], highlighting that PLIN2 can regulate LD turnover and cardiac lipid homeostasis through mechanisms that are not readily predicted from isolated cell systems.

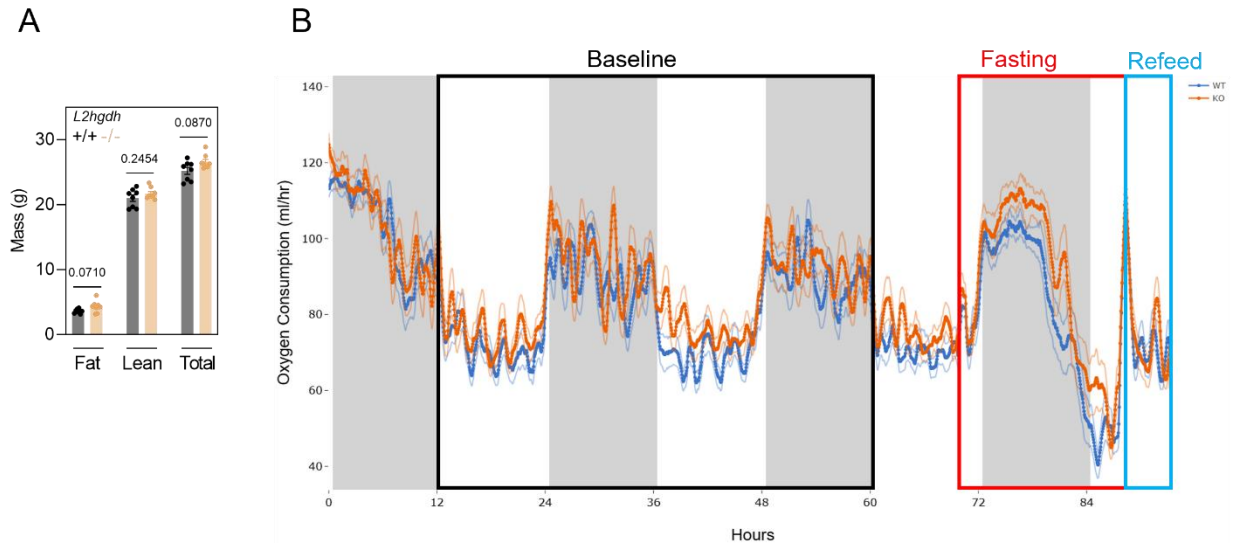

Figure 2.19. L2HG modestly alters whole-body metabolism. A, Fat, lean, and total mass of *L2hgdh*$^{+/+}$ (n=8) and *L2hgdh*$^{-/-}$ (n=8) male mice. Data are presented as mean ± SEM. Data were tested for normality by Shapiro–Wilk test and analyzed by unpaired *t*-test (normal) or Mann–Whitney test (non-normal). **B**, Oxygen consumption rate trace of fasting-refeed experiment in *L2hgdh*$^{+/+}$ (blue, n=8) and *L2hgdh*$^{-/-}$ (orange, n=8) mice, assessed using the Promethion metabolic cage system. Results are outlined in **Tables 2.2–2.6**.

Stable isotope tracing provided direct evidence that OL2HG increases lipogenic flux from exogenous oleate into TG, as demonstrated by increased formation of TG($3\times^{13}C_{18}$-oleate) in multiple cell types. Although the temporal kinetics differed across cell types, the conserved directional effect indicates that OL2HG enhances the capacity of cells to esterify incoming fatty acids into TG. This observed increase in labeled TG formation could, in principle, arise from several non-mutually exclusive mechanisms. Notably, because cells were pre-treated with OL2HG prior to exposure to labeled oleate, enhanced appearance of labeled TG may reflect altered fatty acid uptake (for example, *via* changes in the activity, expression, or surface localization of fatty acid transporters, although we did not detect consistent upregulation of known fatty acid transport genes or proteins in unbiased proteomics and transcriptomics analyses under the same conditions). Alternatively, OL2HG may increase the efficiency with which incoming fatty acids are partitioned into TG, through effects on any step of glycerolipid assembly or remodeling, including the G3P pathway, MAG recycling, or interconversion of phospholipid intermediates. Importantly, these experiments measure net TG accumulation rather than *de novo* lipogenesis *per se*; labeled TGs may arise not only from direct incorporation of exogenous oleate into newly synthesized TG but also from remodeling of pre-existing phospholipids or altered flux through multiple converging pathways that ultimately feed the TG pool. Consequently, while these data demonstrate that OL2HG increases overall TG biogenic flux, they do not pinpoint a specific enzymatic step within the TG synthesis pathway. Future work using complementary approaches – such as measuring labeled incorporation into defined phospholipid intermediates, selectively inhibiting individual glycerolipid assembly enzymes, or performing *in vitro* enzymatic assays with purified GPAT, AGPAT, or DGAT enzymes in the presence of L2HG – will be required to resolve which reactions (if any) are directly modulated by L2HG and to distinguish effects on fatty acid uptake, pathway partitioning, and enzyme activity.

In parallel, pulse–chase experiments using stable isotope tracing with heavy oleate demonstrated reduced clearance of pre-labeled TGs, indicating that OL2HG suppresses TG breakdown and/or turnover. However, an apparent reduction in labeled TG clearance could also reflect continued re-esterification of fatty acids derived from labeled phospholipids or partial remodeling of the glycerolipid pool, rather than a true decrease in lipolytic flux. Thus, the persistence of labeled TGs may arise from ongoing DGAT-dependent re-synthesis during the chase period, even in the absence of net TG loss. Future experiments incorporating pharmacologic or genetic inhibition of DGAT

during the chase phase will be required to prevent new TG formation and thereby isolate *bona fide* TG clearance. Taken together, these data support a dual mechanism underlying OL2HG-induced TG accumulation: enhanced net appearance of TGs alongside reduced apparent loss. It is important to note, however, that these flux measurements quantify only a single fully labeled TG species [*i.e.*, TG(3×$^{13}C_{18}$-oleate)], and although $^{13}C_{18}$-oleate is also incorporated into partially labeled TGs, comprehensive quantification of all such species is technically intractable; therefore, the conclusions regarding increased TG appearance and decreased clearance are specific to this oleate-containing TG species and may not necessarily extend to TGs containing other fatty acids.

A key observation is that OL2HG influenced TG synthesis and clearance on different time scales. The inhibition of TG clearance was evident with relatively short OL2HG exposure, whereas increased TG synthesis required longer exposure, implying mechanistically distinct control points. One plausible interpretation is that OL2HG rapidly influences lipolytic processes (*e.g.,* lipase access to droplets, coactivator availability, or post-translational regulation of lipases or PLINs), while longer exposures are required to reprogram metabolic flux into TG synthesis through slower processes such as changes in lipid transport, enzyme abundance, organelle remodeling, or transcriptional regulation. This temporal dissociation is consistent with a model in which early OL2HG exposure suppresses TG mobilization, enabling expansion of droplet TG stores, while prolonged exposure increases the steady-state capacity to channel fatty acids into TG. Moreover, DGAT inhibition fully abrogated the OL2HG-induced LD expansion. This result provides functional evidence that OL2HG-induced droplet accumulation reflects net TG synthesis rather than merely altered droplet morphology or dye uptake. However, RNA-seq analyses did not reveal a consistent or coordinated transcriptional signature across canonical TG synthesis, catabolism, and *de novo* lipogenesis pathways, suggesting that transcriptional regulation alone is insufficient to explain the conserved TG phenotype. This discordance between robust metabolic phenotypes and limited coherent transcriptional remodeling motivates two mechanistic inferences. First, OL2HG likely acts through post-transcriptional and/or post-translational mechanisms that alter flux without requiring broad changes in gene expression. Second, OL2HG may influence lipid metabolism primarily through substrate partitioning and organelle-level organization (*e.g.,* LD growth, altered contact with mitochondria/ER, and/or altered access of lipases), which could produce large shifts in TG abundance and flux without a strong transcriptional footprint.

Since L2HG is known to inhibit αKG-dependent enzymes (see Section 1.5.1), we tested whether co-treatment with OαKG modulates OL2HG effects on TG synthesis and clearance. OαKG prevented the OL2HG-induced increase in TG synthesis yet paradoxically enhanced OL2HG-induced inhibition of TG clearance, while fully preventing the net increase in total trioleylglycerol. These divergent effects reinforce the conclusion that OL2HG regulates TG synthesis and TG clearance through separable mechanisms. The OαKG rescue of net TG accumulation supports involvement of αKG-sensitive pathways in the integrated phenotype, but the directionally opposite effects on synthesis *versus* clearance indicate that αKG supplementation does not simply "reverse" OL2HG biology; rather, it reshapes the balance between parallel fluxes. Furthermore, consistent with canonical L2HG biology (see Sections 1.3 and 1.5.1.3), OL2HG stabilized HIF-1α protein and activated a HIF transcriptional program. HIF-1α knockdown attenuated OL2HG-induced PLIN2 upregulation modestly but did not abolish it, indicating that HIF contributes but is not required. This is in contrast to OL2HG-induced stabilization of the lipid metabolism-linked transcript factor SREBP1, which had no effect on PLIN2 upregulation. Moreover, hypoxia-induced HIF stabilization decreased TG abundance in HCMs, consistent with previous observations in adipocytes[71], demonstrating that HIF activation alone is not sufficient to phenocopy OL2HG-driven TG accumulation. Taken together, these data argue that OL2HG-driven lipid remodeling cannot be explained as a generic pseudohypoxic response. Instead, OL2HG appears to engage additional pathways that collectively shape the TG phenotype, potentially including non-HIF αKG-dependent targets, redox-driven metabolic partitioning, lipid uptake pathways, and organelle contact dynamics. We identified one of these pathways to be mediated by increased expression of VLDLR and, subsequently, enhanced VLDL uptake, as identified and validated by LC–MS/MS-based proteomics, immunoblotting, and confocal microscopy.

Given that TG mobilization provides fatty acids for FAO (see Sections 2.1.4 and 2.1.5), TG accumulation could reflect either increased lipid input or reduced oxidative clearance. Direct measurement of palmitate oxidation, as proxied by formation of radiolabeled CO_2 from cells treated with radiolabeled palmitate, demonstrated that OL2HG suppresses FAO in both HCMs (under oleate pre-loading) and PAECs (independent of pre-loading) under glucose deprivation. Complementary isotope tracing with labeled oleate revealed reduced steady-state abundance of labeled oleoylcarnitine following prolonged OL2HG exposure; however, because oleoylcarnitine is a transient intermediate rather than a metabolic end product, this decrease may reflect reduced

formation, enhanced downstream clearance, or both, and thus cannot be interpreted as a direct measure of fatty acid import or oxidation flux *per se*. Shorter-term tracing designs suggested more nuanced temporal behavior, with early increases in unlabeled oleoylcarnitine but later suppression, indicating that OL2HG affects fatty acid handling dynamically, perhaps reflecting initial compensatory shuttling followed by progressive suppression of oxidative throughput. These L2HG-induced alterations in FAO or flux through the carnitine shuttle are consistent with the observed differential expression of short chain acylcarnitines, as assessed by LC–MS-based metabolomics; however, we did not directly test whether L2HG inhibits oxidation of short chain fatty acids. Moreover, we did not establish unambiguously whether the observed inhibition of FAO is specific to mitochondria, an important consideration given the growing appreciation that peroxisomal FAO contributes substantially to lipid homeostasis and disease pathophysiology[72]. Furthermore, our assessment of FAO did not distinguish between different forms of FAO, for example, β- versus ω-FAO[73].

The *in vivo* findings reinforce the central conclusion that L2HG functions as a regulator of TG and fatty acid metabolism, while also revealing a strong dependence on physiological context. Systemic elevation of L2HG in *L2hgdh*$^{-/-}$ mice produced robust hypertriglyceridemia in both sexes, mirroring the OL2HG-induced TG accumulation observed across multiple primary human cell types and supporting a conserved metabolic effect of L2HG. However, the emergence of sex-dependent remodeling of circulating acylcarnitines under basal conditions indicates that L2HG does not impose a uniform lipid program but instead intersects with sex-specific determinants of lipid handling. Indeed, sexual dimorphism in lipid metabolism in humans arises partly because pre-menopausal women, largely under estrogenic regulation, preferentially store fatty acids in lower-body subcutaneous depots and exhibit greater VLDL–TG clearance and direct fatty acid storage relative to energy needs, whereas men, under androgenic influence, display greater visceral fat accumulation, higher circulating VLDL–TG, and distinct patterns of fatty acid mobilization and storage[74]. Moreover, women produce fewer but TG-richer VLDLs than men[75], and males preferentially accumulate TGs in the liver with accelerated steatosis, whereas females divert TGs toward adipose depots, conferring relative protection from hepatic TG accumulation and metabolic injury[76].

A consideration relevant to interpretation of the *ex vivo* perfusion experiments is the duration of the perfusion protocol itself. The 90 min perfusion timepoint used in this study was selected primarily for consistency with previously established protocols published by our laboratory[60], and shorter pulse–perfusion approaches or multiple intermediate timepoints were not investigated. However, given the substantial metabolic turnover that can occur during prolonged *ex vivo* perfusion, together with the marked differences in substrate composition and nutrient availability between the *in vivo* circulation and the perfusion buffer, it is plausible that longer perfusion durations progressively amplify metabolic alterations that may not fully reflect the native physiological state[78]. Consequently, some of the observed changes in metabolomic flux and 2HG dynamics may represent both direct effects of the experimental perturbation and secondary adaptations that emerge during extended perfusion. Future studies incorporating shorter and temporally resolved perfusion paradigms may therefore help distinguish acute metabolic responses from downstream remodeling events, although this was beyond the scope of the present work.

Of importance, the preferential association we observed between circulating 2HG and lower-carbon-number TG species suggests that 2HG alters qualitative features of the TG pool, potentially by biasing acyl-CoA availability or constraining elongation- and remodeling-dependent pathways[77]. The replication of these 2HG–TG and TG–TG correlations in the circulation across mice and humans argues that this organizational structure reflects conserved constraints in TG metabolism that become apparent under conditions of elevated 2HG.

At the tissue and organismal levels, the metabolic effects of L2HG were revealed primarily under conditions of substrate limitation or stress rather than at baseline. Despite systemic hypertriglyceridemia, cardiac and hepatic TG content remained unchanged under steady-state conditions, whereas fatty acid deprivation unmasked accelerated depletion of cardiac TG stores in hearts of *L2hgdh*$^{-/-}$ mice, accompanied by downregulation of PLINs. This contrast with OL2HG-induced LD expansion in cultured cells underscores the context dependence of L2HG action and suggests that L2HG modulates the balance between TG storage and mobilization rather than enforcing fixed lipid accumulation. During ischemia, sex-dependent attenuation of long-chain acylcarnitine accumulation and TG buffering point to altered lipid handling and raise the possibility that regulated TG storage and fatty acid metabolism contribute to L2HG-associated cardioprotection, as we reported previously[60]. Consistent with this view, whole-body metabolic

phenotyping showed that L2HG-driven increases in oxygen consumption emerge specifically during fasting, indicating that L2HG reshapes whole-body metabolism under nutrient stress. These findings support a model in which L2HG acts as a conditional metabolic regulator that remodels TG partitioning and fatty acid flux in response to energetic demand, rather than functioning as a static metabolic signal.

2.5 Conclusions and future directions

Collectively, the data presented in this chapter support a model in which L2HG rewires the balance between lipid storage and lipid utilization through multiple convergent mechanisms. In primary human cells, L2HG increases TG abundance and LD expansion by enhancing TG synthesis, suppressing TG clearance, and promoting lipid uptake *via* VLDLR, while concurrently suppressing mitochondrial FAO and remodeling acylcarnitine pools. These coordinated effects shift cells toward a LD–expanding state characterized by increased sequestration of fatty acids into TG and decreased oxidative throughput. *In vivo*, chronic L2HG elevation produces systemic hypertriglyceridemia and nutrient- and sex-dependent remodeling of acylcarnitines and organ lipid handling, suggesting that L2HG modulates lipid metabolism across multiple physiological scales. Given our prior observations that L2HG is protective in myocardial ischemia[60], these lipid remodeling effects raise the possibility that L2HG-mediated TG buffering, altered LD dynamics, and restrained FAO-derived stress contribute to cardioprotection, although the mechanistic links between these phenotypes and ischemic outcomes require targeted testing. Future work should define the proximal biochemical targets through which L2HG modulates lipid flux, determine whether LD–mitochondria contact dynamics are altered by L2HG, and establish causality (or lack thereof) between L2HG-induced lipid remodeling and ischemic cardioprotection.

Table 2.2. Comparison of mass-dependent parameters in *L2hgdh*$^{-/-}$ *vs. L2hgdh*$^{+/+}$ mice under baseline conditions. P values are shown. *, $p<0.05$

	Full Day			Light			Dark		
Effect	**Mass**	**Group**	**Inter-action**	**Mass**	**Group**	**Inter-action**	**Mass**	**Group**	**Inter-action**
Food consumed (kcal/period)	0.2229	0.3641		0.5974	0.7704		0.2181	0.3294	
Water consumed (ml/period)	0.3231	0.3419		0.2428	0.0455*	0.0463*	0.2327	0.2302	
Energy expenditure (kcal/period)	0.0064**	0.8278		0.0193*	0.5155		0.0097**	0.7721	
O_2 consumption (ml/h)	0.0079**	0.6666		0.0189*	0.3948		0.0124*	0.9163	
CO_2 production (ml/h)	0.0067**	0.6157		0.0377*	0.9725		0.0081**	0.4019	

Table 2.3. Comparison of mass-independent parameters in *L2hgdh*$^{-/-}$ *vs. L2hgdh*$^{+/+}$ mice under baseline conditions. P values are shown. *, $p<0.05$

	Full Day	Light	Dark
Effect	**Group**	**Group**	**Group**
Pedestrian locomotion (m)	0.0216*	0.0207*	0.0258*
Total distance in cage (m)	0.0514	0.0486*	0.0584
Respiratory exchange ratio	0.4493	0.5808	0.4237
Locomotor activity (beam breaks)	0.5747	0.6957	0.5440
Energy balance (kcal/period)	0.4487	0.5827	0.5368

Table 2.4. Comparison of mass-independent parameters in *L2hgdh*$^{-/-}$ *vs. L2hgdh*$^{+/+}$ mice under fasting conditions. P values are shown. *, $p<0.05$

	Full Day	Light	Dark
Effect	**Group**	**Group**	**Group**
Pedestrian locomotion (m)	0.6648	0.5832	0.6927
Total distance in cage (m)	0.8187	0.7140	0.8529
Respiratory exchange ratio	0.3987	0.3743	0.4951
Locomotor activity (beam breaks)	0.9695	0.6862	0.8355
Energy balance (kcal/period)	0.7882	0.0105*	0.9286

Table 2.5. Comparison of mass-dependent parameters in *L2hgdh*$^{-/-}$ *vs. L2hgdh*$^{+/+}$ mice under fasting conditions. P values are shown. *, $p<0.05$

	Full Day			Light			Dark		
Effect	**Mass**	**Group**	**Inter-action**	**Mass**	**Group**	**Inter-action**	**Mass**	**Group**	**Inter-action**
Food consumed (kcal/period)	0.3545	0.3304		0.5969	0.3609		0.3488	0.3349	
Water consumed (ml/period)	0.5720	0.2112		0.0678	0.1595		0.7563	0.2384	
Energy expenditure (kcal/period)	0.5492	0.1279		0.6291	0.0524		0.3965	0.1988	
O_2 consumption (ml/h)	0.6219	0.1071		0.5527	0.0418		0.4501	0.1719	
CO_2 production (ml/h)	0.2934	0.2945		0.9599	0.1717		0.2190	0.3885	

Table 2.6. Comparison of mass-dependent parameters in *L2hgdh*$^{-/-}$ *vs. L2hgdh*$^{+/+}$ mice under refed conditions. P values are shown. *, $p<0.05$

Effect	Mass	Group	Interaction
Food consumed (kcal/period)	0.2095	0.4007	
Water consumed (ml/period)	0.6982	0.2714	
Energy expenditure (kcal/period)	0.6869	0.6386	
O_2 consumption (ml/h)	0.7749	0.5165	
CO_2 production (ml/h)	0.4088	0.8028	

Table 2.7. Comparison of mass-independent parameters in *L2hgdh*$^{-/-}$ *vs. L2hgdh*$^{+/+}$ mice under refed conditions. P values are shown. *, $p<0.05$

Effect	Group
Pedestrian locomotion (m)	0.4800
Total distance in cage (m)	0.4072
Respiratory exchange ratio	0.1128
Locomotor activity (beam breaks)	0.2375
Energy balance (kcal/period)	0.7417

2.6 References

1 Prentki, M. & Madiraju, S. R. Glycerolipid metabolism and signaling in health and disease. *Endocrine Reviews* **29**, 647–676 (2008).

2 Wang, H., Airola, M. V. & Reue, K. How lipid droplets "TAG" along: Glycerolipid synthetic enzymes and lipid storage. *Biochimica et Biophysica Acta (BBA) – Molecular and Cell Biology of Lipids* **1862**, 1131–1145 (2017).

3 Ference, B. A., Graham, I., Tokgozoglu, L. & Catapano, A. L. Impact of Lipids on Cardiovascular Health: JACC Health Promotion Series. *Journal of the American College of Cardiology (JACC)* **72**, 1141–1156 (2018).

4 Soppert, J., Lehrke, M., Marx, N., Jankowski, J. & Noels, H. Lipoproteins and lipids in cardiovascular disease: from mechanistic insights to therapeutic targeting. *Advanced Drug Delivery Reviews* **159**, 4–33 (2020).

5 Yoon, H., Shaw, J. L., Haigis, M. C. & Greka, A. Lipid metabolism in sickness and in health: Emerging regulators of lipotoxicity. *Molecular Cell* **81**, 3708–3730 (2021).

6 Gancheva, S., Jelenik, T., Álvarez-Hernández, E. & Roden, M. Interorgan Metabolic Crosstalk in Human Insulin Resistance. *Physiological Reviews* **98**, 1371–1415 (2018).

7 Yen, C. L., Stone, S. J., Koliwad, S., Harris, C. & Farese, R. V., Jr. Thematic review series: glycerolipids. DGAT enzymes and triacylglycerol biosynthesis. *Journal of Lipid Research* **49**, 2283–2301 (2008).

8 Hishikawa, D., Hashidate, T., Shimizu, T. & Shindou, H. Diversity and function of membrane glycerophospholipids generated by the remodeling pathway in mammalian cells. *Journal of Lipid Research* **55**, 799–807 (2014).

9 Hannun, Y. A. & Obeid, L. M. Sphingolipids and their metabolism in physiology and disease. *Nature Reviews Molecular Cell Biology* **19**, 175–191 (2018).

10 Plat, J. *et al.* Plant-based sterols and stanols in health & disease: "Consequences of human development in a plant-based environment?". *Progress in Lipid Research* **74**, 87–102 (2019).

11 Spriet, L. L. New insights into the interaction of carbohydrate and fat metabolism during exercise. *Sports Medicine* **44 Suppl 1**, S87–96 (2014).

12 Coleman, R. A. & Mashek, D. G. Mammalian triacylglycerol metabolism: synthesis, lipolysis, and signaling. *Chemical Reviews* **111**, 6359–6386 (2011).

13 Madiraju, S. R. M., Possik, E., Al-Mulla, F., Nolan, C. J. & Prentki, M. Glycerol and Glycerol-3-Phosphate: Multifaceted Metabolites in Metabolism, Cancer, and Other Diseases. *Endocrine Reviews* **47**, 93–120 (2026).

14 Singh, H., Beckman, K. & Poulos, A. Exclusive localization in peroxisomes of dihydroxyacetone phosphate acyltransferase and alkyl-dihydroxyacetone phosphate synthase in rat liver. *Journal of Lipid Research* **34**, 467–477 (1993).

15 Rock, C. O., Fitzgerald, V. & Snyder, F. Properties of dihydroxyacetone phosphate acyltransferase in the harderian gland. *Journal of Biological Chemistry* **252**, 6363–6366 (1977).

16 Shi, Y. & Cheng, D. Beyond triglyceride synthesis: the dynamic functional roles of MGAT and DGAT enzymes in energy metabolism. *American Journal of Physiology – Endocrinology and Metabolism* **297**, E10–18 (2009).

17 Olzmann, J. A. & Carvalho, P. Dynamics and functions of lipid droplets. *Nature Reviews Molecular Cell Biology* **20**, 137–155 (2019).

18 Zadoorian, A., Du, X. & Yang, H. Lipid droplet biogenesis and functions in health and disease. *Nature Reviews Endocrinology* **19**, 443–459 (2023).

19 Walther, T. C. & Farese, R. V., Jr. Lipid droplets and cellular lipid metabolism. *Annual Review of Biochemistry* **81**, 687–714 (2012).

20 Thiam, A. R. & Beller, M. The why, when and how of lipid droplet diversity. *Journal of Cell Science* **130**, 315–324 (2017).

21 Schaffer, J. E. Lipotoxicity: when tissues overeat. *Current Opinion in Lipidology* **14**, 281–287 (2003).

22 Obaseki, E., Adebayo, D., Bandyopadhyay, S. & Hariri, H. Lipid droplets and fatty acid-induced lipotoxicity: in a nutshell. *FEBS Letters* **598**, 1207–1214 (2024).

23 Grabner, G. F., Xie, H., Schweiger, M. & Zechner, R. Lipolysis: cellular mechanisms for lipid mobilization from fat stores. *Nature Metabolism* **3**, 1445–1465 (2021).

24 Zechner, R., Madeo, F. & Kratky, D. Cytosolic lipolysis and lipophagy: two sides of the same coin. *Nature Reviews Molecular Cell Biology* **18**, 671–684 (2017).

25 Fischer, J. *et al.* The gene encoding adipose triglyceride lipase (PNPLA2) is mutated in neutral lipid storage disease with myopathy. *Nature Genetics* **39**, 28–30 (2007).

26 Haemmerle, G. *et al.* ATGL-mediated fat catabolism regulates cardiac mitochondrial function via PPAR-α and PGC-1. *Nature Medicine* **17**, 1076–1085 (2011).

27 Albert, J. S. *et al.* Null mutation in hormone-sensitive lipase gene and risk of type 2 diabetes. *New England Journal of Medicine* **370**, 2307–2315 (2014).

28 Lindberg, S. *et al.* Osteoprotegerin levels change during STEMI and reflect cardiac function. *Canadian Journal of Cardiology* **30**, 1523–1528 (2014).

29 Belfrage, P., Fredrikson, G., Nilsson, N. O. & Strålfors, P. Regulation of adipose-tissue lipolysis by phosphorylation of hormone-sensitive lipase. *International Journal of Obesity* **5**, 635–641 (1981).

30 Strålfors, P., Björgell, P. & Belfrage, P. Hormonal regulation of hormone-sensitive lipase in intact adipocytes: identification of phosphorylated sites and effects on the phosphorylation by lipolytic hormones and insulin. *Proceedings of the National Academy of Sciences of the United States of America (PNAS)* **81**, 3317–3321 (1984).

31 Strålfors, P. & Belfrage, P. Phosphorylation of hormone-sensitive lipase by cyclic AMP-dependent protein kinase. *Journal of Biological Chemistry* **258**, 15146–15152 (1983).

32 Krintel, C., Mörgelin, M., Logan, D. T. & Holm, C. Phosphorylation of hormone-sensitive lipase by protein kinase A in vitro promotes an increase in its hydrophobic surface area. *The FEBS Journal* **276**, 4752–4762 (2009).

33 Hofer, P., Taschler, U., Schreiber, R., Kotzbeck, P. & Schoiswohl, G. The Lipolysome-A Highly Complex and Dynamic Protein Network Orchestrating Cytoplasmic Triacylglycerol Degradation. *Metabolites* **10** (2020).

34 Niu, Y. J. *et al.* Perilipins: key targets for regulating lipid metabolism and alleviating abnormal lipid metabolism through exercise. *Diabetology & Metabolic Syndrome* **17**, 392 (2025).

35 Granneman, J. G., Moore, H. P., Krishnamoorthy, R. & Rathod, M. Perilipin controls lipolysis by regulating the interactions of AB-hydrolase containing 5 (Abhd5) and adipose triglyceride lipase (Atgl). *Journal of Biological Chemistry* **284**, 34538–34544 (2009).

36 Farese, R. V. & Walther, T. C. Essential Biology of Lipid Droplets. *Annual Review of Biochemistry* **94**, 447–477 (2025).

37 Klemm, R. W. & Carvalho, P. Lipid Droplets Big and Small: Basic Mechanisms That Make Them All. *Annual Review of Cell and Developmental Biology* **40**, 143–168 (2024).

38 Reue, K. A thematic review series: lipid droplet storage and metabolism: from yeast to man. *Journal of Lipid Research* **52**, 1865–1868 (2011).

39 Zierler, K. L. Fatty acids as substrates for heart and skeletal muscle. *Circulation Research* **38**, 459–463 (1976).

40 Ellis, J. M., Frahm, J. L., Li, L. O. & Coleman, R. A. Acyl-coenzyme A synthetases in metabolic control. *Current Opinion in Lipidology* **21**, 212–217 (2010).

41 Hoppel, C. The role of carnitine in normal and altered fatty acid metabolism. *American Journal of Kidney Diseases* **41**, S4–S12 (2003).

42 Shi, L. & Tu, B. P. Acetyl-CoA and the regulation of metabolism: mechanisms and consequences. *Current Opinion in Cell Biology* **33**, 125–131 (2015).

43 Merritt, J. L., 2nd, Norris, M. & Kanungo, S. Fatty acid oxidation disorders. *Annals of Translational Medicine* **6**, 473 (2018).

44 Cui, L. & Liu, P. Two Types of Contact Between Lipid Droplets and Mitochondria. *Frontiers in Cell and Developmental Biology* **8**, 618322 (2020).

45 Veliova, M., Petcherski, A., Liesa, M. & Shirihai, O. S. The biology of lipid droplet-bound mitochondria. *Seminars in Cell & Developmental Biology* **108**, 55–64 (2020).

46 Talari, N. K. *et al.* Lipid-droplet associated mitochondria promote fatty-acid oxidation through a distinct bioenergetic pattern in male Wistar rats. *Nature Communications* **14**, 766 (2023).

47 Smolková, K. & Gotvaldová, K. Fatty Acid Trafficking Between Lipid Droplets and Mitochondria: An Emerging Perspective. *International Journal of Biological Sciences* **21**, 1863–1873 (2025).

48 Liebisch, G. *et al.* Update on LIPID MAPS classification, nomenclature, and shorthand notation for MS-derived lipid structures. *Journal of Lipid Research* **61**, 1539–1555 (2020).

49 Cajka, T. & Fiehn, O. Comprehensive analysis of lipids in biological systems by liquid chromatography-mass spectrometry. *Trends in Analytical Chemistry* **61**, 192–206 (2014).

50 Navarrete-Perea, J., Yu, Q., Gygi, S. P. & Paulo, J. A. Streamlined Tandem Mass Tag (SL-TMT) Protocol: An Efficient Strategy for Quantitative (Phospho)proteome Profiling Using Tandem Mass Tag-Synchronous Precursor Selection-MS3. *Journal of Proteome Research* **17**, 2226–2236 (2018).

51 Li, J. *et al.* TMTpro reagents: a set of isobaric labeling mass tags enables simultaneous proteome-wide measurements across 16 samples. *Nature Methods* **17**, 399–404 (2020).

52 Schweppe, D. K., Rusin, S. F., Gygi, S. P. & Paulo, J. A. Optimized Workflow for Multiplexed Phosphorylation Analysis of TMT-Labeled Peptides Using High-Field Asymmetric Waveform Ion Mobility Spectrometry. *Journal of Proteome Research* **19**, 554–560 (2020).

53 Chambers, M. C. *et al.* A cross-platform toolkit for mass spectrometry and proteomics. *Nature Biotechnology* **30**, 918–920 (2012).

54 Beausoleil, S. A., Villén, J., Gerber, S. A., Rush, J. & Gygi, S. P. A probability-based approach for high-throughput protein phosphorylation analysis and site localization. *Nature Biotechnology* **24**, 1285–1292 (2006).

55 Huttlin, E. L. *et al.* A tissue-specific atlas of mouse protein phosphorylation and expression. *Cell* **143**, 1174–1189 (2010).

56 Elias, J. E. & Gygi, S. P. Target-decoy search strategy for mass spectrometry-based proteomics. *Methods in Molecular Biology* **604**, 55–71 (2010).

57 Elias, J. E. & Gygi, S. P. Target-decoy search strategy for increased confidence in large-scale protein identifications by mass spectrometry. *Nature Methods* **4**, 207–214 (2007).

58 McAlister, G. C. *et al.* Increasing the multiplexing capacity of TMTs using reporter ion isotopologues with isobaric masses. *Analytical Chemistry* **84**, 7469–7478 (2012).

59 Huynh, F. K., Green, M. F., Koves, T. R. & Hirschey, M. D. Measurement of fatty acid oxidation rates in animal tissues and cell lines. *Methods in Enzymology* **542**, 391–405 (2014).

60 He, H. *et al.* L-2-Hydroxyglutarate Protects Against Cardiac Injury via Metabolic Remodeling. *Circulation Research* **131**, 562–579 (2022).

61 Ježek, P. 2-Hydroxyglutarate in Cancer Cells. *Antioxidants & Redox Signaling* **33**, 903–926 (2020).

62 Shim, E. H. *et al.* L-2-Hydroxyglutarate: an epigenetic modifier and putative oncometabolite in renal cancer. *Cancer Discovery* **4**, 1290–1298 (2014).

63 Reiter-Brennan, C., Semmler, L. & Klein, A. The effects of 2-hydroxyglutarate on the tumorigenesis of gliomas. *Contemporary Oncology (Poznań)* **22**, 215–222 (2018).

64 Zhao, G. *et al.* Validation of diacyl glycerolacyltransferase I as a novel target for the treatment of obesity and dyslipidemia using a potent and selective small molecule inhibitor. *Journal of Medicinal Chemistry* **51**, 380–383 (2008).

65 Futatsugi, K. *et al.* Discovery and Optimization of Imidazopyridine-Based Inhibitors of Diacylglycerol Acyltransferase 2 (DGAT2). *Journal of Medicinal Chemistry* **58**, 7173–7185 (2015).

66 Rzem, R. *et al.* A mouse model of L-2-hydroxyglutaric aciduria, a disorder of metabolite repair. *PLOS ONE* **10**, e0119540 (2015).

67 de Goede, K. E. *et al.* d-2-Hydroxyglutarate is an anti-inflammatory immunometabolite that accumulates in macrophages after TLR4 activation. *Biochimica et Biophysica Acta – Molecular Basis of Disease* **1868**, 166427 (2022).

68 Kaul, H. *et al.* 2-hydroxyglutarate mediates whitening of brown adipocytes coupled to nuclear softening upon mitochondrial dysfunction. *Nature Metabolism* **7**, 1593–1613 (2025).

69 Huttlin, E. L. *et al.* The BioPlex Network: A Systematic Exploration of the Human Interactome. *Cell* **162**, 425–440 (2015).

70 Mardani, I. *et al.* Plin2-deficiency reduces lipophagy and results in increased lipid accumulation in the heart. *Scientific Reports* **9**, 6909 (2019).

71 Hashimoto, T. *et al.* Modest hypoxia significantly reduces triglyceride content and lipid droplet size in 3T3-L1 adipocytes. *Biochemical and Biophysical Research Communications* **440**, 43–49 (2013).

72 Poirier, Y., Antonenkov, V. D., Glumoff, T. & Hiltunen, J. K. Peroxisomal beta-oxidation--a metabolic pathway with multiple functions. *Biochimica et Biophysica Acta (BBA)* **1763**, 1413–1426 (2006).

73 Miura, Y. The biological significance of ω-oxidation of fatty acids. *Proceedings of the Japan Academy, Series B: Physical and Biological Sciences* **89**, 370–382 (2013).

74 Santosa, S. & Jensen, M. D. The Sexual Dimorphism of Lipid Kinetics in Humans. *Frontiers in Endocrinology* **6**, 103 (2015).

75 Magkos, F., Patterson, B. W., Mohammed, B. S., Klein, S. & Mittendorfer, B. Women produce fewer but triglyceride-richer very low-density lipoproteins than men. *Journal of Clinical Endocrinology & Metabolism* **92**, 1311–1318 (2007).

76 Meyer, J. *et al.* Sex differences in diet-induced MASLD - are female mice naturally protected? *Frontiers in Endocrinology* **16**, 1567573 (2025).

77 Wunderling, K., Zurkovic, J., Zink, F., Kuerschner, L. & Thiele, C. Triglyceride cycling enables modification of stored fatty acids. *Nature Metabolism* **5**, 699–709 (2023).

78 Olkowicz, M. *et al*. Dynamic Metabolic Changes During Prolonged Ex Situ Heart Perfusion Are Associated With Myocardial Functional Decline. *Frontiers in Immunology* **13**, 859506 (2022).

Chapter 3

L-2-Hydroxyglutarate Regulates the Kennedy Pathway of Phosphatidylethanolamine Metabolism

3.1 Introduction

The preceding chapter established that L-2-hydroxyglutarate (L2HG) induces a robust accumulation of triglycerides (TGs) across multiple primary human cell types, implicating L2HG as a previously unrecognized regulator of neutral lipid metabolism. These findings raised an important conceptual question that extends beyond TG biology: since the glycerol backbone and fatty acyls are common precursors shared with numerous other lipid classes, preferential channeling of these substrates into TGs may necessarily occur at the expense of other glycerol(phospho)lipid pools. In this context, the accumulation of TGs in response to L2HG may reflect not only enhanced neutral lipid storage, but also broader remodeling of lipid partitioning within the cell.

Phospholipids are essential structural and functional components of cellular membranes, contributing not only to bilayer integrity but also to membrane curvature and signaling pathways[1-3]. Among these, phosphatidylethanolamine (PE) and phosphatidylcholine (PC) together account for the majority of phospholipid mass in eukaryotic cells, yet they are not functionally redundant[1]. PC is typically enriched in the outer leaflet of cell membranes and is critical for maintaining membrane stability, whereas PE is enriched in the inner leaflet and contributes to membrane fluidity and plasticity by, at least in part, allowing bilayer reorganization, protein embedding, and adaptive changes in protein conformation[4,5]. Perturbations in PE abundance or distribution have been linked to, for example, defects in mitochondrial respiration[6] and autophagy[7], underscoring the importance of maintaining appropriate PE homeostasis. For a more detailed review of PE in health and disease, the reader is referred to Ref.[8].

The biosynthesis of PE and PC occurs predominantly through the Kennedy pathway, a conserved metabolic route discovered in 1956 by Kennedy and Weiss[9]. In the PE branch of this pathway, ethanolamine (Etn) is phosphorylated by Etn kinases (ETNK1 and ETNK2) to generate phosphoethanolamine (PEtn), which is subsequently converted to cytidine 5′-diphosphate (CDP)-Etn by CTP:phosphoethanolamine cytidylyltransferase (PCYT2), which is the rate-limiting enzyme of the Kennedy pathway. CDP-Etn then reacts with diacylglycerol (DAG) *via* Etn phosphotransferase (EPT1, encoded by *SELENOI*) to produce PE. Stepwise de-acylation of PE forms lyso-PE (also referred to as acyl-glycerophosphoethanolamine) and

glycerophosphoethanolamine (glycero-PEtn). The PC branch proceeds analogously through phosphorylation of choline (Chol) to phosphocholine (PChol), formation of CDP-Chol, reaction of CDP-Chol with DAG to form PC, and stepwise de-acylation of PC to form lyso-PC and, subsequently, glycerophosphocholine (glycero-PChol). Importantly, both branches converge on DAG as a shared substrate, placing the Kennedy pathway at a metabolic crossroads between phospholipid synthesis and TG production.

Glycerol-3-phosphate (G3P) occupies a central position at the intersection of glycerolipid and phospholipid synthesis (see Section 2.1.1). In addition to serving as the backbone for TGs, G3P is a key precursor for the synthesis of major phospholipid classes, including PE and PC. As such, increased flux of G3P into TG synthesis has the potential to compete with, and thereby constrain, phospholipid biosynthesis. This notion is supported by the observations of Rong and colleagues showing that diacylglycerol *O*-acyltransferase 2 (DGAT2) inhibition in hepatocytes shunts DAG flux toward phospholipid synthesis, particularly PE synthesis in the endoplasmic reticulum (ER)[10]. Furthermore, Lee *et al.*[11] showed that DGAT1/2 inhibition reduces TG synthesis and LD formation, redirecting free fatty acids (particularly polyunsaturated ones) from TGs into phospholipids, including PE. Although compensatory mechanisms, such as increased glycerol production or enhanced glycerol phosphorylation (reviewed in Ref.[12]), could theoretically offset this competition, such adaptations are neither guaranteed nor necessarily sufficient to preserve neutral lipid and phospholipid homeostasis. Consequently, L2HG-induced TG accumulation may be coupled to depletion or remodeling of specific phospholipid classes, particularly those that draw upon the same precursor pools.

This conceptual framework of compensatory regulation between phospholipids and TGs is consistent with our initial observation in the previous chapter that numerous PE species were significantly downregulated in HCMs treated with octyl-L-2-hydroxyglutarate (OL2HG) (**Fig. 2.1C**). This finding suggests that PE metabolism may be particularly sensitive to L2HG-induced alterations in lipid flux, a notion further supported by recent reports demonstrating that (i) L2HG increases intracellular PEtn while decreasing PChol and glycero-PChol in colorectal cancer cells[13], (ii) D2HG elevates PEtn levels in macrophages[14], and (iii) *L2hgdh*$^{-/-}$ mice exhibit increased Etn levels in the brain relative to *L2hgdh*$^{+/+}$ wild-type controls[15]. On this basis, the present chapter was designed to test the hypothesis that L2HG-induced TG accumulation is accompanied by

coordinated remodeling of phospholipid metabolism, with a particular focus on PE and its biosynthetic precursors.

Rather than presupposing a direct mechanistic link between TG accumulation and PE depletion, we sought to determine systematically whether such a relationship exists and, if so, to identify the metabolic node(s) at which it arises. To this end, we combined lipidomics, metabolomics, isotope-tracing, pharmacological, and transcriptomics approaches across multiple cell types to interrogate whether L2HG alters PE abundance, precursor pools, and pathway dynamics. By examining both acute (24 h) OL2HG supplementation *in vitro* and chronic systematic L2HG elevation induced by global genetic deletion of *L2hgdh*$^{-/-}$, we sought to extend the findings of the previous TG-focused work by situating TG accumulation within a wider lipid metabolic context. Rather than viewing TG accumulation as an isolated endpoint, we propose that L2HG induces a coordinated reprogramming of glycerolipid metabolism, favoring neutral lipid storage at the expense of specific phospholipid pools. The results presented herein provide evidence that PE and its Kennedy pathway intermediates are particularly responsive to L2HG, thereby uncovering a previously unrecognized axis through which L2HG may influence membrane biology and cellular function.

3.2 Methods and materials

Except where otherwise specified below, the Methods and Materials for the present chapter are identical to those described in Sections 2.2.1 (Chemicals and reagents), 2.2.2 (Cell culture and treatments), 2.2.4 (RNA sequencing), 2.2.5 (Semi-targeted metabolomics, non-targeted lipidomics, and stable-isotope-based fluxomics), 2.2.13 (Mouse models), and 2.2.14 (Statistics).

3.2.1 Chemicals and reagents

O-phosphorylethanolamine (cat. no. P0503) was purchased from Sigma. $^{13}C_2$-ethanolamine (cat. no. CLM-274-PK) was purchased from Cambridge Isotope Laboratories.

3.2.2 Bone marrow–derived macrophage (BMDM) culture

Bone marrow–derived macrophages (BMDMs) were isolated and differentiated from the bone marrow of 5-month-old male mice (*L2hgdh*$^{+/+}$, n = 1; *L2hgdh*$^{-/-}$, n = 1), as previously described[16]. Mice were euthanized by intraperitoneal injection of an overdose of ketamine (240–300 mg kg^{-1})

and xylazine (15–30 mg kg^{-1}). Femurs and tibias were dissected free of surrounding muscle and connective tissue, washed in Dulbecco's Modified Eagle Medium (DMEM, cat. no. 11965084, Thermo Fisher Scientific), transferred to a sterile mortar, and gently crushed using a sterile pestle in DMEM to release bone marrow cells. The resulting cell suspension was passed through a 70-µm cell strainer (cat. no. 352350, Corning) to remove bone debris. Erythrocytes were lysed by incubation with 1 mL red blood cell lysis buffer (cat. no. 555899, BD Biosciences) for 5 min on ice.

The remaining bone marrow cells were cultured at a density of 1×10^6 cells per mL in DMEM supplemented with 10% (v/v) heat-inactivated fetal bovine serum (FBS), 100 U/mL penicillin, 100 µg/mL streptomycin, and 20 ng/mL mouse macrophage colony-stimulating factor (M-CSF; cat. no. 315-02, Thermo Fisher Scientific). The culture medium was replaced on day 3. Non-activated, proliferative BMDMs were used for downstream experiments on day 5.

3.2.3 Flow cytometry analysis of BMDM purity and viability

For flow cytometric analysis, day 5 BMDMs were gently detached using a cell scraper, collected, and centrifuged (2,000 x *g*, 5 min, 4 °C). Cells were washed once with 1 mL DPBS and resuspended in 100 µL DPBS. Cells were incubated with fluorochrome-conjugated monoclonal antibodies against CD45 (cat. no. 157214, BioLegend), CD11b (cat. no. 101208, BioLegend), and F4/80 (cat. no. 123116, BioLegend) for 30 min at 4 °C in the dark. Following staining, cells were washed with 1 mL DPBS, centrifuged (2,000 x *g*, 5 min, 4 °C), resuspended in 100 µL DPBS, and transferred to 96-well plates. Immediately prior to acquisition, 100 µL of 2 µg/mL DAPI in DPBS (final concentration, 1 µg/mL) was added to each well to exclude nonviable cells. Samples were acquired on a CytoFLEX flow cytometer (Beckman Coulter). BMDMs were identified as a $CD45^+$ $CD11b^+$ $F4/80^+$ $DAPI^-$ population. Data were analyzed using CytExpert 2.0 software.

3.3 Results

3.3.1 O2HG enantiomers differentially decrease PE bioavailability *in vitro*

In addition to the accumulation of TGs observed in Chapter 2, we noted that numerous PE species were significantly downregulated in HCMs treated with OL2HG (**Fig. 2.1C**). Quantitative

lipidomics analysis revealed that OL2HG, but not OD2HG, significantly decreased total cellular PE content, computed by summating the normalized abundances of all individual PE species (**Fig. 3.1A**). In contrast, total PC abundance remained unchanged following treatment with either enantiomer (**Fig. 3.1B**). Since PEs and PCs together constitute the predominant phospholipid classes in mammalian cells[17,18], we next examined whether OL2HG alters their relative abundance. This analysis was motivated by evidence linking dysregulation of the PE-to-PC ratio to disease pathogenesis, including steatohepatitis[19], muscular dystrophy[20], obesity[21], and insulin resistance[22]. Consistent with the selective reduction in PE content, the PE-to-PC ratio was significantly decreased in OL2HG-treated cells, whereas no change was observed following OD2HG treatment (**Fig. 3.1C**).

We next assessed whether the OL2HG-mediated decrease in PEs was selective for specific acyl-chain compositions, similar to our analysis of individual TG and DG species in **Figs. 2.1F**–**G**. Stratification of PE species by total acyl-chain carbon number and degree of saturation demonstrated that all detectable PE species were uniformly downregulated by OL2HG, independent of acyl-chain composition (**Fig. 3.1D**). Conversely, OD2HG produced no significant change, or only modest decreases, across individual PE species (**Fig. 3.1D**). Although total PC abundance was unchanged (**Fig. 3.1B**), several individual PC species were modestly upregulated following OL2HG treatment, with smaller or negligible effects observed with OD2HG (**Fig. 3.1E**). Taken together, these data demonstrate that OL2HG induces a robust remodeling of cellular phospholipid composition characterized by a global reduction in PEs, while largely sparing total PC levels. While these data are consistent with potential stereospecific effects, given that OD2HG did not elicit comparable phenotypic alterations to OL2HG, the broader implications of this interpretation are discussed in detail in Section 5.2.

3.3.2 OL2HG potentiates preferential oleate partitioning into TGs over PEs and PCs

Since the G3P pathway of TG biosynthesis intersects with phospholipid synthesis (see Section 2.1.1), TGs and phospholipids effectively compete for a shared glycerol backbone. We therefore examined whether OL2HG alters the partitioning of extracellularly supplemented oleate into TG *versus* PE and PC in PAECs. As shown in Chapter 2, OL2HG potentiated oleate-induced TG synthesis (**Fig. 3.2A**). In parallel, oleate supplementation reduced PE and PC abundance (**Fig.**

3.2B–C), consistent with substrate (*i.e.,* glycerol) competition between these lipid classes. Notably, this reduction in PE and PC abundance was further potentiated by co-treatment with OL2HG (**Fig. 3.2B–C**). These results reveal a functional interplay between TG and phospholipid metabolism and indicate that OL2HG biases oleate utilization toward TG synthesis at the expense of PE and PC.

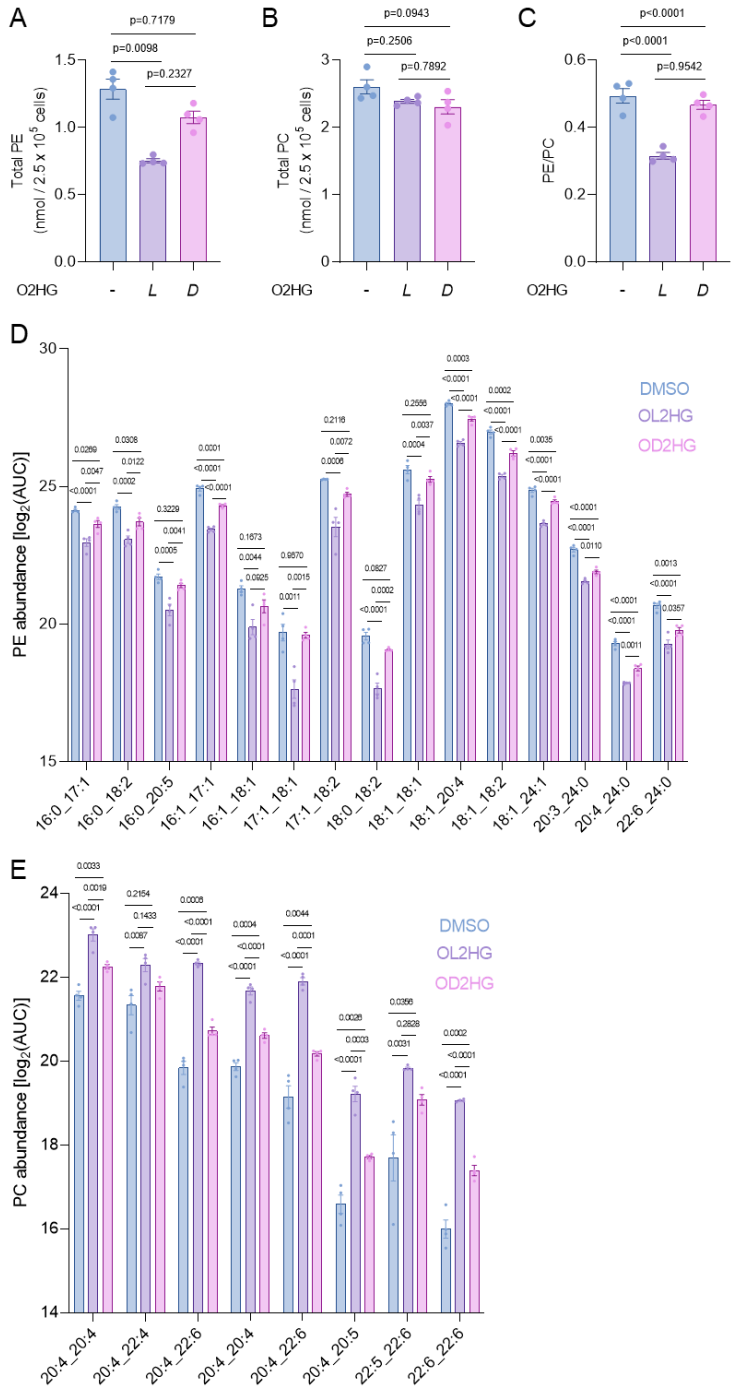

Figure 3.1. OL2HG, but not OD2HG, decreases intracellular PE bioavailability. A, Total intracellular PE, **B**, PC, and **C**, PE-to-PC ratio in HCMs treated with DMSO (n=4), 500 µM OL2HG (n=4), or 500 µM OD2HG (n=4) for 24 h. **D** and **E**, Signal intensity (expressed as the logarithm of the peak area under the curve, AUC) of individual PE and PC species with different acyl chain compositions in HCMs treated with DMSO (n=4), 500 µM OL2HG (n=4), or 500 µM OD2HG (n=4) for 24 h. Data are presented as mean ± SEM. Data were tested for normality by Shapiro–Wilk test. Normal data were analyzed by ordinary one-way ANOVA. Non-normal data were analyzed by the Kruskal–Wallis test.

Next, we sought to further interrogate the interplay between TG and phospholipid synthesis and to determine how OL2HG modulates this balance. To this end, PAECs were treated with OL2HG in the presence or absence of pharmacological inhibitors of DGAT1 and DGAT2, the enzymes that catalyze the final step of TG synthesis (see Section 2.1.1). DGAT1 and DGAT2 were inhibited using A-922500[23] and PF-06424439[24], respectively. Principal component analysis (PCA) of lipidomic profiles demonstrated distinct clustering of the three experimental groups (**Fig. 3.3A**), indicating condition-specific lipidomic remodeling. Consistent with competitive utilization of a shared glycerol backbone, DGAT inhibition (DGATi) increased PE abundance, an effect that was reversed by co-treatment with OL2HG (**Fig. 3.3B**). In contrast, the total PC pool was not altered by OL2HG in the presence or absence of DGATi (**Fig. 3.3C**). Taken together, these findings reveal a selective sensitivity of PE, but not PC, to perturbations in TG synthesis and further support the conclusion that OL2HG promotes preferential partitioning of lipid substrates toward TG synthesis at the expense of PE.

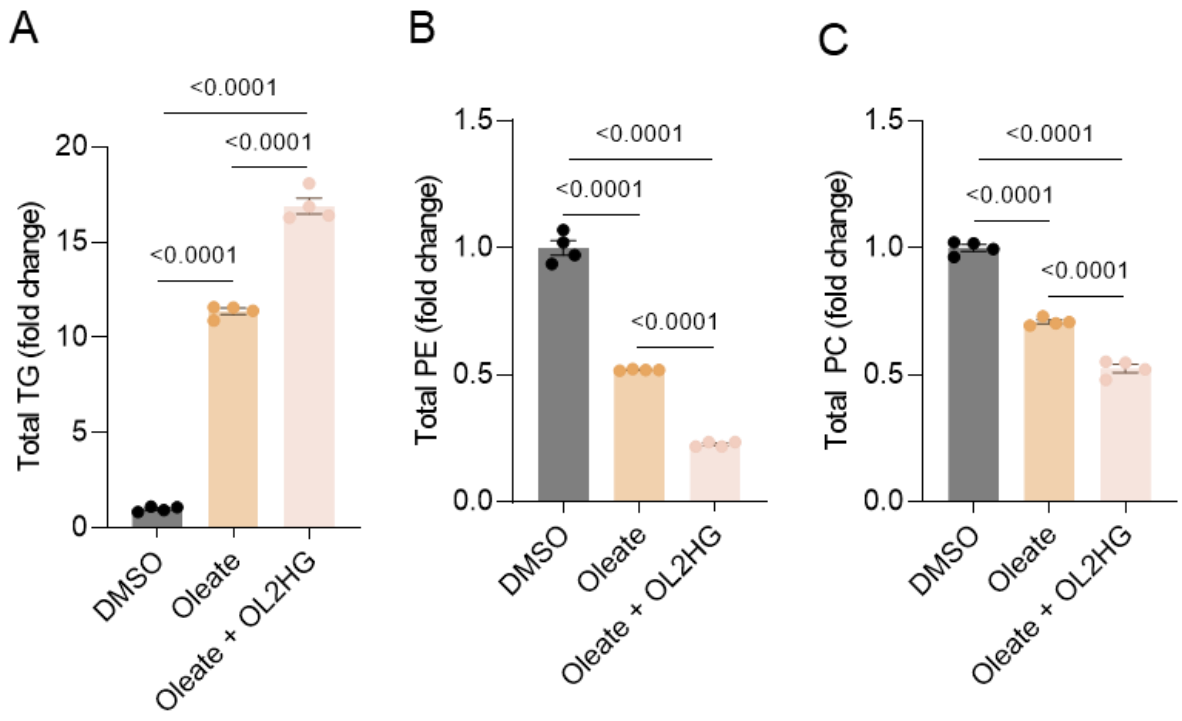

Figure 3.2. OL2HG potentiates preferential partitioning of oleate into TG. A, Total intracellular TG, **B**, PE, and **C**, PC in PAECs treated with DMSO (n=4), 50 µM oleate (n=4) or 50 µM oleate + 500 µM OL2HG (n=4) for 24 h. Data are presented as mean ± SEM. Data were tested for normality by Shapiro–Wilk test. Normal data were analyzed by ordinary one-way ANOVA. Non-normal data were analyzed by the Kruskal–Wallis test.

3.3.3 OL2HG differentially regulates intermediates of the Kennedy pathway for PE synthesis

Given our findings that OL2HG shifts lipid metabolism away from PE and toward TG synthesis, we next examined whether OL2HG regulates the abundance of intermediates in the Kennedy pathway for PE synthesis, the predominant route by which mammalian cells generate PE (see Section 3.1). A schematic overview of the Kennedy pathway is shown in **Fig. 3.4A**. Of note, PEtn was quantified by absolute quantification using a standard curve generated from an authentic reference standard, whereas CDP-Etn and glycero-PEtn were assessed as normalized abundances (integrated peak areas normalized to the total metabolite signal *per* sample), owing to the absence of these authentic standards in our in-house reference library.

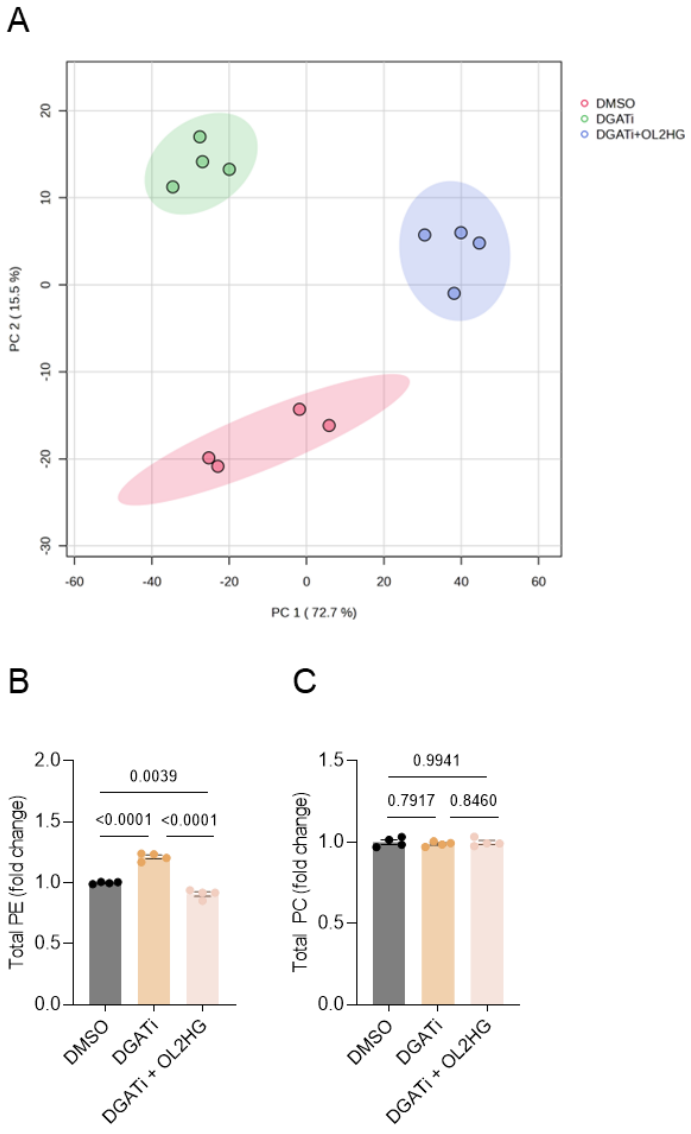

Figure. 3.3. OL2HG prevents PE accumulation induced by inhibition of DGAT1/2. **A**, Principal component analysis of lipidomic data obtained from PAECs treated with DMSO (n=4) or DGAT1/2 inhibitors (DGATi, 10 µM A-922500 and 10 µM PF-06424439) in the absence (n=4) or presence (n=4) of 500 µM OL2HG for 24 h. The plot was generated using MetaboAnalyst 6.0. The total abundance of PE and PC in these cells is quantified in **B** and **C**, respectively. Data are presented as mean ± SEM. Data were tested for normality by Shapiro–Wilk test. Normal data were analyzed by ordinary one-way ANOVA. Non-normal data were analyzed by the Kruskal–Wallis test.

Notably, OL2HG increased both intracellular and extracellular concentrations of PEtn, with a more modest increase observed following OD2HG treatment in HCMs (**Fig. 3.4B–C**). In parallel, OL2HG resulted in a modest increase in CDP-Etn (**Fig. 3.4D**) and a significant decrease in G-3-PEtn (**Fig. 3.4E**). Importantly, similar alterations were observed in HCFs (**Fig. 3.4F–I**) and PAECs (**Fig. 3.4J–M**), suggesting that OL2HG-mediated remodeling of Kennedy pathway intermediates is not restricted to a single cell type. Taken together, these patterns indicate that OL2HG leads to accumulation of intermediates upstream of PE with a concomitant reduction in downstream intermediates.

To further interrogate the metabolic intersection linking TGs, PEs, and PCs, we assessed the abundance of intermediates in the Kennedy pathway for PE and PC synthesis in PAECs in the presence or absence of oleate pre-loading. Oleate treatment increased the abundance of PEtn and CDP-Etn, but not glycero-PEtn (**Fig. 3.5A**). In contrast, oleate decreased PChol abundance while increasing CDP-Chol and glycero-PChol (**Fig. 3.5B**). Notably, OL2HG potentiated these trends, most prominently enhancing the oleate-induced upregulation of PEtn and CDP-Etn and reducing glycero-PEtn (**Fig. 3.5A**).

3.3.4 PEtn paradoxically potentiates the OL2HG-induced PE downregulation and TG accumulation

To determine whether accumulation of PEtn through exogenous supplementation is sufficient to promote preferential synthesis of PE over TG, PAECs were treated with OL2HG (500 μM, 24 h) in the presence or absence of PEtn (1 mM, 24 h). As expected, PEtn supplementation increased intracellular PEtn and CDP-Etn abundance (**Fig. 3.6A–B**), consistent with cellular uptake and entry into the Kennedy pathway for PE synthesis. However, PEtn supplementation did not alter glycero-PEtn abundance (**Fig. 3.6C**), suggesting that increased flux through proximal Kennedy pathway intermediates does not necessarily propagate through the pathway to PE and may not uniformly regulate downstream intermediates. Unexpectedly, PEtn potentiated the OL2HG-induced decrease in total PE and concomitant increase in total TG (**Fig. 3.6D–E**), suggesting that OL2HG-driven accumulation of PEtn may contribute, at least in part, to this differential regulation of PE and TG. Notably, supplementation with PEtn alone did not increase total PE content but significantly increased the pool of lysophosphatidylehanolamine species (data not shown).

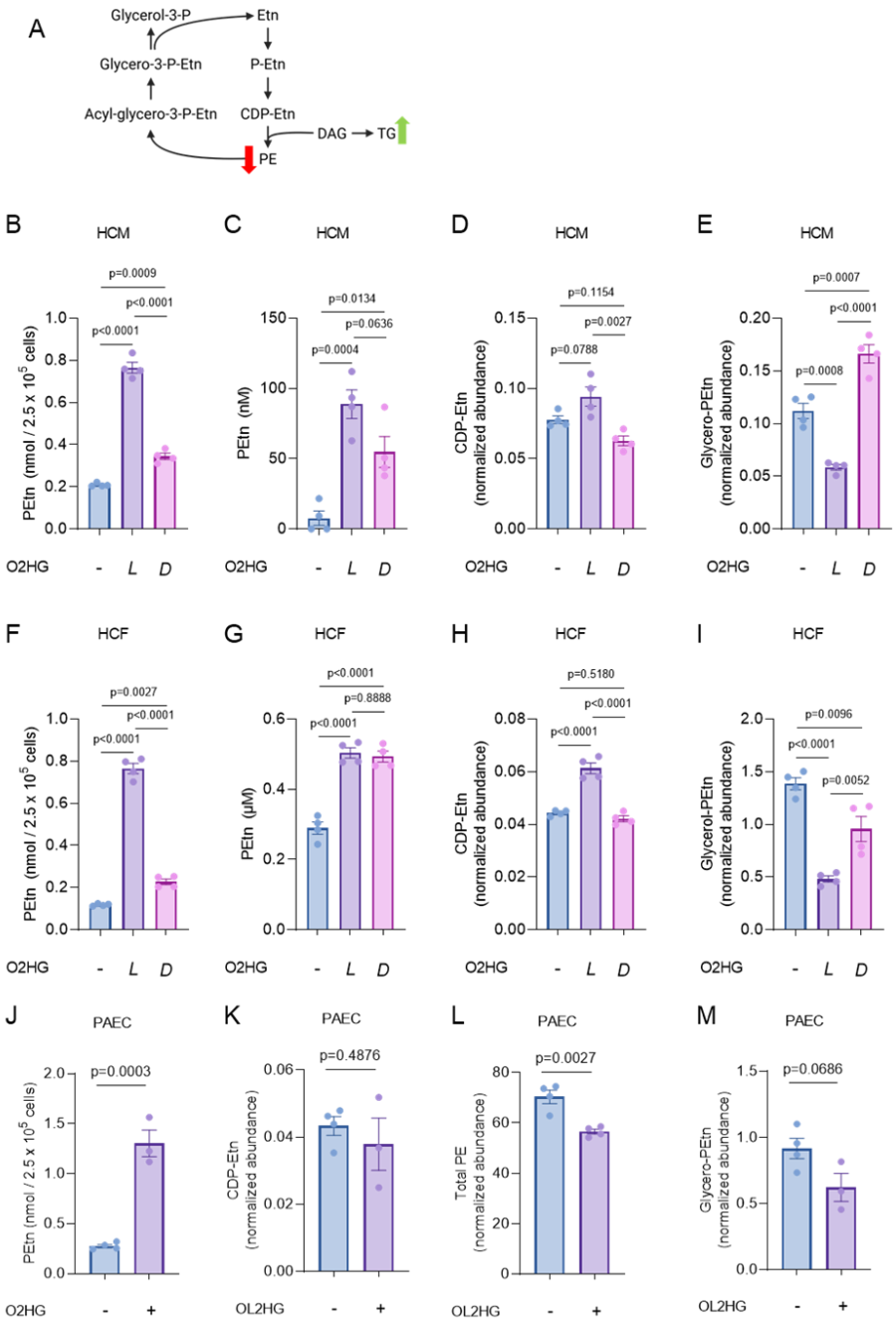

Figure 3.4. OL2HG alters expression of PE Kennedy pathway metabolic intermediates. **A**, Schematic illustration of PE Kennedy pathway metabolism, highlighting L2HG-induced upregulation of TG and downregulation of PE. Expression of **A**, intracellular PEtn, **B**, extracellular PEtn, **C**, CDP-Etn, and **D**, glycerol-PEtn in HCMs treated with DMSO (n=4), 500 μM OL2HG (n=4), or 500 μM OD2HG (n=4) for 24 h. Expressions of these metabolites in HCFs and PAECs are shown in **F**–**I** and **J**–**M**, respectively. Data are presented as mean ± SEM. Data were tested for normality by Shapiro–Wilk test. Normal data were analyzed by ordinary one-way ANOVA (>2 groups) or unpaired *t*-test (pairwise). Non-normal data were analyzed by the Kruskal-Wallis test (> 2 groups) or Mann–Whitney test (pairwise).

3.3.5 OL2HG alters steady-state labeling of downstream Kennedy pathway intermediates from Etn without affecting PEtn labeling

Given our observations that OL2HG induces intracellular accumulation of PEtn, we next sought to determine whether this accumulation arises from increased phosphorylation of ethanolamine to PEtn. To address this question, we performed stable isotope tracing experiments in PAECs using $^{13}C_2$-Etn (200 µM, 24 h) and quantified isotopically labeled (M+2) Kennedy pathway intermediates by LC–MS. Phosphorylation of $^{13}C_2$-Etn by ETNK1/2 yields $^{13}C_2$-PEtn, which is subsequently converted by PCYT2, the rate-limiting step of the PE Kennedy pathway (see Section 3.1) into $^{13}C_2$-CDP-Etn. In addition, turnover of labeled PE generates $^{13}C_2$-glycero-PEtn.

Consistent with earlier experiments (**Fig. 3.4J–M**), OL2HG treatment increased the abundance of unlabeled (M+0) PEtn and decreased unlabeled glycero-PEtn, although the latter did not reach statistical significance (**Fig. 3.7A–C**). In contrast, OD2HG reduced the abundance of unlabeled PEtn, CDP-Etn, and glycero-PEtn (**Fig. 3.7A–C**), indicating enantiomer-specific effects. Notably, OL2HG and OD2HG exerted distinct, enantiomer-specific effects on isotopic labeling of PEtn, CDP-Etn, and glycero-PEtn. Specifically, OL2HG did not alter $^{13}C_2$-PEtn abundance (**Fig. 3.7A**), suggesting that the initial uptake and subsequent phosphorylation of Etn is not affected. By contrast, OL2HG significantly reduced $^{13}C_2$-CDP-Etn (**Fig. 3.7B**) as well as $^{13}C_2$-glycero-PEtn (**Fig. 3.7C**). The preservation of PEtn labeling alongside reduced formation of downstream labeled intermediates implicates impaired flux through the second step of the pathway (i.e., conversion of PEtn to CDP-Etn by PCYT2), rather than altered ethanolamine phosphorylation, as a contributor to OL2HG-mediated remodeling of PE metabolism. Nevertheless, unambiguous evaluation of this hypothesis requires time-resolved flux measurements to derive true reaction rates of individual pathway steps, as recommended in Ref.[25]. This caveat is particularly relevant because the present experiments quantify steady-state isotopic labeling rather than metabolic flux. Under such conditions, unchanged levels of labeled PEtn do not necessarily indicate unaltered flux through the phosphorylation reaction, as steady-state pool sizes can remain constant despite substantial changes in both synthesis and clearance rates. Accordingly, steady-state tracer experiments such as those performed here cannot, on their own, resolve absolute pathway fluxes. Nevertheless, the hypothesis that OL2HG alters the rate-limiting step of the PE Kennedy pathway, rather than affecting upstream Etn uptake or phosphorylation, is supported by transcriptomic data showing a

consistent downregulation of *PCYT2* transcripts in both PAECs and HCMs (**Fig. 3.8A–B**). This effect was observed despite cell type–specific alterations in *SELENOI* (encoding Etn phosphotransferase 1, which catalyzes the transfer of PEtn from CDP-Etn to DAG to form PE) and *ETNK1* in PAECs and HCMs, respectively (**Fig. 3.8A–B**).

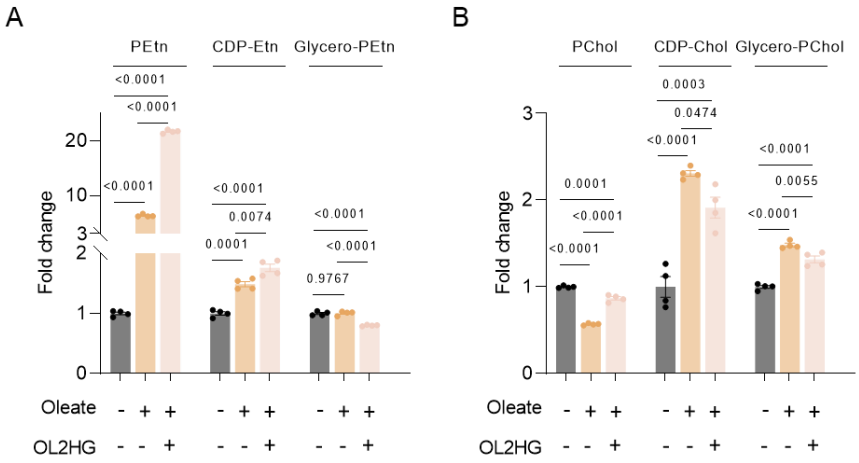

Figure 3.5. OL2HG potentiates oleate-induced regulation of Kennedy pathway metabolic intermediates. Expression of intracellular **A**, PEtn, CDP-Etn, and glycerol-PEtn, as well as **B**, PChol, CDP-Chol, and glycerol-Pchol in PAECs treated with DMSO (n=4), 50 µM oleate (n=4), or 50 µM oleate + 500 µM OL2HG (n=4) for 24 h. Data are presented as mean ± SEM. Data were tested for normality by Shapiro–Wilk test. Normal data were analyzed by ordinary one-way ANOVA. Non-normal data were analyzed by the Kruskal–Wallis test.

3.3.6 L2HG decreases PE and its precursors in BMDMs

Finally, we sought to determine whether our *in vitro* observations that OL2HG alters PE metabolism could be recapitulated in BMDMs isolated from male *L2hgdh*$^{+/+}$ and *L2hgdh*$^{-/-}$ mice. The use of BMDMs was motivated by recent reports showing that L2HG accumulates in macrophages following lipopolysaccharide activation[26]. BMDMs were identified by flow cytometry as a CD45^{+} CD11b^{+} F4/80^{+} DAPI^{-} population, with 99.33% and 99.14% of events falling within the defined gate in representative samples from *L2hgdh*$^{+/+}$ and *L2hgdh*$^{-/-}$ cells, respectively (**Fig. 3.9A–B**). LC–MS-based semi-targeted metabolomics was then performed, as described in Section 2.2.5, and differentially regulated metabolites were defined using a threshold of |fold change| > 1.5 and $p < 0.05$.

Pathway and enrichment analysis using MetaboAnalyst 6.0 revealed glycerophospholipid metabolism as the most significantly enriched pathway among metabolites altered in *L2hgdh*$^{-/-}$ BMDMs relative to wild-type controls (**Fig. 3.9C–D**). PEtn, CDP-Etn, glycero-PEtn, and PChol were all significantly downregulated in *L2hgdh*$^{-/-}$ cells when compared to *L2hgdh*$^{+/+}$ cells (**Fig. 3.9E**). Notably, total PE abundance was also significantly reduced in *L2hgdh*$^{-/-}$ cells when compared to *L2hgdh*$^{+/+}$ cells (**Fig. 3.9F**), although total PC abundance was unchanged (**Fig. 3.9G**). Taken together, these results suggest that similar to OL2HG supplementation *in vitro*, systemic elevation of L2HG resulting from global deletion of *L2hgdh* gene is associated with reduced PE abundance and precursor intermediates in BMDMs. However, these observations should be interpreted with caution and require replication in larger cohorts, as only a single mouse *per* genotype was practically feasible in the present study.

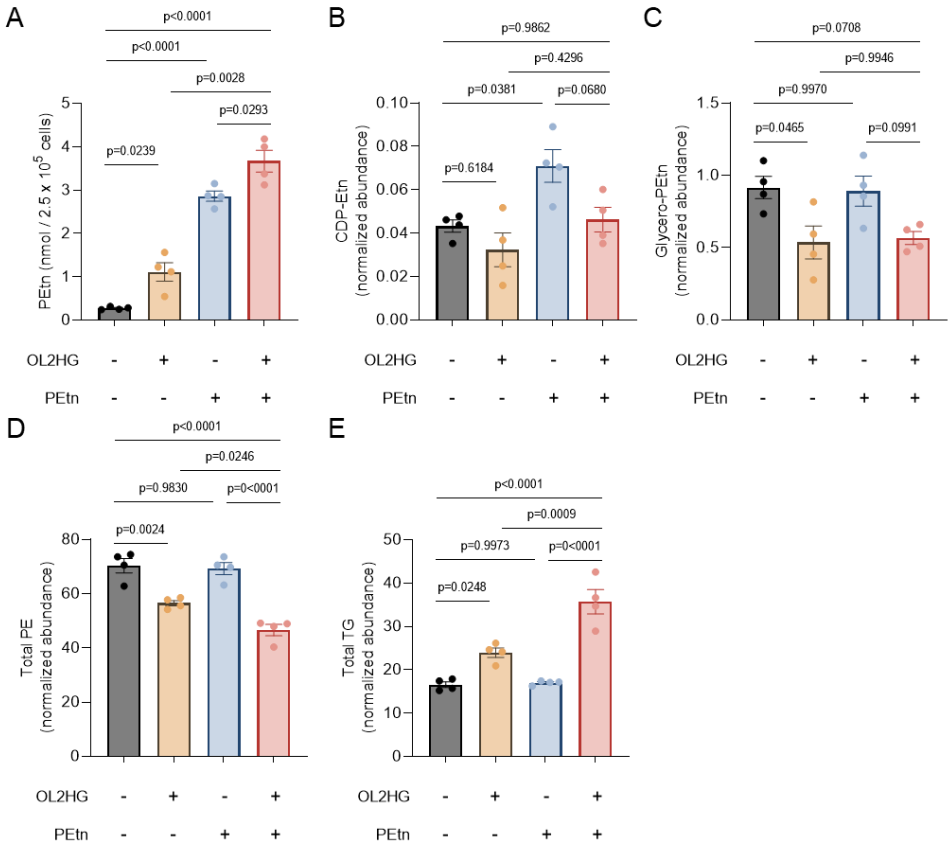

Figure 3.6. PEtn enhances OL2HG-induced PE depletion and TG accumulation. Expression of intracellular **A**, PEtn, **B**, CDP-Etn, **C**, glycerol-PEtn, **D**, total PE, and **E**, total TG in PAECs treated with DMSO (n=4), 500 µM OL2HG (n=4), 1 mM PEtn (n=4), or 500 µM OL2HG + 1 mM PEtn (n=4) for 24 h. Data are presented as mean ± SEM. Data were tested for normality by Shapiro–Wilk test. Normal data were analyzed by ordinary one-way ANOVA. Non-normal data were analyzed by the Kruskal–Wallis test.

3.4 Discussion

The findings presented in this chapter extend the central observation of the preceding chapter, that L2HG promotes TG accumulation, by placing this phenotype within a broader framework of lipid metabolic remodeling. We show that rather than occurring in isolation, TG accumulation is accompanied by coordinated changes in phospholipid metabolism, most notably a reduction in PE abundance and alterations in the expression of its biosynthetic precursors. These data support the notion that L2HG reshapes lipid partitioning within the cell, favoring neutral lipid storage while constraining specific glycerophospholipid pools. Nevertheless, the present results are inherently correlative, and do not establish whether PE depletion is a direct consequence of TG accumulation, a compensatory adaptation to altered lipid flux, or an independent effect of L2HG acting at shared metabolic nodes. Discriminating among these possibilities represents a key limitation of the current work and an important direction for future studies.

A central conceptual framework emerging from this chapter is substrate competition between TGs and glycerophospholipids (although this notion may or may not extend to sphingophospholipids). TGs, PEs, and PCs rely on shared precursors, including G3P, DAG, and fatty acyl-CoAs, such that increased diversion of these substrates toward TG synthesis could constrain phospholipid biosynthesis. This framework is supported by prior studies demonstrating reciprocal regulation between TG and phospholipid pools under conditions of altered DGAT activity[10,11]. Moreover, free fatty acids liberated from phospholipid turnover in the plasma membrane can be channeled toward TG synthesis[27], and deficiency in PE[28] and PC[29] *de novo* synthesis have been shown to drive TG synthesis. Furthermore, Singh *et al.* demonstrated that single-allele deficiency of *PCYT2* in mice leads to hypertriglyceridemia due to increased hepatic and intestinal lipoprotein secretion and suppressed lipoprotein lipase activity leading to attenuated plasma lipolysis[30]. However, the extent and direction of compensation between phospholipids and TGs are likely cell type–dependent and may vary with the magnitude of lipid perturbation. Notably, while TG accumulation may initially occur at the expense of phospholipids, continued LD expansion ultimately requires sufficient phospholipid availability, as LDs are bounded by a phospholipid monolayer. Consistent with this constraint, Payne *et al.* reported that depletion of PC *via* loss-of-function mutations in *PCYT1A* (encoding the rate-limiting enzyme for PC synthesis *via* the Kennedy pathway and the functional analogue of PCYT2 for PE) results in decreased, rather than increased, neutral lipid

accumulation in adipocytes[31]. Nevertheless, while substrate competition provides a parsimonious explanation for the observed phenotypes, the present study does not directly quantify flux through competing pathways. Future work employing time-resolved isotope tracing, kinetic flux modeling, or acute genetic manipulation of key branchpoint enzymes will be required to directly test whether TG accumulation causally limits PE synthesis (or *vice versa*) under L2HG exposure.

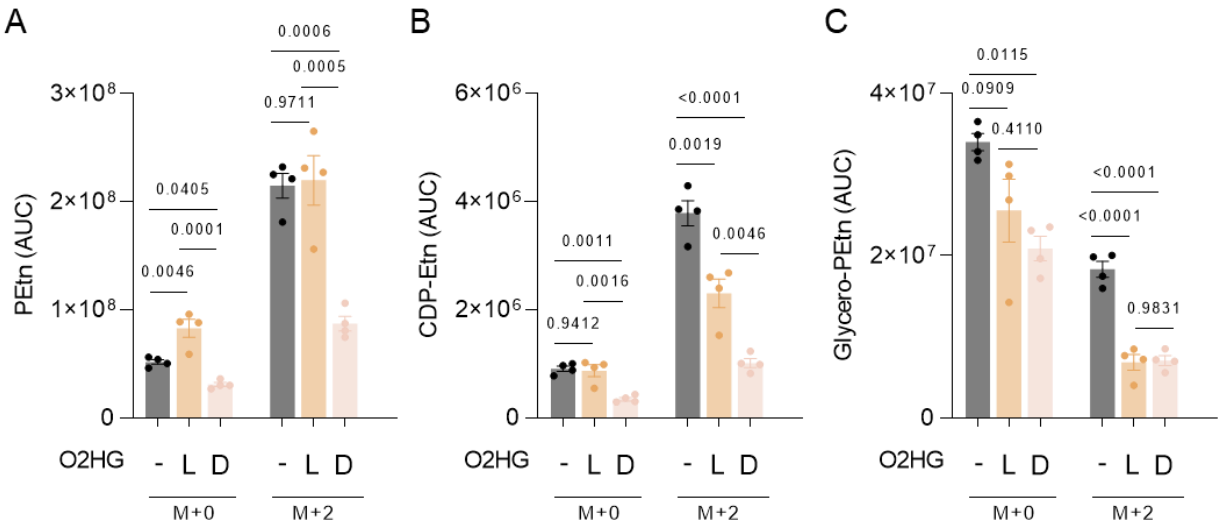

Figure 3.7. OL2HG alters the steady state pools of PE Kennedy pathway intermediates derived from exogenous Etn. Signal intensity of unlabelled (M+0, $^{13}C_0$) and isotopically labelled (M+2, $^{13}C_2$) **A**, PEtn, **B**, CDP-Etn, and **C**, glycero-PEtn in PAECs supplemented with 200 µM $^{13}C_2$-Etn and treated with DMSO (n=4), 500 µM OL2HG (n=4), or 500 µM OD2HG (n=4) for 24 h. Signal intensity was quantified by peak integration and data are presented as areas under the curve (AUC). Data are presented as mean ± SEM. Data were tested for normality by Shapiro–Wilk test. Normal data were analyzed by ordinary one-way ANOVA. Non-normal data were analyzed by the Kruskal–Wallis test.

In addition to substrate competition, an alternative, non-exclusive interpretation is that PE depletion reflects an adaptive remodeling response rather than passive substrate limitation. PE plays a central role in membrane curvature, mitochondrial function, and autophagy[4,6,7,32], and reductions in PE abundance may therefore enable cellular adaptations that give rise to secondary or higher-order effects, which collectively favor increased neutral lipid storage. Importantly, because phospholipid synthesis is tightly coupled to membrane biogenesis[33], the consequences of altered PE (and potentially PC) metabolism may differ substantially between terminally differentiated cells and actively proliferating cells that require continuous membrane synthesis. In this context, L2HG-induced perturbations in glycerophospholipid metabolism may be tolerated

differently in non-proliferating cells, while imposing distinct constraints in proliferative settings. Consistent with this idea, we have observed that OL2HG inhibits proliferation in primary human cells (Chandra, Vigder and Loscalzo, Brigham and Women's Hospital, Harvard Medical School, unpublished), a phenotype that would be expected to reduce cellular demand for membrane synthesis and, consequently, for PE.

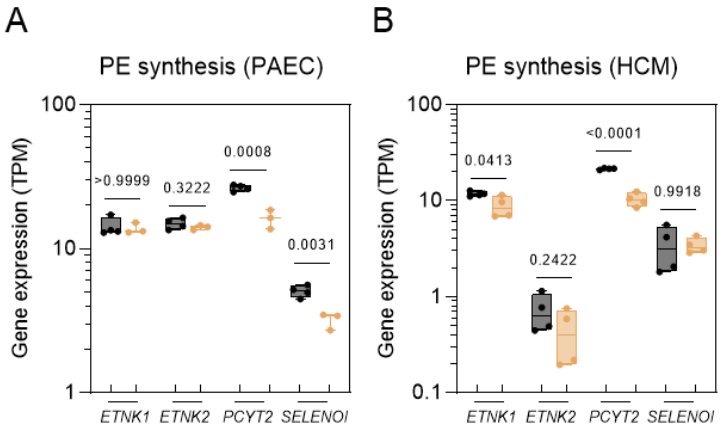

Figure 3.8. OL2HG downregulates PCYT2 transcriptional expression. Expression of genes involved in the PE Kennedy pathway in **A**, PAECs and **B**, HCMs following treatment with DMSO (n=4) or OL2HG (n=4) for 24 h. Data are expressed as transcripts *per* million (TPM). Data were tested for normality by Shapiro–Wilk test. Normal data were analyzed by unpaired *t*-test. Non-normal data were analyzed by the Mann–Whitney test.

At the level of biosynthetic regulation, the accumulation of PEtn provides insight into where L2HG-mediated remodeling may occur within the Kennedy pathway. OL2HG-induced accumulation of PEtn may also provide a mechanistic link to L2HG-associated alterations in mitochondrial energetics (see Section 1.3), as PEtn has been shown to decrease the oxygen consumption rate in multiple biological systems[34]. Here, OL2HG consistently increased PEtn while reducing glycero-PEtn and, in some cell types, CDP-Etn. Stable-isotope tracing further indicated that although OL2HG does not affect the steady state pool of PEtn derived from extracellular Etn, it attenuates downstream label propagation into CDP-Etn, suggesting that the conversion of PEtn to CDP-Etn by PCYT2 may be selectively perturbed by L2HG. However, these conclusions are necessarily constrained due to the use of steady-state isotope labeling, which does not resolve absolute labeling rate and metabolic flux *per se* (discussed in detail in Ref.[25]). As discussed in Section 3.3.3, unchanged steady state labeling of PEtn does not preclude altered flux, as steady state pool sizes can mask simultaneous changes in synthesis and turnover. Addressing this limitation will require time-course tracing experiments and formal flux calculations to determine whether specific reactions are kinetically constrained[25], and whether such constraints differ between proliferative and non-proliferative cellular states.

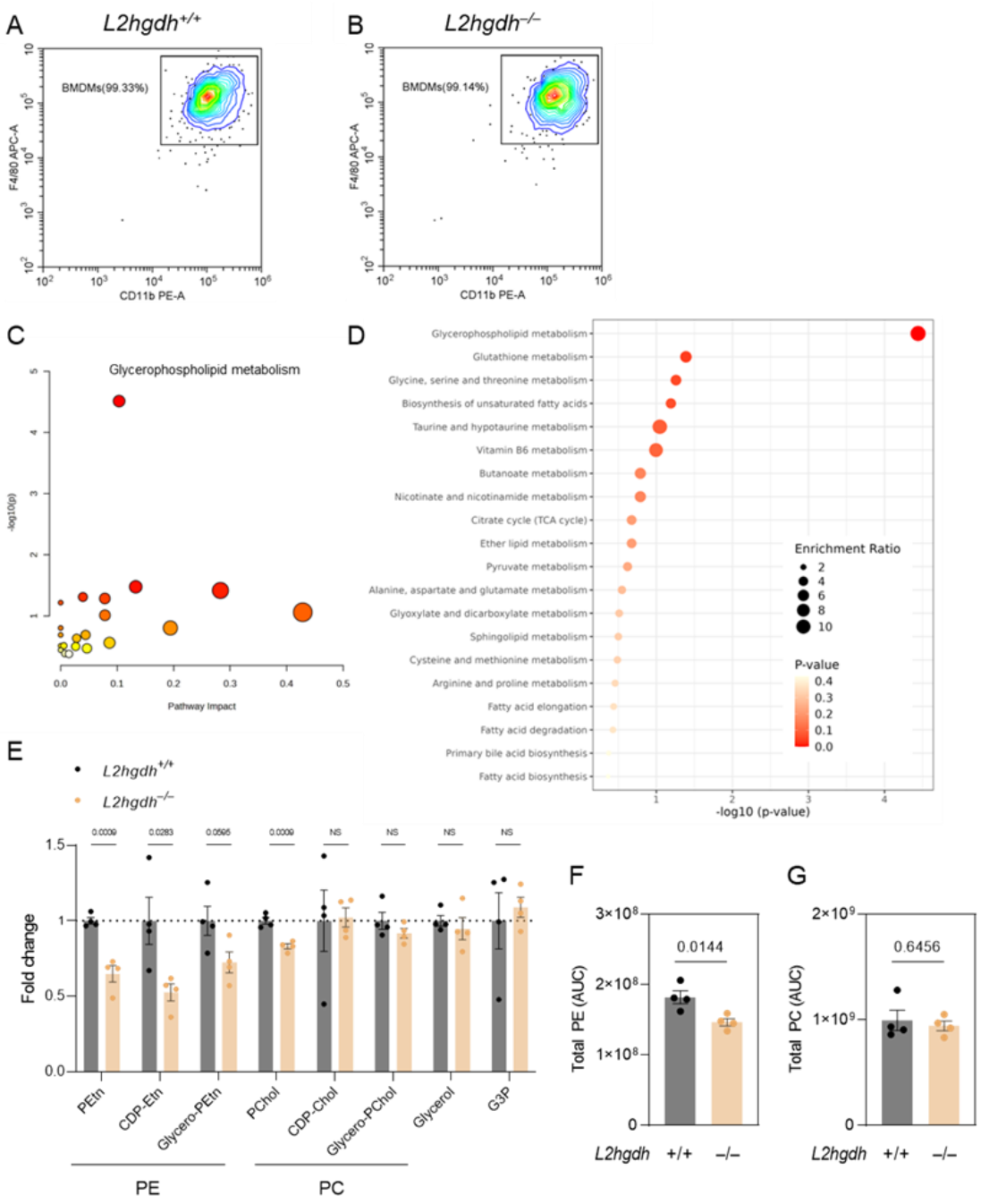

Figure 3.9. *L2hgdh* knock-down leads to downregulation of PE and its precursors in bone marrow-derived macrophages (BMDMs). **A** and **B**, Flow cytometry density plots showing the gating strategy used to identify $CD45^+$ $CD11b^+$ $F4/80^+$ $DAPI^-$ BMDMs. **C**, Pathway analysis and **D**, enrichment analysis of differentially regulated metabolites in *L2hgdh*$^{-/-}$ *vs. L2hgdh*$^{+/+}$ BMDMs. Plots were generated using MetaboAnalyst 6.0. **E**, Expression of intracellular PE and PC Kennedy pathway intermediates, as well as **F**, total PE and **G**, total PC in *L2hgdh*$^{-/-}$ *vs. L2hgdh*$^{+/+}$ BMDMs. Intensity data in **F** and **G** are expressed as area under the curve (AUC). NS, not significant ($p > 0.05$). Data are presented as mean ± SEM. Data were tested for normality by Shapiro–Wilk test. Normal data were analyzed by unpaired *t*-test. Non-normal data were analyzed by the Mann–Whitney test.

The convergence of metabolomic and transcriptomic data implicating PCYT2 provides supportive, but still indirect, evidence for OL2HG-mediated regulation at the rate-limiting step of the PE Kennedy pathway. While consistent downregulation of PCYT2 transcripts across cell types strengthens this hypothesis, transcript abundance does not necessarily reflect enzyme activity. Moreover, we did not observe differential regulation of PCYT2 at the protein level (**Supplementary Data S2.4**), assessed by unbiased LC–MS/MS-based proteomics as described in Section 2.2.6. Post-transcriptional regulation, protein stability, subcellular localization, and allosteric control could all contribute to altered pathway behavior (concepts discussed in detail in Chapter 4). Future studies incorporating targeted proteomics, enzyme activity assays, and genetic rescue approaches will be necessary to determine whether PCYT2 represents a direct functional target of L2HG-mediated regulation of PE.

The extension of our *in vitro* findings to BMDMs isolated from *L2hgdh*-deficient mice supports the physiological relevance of the L2HG–PE axis, but this aspect of the study is limited by sample size. With only one mouse *per* genotype, these results should be interpreted as preliminary and hypothesis-generating. Replication in larger cohorts, inclusion of additional tissues with differing proliferative capacities, and assessment of functional macrophage phenotypes will be essential to determine the robustness and biological significance of PE remodeling *in vivo*.

3.5 Conclusions and future directions

In summary, this chapter demonstrates that L2HG-induced TG accumulation is accompanied by coordinated remodeling of PE metabolism, characterized by reduced PE abundance and altered regulation of its biosynthetic pathway. While the data are consistent with a model in which TG accumulation and PE depletion are linked through shared substrate pools, the directionality and causality of this relationship remain unresolved. By explicitly identifying these limitations and outlining experimental strategies to address them, this work establishes a foundation for future studies aimed at defining how L2HG reshapes lipid partitioning in health and disease.

3.6 References

1 Calzada, E., Onguka, O. & Claypool, S. M. Phosphatidylethanolamine Metabolism in Health and Disease. *International Review of Cell and Molecular Biology* **321**, 29–88 (2016).

2 van der Veen, J. N. *et al.* The critical role of phosphatidylcholine and phosphatidylethanolamine metabolism in health and disease. *Biochimica et Biophysica Acta (Biomembranes)* **1859**, 1558–1572 (2017).

3 Gibellini, F. & Smith, T. K. The Kennedy pathway--De novo synthesis of phosphatidylethanolamine and phosphatidylcholine. *IUBMB Life* **62**, 414–428 (2010).

4 Dawaliby, R. *et al.* Phosphatidylethanolamine Is a Key Regulator of Membrane Fluidity in Eukaryotic Cells. *Journal of Biological Chemistry* **291**, 3658–3667 (2016).

5 Dowhan, W., Vitrac, H. & Bogdanov, M. Lipid-Assisted Membrane Protein Folding and Topogenesis. *The Protein Journal* **38**, 274–288 (2019).

6 Tasseva, G. *et al.* Phosphatidylethanolamine deficiency in Mammalian mitochondria impairs oxidative phosphorylation and alters mitochondrial morphology. *Journal of Biological Chemistry* **288**, 4158–4173 (2013).

7 Rockenfeller, P. *et al.* Phosphatidylethanolamine positively regulates autophagy and longevity. *Cell Death & Differentiation* **22**, 499–508 (2015).

8 Patel, D. & Witt, S. N. Ethanolamine and Phosphatidylethanolamine: Partners in Health and Disease. *Oxidative Medicine and Cellular Longevity* **2017**, 4829180 (2017).

9 Kennedy, E. P. & Weiss, S. B. The function of cytidine coenzymes in the biosynthesis of phospholipides. *Journal of Biological Chemistry* **222**, 193–214 (1956).

10 Rong, S. *et al.* DGAT2 inhibition blocks SREBP-1 cleavage and improves hepatic steatosis by increasing phosphatidylethanolamine in the ER. *Cell Metabolism* **36**, 617–629.e617 (2024).

11 Lee, H. *et al.* Cell cycle arrest induces lipid droplet formation and confers ferroptosis resistance. *Nature Communications* **15**, 79 (2024).

12 Madiraju, S. R. M., Possik, E., Al-Mulla, F., Nolan, C. J. & Prentki, M. Glycerol and Glycerol-3-Phosphate: Multifaceted Metabolites in Metabolism, Cancer, and Other Diseases. *Endocrine Reviews* **47**, 93–120 (2026).

13 Tabata, S. *et al.* L-2hydroxyglutaric acid rewires amino acid metabolism in colorectal cancer via the mTOR-ATF4 axis. *Oncogene* **42**, 1294–1307 (2023).

14 de Goede, K. E. *et al.* d-2-Hydroxyglutarate is an anti-inflammatory immunometabolite that accumulates in macrophages after TLR4 activation. *Biochimica et Biophysica Acta (Molecular Basis of Disease)* **1868**, 166427 (2022).

15 Rzem, R. *et al.* A mouse model of L-2-hydroxyglutaric aciduria, a disorder of metabolite repair. *PLOS ONE* **10**, e0119540 (2015).

16 Toda, G., Yamauchi, T., Kadowaki, T. & Ueki, K. Preparation and culture of bone marrow-derived macrophages from mice for functional analysis. *STAR Protocols* **2**, 100246 (2021).

17 Morita, S. Y. & Ikeda, Y. Regulation of membrane phospholipid biosynthesis in mammalian cells. *Biochemical Pharmacology* **206**, 115296 (2022).

18 Vance, J. E. Phospholipid synthesis and transport in mammalian cells. *Traffic* **16**, 1–18 (2015).

19 Li, Z. *et al.* The ratio of phosphatidylcholine to phosphatidylethanolamine influences membrane integrity and steatohepatitis. *Cell Metabolism* **3**, 321–331 (2006).

20 Sher, R. B. *et al.* A Rostrocaudal Muscular Dystrophy Caused by a Defect in Choline Kinase Beta, the First Enzyme in Phosphatidylcholine Biosynthesis*. *Journal of Biological Chemistry* **281**, 4938–4948 (2006).

21 Fullerton, M. D., Hakimuddin, F., Bonen, A. & Bakovic, M. The Development of a Metabolic Disease Phenotype in CTP:Phosphoethanolamine Cytidylyltransferase-deficient Mice*. *Journal of Biological Chemistry* **284**, 25704–25713 (2009).

22 Funai, K. *et al.* Skeletal Muscle Phospholipid Metabolism Regulates Insulin Sensitivity and Contractile Function. *Diabetes* **65**, 358–370 (2015).

23 Zhao, G. *et al.* Validation of diacyl glycerolacyltransferase I as a novel target for the treatment of obesity and dyslipidemia using a potent and selective small molecule inhibitor. *Journal of Medicinal Chemistry* **51**, 380–383 (2008).

24 Futatsugi, K. *et al.* Discovery and Optimization of Imidazopyridine-Based Inhibitors of Diacylglycerol Acyltransferase 2 (DGAT2). *Journal of Medicinal Chemistry* **58**, 7173–7185 (2015).

25 Jang, C., Chen, L. & Rabinowitz, J. D. Metabolomics and Isotope Tracing. *Cell* **173**, 822–837 (2018).

26 Williams, N. C. *et al.* Signaling metabolite L-2-hydroxyglutarate activates the transcription factor HIF-1α in lipopolysaccharide-activated macrophages. *Journal of Biological Chemistry* **298**, 101501 (2022).

27 Igal, R. A., Caviglia, J. M., de Gómez Dumm, I. N. & Coleman, R. A. Diacylglycerol generated in CHO cell plasma membrane by phospholipase C is used for triacylglycerol synthesis. *Journal of Lipid Research* **42**, 88–95 (2001).

28 Fullerton, M. D., Hakimuddin, F. & Bakovic, M. Developmental and metabolic effects of disruption of the mouse CTP:phosphoethanolamine cytidylyltransferase gene (Pcyt2). *Molecular and Cellular Biology* **27**, 3327–3336 (2007).

29 Caviglia, J. M., De Gómez Dumm, I. N., Coleman, R. A. & Igal, R. A. Phosphatidylcholine deficiency upregulates enzymes of triacylglycerol metabolism in CHO cells. *Journal of Lipid Research* **45**, 1500–1509 (2004).

30 Singh, R. K., Fullerton, M. D., Vine, D. & Bakovic, M. Mechanism of hypertriglyceridemia in CTP:phosphoethanolamine cytidylyltransferase-deficient mice. *Journal of Lipid Research* **53**, 1811–1822 (2012).

31 Payne, F. *et al.* Mutations disrupting the Kennedy phosphatidylcholine pathway in humans with congenital lipodystrophy and fatty liver disease. *Proceedings of the National Academy of Sciences of the United States of America* **111**, 8901–8906 (2014).

32 Becker, T. *et al.* Role of phosphatidylethanolamine in the biogenesis of mitochondrial outer membrane proteins. *Journal of Biological Chemistry* **288**, 16451–16459 (2013).

33 Tzagoloff, A. in *Membrane Biogenesis: Mitochondria, Chloroplasts, and Bacteria* (ed Alexander Tzagoloff) 1–14 (Springer US, 1975).

34 Modica-Napolitano, J. S. & Renshaw, P. F. Ethanolamine and phosphoethanolamine inhibit mitochondrial function in vitro: implications for mitochondrial dysfunction hypothesis in depression and bipolar disorder. *Biological Psychiatry* **55**, 273–277 (2004).

Chapter 4

Network Medicine and Proteomics Link L-2-Hydroxyglutarate to Major Vault Protein: an MVP Discovery?

4.1 Introduction

Biological systems are inherently complex, with cellular phenotypes emerging not from the behavior of individual molecular components in isolation, but from the structure and dynamics of their interactions. As outlined in the accompanying book chapter, network medicine provides a formal framework for capturing this complexity by modeling biological systems as networks of interacting components, thereby enabling the investigation of disease as a system-level perturbation rather than a reductionist consequence of single-gene effects.

Within this framework, protein–protein interaction (PPI) networks are particularly well suited for the analysis of proteomics data, as they place quantitative changes in protein abundance into a broader topological and functional context, allowing emergent properties such as modularity, centrality, and network proximity to guide biological interpretation. The following book chapter[1] provides the conceptual and methodological foundation of network medicine that underpins the analyses and interpretations presented in this chapter.

16

Network Medicine: A New Paradigm for Cardiovascular Disease Research and Beyond

Niv Vigder[1,2], Stuart J. Cordwell[2,3,4,5], and Joseph Loscalzo[1]

[1] *Department of Medicine, Brigham and Women's Hospital, Harvard Medical School, Boston, MA, USA*
[2] *Faculty of Science, School of Life and Environmental Sciences, The University of Sydney, Sydney, NSW, Australia*
[3] *Faculty of Medicine and Health, School of Medical Sciences, The University of Sydney, Sydney, NSW, Australia*
[4] *Charles Perkins Centre, The University of Sydney, Sydney, NSW, Australia*
[5] *Sydney Mass Spectrometry, The University of Sydney, Sydney, NSW, Australia*

16.1 Introduction to Network Medicine

The molecular components of cells are structurally and functionally interdependent. Biological processes are governed by these components (e.g. genes, proteins, metabolites, etc.) and their intra- and inter-cellular interactions, as well as across organs by means of, for example, the circulatory system. This interconnectivity implies that complex, multi-dimensional biological systems – rather than individual loci – determine the way in which genotypes manifest as phenotypes. Specific perturbations to one or a few biological entities can propagate throughout these systems, implying that disease cannot be defined by the original perturbation alone. This complexity is underappreciated by the reductionist "One Gene-One Disease" Oslerian paradigm that permeates contemporary biomedical research and medicine.

The past few decades have witnessed substantial expansion of the generation of genetic – and, more recently, multi-omic – human (and other organismal) data. As such, contemporary medicine is ideally positioned to turn away from scientific reductionism and progress toward a more holistic, integrated formalism of biology and disease. Facilitating this transition are the tools provided by network medicine, an emerging discipline that combines principles and approaches from network science and systems biology to deepen understanding of complex human disease. By summarizing biological complexity as components (nodes) and their interactions (edges), network-based approaches can effectively model biological phenomena in computationally efficient ways. Network medicine acknowledges that to understand the role of a specific gene/protein in a given biological/disease process, one should understand the network context of that gene/protein. The importance of network context derives from the emergent behavior of biological systems: namely, the behavior of a system is not explicable by assessment of its components in isolation. In this way, network-based approaches to human biology and disease offer an integrative platform through which to assess the effects of cellular interconnectedness on (patho)biology. In this chapter, we present an overview of network medicine, its applications, and future directions in the context of CVD research. Given the proteomic-centered theme of this book, we chose to focus primarily on PPI networks, although biological networks can represent the interactions between different types of biomolecules (e.g. mRNA, metabolites, etc.).

Cardiovascular Proteomics Techniques: Applications for Clinical and Laboratory Research, First Edition.
Edited by Cristina Banfi.

16.2 Introduction to Network Science and Biological Networks

Complex biological data generated from large-scale, often multi-omic studies require analysis and visualization tools that provide a comprehensive means of analyzing this complexity to identify previously unrecognized relationships and novel testable hypotheses. Network analysis offers tools for integrating rigorously such complex biological data. This section introduces key aspects of network analysis in the context of biological networks.

16.2.1 Nodes and Links

Networks (or graphs) depict the components of a complex system as nodes (or vertices) and the interaction between these nodes as links (or edges). There are several types of biological networks, including structural and correlation networks. Correlation networks depict correlations between two biological entities (e.g. co-expression of mRNA or metabolites). In structural networks, nodes represent molecular components whose biological relationships are depicted by links. For example, in PPI networks, nodes correspond to proteins, and two nodes are linked if there exists evidence for a direct (physical) interaction between the corresponding two proteins. One justification for the inclusion of only physical – rather than merely functional – PPIs in these networks relates to the finding that germline mutations are preferentially located in genetic regions encoding PPI interfaces (Cheng et al. 2021).

16.2.2 Weighted and Unweighted Networks

Biological networks can be weighted or unweighted (Figure 16.1a). Unweighted networks assume that a relationship between two biological entities is binary, that is, an interaction or correlation between two components is present or absent. In other words, an unweighted network overlooks the magnitude or strength of the relationship between the two nodes. For example, the affinity of a physical interaction between two proteins is not accounted for in most PPI networks. Although biological interactions are dynamic rather than binary and static, biological systems are often depicted as unweighted networks because it is challenging to measure and/or estimate accurately and reliably all of these potential relationships. Indeed, the strength of an interaction between two proteins in cellular systems depends on numerous factors, including but not limited to the equilibrium dissociation constant (K_D) and the presence of competing substrates and local inhibitors. As such, it is difficult to estimate reliably – experimentally or computationally – the true weights of links connecting two nodal proteins. One does not assume that biological interactions are binary in weighted networks, wherein nodes and/or links exhibit differential influence or strength of association. For example, in disease networks, each node represents a distinct disease, and two diseases are linked if they share gene associations (referred to as disease genes/proteins) (Goh et al. 2007). In these disease networks, nodal weight (depicted by the size of a node) corresponds to the number of disease genes associated with the disease, and edgetic weight (depicted by the thickness of a link) corresponds to the number of disease genes shared between two diseases. Disease networks are reviewed in more detail in Section 16.8.

16.2.3 Directed and Undirected Networks

Links within biological networks can be directed or undirected (Figure 16.1a). In PPI networks, links depict undirected physical interactions involving both nodal proteins. However,

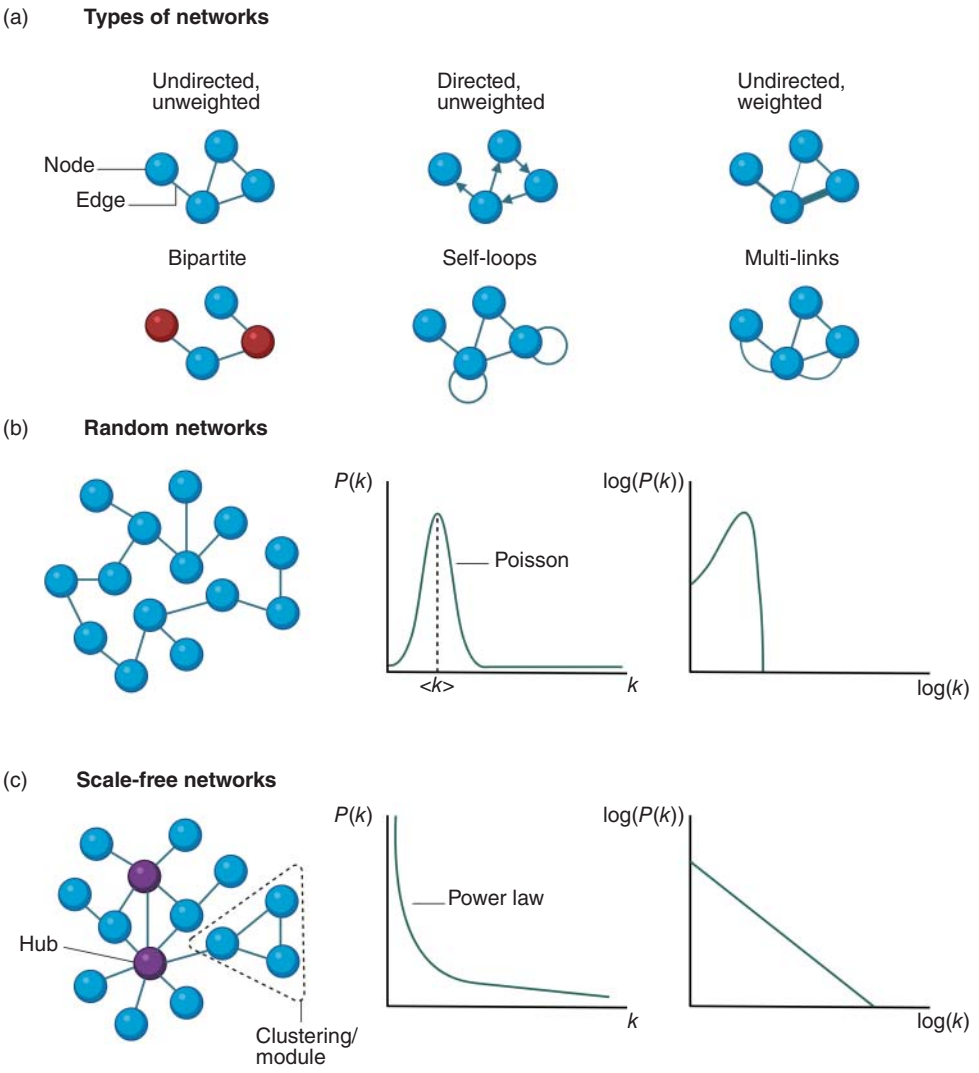

Figure 16.1 Key concepts in network science. (a) Visual representation of different types of networks and network parameters. (b) Depiction of the connectivity of a random network and its Poissonian degree distribution, $P(k)$, on a linear (left) and logarithmic (right) scale. The vast majority of nodes in random networks have degrees similar to the average node degree of the network, $<k>$, while very few (if any) nodes have very low or very high degrees (see Section 16.2.10.1). (c) Depiction of the connectivity of a scale-free network and its power law degree distribution on a linear (left) and logarithmic (right) scale; in the latter, the slope of the line is the degree exponent, γ (see Section 16.2.10.2). In scale-free networks, the overwhelming majority of nodes have very small degrees, while very few nodes have very high degrees (hubs). Groups of nodes that are highly clustered are referred to as modules (see Section 16.2.9). *Source:* Created with BioRender.com.

relationships between two biological entities can be unidirectional. For example, irreversible biochemical reactions in metabolic networks are depicted by directed links connecting two nodal metabolites. Arrows are used to depict the direction of the flow of information through a directed link.

16.2.4 Unipartite and Bipartite Networks

The examples described above outline networks that comprise only a single type of node. These networks are called unipartite. An additional layer of complexity can be added to a biological network by introducing a second type of node. Networks that contain two types of nodes are called bipartite (Figure 16.1a). In bipartite networks, a link connects two nodes of different types. For example, gene-regulatory networks contain transcription factor (TF) nodes and gene nodes and link connect TFs to the genes they regulate. Such gene-regulatory networks can have different link types (i.e. depicting activation or repression of gene expression) and weights (i.e. depicting the magnitude of activation or repression).

16.2.5 Simple Networks and Self-Loops

Most biological networks are simple (i.e. two nodes are linked by no more than one edge) and do not permit self-loops (i.e. links connecting a single node to itself) (Figure 16.1a). An exception to this last point is that of proteins that self-associate to form homomultimers.

16.2.6 Degree and Average Degree

The degree of node i (denoted as k_i) refers to the number of links connected to it. Since biological networks are simple (see Section 16.2.5), k_i also denotes the number of nodes connected to node i (referred to as neighbors). In PPI networks, the degree of a nodal protein refers to the number of other proteins a particular protein *can* interact with physically. Importantly, the representation of PPIs in static networks overlooks the fact that a protein need not interact with all of its associated proteins simultaneously. In fact, a link between two nodal proteins in a PPI network denotes a possible physical interaction rather than a biologically active one. To this end, the degree of a nodal protein does not (necessarily) represent the number of other proteins with which it interacts at a given time. PPI (binding) depends upon the concentrations of the two proteins and their dissociation constant (free energy of binding), as well as allosteric modulation and posttranslational modification (see below). Mathematical descriptions for node degree, link count, and average degree for directed and undirected networks are outlined in Table 16.1.

16.2.7 Adjacency Matrix

A network can be represented mathematically through an adjacency matrix, the number of rows and columns of which are equal to the number of nodes in the network (i.e. $N \times N$ square matrix for a network with N nodes). The entries of the adjacency matrix describe whether two particular nodes are linked (and, in weighted networks, the link weight). In unweighted simple networks, the entries are either one (denoting the presence of a link) or zero (denoting the absence of a link). For example, if A_{ij} (the entry in the ith row and jth column of the adjacency matrix) =1, nodes i and j are linked; if $A_{ij} = 0$, nodes i and j are not linked. In weighted networks, the nonzero entries of the adjacency matrix can be integers greater than one (or normalized over the entire network to a value greater than 0 but less than or equal to 1), thereby representing the magnitude of the connection between two nodes. Given that biological networks do not typically permit self-loops (see Section 16.2.5), the diagonal of the adjacency matrix is filled with zeros. In undirected networks, a link between nodes i and j is equivalent to that between j and i (i.e. $A_{ij} = A_{ji}$), making the adjacency matrix symmetrical about the diagonal. This symmetry does not hold for directed networks.

Given that biological networks are sparse (i.e. most nodes have small degrees, see Section 16.2.10.2), the majority of the adjacency matrix is filled with zeros. For this reason, it is inefficient

Table 16.1 Comparison of common network parameters in undirected and directed networks.

Parameter	Description	Mathematical formalism	
		Undirected networks	**Directed networks**
k_i	Number of links connected to node i	–	$k_i = k_i^{in} + k_i^{out}$
L	Number of links in a network	$L = \frac{1}{2}\sum_{i=1}^{N} k_i$	$L = \sum_{i=1}^{N} k_i^{in} = \sum_{i=1}^{N} k_i^{out}$
$<k>$	Average degree of all nodes in a network	$<k>= \frac{1}{N}\sum_{i=1}^{N} k_i = \frac{2L}{N}$, where N denotes the number of nodes in the network	$<k^{in}>= \frac{1}{N}\sum_{i=1}^{N} k_i^{in} =$ $<k^{out}>= \frac{1}{N}\sum_{i=1}^{N} k_i^{out} = \frac{L}{N}$
C_i	Local clustering coefficient	$C_i = \frac{2L_i}{k_i(k_i-1)}$, where L_i refers to the total number of links between the k_i neighbors of node i	As for undirected networks
$<C>$	Average clustering coefficient	$<C>= \frac{1}{N}\sum_{i=1}^{N} C_i$	As for undirected networks

computationally to store biological networks as adjacency matrices. Rather, edge lists (i.e. lists of linked node pairs) can be used to improve computational efficiency as they store only the nonzero values in the adjacency matrix (Barabási 2016).

16.2.8 Network Paths and Distances

In network science, a path refers to a route that passes along the links and connects two particular nodes. The path length (denoted as l) represents the number of links (or nodes) that a path contains. The shortest path length (denoted as d_s, also known as the geodesic path) refers to the number of links contained in the shortest route connecting two nodes. Two discrete nodes can be connected *via* multiple shortest paths of equal length d_s.

The network distance separating two biological components offers biological insight. For example, the shortest path length separating two nodal genes/gene products is proportional to their biological similarity, often evident by their gene ontology (GO) term similarity (Menche et al. 2015). The diameter of a network (denoted as d_{max}) refers to the longest of all shortest paths (i.e. the maximum number of links separating any two nodes).

The average distance connecting any two nodes (denoted as $<d>$) is smaller than expected intuitively even in large networks. $<d>$ follows different mathematical formulae depending on the nature of the network (i.e. random or scale free, see Section 16.2.10). In scale-free networks (e.g. most biological networks), this high interconnectivity of nodes manifests as the ultra-small-world property, that is, any two nodes selected at random are separated by a surprisingly small number of other nodes. The human PPI network has a diameter $d_{max} = 13$ and a mean distance between all protein pairs $<d> = 3.4$ (Menche and Barabási 2016), suggesting that: (1) the "farthest" two proteins in the network are only 13 proteins apart; and (2) for any protein pair chosen at random, the two corresponding proteins are separated by as little as ~3–4 links. This "ultra-small-world" phenomenon

is a consequence of the presence of hubs (i.e. highly connected nodes) that decrease substantially the network distance between any two topologically distant nodes. The presence of hubs is a consequence of the scale-free property of most biological networks (see Section 16.2.10.2). Additional path parameters are the Eulerian and Hamiltonian paths, which refer to routes that connect two nodes while traversing each link or each node exactly once, respectively (Barabási 2016).

16.2.9 Connectedness

The connectedness of a node is a measure of its topological importance (i.e. the extent to which a node facilitates the flow of information through the network). Centrality is a measure of node connectedness (Bonacich 1987; Nieminen 1974). There are several measures of centrality, and these can be measured based on different nodal attributes, including degrees and path lengths.

Degree centrality assigns nodal importance based on the degree of a node, thereby representing low-degree nodes and hubs as minimally and highly central, respectively. This measure reduces all edges to equal importance (i.e. an edge linking two hubs is equal to an edge linking two low-degree nodes). As such, a node with a single connection to a hub and a node with a single connection to a low-degree node both have a degree centrality of one. However, in biological networks, the attributes of a node's neighbor are major determinants of its biological importance, rendering degree centrality *per se* a relatively poor parameter in predicting biological importance.

By contrast to degree centrality, closeness centrality and betweenness centrality assign nodal importance based on a node's overall connectivity to the entire network (Freeman 1977). Closeness centrality measures the average of all shortest path lengths connecting a particular node to all other nodes in the network and is indirectly proportional to importance (i.e. a node that connects to all other nodes *via* only a small number of edges is of high closeness centrality). Contrastingly, betweenness centrality refers to the fraction of shortest paths in the network that traverse a particular node and is calculated by the number of shortest paths that traverse it divided by the total number of shortest paths. In this way, betweenness centrality can be used to assess the importance of a node in connecting two components (subnetworks, modules) of a network. For example, Samokhin et al. (2018) used betweenness centrality to identify neural precursor cell expressed, developmentally down-regulated 9 (NEDD9) as a novel and critical node regulating the aldosterone-dependent transition between adaptive and pathological fibrosis in pulmonary arterial hypertension.

Other centrality parameters useful for specific biological investigations include eigenvector centrality, radiality centrality, integration centrality, motif-based centrality, and control centrality [reviewed in Koschützki and Schreiber 2008 and Jalili et al. (2016)]. For a detailed comparison of different centrality measures and their usefulness in predicting influential proteins in a yeast PPI network, refer to Jalili et al. (2016).

An additional measure of connectedness is the clustering coefficient (Watts and Strogatz 1998), which assesses the connectivity of a node's neighbors. The local clustering coefficient (denoted as C_i) measures the extent to which the neighbors of a node are linked (Table 16.1). The average clustering coefficient, denoted as $<C>$ and defined as the average of the local clustering coefficients of all nodes in a network, captures the degree of clustering of a whole network (Table 16.1). Network transitivity (denoted as C_{net}) is yet an additional measure of the global clustering of a whole network.

16.2.10 Degree Distributions

An important parameter of a network that is used to calculate numerous other network properties is the degree distribution, p_k, which describes the probability that a randomly selected node has

Table 16.2 Comparison of common network parameters in random and scale-free networks.

		Mathematical formalism	
Parameter	**Description**	**Random networks**	**Scale-free networks**
p_k	Degree distribution	Binomial distribution: $p_k = \left(\frac{N-1}{k}\right) p^k (1-p)^{N-1-K}$ or Poisson distribution: $p_k = e^{-<k>} \frac{<k>^k}{k!}$	Power law distribution: $p_k \sim k^{-\gamma}$, where γ is the degree exponent
σ^2	Variance of the degree distribution	$\sigma^2 = <k>$ σ^2 is finite	$\sigma^2 = <k^2> - <k>^2$ σ^2 diverges as $N \to \infty$
$<d>$	Average distance connecting any two nodes	$<d> \sim ln\, N$	$<d> \sim \ln(lnN)$
k_{max}	Degree of the largest node	$k_{max} \sim \ln N$	$k_{max} = k_{min} N^{\frac{1}{\gamma-1}}$
f_c	Critical percolation threshold beyond which the removal of nodes fragments or disrupts a network	$f_c \ll 1$ as $N \to \infty$ for random node removal	$f_c \to 1$ as $N \to \infty$ for random node removal

degree k. p_k is calculated by dividing the number of nodes with degree k (N_k) by the total number of nodes (i.e. $p_k = \frac{N_k}{N}$) (Table 16.2). Of note, p_k follows different probability distributions depending on the nature of the network, e.g. regular, random, or scale free (Table 16.2).

16.2.10.1 Regular and Random Networks

In regular networks, such as in a square lattice of a crystal, all nodes have the same degree (i.e. p_k is constant). In contrast, random networks (also known as Erdős–Rényi networks) are truly random insofar as any two nodes chosen at random have an equal probability of being linked as any other two nodes (i.e. edges between N nodes are generated independently and are identically distributed) (Steuer and Lopez 2008). In this way, N nodes can be connected to generate $2^{\frac{N(N-1)}{2}}$ variations of random networks. Random networks were first constructed to model real networks. The degree distribution of random networks follows a binomial distribution that can be approximated by a (discrete) Poisson distribution if $<k>$ is substantially smaller than N (Table 16.2 and Figure 16.1b). A consequence of the binomial/Poisson degree distribution is that the overwhelming majority of nodes in random networks have comparable degrees that are similar to $<k>$ (i.e. $<k>$ serves as the internal scale). The presence of a scale in random networks implies that nodes with very small or large degrees (i.e. hubs) are not permitted. In other words, the variance of the degree distribution (denoted as ${\sigma_k}^2$) of random networks, as measured by the second moment $<k^2>$ (${\sigma_k}^2 = <k^2> - <k>^2$), is finite (Table 16.2). Indeed, the standard deviation (σ_k) of random networks follows $\sigma_k = k^{1/2}$, implying that any node would likely have a degree that falls within $<k> \pm k^{1/2}$. However, the degree distributions of real networks, e.g. PPI and metabolic networks, do not generally fit binomial/Poisson distributions (Barabási and Albert 1999).

16.2.10.2 Scale-Free Networks

The discovery that random networks poorly model real networks facilitated the development of the Barabási–Albert model describing scale-free networks (Barabási and Albert 1999). In scale-free

networks, the degree distribution follows a power law ($p_k \sim k^{-\gamma}$, Table 16.2 and Figure 16.1c). The degree exponent γ follows $2 < \gamma < 3$ for biological networks ($\gamma = 2.89$ in protein interaction networks [Barabási 2016]). It can be derived from the power law equation that $\log(p_k) \sim -\gamma \log(k)$, implying that the logarithm of the degree distribution of a scale-free network depends linearly on $\log(k)$ with the degree exponent γ being the slope of this line (Figure 16.1c). Unlike in random networks, in scale-free networks, node degrees do not scale around $<k>$ (hence "scale-free", or, put another way, γ is invariant with respect to the size of the network), and the variance of node degrees diverges (Table 16.2). A direct consequence of the power law degree distribution is that the vast majority of nodes have small degrees and only a few nodes have very large degrees (i.e. are hubs) (Figure 16.1c). The presence of hubs increases the interconnectedness of nodes substantially, manifesting as the ultra-small-world property (see Section 16.2.8). This interconnectedness is illustrated by the fact that the average distance connecting any two nodes in a scale-free network ($<d> \sim \ln(\ln N)$) grows substantially slower than in random networks ($<d> \sim \ln N$). In addition, the size of the largest hub (denoted as k_{max}) in a scale-free network depends linearly on the size of the smallest node (denoted as k_{min}) and polynomially on the number of nodes N in the network ($k_{max} = k_{min} N^{\frac{1}{\gamma-1}}$), suggesting that the smallest and largest nodes can vary in size by several orders of magnitude. By contrast, the logarithmic dependence of k_{max} on N ($k_{max} \sim \ln N$) in random networks implies that the growth of the largest node is considerably slower than in scale-free networks, suggesting that hubs are virtually forbidden.

16.2.11 Emergence of the Scale-Free Property

The scale-free property of real networks emerges as a result of two phenomena: growth and preferential attachment (Barabási and Albert 1999). These two ingredients are the fundamental basis of the Albert–Barabási model of scale-free networks. Growth refers to the notion that the size of real networks continually grows owing to the addition of one node at a time. In biological networks, for example, the addition of nodes mirrors evolutionary changes (Barabási 2016). By contrast, preferential attachment refers to the fact that newly added nodes prefer to link to the more connected nodes. In other words, the probability that a new node connects to a pre-existing node i depends on the degree k_i (e.g. a new node is twice as likely to link to a node with four neighbors than a node with two neighbors). Consistent with preferential attachment, Eisenberg and Levanon (2003) used a cross-genome comparison to show that the degree of nodal proteins correlates with the evolutionary age of that protein and that its connectivity is proportional to the growth of its degree during its evolution. Importantly, growth and preferential attachment are both required for the emergence of scale-free networks.

In addition to network growth and preferential attachment, other processes govern the structure of real networks. These processes are dynamic and include: (1) nodal fitness (i.e. the probability that a new node links to a pre-existing node i also depends on its fitness η_i); (2) nodal aging (i.e. the decrease in nodal fitness with time); (3) nodal initial attractiveness (i.e. an extension of preferential attachment, which increases the probability that new nodes link to small degree nodes); and (4) node and link deletion (i.e. removal of nodes/links due to network perturbations). For an extensive review of these processes, the reader is referred to Barabási (2016).

16.2.12 Robustness to Perturbations

A fundamental property of complex biological systems is robustness. Biological robustness facilitates the maintenance of homeostasis in the presence of external and internal perturbations,

including genetic mutations (Kitano 2004; Stelling et al. 2004; Barkai and Leibler 1997). This biological robustness is mediated by a combination of feedback control, structural stability, redundancy, modularity, and adaptation (Barkai and Leibler 1997). The mathematical underpinning of robustness is offered by percolation theory, which suggests that the removal of random nodes and/or links will have only a modest effect on the topology of a network unless the fraction of nodes/links removed exceeds a critical threshold (denoted as f_c) (Albert et al. 2000), equivalent to a system phase transition. For scale-free networks, f_c converges to one as the network size increases ($f_c \to 1$ as $N \to \infty$, Table 16.2), implying that the vast majority of the nodes need to be removed before a large scale-free network is fragmented. This extreme robustness to random node/link failure is a consequence of the fact that scale-free networks are overwhelmingly abundant in small-degree nodes. As such, a random perturbation is more likely to affect a small degree node than a hub. This robustness is less prominent in random networks as f_c remains small as $N \to \infty$ (Table 16.2), suggesting that removal of a relatively small fraction of nodes is sufficient to fragment the network. Computing the robustness of a biological network is an effective approach to simulating the impact of various perturbations on biological systems. For example, Jeong et al. (2001) used percolation theory to show that protein connectivity determines the robustness against mutations in yeast and is directly correlated with protein essentiality (i.e. hub proteins are more likely to be essential for survival than small-degree proteins, and given their infrequency in scale-free networks, the likelihood of network failure is far lower than in random networks). More recently, Liu et al. (2020) used a computational framework to determine the extent to which certain genes contribute to the overall system robustness by using a multi-layered biological network compiling a gene regulatory layer, a PPI layer, and a metabolic layer. The multilayered (multi-omic) structure of the system enhances robustness compared with single-layered systems.

A complementary consequence of the presence of hubs in biological networks is the low tolerance to deliberate attacks (i.e. the strategic removal of hubs). Because hubs interconnect many nodes of small degrees, the removal of even a small number of hubs results in the fragmentation of the network and the breakdown of its topology. In other words, f_c is remarkably low under attack. Interestingly, hubs are more likely to represent essential genes than nonessential genes (Goh et al. 2007), consistent with the notion that perturbations to essential genes (i.e. hubs) often lead to embryonic lethality.

16.2.13 Network Communities

Biological functions are governed by interactions among many interacting components (e.g. genes, proteins, and metabolites) that form modules (Hartwell et al. 1999). As such, a biological system cannot be understood by investigating a single component, or a few of its components, in isolation. Rather, appreciation of the complexity of a biological system requires the study of the interactions among its components. This behavior of complex systems is referred to as "emergent" (Funtowicz and Ravetz 1994).

Biological networks (as well as other real networks) partition into computationally decipherable subgraphs referred to as modules or communities (Figure 16.1c). There are three types of network modules in biological networks: topological, functional, and disease modules (Barabási et al. 2011; Silverman and Loscalzo 2016). Topological modules depend purely on the network topology and refer to locally dense connected subgraphs or subnetworks in which nodes are more likely to interact with each other than with nodes outside of that module (Figure 16.1c). Identification of topological modules relies on the maximal modularity hypothesis, which states that the network partition with the maximum modularity (i.e. a quantitative measure of the strength of a partition)

offers the best community structure (Barabási 2016). By contrast, functional modules are governed by a subset of interconnected nodes that share a biological function, and disease modules are comprised of nodes whose perturbations are linked to common pathophenotypes.

Network medicine posits four hypotheses that link topological modules to functional and disease modules. First, the *local hypothesis* suggests that proteins involved in the same disease are more likely to interact with each other than with other proteins in the interactome that are not involved in the disease. Second, the *disease module hypothesis* posits that proteins involved in the same disease tend to form subnetworks or network modules. Third, the *functional coherence hypothesis* suggests that proteins in a disease module tend to be involved in the same biological processes. Last, the *shared components hypothesis* suggests that related diseases are localized in the same interactome neighborhood from which other diseases are clearly separated. Together, these four hypotheses imply that topological, functional, and disease modules overlap. A corollary of this overlap is that functional modules are mirrored to an extent by topological modules, the study of which offers insight into disease modules and, therefore, disease mechanism(s). Evidence supporting these fundamental hypotheses is discussed in Sections 16.7 and 16.8.

16.2.14 Statistical Tools in Network Analysis

Given that biological networks do not follow Gaussian degree distributions, statistical tests that assume data normality cannot be used when assessing the significance of network-based findings. Instead, null network models can be used for statistical comparisons. These models can be obtained by algorithms that randomize the network topology to yield a random network (see Section 16.2.10.1). Complete or full randomization of the network topology removes the scale-free property of the network. However, statistical analysis of network parameters that depend on the degree distribution requires the preservation of node degrees. Degree-preserving randomization can be performed, e.g. by a switching algorithm (Maslov and Sneppen 2002) or a matching algorithm (Menche and Barabási 2016). Other randomization approaches can preserve different topological properties, e.g. the clustering coefficients. Generally, topological randomization is used to determine whether a particular network-based finding depends on the overall network topology. Alternatively, one can assess statistically whether a given network-based characteristic depends on a particular nodal attribute by randomizing that attribute. This goal can be achieved by degree-preserving or random label permutation, which randomly distributes the desired nodal attribute on the network, with or without preserving the node degrees, respectively. The reader is referred to Albert and Barabási (2002) for a more extensive review of statistical tools for network analysis.

16.2.15 Biological Networks Do Not Obey Pure Power Law Distributions

The scale-free property applies to a wide range of real networks from various disciplines, e.g. from biological networks depicting physical PPIs to social networks depicting friendships. This property of scale-free networks is referred to as "universality" (Barabási 2016). However, while early work suggested that most biological networks are scale-free, more recent observations suggest that they fall into a variety of non-Poissonian, long-tailed distributions, including gamma and exponential distributions. Deviations from true power law distributions tend to occur at both ends of the degree distribution (i.e. at very small and large k), manifesting as phenomena referred to as low degree saturation and high degree cutoff (Barabási 2016). To this end, it is important

to remember that biological systems are not modeled perfectly by mathematical formulae that describe true scale-free networks. A better understanding of the complexity of biological systems will require more precise modeling of these systems (e.g. by virtue of increased content and resolution of multi-omic data).

16.3 Progress Toward Reference Organismal Interactomes

The usefulness of PPI networks in modeling biological complexity is proportional to the quality and richness of the network model. Ultimately, the completeness of a PPI network (i.e. the extent to which it covers all true protein interactions within cells), as well as its quality (i.e. the number of false positive interactions included), determine its effectiveness with regard to the study of biology and disease. There exist several means to map and model PPI, with the aim of constructing new PPI networks for different species or expanding on pre-existing ones. Given the vastness of the human proteome [~130,000 ± 30,000 binary interactions (Venkatesan et al. 2009) among ~200 million possible combinations (Rolland et al. 2014)], high-throughput mapping of interactome networks at the proteome scale, rather than small-scale interaction mapping experiments, is necessary. There are three distinct approaches that are routinely used to model proteome-scale PPI networks: literature curation and text mining; computational/*in silico* predictions based on orthogonal data; and high-throughput, systematic, and unbiased experimental proteome-scale mapping (Figure 16.2). Notably, these strategies are fundamentally different not only in their approach but also in the information they generate, the interpretations that one can make from the generated maps, and the limitations they exhibit. The use of protein interactomes by an investigator in the study of biological and disease processes necessitates the investigator's understanding of, and appreciation for, these factors. In addition, these mapping approaches elucidate distinct parts of the interactome, and protein-interaction databases should report unambiguously which approach(es) was(/were) used to generate the interaction information, ultimately allowing investigators to incorporate inclusion and exclusion criteria depending on the desired investigation. Furthermore, an interaction identified by any of the three approaches outlined above is insufficient to guarantee a true positive interaction that occurs *in vivo* under native conditions. Thus, estimating the interaction error rates of mapping assays is paramount for benchmarking systematically publicly available interactome datasets (Hart et al. 2006).

16.3.1 Literature Curation

There exists an enormous amount of information regarding protein interactions within the scientific literature as well as in open-source databases; curation of this information by text mining can be used to map protein interaction networks (Roberts 2006). However, networks generated by this approach suffer from various limitations. Importantly, these shortcomings include inspection bias because literature-curated protein interactions are often mined from small-scale mapping experiments of already well-studied proteins. As such, information regarding interactions between poorly studied proteins can be lost, inevitably limiting the completeness of such networks. In addition, the quality of a curated interactome depends on the quality of the published data from which it was curated (Cusick et al. 2009). Nevertheless, because data curation utilizes already available information, it remains a common approach for the generation of protein interactomes (Vidal et al. 2011).

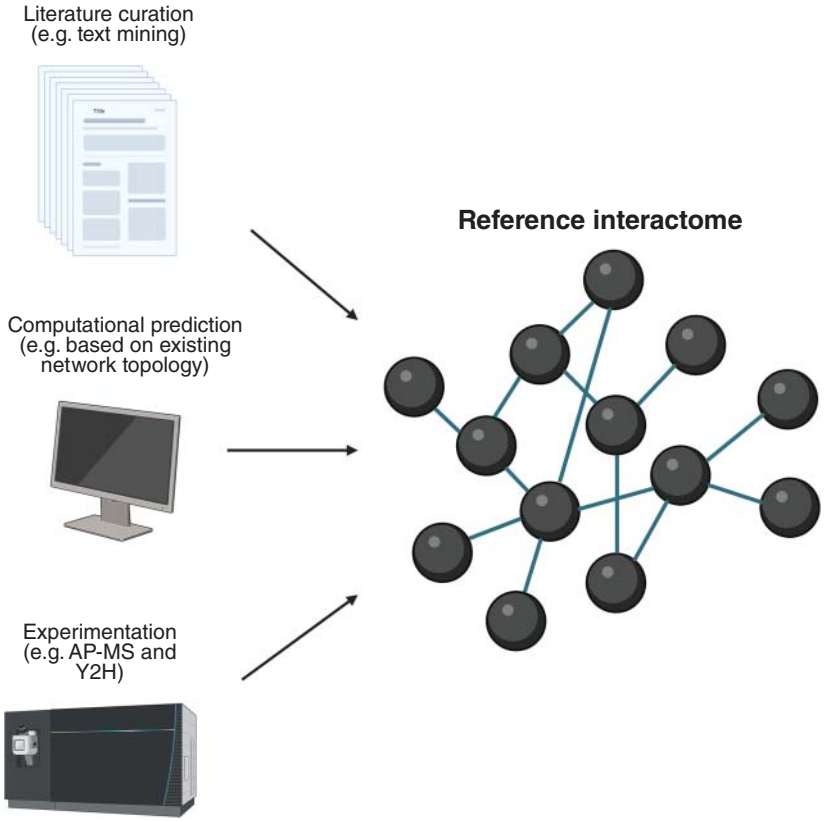

Figure 16.2 Protein interaction mapping approaches. The literature is replete with small-scale experiments aimed at revealing the interaction partners of one (or a few) proteins of interest. This overwhelmingly large body of information can be curated to construct interactomes (see Section 16.3.1). Protein interactions can also be predicted computationally based on orthogonal data (see Section 16.3.2). For example, algorithms predict putative interaction candidates based on protein structure and/or co-expression data. Alternatively, network-based prediction tools rank interaction candidates based on known network topology. In addition, high-throughput, strategic, and unbiased mapping of protein interactions at proteome scale involves identification of the constituents of protein complexes (i.e. co-complex associations) and/or screening for binary physical interactions; the former can be achieved by affinity purification mass spectrometry (AP-MS) and the latter by yeast two-hybrid (Y2H) technology (see Section 16.3.3). *Source:* Created with BioRender.com.

16.3.2 Computational Prediction Tools

Computational prediction tools utilize the evolving body of data pertaining to protein structural information, coupled with gene co-expression correlations and/or phenotypic profiling (Vidal 2001). Structural information of proteins includes amino acid sequences as well as three-dimensional structures from the Protein Data Bank (Berman et al. 2000), as deciphered, e.g. by orthogonal experimental techniques (e.g. X-ray crystallography and mass spectrometry) or accurate computational approaches (e.g. AlphaFold [Jumper et al. 2021)]. Another approach for predicting protein interactomes computationally utilizes information pertaining to chromosome proximity (i.e. the likelihood that two proteins interact physically is proportional to the chromosomal proximity of the corresponding genes) (reviewed in Rao et al. [2014]). Additionally, network-based link prediction algorithms utilize pre-existing protein network topologies to

connect previously unlinked proteins based on their biological and/or network similarity. Such link prediction methods are premised on the triadic closure principle originating from social network science, i.e. the observation that the probability of two individuals knowing each other depends on the number of common friends shared between them. Kovács et al. (2019) developed a superior network-based algorithm to predict previously unknown protein interactions, grounded in the finding that proteins interact not based on their mutual similarity but, rather, on the similarity of one of them to the other's pre-existing binding partner(s). Nonetheless, the quality of protein interaction networks generated by computational prediction strategies is limited to the quality of pre-existing knowledge of biological systems or networks. In addition, computationally predicted protein interactions should be verified experimentally prior to their incorporation as edges in protein interactomes.

16.3.3 High-Throughput, Proteome-Scale Experimental Mapping

There exist two key approaches for high-throughput, strategic, and unbiased mapping of protein interactions that are feasible at the proteome scale: identification of the constituents of protein complexes (i.e. co-complex associations) and screening for binary physical interactions.

16.3.3.1 Affinity Purification-Mass Spectrometry and Yeast Two-Hybrid Systems

The most widely utilized strategy for the study of co-complex associations is affinity purification mass spectrometry (AP-MS) (Figure 16.3a). This approach utilizes protein complex immunoprecipitation coupled with mass spectrometry to identify the proteins associated with the "bait" protein(s). A limitation of AP-MS is that information elucidated by this approach often represents stable interactions connecting highly abundant proteins, overlooking transient interactions between low abundant proteins that are easily lost during cell lysis and that are common in signaling pathways. AP-MS also suffers from the fact that direct and indirect protein interactions are indistinguishable from each other (i.e. proteins in a complex need not interact directly with all other proteins in that complex). These limitations notwithstanding, numerous multi-institutional efforts, such as the BioPlex project (Huttlin et al. 2015), have utilized AP-MS to create proteome scale, cell-line-specific PPI networks (e.g. BioPlex mapped 23,744 PPIs among 7,668 human proteins in HEK293T cells). By contrast, the most common approach for studying highly reproducible binary biophysical protein interactions at a proteome scale stems from the original yeast two-hybrid (Y2H) technology (Chien et al. 1991) (Figure 16.3b). In Y2H, physical interaction between bait and prey proteins within the yeast cell nucleus reconstitutes a TF that activates the expression of a reporter gene. In this way, the expression of a reporter gene (generally) indicates a biophysical interaction between the bait and prey proteins. Although Y2H may also detect indirect protein interactions bridged by a third protein, this approach readily detects transient interactions irrespective of protein abundance.

In 2005, Rual et al. (2005) and Stelzl et al. (2005) used stringent, high-throughput Y2H systems to generate the first versions of the proteome-scale map of human binary PPI. Rual et al. (2005) screened for binary interactions between the products of ~8,100 open reading frames, detecting ~2,800 interactions among which >300 were (at the time) novel. In contrast, Stelzl et al. (2005) detected interaction pairs among 4,456 baits and 5,637 prey, identifying 3,186 interactions among 1,705 proteins. Despite being far from comprehensive and of insufficient quality, these initial human interactomes provided network-based explanations for some genotype–phenotype relationships. Venkatesan et al. (2009) devised an empirical framework to calculate the completeness, sensitivity, and precision of binary protein interaction maps. Through quality assurance,

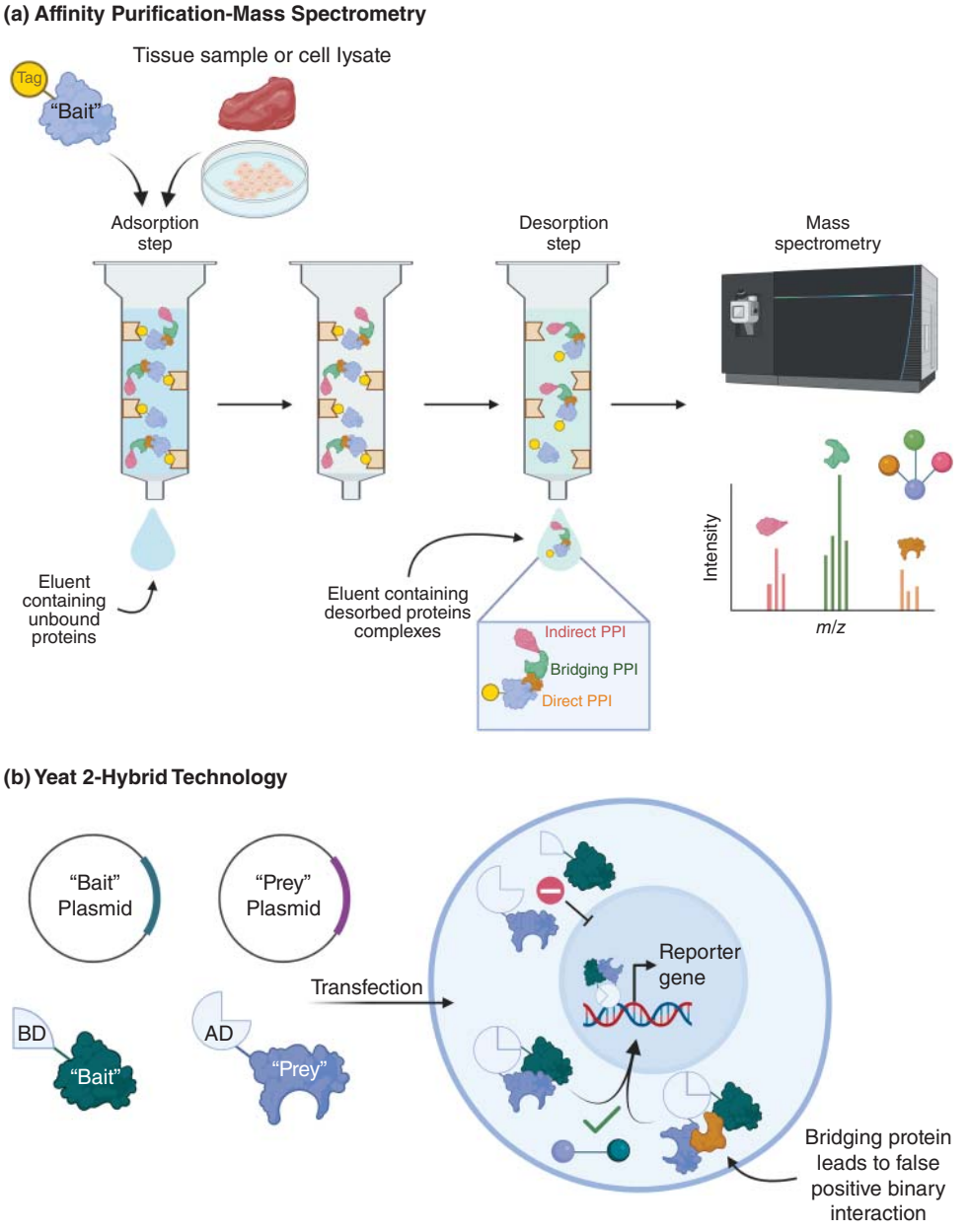

Figure 16.3 Strategies for proteome-scale experimental protein interaction mapping. (a) In affinity purification mass spectrometry (AP-MS), tagged "bait" proteins (blue protein with yellow tag) and protein extracts from tissue or cell lysates flow through a column/cartridge that contains a sorbent known to bind the tag specifically. Protein complexes that are formed around the tagged "bait" adsorb to the sorbent, subsequently desorbed by a different solvent, and, last, analyzed by mass spectrometry. Using AP-MS, proteins (pink) that are bound indirectly to the "bait" *via* (a) bridging protein(s) (green) are, nevertheless, considered as direct binding partners (as illustrated by the network example) (b) In yeast 2-hybrid (Y2H), yeast cells are transfected with plasmids encoding a TF BD-tagged "bait" protein and TF activating domain (AD)-tagged "prey" protein. Interaction between the "bait" and "prey" proteins reconstitutes a TF that activates the expression of a reporter gene. False negative binary interactions can result from the binding of the "bait" and "prey" proteins *via* (a) bridging protein(s) (yellow). *Source:* Created with BioRender.com.

this empirical framework provides a means to benchmark systematically the coverage, accuracy, and quality of interaction maps generated by Y2H studies, enabling large numbers of reproducible, binary interactions to be mapped. Using this framework, Rolland et al. (2014) constructed an updated human interactome data set comprising 14,000 high-quality binary interactions. In 2020, the coverage of human binary interaction data sets exploded with the publication of the human reference interactome (HuRI), encompassing approximately 53,000 binary, physical interactions between the gene products of open reading frames curated from ~90% of the protein-coding genome (Luck et al. 2020). Future advances in Y2H technology, quality assurance frameworks, and computational power will enable the expansion of the current HuRI.

16.3.3.2 Cross-linking Mass Spectrometry and Proximity Labeling

Other interactome mapping strategies employing mass spectrometry have been gaining popularity over the last few years. For example, cross-linking mass spectrometry (XL-MS) utilizes chemical cross-linkers (e.g. commercially available disuccinimidyl sulfoxide [Kao et al. 2011]) to connect two lysine residues that are in close proximity to each other in their native environment. Cross-linkers are typically composed of two primary amine (i.e. lysine) reactive groups separated by a short spacer arm. Because the spacer arm of the cross-linker is short in length (~10–30 Å), the formation of a cross-link between lysine residues of different proteins implies a physical interaction, the binding site of which can be imputed. Cross-linking stabilizes protein interactions in complex biological samples (e.g. intact cells and tissues), which is followed by conventional proteomic workflows (e.g. reduction, alkylation, and digestion) and subsequent analysis of cross-linked peptides by MS. More recently, efforts to incorporate isobaric labeling approaches [e.g. using commercialized tandem mass tags, TMT (Ruwolt et al. 2022)], or the in-house synthesized biotinylated peptidic cross-linker biotin aspartate proline-*N*-hydroxyphtalamide [BDP-NHP (Chavez et al. 2020)] for quantitative XL-MS enables the generation of weighted protein interaction networks. An advantage of quantitative XL-MS is the study of differentially abundant PPIs in biological systems, akin to differential analysis of protein abundance by conventional proteomics. For example, Caudal et al. (2022) used BDP-NHP to cross-link mitochondrial proteins isolated from healthy and failing mouse hearts following transverse aortic constriction, thereby elucidating 588 statistically significant cross-linked peptide interactions with implications for mitochondrial remodeling in failing hearts. In addition, by using BDP-NHP, Chavez et al. (2018) studied protein interactions in mouse hearts *ex vivo* and developed protein interaction models for sarcomere and respirasome protein complexes. Importantly, there exist reproducible, publicly available protocols for mapping protein interactomes in cells and tissues by XL-MS (Klykov et al. 2018; Chavez et al. 2019). XL-MS data can also be used to verify computationally predicted protein interactions (Burke et al. 2023).

An alternative MS-based strategy for interactome mapping is proximity labeling (Qin et al. 2021). In this approach, proteins of interest are tagged to specific enzymes (e.g. peroxidases or biotin ligases), the presence of which generates a short-lived, diffusible reactive species (e.g. radicals) that can react with neighboring biomolecules (e.g. proteins). Tagged proteins are then identified and quantified by mass spectrometry. The reader is referred to the review by Richards et al. (2021) for a more comprehensive discussion of MS-based protein interactome mapping techniques.

16.3.3.3 Protein–Metabolite Interaction Networks

In addition to PPI interactomes, recent efforts have been made to map non-covalent protein–ligand (e.g. drug or metabolite) interaction networks on a proteome scale. For example, Piazza et al. (2018) developed and utilized a novel chemoproteomic workflow to elucidate 1,678 metabolite–protein

interactions and 7,435 putative binding sites in *Escherichia coli*. Similarly, Luzarowski et al. (2021) applied a biochemical approach named Patient-Reported Outcomes Measurement Information System (PROMIS) to interrogate the protein–metabolite interaction network in *Saccharomyces cerevisiae*, generating a publicly available repository comprising 74 small molecules and 3,982 proteins, as well as 225 experimentally validated binding sites. In brief, MS-based efforts to map protein–ligand interactions are often based on the principle that ligand binding can alter the thermodynamic stability of a protein target, as assessed by its proteolytic susceptibility. In principle, a ligand interaction (allosteric or otherwise) can alter the tertiary structure of a target protein, thereby leading to its (de)stabilization and, consequently, a shift in its melting curve when subjected to a denaturing stress (e.g. heat, organic solvent, or digestive enzyme). These approaches include protein- or peptide-centric analyses, such as the cellular thermal shift assay (CETSA [Molina et al. 2013]), thermal proteome profiling (TPP [Savitski et al. 2014]), drug affinity responsive target stability (DARTS [Lomenick et al. 2009]), and limited proteolysis-MS (LiPMS [Schopper et al. 2017]). While sufficient to map relatively strong interactions between proteins and drugs, these methods arguably do not offer the sensitivity required to map weak protein–ligand interactions. This is an important limitation because naturally occurring metabolites interact non-covalently with proteins with often substantially weaker binding affinities than pharmacological agents, making it more challenging to map protein–metabolite than protein–drug interactions experimentally. Recent developments have modified the aforementioned methods to increase their sensitivity and throughput, such as the peptide-centric local stability assay (PELSA [Li et al. 2025]), a more sensitive, modified version of LiPMS, which uses larger amounts of trypsin to ensure digestion of lower energy state protein segments. Li et al. (2025) used PELSA to validate known and reveal novel protein targets of the tricarboxylic acid metabolite, α-ketoglutarate, and its reduced equivalent, D-2-hydroxyglutarate. The potential of these methods notwithstanding, it is important to note that such approaches often cannot discriminate between first- and second-order binding to target proteins. Despite recent advancements, progress toward a reference human proteome–metabolite interactome remains in its infancy, particularly owing to poor coverage of weaker interactions involving low-abundant proteins and/or metabolites.

16.4 Complex Diseases Manifest as Nodal and Edgetic Perturbations

The utility of network medicine lies partly in the premise that phenotyping variations can be modeled by network perturbations. As such, disease processes can be investigated by interrogating the impact of a biological perturbation on the network topology (Figure 16.4). For example, loss-of-function mutations may result in the inability of the corresponding gene product to bind its original partner(s), manifesting as the removal of its edge(s). Likewise, gain-of-function mutations may enable the gene product to bind new partners, resulting in the addition of neighboring nodes and the increase in its degree (Cusick et al. 2016). Notably, different types of genetic mutations manifest as distinct network perturbations. Nonsense mutations and mutations affecting splicing often result in the absence of a gene product, and, thus, the removal of the corresponding node. Node removal can also result from complete pharmacological inhibition or mutations that culminate in complete protein dysfunction, such as those impacting deleteriously the interaction domain(s) of proteins. By contrast, "edgetic" perturbations refer to biological insults (as manifest by, e.g. allelic heterogeneity) that perturb a protein's interaction with some but not all its partners, manifesting as the removal of a single or few of its neighbors (Cusick et al. 2016). Edgetic perturbations may

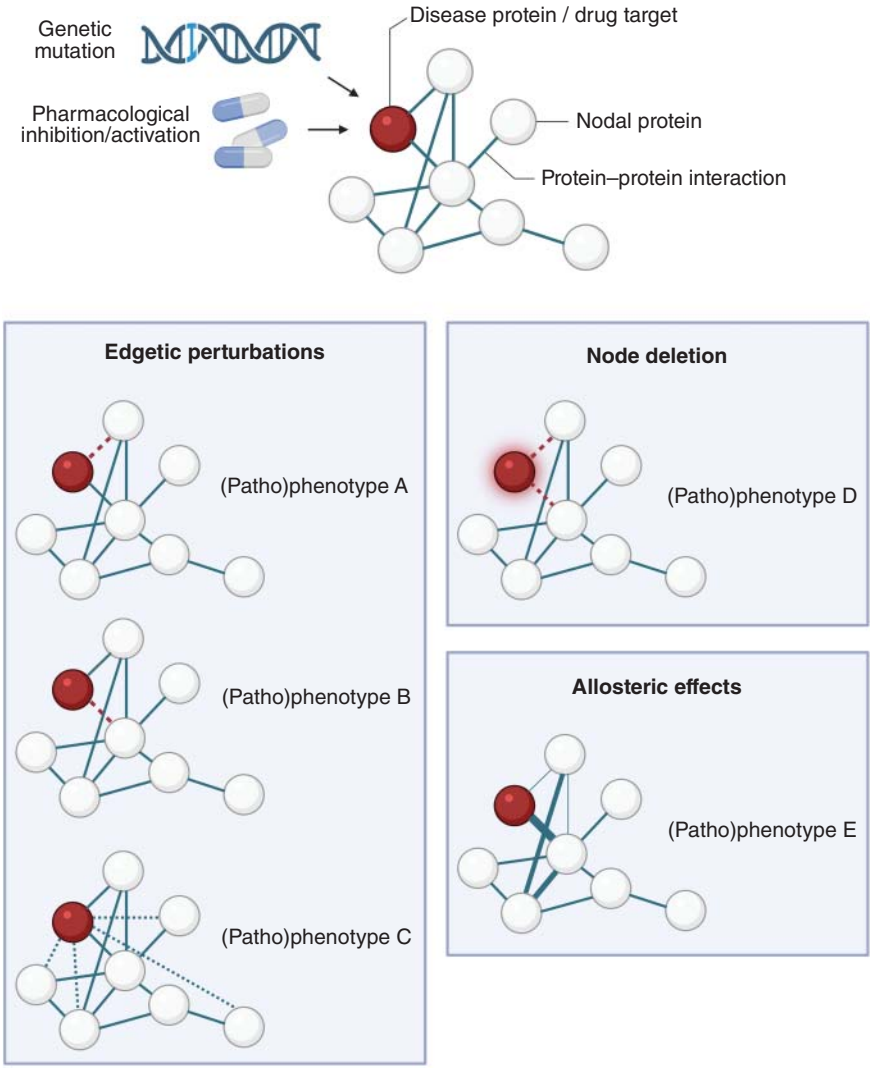

Figure 16.4 Network-based modeling of pathophenotypic perturbations and pharmacotherapy. Genetic mutations and pharmacotherapy manifest as edgetic perturbations and node deletions. Edgetic perturbations involve the removal of some of the edges linked to a disease/target protein (red). These perturbations can result from genetic mutations that affect deleteriously a specific interaction site of the disease protein, thereby eliminating that interaction with the given neighbor only (dashed red edges) [(Patho)phenotypes A and B]. Alternatively, certain mutations and pharmacotherapies can modify a disease protein to enable its interaction with (combinations of) new protein partners (dashed blue edges) [(Patho)phenotype C]. By contrast, node deletion refers to the removal of a node and all of its connections (glowing red node and dashed red edges) [(Patho)phenotype D]. Last, allosteric effects caused by genetic mutations or drug–target interactions can modify the affinities of certain interactions, manifesting as differential edge weights (different blue edge thicknesses) [(Patho)phenotype E]. Importantly, the aforementioned perturbations can cause extended effects on neighbors of neighbors, etc. The different combinations of network perturbations result in distinct (patho)phenotypes. *Source:* Created with BioRender.com.

result from small indels or missense mutations, as well as partial pharmacological inhibition. Importantly, node removal and edgetic perturbations confer distinct functional consequences (Zhong et al. 2009), because perturbation to different interfaces of a protein (*via* genetic mutation or pharmacological inhibition) can result in distinct (patho)phenotypic variations by means of alteration to distinct protein interactions. Consequently, distinguishing between nodal and edgetic biological insults enables a more nuanced understanding of the disease. A further dimension of complexity is introduced in weighted interactomes, wherein perturbations may alter the strength of interaction(s) leading to altered edge weights (which can be approximated, e.g. by the strength of association between two proteins as manifest by the K_d, their absolute concentrations, and their individual degree). Node removal can similarly be replaced with nodes of different weights (concentrations) as another continuous variable in the system, and differential expression of a protein can be represented correspondingly by altered nodal weight.

16.5 Expanding the Interactome to Incorporate Complex Biological Phenomena

As discussed in Section 16.4, protein interaction networks can be used to model biological and disease processes *via* analysis of the consequences of biological perturbations to network topologies. However, there are additional levels of biological complexity that are seldom addressed in existing protein interactome datasets. Addressing this biological complexity is crucial for a deeper understanding of disease.

16.5.1 Allostery, Alternative Splicing, and Interaction Motifs

Further complexity is introduced to existing interactome datasets by addressing the problem of allostery (i.e. how the binding of one partner influences the binding of others, the average number of which is ~11–12 in the PPI) and the implications in its modulation of edge weights for any given interaction. (Patho)phenotypic variations can be further explained by alternative protein isoforms resulting from alternative splicing; incorporation of this complexity into protein interaction networks, albeit uncommon, will inevitably augment the resolution, and consequently, the relevance of existing interactomes. In addition, interactomes often represent proteins as homogeneous nodes, and information pertaining to the domain responsible for interaction (and its amino acid sequence) with any given partner is often missing. XL-MS offers an approach for elucidating binding domains (BDs) on a proteome scale (see Section 16.3.3.2), as does fragment-based Y2H approaches (Boxem et al. 2008). Castel et al. (2021) developed a novel approach termed protein domain mapping using yeast 2 hybrid-next generation sequencing (DoMY-Seq) for mapping PPI motifs using a combination of Y2H and next-generation sequencing techniques.

16.5.2 Posttranslational Modifications

Posttranslational modifications (PTMs) are (bio)chemical alterations to amino acid side chains of proteins that occur after their biosynthesis. There are more than 400 PTMs affecting a plethora of protein functions (Ramazi and Zahiri 2021), thereby acting as a key mechanism to increase proteome diversity without increasing gene count. PTMs can be deterministic (e.g. enzyme-dependent phosphorylation) or stochastic (e.g. oxidation of the thiol moiety of cysteines

by reactive oxygen species), and their role in the pathogenesis of CVD is well documented in the literature (Liddy et al. 2013; Yan et al. 2019; Gajjala et al. 2015). These modifications can augment or decrease the activity of proteins. Furthermore, PTMs can determine the stability of proteins and, therefore, their concentration, ultimately influencing not only the particular protein but also its interaction partners. Since PTMs can generate or eliminate protein interaction sites (by means of, e.g. steric hindrance), these modifications can result in edgetic perturbations, influencing the topology of the corresponding network module and beyond (Lippens et al. 2016). Moreover, PTMs may alter the spatial distribution of proteins, thereby indirectly altering the likelihood of certain protein interactions (Wang et al. 2022). For example, kinase-mediated phosphorylation of TFs can result in their translocation to the nucleus, thereby decreasing or increasing the probability of their binding to cytosolic or nuclear binding partners, respectively. In addition, PTMs can have allosteric effects on certain proteins, altering the binding affinity of any given protein partner. Irreversible PTMs, including eventual conversion of the thiol moiety of cysteines to sulfinic and sulfonic acids during states of oxidative stress, can similarly alter protein structure and, consequently, network perturbation(s) analogous to node removal (in the case of complete protein dysfunction) or edgetic perturbation (in the case of partial inhibition of activity). Interestingly, the susceptibility of proteins to different types of PTMs seems to correlate with their positioning in the interactome; in an analysis of twelve main PTM types across nine species, proteins susceptible to PTMs were found to be generally involved in more interactions and to be positioned more centrally in the interactome than non-PTM proteins, and phosphorylated proteins were found to be located centrally, whereas glycosylated proteins were preferentially located more peripherally (Duan and Walther 2015). Notwithstanding the complexity added to interactomes by means of PTMs, most interactome datasets do not incorporate information pertaining to PTMs (although some do include phosphorylation), thereby overlooking their implications for the spatiotemporal dimension of protein interactions.

MS-based proteomics is arguably the most common experimental approach for PTM analysis (Baker et al. 2012). This approach utilizes common proteomic workflows coupled with enrichment steps aimed at concentrating proteins/peptides with the desired PTM while removing unmodified ones. For example, most common enrichment protocols for phosphopeptides involve affinity purification using a positively charged stationary phase to adsorb negatively charged phosphate moieties or immunoprecipitation by phospho-specific antibodies [reviewed in Fíla and Honys (2012) and Dunn et al. (2010)]. Great efforts have been made to map systematically the phosphoproteome, as evidenced by the development of publicly available repositories like PhosphoSitePlus (Hornbeck et al. 2012). Drummond et al. (2020) used quantitative proteomics and AP-MS to map the phosphorylated tau interactome in the human Alzheimer's disease brain. However, incorporating the entire phosphoproteome and other PTM types (as opposed to one, or a few, proteins of interest) into the interactome remains a challenge. Nonetheless, several tools have been developed for this purpose, including the Cytoscape app PTMOracle and its extended features OraclePainter, OracleTools, and OracleResults for systematically visualizing and analyzing PTMs within interactomes (Tay et al. 2017; Tay et al. 2019). Overall, incorporating information pertaining to PTM into existing interactome datasets will inevitably improve the resolution of such networks, ultimately offering more precise models of biology and disease. In this sense, one can consider the distribution of each type of PTM throughout the interactome as a unique instantiation of that interactome with potentially unique functional consequences. Compiling these different instantiations into a (statistical) ensemble would provide highly detailed network-based information that may correlate with unique phenotypes.

16.6 Context-Specific Interactomes Resolve Complex Biological Heterogeneity

Reference organismal interactomes commonly disregard complex (intra- and inter-) cellular heterogeneity, implying the assumption that all biological systems display a shared, uniform set of protein interactions irrespective of biological context. The simplification of molecular detail by such interactomes enables one to model phenotypic variation at the scale of whole cells (Vidal et al. 2011); however, this "one-size-fits-all" model of protein interaction maps, arguably, overlooks the impact of biological context on cellular phenotype.

16.6.1 Spatial Proteomics

Cells harboring identical genomes can exhibit extensive molecular and phenotypic differences (as manifest by, e.g. differentially expressed proteins and metabolites), and the collective behavior of a population of "seemingly identical" cells need not represent that of any individual cell (Altschuler and Wu 2010). Heterogeneity can be reduced by sorting cell populations based on cell type, and incorporating this distinction into protein interaction networks, albeit computationally challenging, improves their resolution and consequently their ability to model complex biological systems. Cell-type-specific interactomes can be constructed by integrating a reference interactome with single-cell gene-expression profiles, as done by the computational frameworks SCPPIN (Klimm et al. 2020), SCINET (Mohammadi et al. 2019), and scHumanNet (Cha et al. 2023). However, stochastic gene expression (or "noise"), although essential for many biological processes (Raj and van Oudenaarden 2008; Elowitz et al. 2002), complicates interpretations made from single-cell transcriptomic data. By contrast, advances in miniaturized sample processing as well as nanoflow chromatographic separations and ultrasensitive mass spectrometry have enabled the development of single-cell proteome profiling, a relatively novel yet increasingly comprehensive and quantitative technique used to quantify >1,000 proteins from cell culture and, more recently, tissue samples (Kelly 2020). For example, recent work has developed a truly in-depth, single-cell-derived proteomics pipeline that combines fluorescence-activated cell sorting and trapped ion mobility MS to generate single-cell proteome information in cultured cells (Brunner et al. 2022).

Cellular heterogeneity can be explained further by differences in the spatial distributions of cells within tissues. Furthermore, cellular phenotypes are influenced largely by their microenvironment (i.e. a combination of extracellular matrix, other [heterotypic] cells, and interstitial fluid through various mechanisms [physical, electrical, biomechanical, and/or biochemical]) (Warrick et al. 2008). For example, cues derived from the microenvironment impact the function of cardiomyocytes during myocardial repair (Wanjare and Huang 2017). Moreover, the spatial distribution of proteins across different organs has direct links to the interactome topology. Kitsak et al. (2016) showed computationally that genes/proteins expressed in a specific tissue tend to be localized in the same interactome neighborhood, whereas genes expressed in distinct tissues segregate in different network neighborhoods. The same study provides evidence showing that disease manifestation in selected tissues correlates with the extent to which the complete set of genes comprising a disease module (see Section 16.2.13) is expressed in those tissues. Thus, the greater the number of disease genes that are expressed in a tissue, the greater the likelihood of that particular disease being manifest (in some clinically ascertainable way) in that tissue. Notwithstanding this clear influence of the spatial distribution of proteins on phenotype, reference interactomes seldom address this spatial complexity and its effects on cellular variations.

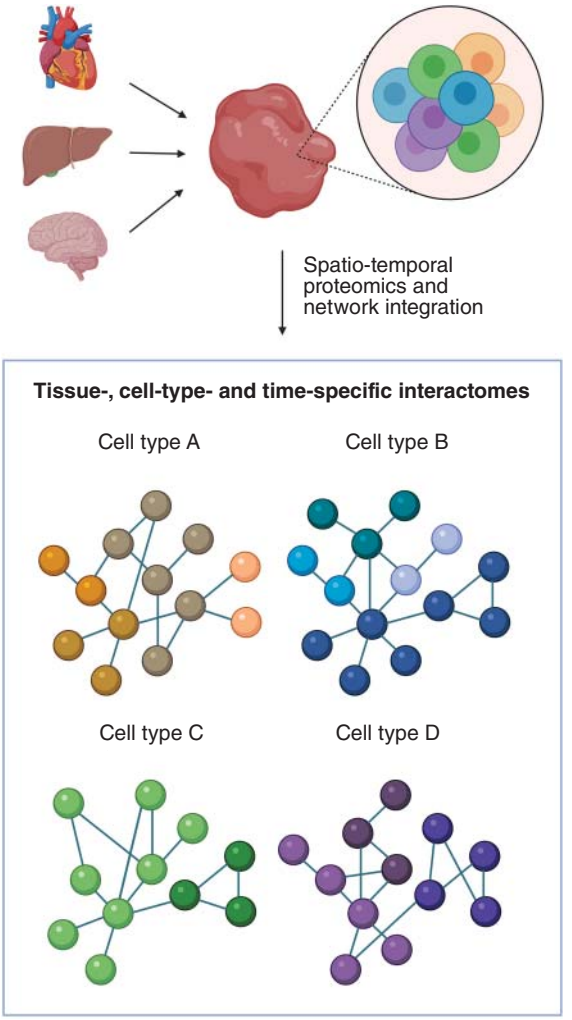

Figure 16.5 Context-specific interactomes to resolve complex biological heterogeneity. Biological samples obtained for biomedical research or diagnostic purposes harbor complex heterogeneity in cellular composition and underlying molecular phenotype. Bulk omic analyses average this heterogeneity across the tissue sample, thereby removing nuanced complexity that may infer important phenotypic insight. By contrast, advances in mass spectrometry and computational power enable the resolution of this (intra- and inter-cellular) spatial and temporal complexity. In this way, one can generate from a single sample several cell-type-specific interactomes, with the temporal dimension depicted by the shades of the node. *Source:* Created with BioRender.com.

Constructing spatially resolved protein interaction maps (Figure 16.5) could be achieved by integrating existing interactomes with data generated by spatial proteomics, an emerging strategy for mapping proteome heterogeneity of biological samples [reviewed in Mund et al. (2022a)]. For example, Mund et al. (2022b) describe a novel technology, deep visual proteomics (DVP), that integrates high-resolution imaging and artificial intelligence (AI)-guided image analysis for phenotyping with laser microdissection and ultra-high-sensitive MS, aimed at analyzing proteomes of cultured cells within their native, subcellular context. An extension of DVP, single cell DVP (scDVP), was recently developed to enable in-depth, high-throughput, spatially resolved single-cell proteomic analysis of not only cell culture but also tissue samples (Rosenberger et al. 2023). An alternative framework called Expansion Proteomics (ProteomEx) utilizes tissue expansion (physical magnification of samples by embedding tissue or cultured cells in a swellable hydrogel) with MS-based proteomics to enable quantitative profiling of the proteome in mammalian tissues in a spatial-specific manner (Li et al. 2022). In addition, organelle-specific spatial proteomic data can be generated by tissue subcellular fractionation followed by conventional MS-based proteomics (Cox and Emili 2006; Mulvey et al. 2017). Notably, however,

spatial proteomic profiling is biased toward certain subcellular localizations since common protocols extract proteins from different localities with different efficiencies (e.g. hydrophilic, cytosolic proteins are often more readily extracted and with greater recoveries than lipophilic, membrane-bound proteins). This bias implies that different sample preparation protocols favor certain parts of the interactome. If this bias is estimated and addressed appropriately [by means of, e.g. a universal sample preparation workflow as introduced in Wiśniewski et al. (2009)], integrating in-depth, high-throughput cell type and (intra- and/or inter-cellular) spatially-resolved proteomic information into existing reference interactomes, although far from common practice, will inevitably improve the relevance of these network models to true biological processes.

16.6.2 Temporal Proteomics

Time-dependent proteome remodeling is an intrinsic part of the cell cycle. Accordingly, the temporal regulation of protein abundance implies that the set of protein interactions that occur within cells is dynamic over time. For example, using centrifugal elutriation combined with MS-based proteomics, Ly et al. (2014) identified extensive variations in protein abundance, isoform expression, and phosphorylation at different cell cycle stages in minimally perturbed human myeloid leukemia cells. Extensive variation in proteome expression was also observed in human myeloid leukemia cells arrested at different phases of the cell cycle (Ly et al. 2015). The same group developed and implemented a fluorescent-activated cell sorting and MS-based approach (PRIMMUS), which enables an unbiased proteome-wide and time-dependent analysis of protein expression, to show extensive proteome remodeling between prophase, prometaphase, and anaphase (Ly et al. 2017).

Similar to changes in protein abundance during different stages of the cell cycle, proteome profiles of diseased whole tissue samples ("bulk" proteomes) often differ during different stages of disease progression as a consequence of distinct molecular signatures. For example, myocardial repair and remodeling following a myocardial infarction can be (broadly) divided temporally into early stimulation of inflammatory signaling to clear dead cells from the infarcted area, followed by timely repression of inflammatory mediators to protect the heart from overt inflammatory injury (Frangogiannis 2014). Similarly, atherosclerotic plaque formation evolves over time, initiating endothelial dysfunction and subsequent smooth muscle cell emigration from the media to the intima, followed by the formation of macrophage-derived "foam cells" (Rafieian-Kopaei et al. 2014). Consequently, it is obvious that the proteome profile of whole tissue samples (averaged across the whole sample) will differ across disease stages. As such, integrating a time-dependent continuous dimension into existing, static reference interactomes (Figure 16.5) will increase the subtlety and nuance of these network models, as well as their predictive power ideally (Przytycka et al. 2010). Such efforts have been made by, e.g. Bisson et al. (2011) using affinity purification selected reaction monitoring (AP-SRM) to identify and quantify 90 proteins dynamically interacting with growth factor receptor bound protein 2 (GRB2) in HEK293T cells in a time-dependent manner. Similarly, Collins et al. (2013) used affinity purification coupled with sequential window acquisition of all theoretical spectra (AP-SWATH) MS to study the dynamics of the 14-3-3β scaffold protein interactome after stimulation of the insulin- phosphatidylinositol 3-kinase (PI3K)-protein kinase B (AKT) pathway, consistently and reproducibly quantifying 1,967 interaction partners across several time points. Using proximity labeling with ascorbic acid peroxidase followed by MS (see Section 16.3.3.2), Lobingier et al. (2017) developed an experimental framework to assess simultaneously both the spatial and temporal dimensions of protein interactions in living cells and applied this approach to study the binding

partners of G-protein-coupled receptors as they dynamically signal and traffic in response to ligand-induced activation. Nevertheless, these techniques are limited in that they assess the dynamic interactome of a single (or a few) protein(s) of interest. Advances in temporal proteomics, perhaps in combination with XL-MS, will facilitate the construction of a dynamic interactome on a proteome scale. Other approaches, however, have been implemented previously to construct spatio-temporal protein networks on a proteome scale. For example, Lage et al. (2010) combined detailed phenotype information from deleterious mutations with high-confidence experimental interactome data to construct a spatio-temporal interactome. In this way, the authors provide evidence to suggest a temporal correlation between developmental cardiac complexity and the number of discrete functional modules coordinating morphogenesis.

The temporal signature of protein expression depends not only on the cell cycle and disease progression, but also the rate of protein turnover (as manifest by the rates of synthesis and degradation). The rate of protein turnover is unique to each protein and can range from seconds to months (Ohsumi 2006). Rapid turnover can be stochastic or regulated partly by certain PTMs, and slower turnover can be manipulated by the overall cellular protein content (Ross et al. 2021; Doherty et al. 2009). A common approach to mapping protein degradation involves the use (and incorporation) of stable-isotope-labeled amino acids (SILAC) followed by mass spectrometry to inspect mass shifts in tryptic peptides, as done by Andersen et al. (2005) in HeLa cell nucleoli, Doherty et al. (2009) in human adenocarcinoma cells, and Pratt et al. (2002) in *Saccharomyces cerevisiae*. With advances in mass spectrometry, these proteomic turnover analyses can now provide substantial depth of coverage on a proteome scale, with recent studies quantifying the exact half-lives of >5,000 proteins in rat primary hippocampal cultures (Dörrbaum et al. 2018), as well as 4,000–6,000 proteins in several nondividing primary human cells across 10 to >1000 hours (Mathieson et al. 2018). In addition to steady-state protein degradation, endogenous rapid protein degradation is a key mechanism by which cells modulate protein abundance. Li et al. (2021) used the translational inhibitor cycloheximide coupled with advanced quantitative proteomics to measure degradation kinetics for short-lived proteins and generate a large-scale repository of human short-lived proteins under translational arrest (comprising 1,017 proteins with half-lives ≤8 hr). Overall, interactome datasets will benefit from incorporating information pertaining to dynamic proteostasis processes.

16.7 Network Approaches Reveal Novel Disease Genes and Gene Products

As discussed in Section 16.3.2, network-based approaches exist to predict protein interaction partners. Similarly, the topology of an interactome can be utilized to predict genes and gene products associated with disease (referred to as "disease genes/proteins"). In an analysis of 70 human diseases, Ghiassian et al. (2015) showed that disease proteins agglomerate in specific regions of the interactome, forming disease modules. The presence of disease modules implies that network topology can offer insight into previously unknown disease components by providing the missing links that connect disease-associated loci to one another. The initial step of these disease-module-based methods for predicting disease genes/gene products involves the identification of disease modules. However, the identification of disease modules is limited by the incompleteness of current interactome datasets and disease associations, manifesting in the interactome as dispersed, disconnected nodes. Percolation theory predicts that the minimum network coverage required to observe a disease module is indirectly proportional to the original size of the complete module (i.e. $p_c^m \sim \frac{1}{m}$, where m is the size of the original module) (Menche et al. 2015).

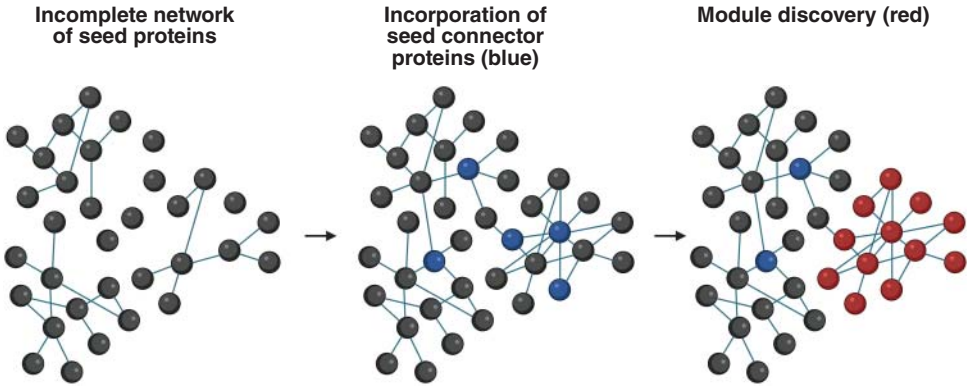

Figure 16.6 Seed Connector Algorithm (SCA) for network module discovery in the incomplete interactome. The incompleteness of reference organismal interactomes, coupled with the incompleteness of the current understanding of disease pathobiology, implies that known disease proteins (seed proteins, gray) appear scattered, rather than clustered in coherent disease modules in the interactome. The SCA incorporates linking proteins (seed connector proteins, blue) to the incomplete network of seed proteins. In this way, the algorithm interconnects known disease proteins to reveal hidden disease modules (red). *Source:* Created with BioRender.com.

This prediction implies that for diseases with fewer than ~25 disease genes, the module is too fragmented to be observable in the current HuRI (Menche et al. 2015). Several algorithms exist to overcome this limitation, including the Disease Module Detection (DIAMOnD) algorithm that ranks potential disease genes based on connectivity significance (Ghiassian et al. 2015), the Seed Connector Algorithm (SCA) that ranks potential linking proteins (seed connectors) in the pool of known disease proteins (seed proteins) (Wang and Loscalzo 2018) (Figure 16.6), and the network-based repurposing and exploration platform (NeDRex) that integrates several data sources covering genes, drugs, drug targets, disease annotations, and their relationships (Sadegh et al. 2021). Using the SCA algorithm, Wang and Loscalzo (2018) used seed proteins curated from a meta-analysis of large-scale genome-wide association studies to map the coronary artery disease module, thereby identifying previously unrecognized disease-related signaling pathways and drug targets. Potential disease proteins predicted by these algorithms are then validated experimentally or computationally. Other methods commonly utilized to predict disease proteins are linkage and diffusion propagation methods, both of which are reviewed in detail elsewhere (Barabási et al. 2011; Lee et al. 2021).

16.8 (Re)defining Relationships Between Diseases Using Network Medicine

Disease proteins are more likely to interact with each other physically than non-disease proteins (the disease module hypothesis, see Section 16.2.13), forming distinct disease modules (Goh et al. 2007). A corollary of the disease module hypothesis is that diseases with shared pathobiology should overlap topologically in the interactome, while diseases with distinct biological underpinnings should present in distinct parts of the interactome (shared components hypothesis). Indeed, Menche et al. (2015) showed that the network-based localization of each disease module determines its pathobiological relationship to other diseases, illustrated by the finding that overlapping disease modules show significant co-expression patterns, symptom

similarity, and comorbidity. Moreover, the same study quantified the network-based distance separating two disease modules, denoted as S_{AB} ($S_{AB} = <d_{AB}> - \frac{<d_{AA}>+<d_{BB}>}{2}$, where $<d_{AB}>$ denotes the average shortest network distance between nodes between disease modules A and B, while $<d_{AA}>$ and $<d_{BB}>$ are the average shortest distances *between* each of the nodes *within* modules A and B, respectively). Using this mathematical formalism, the authors showed that the disease modules of myocardial infarction and lymphomas strongly overlap, despite having seemingly distinct pathobiologies. The myocardial infarction module similarly overlapped with that of gliomas and metabolic bone disease. Similarly, and as expected, the modules for myocardial ischemia, myocardial infarction, and coronary artery disease clustered together and segregated from ophthalmological diseases (e.g. retinitis pigmentosa), autoimmune diseases (e.g. rheumatoid arthritis), and respiratory tract diseases (e.g. asthma), consistent with distinct pathobiological underpinnings. The topological localization of disease modules can be quantified (i.e. how strongly the constituent nodal genes localize) by the observable module size and the mean shortest distance connecting any given node pairs within that module, and both parameters correlate directly and indirectly, respectively, with biological localization (i.e. how biologically similar the constituent nodal genes are). Taken together, network medicine offers powerful tools to (re)define the relationship(s) between complex human diseases with distinct or shared pathobiology.

Relationships between human diseases can also be investigated through the diseasome, a weighted, bipartite graph consisting of two sets of nodes: one representing all known human genetic disorders and the other representing all known disease genes in the human genome (curated from the Online Mendelian Inheritance in Man) (Goh et al. 2007). A disease is linked to a gene if mutations in that gene are implicated in that disorder. Two weighted, unipartite networks can be projected from the diseasome: the human disease network and the disease gene network. The human disease network consists of nodal diseases that are linked if there exists at least one gene implicated in both diseases, with nodal weight corresponding to the number of genes associated with that disease and edge weights corresponding to the number of shared genes between any given disease partners. The topology of the human disease network is consistent with well-established relationships between diseases; for example, cardiomyopathy and muscular dystrophy are linked, consistent with known cardiac involvement in patients with muscular dystrophies (Verhaert et al. 2011). By contrast, nodal genes in the disease gene network are linked if they are involved in the same disease, and edge weights represent the number of diseases with which both genes are implicated. Other disease networks link diseases based on metabolic signatures (Lee et al. 2008) or phenotypic characteristics (Hidalgo et al. 2009). A primary advantage of disease networks is that they offer insight into disease pathobiology and pharmacology by revealing hidden connections among seemingly distinct diseases.

16.9 Network Approaches to Disease Reappraisal and Patient Subgrouping

Traditional disease nosology is premised on observational correlation between pathological analysis and clinical syndromes. This clinicopathological description of the disease, albeit serving clinicians well to the current time, inevitably reduces complex human diseases to static and distinct entities irrespective of heterogeneity in etiology, risk, and pathobiology. Furthermore, this traditional paradigm fails to explain incomplete disease penetrance, variable expressivity, and differences in age of onset (Vidal et al. 2011). No less important is the failure to recognize preclinical disease. Indeed, disease classification is often derived from end-stage manifestations

in a dysfunctional organ system, overlooking preclinical pathophenotypes and/or susceptibility factors preceding end-stage dysfunction. It is partly for this reason that myocardial infarction is sometimes described as a "silent killer", since conventional diagnosis often fails to recognize early disease. In addition, the reductionist approach to disease classification neglects disease perturbations beyond the primary disease-defining organ. For example, crosstalk between the liver and heart is seldom addressed in the diagnosis of acute and chronic heart failure despite unequivocal evidence suggesting direct, bidirectional cardiohepatic interactions (El Hadi et al. 2020). Further exemplifying this crosstalk, Cao et al. (2022) computationally predicted and experimentally validated in diverse, inbred strains of mice that liver-derived coagulation factor XI protects against diastolic dysfunction by activating the bone morphogenic protein-suppressor of mother against decapentaplegic (SMAD) 1/5 pathway in the heart and, thereby, inhibiting inflammatory and fibrotic gene expression.

The contemporary reductionist diagnostic strategy suffers further from a lack of sensitivity in defining molecular (deterministic) and environmental (stochastic) determinants that govern disease evolution. Consequently, classical diagnostic methods are excessively inclusive and fail to appreciate the immense clinical heterogeneity derived from nuanced, patient-specific pathophenotypic differences. A classic example of this arbitrary and misleading inclusivity is the case of idiopathic hypertension, the classification of which fails to discriminate among a plethora of definitively distinct genetic and environmental determinants (e.g. high alcohol intake *vs.* aging). Additionally, hypertrophic cardiomyopathy is an ambiguous diagnosis for a seemingly distinctive disease caused by a number of mutations in several sarcomeric proteins (locus heterogeneity), each manifesting in distinct cardiac or molecular phenotypes. This heterogeneity holds even for classical Mendelian disorders, the clinical presentation of which is complicated by, for example, environmental factors and their interaction with disease-modifying polymorphisms. Excitingly, however, the completion of the Human Genome Project and the availability of next-generation sequencing, as well as advances in multi-omic data generation and interpretation by powerful computational approaches, enable the development and implementation of precision medicine-based and personalized classification of – and treatment for – complex human disease, as discussed below.

16.9.1 Modular Network Representations

Network medicine offers powerful tools to facilitate the transition away from reductionism and toward a holistic and individualized disease appraisal approach. For example, modular network representations utilize four modular networks between, and within which interconnected nodes (denoting genes, mRNA, proteins, biochemical properties, and environmental factors) yield a distinct phenotype (Loscalzo et al. 2007). The primary disease network comprises the key molecular perturbations associated with the general disease phenotype (e.g. a network with two nodes representing the two alleles associated with a classic Mendelian disorder); the secondary disease network comprises known disease-modifying genes; the third network (called the intermediate phenotype network) incorporates known polymorphisms or haplotypes that influence (directly or indirectly) the organism's response to stress [e.g. genetic ability to salt response in essential hypertension patients (Sanada et al. 2011)]; and the fourth network comprises environmental determinants. Accordingly, the interaction among nodes within and between these modular networks is individualized and offers an integrative way of defining unequivocally classic Mendelian, polygenic, and environmental disorders alike. The power of this approach derives from the emergent behavior of these interconnected modular networks, decipherable only by interrogating the networks as a whole rather than assessment of the individual components in isolation.

16.9.2 Individualized Networks

Progress in precision and personalized medicine is limited by the variable complexity of disease pathogenesis across individuals. This variability precludes the timely development and approval of systematic approaches for disease subtyping despite extensive new insight into disease pathobiology (Silverman and Loscalzo 2013). Nevertheless, the steadily decreasing costs of

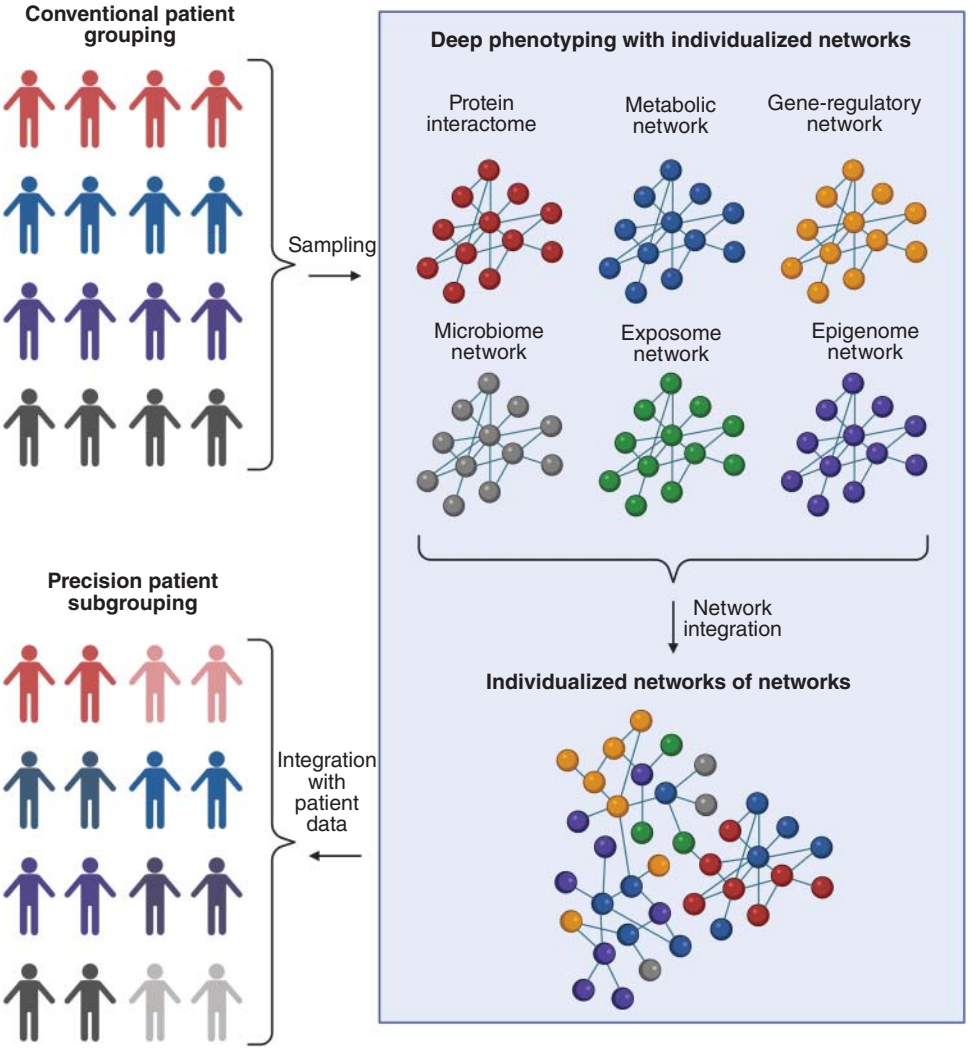

Figure 16.7 Network-based precision and personalized patient subgrouping. Conventional nosology groups patients based on clinicopathological correlations. This reductionist diagnostic strategy suffers from a lack of sensitivity in defining molecular (deterministic) and environmental (stochastic) determinants that govern disease evolution, incomplete disease penetrance, and heterogeneity among patients with phenotypically similar (albeit molecularly distinct) endophenotypes. Network-based patient phenotyping involves the construction of individualized protein interactomes (reticulotypes), metabolic networks, gene-regulatory networks, microbiome networks, exposome networks, and epigenome networks. These networks can be fused to form individualized networks of networks, integration of which with patient-specific phenotypic data can be used to inform precision- and personalized-based patient subgrouping. *Source:* Created with Biorender.com.

next-generation sequencing and MS-based multi-omics facilitate deep phenotyping and molecular subtyping of individuals. Clinical data from electronic health records can now be integrated with exposome, microbiome, metabolome, proteome, transcriptome, and epigenome data by network analysis, effectively subgrouping individuals with similar endophenotypes (Leopold and Loscalzo 2018; Antman and Loscalzo 2016; Sonawane et al. 2022; Wang et al. 2023) (Figure 16.7). For example, Wu et al. (2021) used similarity network fusion followed by network enhancement and spectral clustering to construct networks incorporating mRNA, DNA methylation, and microRNA expression data to obtain high-risk and low-risk clusters of heart failure with preserved ejection fraction (HFpEF) patients. An extensive review outlining different methodologies and criteria used in disease subtyping workflows in the context of CVD is discussed in Maiorino and Loscalzo (2023).

Subgrouping individuals based on distinct pathobiology can be further augmented by the construction of individualized disease modules (called "reticulotypes") (Figure 16.7). The power of reticulotypes for resolving patient-specific variability is exemplified by the proof-of-concept work of Maron et al. (2021), which elegantly showed that reticulotypes can infer distinct patient-specific pathophenotypes in a cohort of hypertrophic cardiomyopathy patients. Similarly, Cava et al. (2021) developed and utilized a computational approach to sort 73 basal breast cancer patients based on individualized protein expression patterns. Overall, by aiding the detailed phenotyping of patients, individualized networks offer a new paradigm to facilitate personalized and precision medicine by improving prognostication, rational polypharmacy, precision medication selection, and enrichment for clinical trial selection. Patient-specific networks can also be filtered into tissue- and cell-specific networks (see Section 16.6).

16.10 Network Approaches to Disease Pharmacology

The classical pharmacological formalism, derived from the work of Paul Ehrlich at the beginning of the 20th century, rests on three fundamental ideas: (1) drugs should be subject to semiempirical phenotyping screening; (2) every disease should be treated by a single, "magic bullet" drug that is minimally harmful; and (3) drugs act on a unique receptor (which, at the time, was a theoretical construct) that is specific to each disease. Taken together, Ehrlich proposed that, in pursuit of discovering a cure for a particular disease, one should empirically screen for several drugs to identify a definitive treatment, the action of which is mediated *via* specific drug–receptor interactions [reviewed in Loscalzo (2012)]. Although advances in biochemistry and molecular biology enabled the functional characterization of macromolecular receptors and highlighted their potential use as drug targets, the modern pharmacological formalism did not require a mechanistic understanding of drug–target interactions (e.g. the binding site for the drug on the drug target) prior to drug approval. A shift away from this lenient pharmacological formalism and towards one of rational drug design, premised on known drug–target interactions, has occurred over the last 30 years. This shift resulted partly from genomic expansion in the post-genomic era, growth in real and virtual drug libraries, and advances in technologies aimed at tertiary structure elucidation (e.g. X-ray crystal structure determinations and magnetic resonance spectroscopy). Notwithstanding this paradigm shift in the drug discovery process, productivity and innovation in the pharmaceutical industry are declining, exemplified by the fact that an overwhelmingly small number of new drugs are approved by the US Food and Drug Administration (FDA) annually when compared to the early 2000s (Loscalzo 2012). Although affected by regulatory forces and costs of drug development, the discrepancy between the steady increases in the rate of growth

in our understanding of biology and the relatively stagnant (or declining) rate by which novel pharmacotherapies are discovered and approved points at a fundamental flaw in the drug discovery process itself.

A significant shortcoming in contemporary pharmacological formalism derives from the reductionist simplicity that is at the heart of target-based drug development. Drug target-based screening fails to recognize not only the nuanced complexity that governs chronic illnesses but also the multifactorial, often seemingly hidden influence(s) that pharmacological agents have on disease pathobiology and evolution. As proven historically, failure to address this complexity often (if not always) results in therapeutic agents yielding negative outcomes in clinical trials, despite extensive evidence suggestive of their high efficacy in less complex biological systems (e.g. *in vitro*). For example, despite extensive epidemiological evidence in support of a clear phenotypic correlation between elevated levels of plasma homocysteine and increased risk of atherothrombosis (Welch and Loscalzo 1998), homocysteine-lowering therapies including folate and vitamin B_{12} have been repeatedly rendered ineffective for the treatment of atherosclerotic vascular disease (Loscalzo 2006; Maron and Loscalzo 2009). Failure to translate these therapies into the clinic is likely the result of several complex factors, not the least of which is an underappreciation for the impact that these drugs have on homocysteine-independent aspects of vascular biology [e.g. folate can promote vascular smooth muscle proliferation and can influence nitric oxide availability (Stanhewicz and Kenney 2017)]. Indeed, the linear paradigm connecting one drug (e.g. folate) to one biological perturbation (e.g. hyperhomocysteinemia) assumes erroneously that drug–target interactions operate in isolation rather than alongside an overwhelmingly large number of interconnected biological factors, the presence of which may offset the benefit of reversing the original perturbation.

16.10.1 Network Approaches to Predict Drug Efficacy

Network medicine defines diseases through disease modules rather than perturbations to one (or a few) biological components. This holistic, module-based definition of disease has several implications for rational polypharmacy. For example, dynamic network-based analysis can be applied to determine combination therapies that yield optimal benefits with minimal adverse consequences to the disease module topology (Silverman and Loscalzo 2013; Hopkins 2008). Cheng et al. (2019) developed a computational, network-based methodology to identify clinically efficacious drug combinations for specific diseases by quantifying the network-based relationship between drug targets and disease proteins in the human interactome. Using antihypertensive combinations as a proof of concept, the authors concluded that the most efficacious combination of (two) drugs requires both drugs to target proteins in distinct neighborhoods of the disease module. In addition, Guney et al. (2016) introduced a computational formalism (drug–disease proximity) to quantify the interplay between drug targets (proteins) and diseases, thereby predicting drug efficacy. The authors implemented this proximity measure in their analysis of 238 drugs used in 78 diseases, showing that drugs do not target the disease module as a whole but, rather, distinct parts of it, and that the therapeutic effect of drugs is localized in a small network neighborhood of the disease module rather than diffusely across the entire network. Interestingly, effective drugs were shown to be preferentially more proximal (as quantified by the proximity measure) to the corresponding disease than palliative drugs. An additional application of network pharmacology is exemplified by the seminal work of Yildirim et al. (2007), who constructed a bipartite network (drug–target network) composed of FDA-approved drugs and proteins linked by known drug–target binary associations. This study showed that well-known drug targets are continuously used as targets of new drugs (leading to inspection bias). Furthermore, the authors

conclude that disease targets localize in distinct parts of the interactome relative to essential proteins, and that most drugs in the drug–target network are palliative and do not directly target disease proteins.

16.10.2 Network Approaches for Drug Repurposing

An additional powerful concept in network pharmacology pertains to drug repurposing (also called drug repositioning), i.e. the use of approved drugs for the treatment of diseases outside the scope of the original approved medical indication (Ashburn and Thor 2004; Pushpakom et al. 2019). The need to repurpose previously approved drugs is illustrated by the steadily increasing costs in drug development and time frames needed for the approval of new drugs. Drug repurposing approaches derive from the hypothesis that a drug which effectively treats a disease will also be effective in treating similar diseases with shared pathobiology. More precisely, drug repurposing assumes that an efficacious drug for one disease will retain its efficacy in the treatment of a different disease if both diseases are caused by (or at least associated with) the same drug target(s). Network-based approaches for drug repurposing assume that diseases with overlapping (or proximal) disease modules could be treated with the same (combination of) drug, given that the drug target is localized proximally to both disease modules. This approach was utilized by Cheng et al. (2018) to predict (computationally) previously unrecognized drug–disease associations for >900 FDA-approved drugs. The authors predicted and validated using patient-level data that carbamazepine (an epilepsy drug) and hydroxychloroquine (a primarily antimalarial drug) are associated with an increased and decreased risk of coronary artery disease, respectively. Paci et al. (2022) developed an adjusted similarity measure using the algorithm SAveRUNNER (Fiscon and Paci 2021; Fiscon et al. 2021) to predict drug candidates that are not only fit for repurposing but are also unlikely to cause adverse side effects. The authors achieved this goal by constructing network modules for nine cardiovascular disorders (comprising disease proteins) and two side effects (comprising proteins associated with adverse side effects). In this way, the authors screened for optimal drug candidates by minimizing the network distance to disease modules, while maximizing the distance to side effect modules. Overall, these innovative, network-based approaches offer powerful means to predict novel drug–target associations, thereby promoting the repurposing of previously approved drugs for other complex (even incurable) diseases.

16.11 Conclusions

The exponential growth in the generation of high-throughput multi-omic data in recent years has, unfortunately, not been met with a commensurate growth in our understanding of complex human disorders. A major reason for this discrepancy stems from the scientific reductionism that is at the heart of the Oslerian medicine paradigm. This reductionism implies that one can study biological and disease processes in a vacuum, without due regard to the interplay between biological components and disease determinants. However, biology is governed by interconnected loci that act as dynamic complex systems. Network medicine summarizes this complexity as nodes and edges, thereby enabling one to model complex biological phenomena computationally. In a way that is beyond the scope of conventional scientific reductionism, biological networks shed light on previously unrecognized links connecting genotypes to phenotypes. Network medicine also offers powerful computational tools to study the relationships between seemingly distinct diseases, revolutionize conventional disease nosology, and advance personalized and precision medicine.

References

Albert, R. and Barabási, A.-L. (2002). Statistical mechanics of complex networks. *Rev. Mod. Phys.* 74: 47–97.

Albert, R., Jeong, H., and Barabási, A.-L. (2000). Error and attack tolerance of complex networks. *Nature* 406: 378–382.

Altschuler, S.J. and Wu, L.F. (2010). Cellular heterogeneity: do differences make a difference? *Cell* 141: 559–563.

Andersen, J.S., Lam, Y.W., Leung, A.K. et al. (2005). Nucleolar proteome dynamics. *Nature* 433: 77–83.

Antman, E.M. and Loscalzo, J. (2016). Precision medicine in cardiology. *Nat. Rev. Cardiol.* 13: 591–602.

Ashburn, T.T. and Thor, K.B. (2004). Drug repositioning: identifying and developing new uses for existing drugs. *Nat. Rev. Drug Discovery* 3: 673–683.

Baker, E.S., Liu, T., Petyuk, V.A. et al. (2012). Mass spectrometry for translational proteomics: progress and clinical implications. *Genome Med.* 4: 63.

Barabási, A.-L. (2016). *Network Science*. Cambridge: Cambridge University Press. https://networksciencebook.com/.

Barabási, A.-L. and Albert, R. (1999). Emergence of scaling in random networks. *Science* 286: 509–512.

Barabási, A.-L., Gulbahce, N., and Loscalzo, J. (2011). Network medicine: a network-based approach to human disease. *Nat. Rev. Genet.* 12: 56–68.

Barkai, N. and Leibler, S. (1997). Robustness in simple biochemical networks. *Nature* 387: 913–917.

Berman, H.M., Westbrook, J., Feng, Z. et al. (2000). The protein data bank. *Nucleic Acids Res.* 28: 235–242.

Bisson, N., James, D.A., Ivosev, G. et al. (2011). Selected reaction monitoring mass spectrometry reveals the dynamics of signaling through the GRB2 adaptor. *Nat. Biotechnol.* 29: 653–658.

Bonacich, P. (1987). Power and centrality: a family of measures. *Am. J. Sociol.* 92: 1170–1182.

Boxem, M., Maliga, Z., Klitgord, N. et al. (2008). A protein domain-based interactome network for *C. elegans* early embryogenesis. *Cell* 134: 534–545.

Brunner, A.D., Thielert, M., Vasilopoulou, C. et al. (2022). Ultra-high sensitivity mass spectrometry quantifies single-cell proteome changes upon perturbation. *Mol. Syst. Biol.* 18: e10798.

Burke, D.F., Bryant, P., Barrio-Hernandez, I. et al. (2023). Towards a structurally resolved human protein interaction network. *Nat. Struct. Mol. Biol.* 30: 216–225.

Cao, Y., Wang, Y., Zhou, Z. et al. (2022). Liver-heart cross-talk mediated by coagulation factor XI protects against heart failure. *Science* 377: 1399–1406.

Castel, P., Holtz-Morris, A., Kwon, Y. et al. (2021). DoMY-Seq: a yeast two-hybrid-based technique for precision mapping of protein-protein interaction motifs. *J. Biol. Chem.* 296: 100023.

Caudal, A., Tang, X., Chavez, J.D. et al. (2022). Mitochondrial interactome quantitation reveals structural changes in metabolic machinery in the failing murine heart. *Nat. Cardiovasc. Res.* 1: 855–866.

Cava, C., Sabetian, S., and Castiglioni, I. (2021). Patient-specific network for personalized breast cancer therapy with multi-omics data. *Entropy (Basel)* 23: 225.

Cha, J., Yu, J., Cho, J.W. et al. (2023). scHumanNet: a single-cell network analysis platform for the study of cell-type specificity of disease genes. *Nucleic Acids Res.* 51: e8.

Chavez, J.D., Lee, C.F., Caudal, A. et al. (2018). Chemical crosslinking mass spectrometry analysis of protein conformations and supercomplexes in heart tissue. *Cell Syst.* 6: 136–141. e5.

Chavez, J.D., Mohr, J.P., Mathay, M. et al. (2019). Systems structural biology measurements by *in vivo* cross-linking with mass spectrometry. *Nat. Protoc.* 14: 2318–2343.

Chavez, J.D., Keller, A., Mohr, J.P., and Bruce, J.E. (2020). Isobaric quantitative protein interaction reporter technology for comparative interactome studies. *Anal. Chem.* 92: 14094–14102.

Cheng, F., Desai, R.J., Handy, D.E. et al. (2018). Network-based approach to prediction and population-based validation of in silico drug repurposing. *Nat. Commun.* 9: 2691.

Cheng, F., Kovács, I.A., and Barabási, A.L. (2019). Network-based prediction of drug combinations. *Nat. Commun.* 10: 1197.

Cheng, F., Zhao, J., Wang, Y. et al. (2021). Comprehensive characterization of protein-protein interactions perturbed by disease mutations. *Nat. Genet.* 53: 342–353.

Chien, C.T., Bartel, P.L., Sternglanz, R., and Fields, S. (1991). The two-hybrid system: a method to identify and clone genes for proteins that interact with a protein of interest. *PNAS* 88: 9578–9582.

Collins, B.C., Gillet, L.C., Rosenberger, G. et al. (2013). Quantifying protein interaction dynamics by SWATH mass spectrometry: application to the 14-3-3 system. *Nat. Methods* 10: 1246–1253.

Cox, B. and Emili, A. (2006). Tissue subcellular fractionation and protein extraction for use in mass-spectrometry-based proteomics. *Nat. Protoc.* 1: 1872–1878.

Cusick, M.E., Yu, H., Smolyar, A. et al. (2009). Literature-curated protein interaction datasets. *Nat. Methods* 6: 39–46.

Cusick, M.E., Charloteaux, B., Rolland, T. et al. (2016). Human interactomes in network medicine. In: *Network Medicine: Complex Systems in Human Disease and Therapeutics* (ed. J. Loscalzo, A.-L. Barabási, and E.K. Silverman), 44–88. Cambridge, Massachusetts: Harvard University Press. ISBN 9780674436534.

Doherty, M.K., Hammond, D.E., Clague, M.J. et al. (2009). Turnover of the human proteome: determination of protein intracellular stability by dynamic SILAC. *J. Proteome Res.* 8: 104–112.

Dörrbaum, A.R., Kochen, L., Langer, J.D., and Schuman, E.M. (2018). Local and global influences on protein turnover in neurons and glia. *Elife* 7: e34202.

Drummond, E., Pires, G., Macmurray, C. et al. (2020). Phosphorylated tau interactome in the human Alzheimer's disease brain. *Brain* 143: 2803–2817.

Duan, G. and Walther, D. (2015). The roles of post-translational modifications in the context of protein interaction networks. *PLoS Comput. Biol.* 11: e1004049.

Dunn, J.D., Reid, G.E., and Bruening, M.L. (2010). Techniques for phosphopeptide enrichment prior to analysis by mass spectrometry. *Mass Spectrom. Rev.* 29: 29–54.

Eisenberg, E. and Levanon, E.Y. (2003). Preferential attachment in the protein network evolution. *Phys. Rev. Lett.* 91: 138701.

El Hadi, H., Di Vincenzo, A., Vettor, R., and Rossato, M. (2020). Relationship between heart disease and liver disease: a two-way street. *Cells* 9: 567.

Elowitz, M.B., Levine, A.J., Siggia, E.D., and Swain, P.S. (2002). Stochastic gene expression in a single cell. *Science* 297: 1183–1186.

Fíla, J. and Honys, D. (2012). Enrichment techniques employed in phosphoproteomics. *Amino Acids* 43: 1025–1047.

Fiscon, G. and Paci, P. (2021). SAveRUNNER: an R-based tool for drug repurposing. *BMC Bioinf.* 22: 150.

Fiscon, G., Conte, F., Farina, L., and Paci, P. (2021). SAveRUNNER: a network-based algorithm for drug repurposing and its application to COVID-19. *PLoS Comput. Biol.* 17: e1008686.

Frangogiannis, N.G. (2014). The inflammatory response in myocardial injury, repair, and remodelling. *Nat. Rev. Cardiol.* 11: 255–265.

Freeman, L.C. (1977). A set of measures of centrality based on betweenness. *Sociometry* 40: 35–41.

Funtowicz, S. and Ravetz, J.R. (1994). Emergent complex systems. *Futures* 26: 568–582.

Gajjala, P.R., Fliser, D., Speer, T. et al. (2015). Emerging role of post-translational modifications in chronic kidney disease and cardiovascular disease. *Nephrol. Dial Transplant.* 30: 1814–1824.

Ghiassian, S.D., Menche, J., and Barabási, A.L. (2015). A DIseAse MOdule Detection (DIAMOnD) algorithm derived from a systematic analysis of connectivity patterns of disease proteins in the human interactome. *PLoS Comput. Biol.* 11: e1004120.

Goh, K.I., Cusick, M.E., Valle, D. et al. (2007). The human disease network. *PNAS* 104: 8685–8690.

Guney, E., Menche, J., Vidal, M., and Barábasi, A.L. (2016). Network-based *in silico* drug efficacy screening. *Nat. Commun.* 7: 10331.

Hart, G.T., Ramani, A.K., and Marcotte, E.M. (2006). How complete are current yeast and human protein-interaction networks? *Genome Biol.* 7: 120.

Hartwell, L.H., Hopfield, J.J., Leibler, S., and Murray, A.W. (1999). From molecular to modular cell biology. *Nature* 402: C47–C52.

Hidalgo, C.A., Blumm, N., Barabási, A.L., and Christakis, N.A. (2009). A dynamic network approach for the study of human phenotypes. *PLoS Comput. Biol.* 5: e1000353.

Hopkins, A.L. (2008). Network pharmacology: the next paradigm in drug discovery. *Nat. Chem. Biol.* 4: 682–690.

Hornbeck, P.V., Kornhauser, J.M., Tkachev, S. et al. (2012). PhosphoSitePlus: a comprehensive resource for investigating the structure and function of experimentally determined post-translational modifications in man and mouse. *Nucleic Acids Res.* 40: D261–D270.

Huttlin, E.L., Ting, L., Bruckner, R.J. et al. (2015). The BioPlex network: a systematic exploration of the human interactome. *Cell.* 162: 425–440.

Jalili, M., Salehzadeh-Yazdi, A., Gupta, S. et al. (2016). Evolution of centrality measurements for the detection of essential proteins in biological networks. *Front. Physiol.* 7: 375.

Jeong, H., Mason, S.P., Barabási, A.L., and Oltvai, Z.N. (2001). Lethality and centrality in protein networks. *Nature* 411: 41–42.

Jumper, J., Evans, R., Pritzel, A. et al. (2021). Highly accurate protein structure prediction with AlphaFold. *Nature* 596: 583–589.

Kao, A., Chiu, C.L., Vellucci, D. et al. (2011). Development of a novel cross-linking strategy for fast and accurate identification of cross-linked peptides of protein complexes. *Mol. Cell. Proteomics* 10 (M110): 002212.

Kelly, R.T. (2020). Single-cell proteomics: progress and prospects. *Mol. Cell. Proteomics* 19: 1739–1748.

Kitano, H. (2004). Biological robustness. *Nat. Rev. Genet.* 5: 826–837.

Kitsak, M., Sharma, A., Menche, J. et al. (2016). Tissue specificity of human disease module. *Sci. Rep.* 6: 35241.

Klimm, F., Toledo, E.M., Monfeuga, T. et al. (2020). Functional module detection through integration of single-cell RNA sequencing data with protein-protein interaction networks. *BMC Genomics* 21: 756.

Klykov, O., Steigenberger, B., Pektaş, S. et al. (2018). Efficient and robust proteome-wide approaches for cross-linking mass spectrometry. *Nat. Protoc.* 13: 2964–2990.

Koschützki, D. and Schreiber, F. (2008). Centrality analysis methods for biological networks and their application to gene regulatory networks. *Gene Regul. Syst. Biol.* 2: 193–201.

Kovács, I.A., Luck, K., Spirohn, K. et al. (2019). Network-based prediction of protein interactions. *Nat. Commun.* 10: 1240.

Lage, K., Møllgård, K., Greenway, S. et al. (2010). Dissecting spatio-temporal protein networks driving human heart development and related disorders. *Mol. Syst. Biol.* 6: 381.

Lee, D.S., Park, J., Kay, K.A. et al. (2008). The implications of human metabolic network topology for disease comorbidity. *PNAS* 105: 9880–9885.

Lee, L.Y., Pandey, A.K., Maron, B.A., and Loscalzo, J. (2021). Network medicine in cardiovascular research. *Cardiovasc. Res.* 117: 2186–2202.

Leopold, J.A. and Loscalzo, J. (2018). Emerging role of precision medicine in cardiovascular disease. *Circ. Res.* 122: 1302–1315.

Li, J., Cai, Z., Vaites, L.P. et al. (2021). Proteome-wide mapping of short-lived proteins in human cells. *Mol. Cell* 81: 4722–4735. e5.

Li, L., Sun, C., Sun, Y. et al. (2022). Spatially resolved proteomics *via* tissue expansion. *Nat. Commun.* 13: 7242.

Li, K., Chen, S., Wang, K. et al. (2025). A peptide-centric local stability assay enables proteome-scale identification of the protein targets and binding regions of diverse ligands. *Nat. Methods.* 22: 278–282.

Liddy, K.A., White, M.Y., and Cordwell, S.J. (2013). Functional decorations: post-translational modifications and heart disease delineated by targeted proteomics. *Genome Med.* 5: 20.

Lippens, G., Gunawardena, J., Landrieu, I. et al. (2016). Post-translational modifications of the proteome: the example of tau in the neuron and the brain. In: *Network Medicine: Complex Systems in Human Disease and Therapeutics* (ed. J. Loscalzo, A.-L. Barabási, and E.K. Silverman), 198–223. Cambridge, Massachusetts: Harvard University Press. ISBN 9780674436534.

Liu, X., Maiorino, E., Halu, A. et al. (2020). Robustness and lethality in multilayer biological molecular networks. *Nat. Commun.* 11: 6043.

Lobingier, B.T., Hüttenhain, R., Eichel, K. et al. (2017). An approach to spatiotemporally resolve protein interaction networks in living cells. *Cell* 169: 350–360. e12.

Lomenick, B., Hao, R., Jonai, N. et al. (2009). Target identification using drug affinity responsive target stability (DARTS). *Proc. Natl. Acad. Sci. USA.* 106: 21984–21989.

Loscalzo, J. (2006). Homocysteine trials--clear outcomes for complex reasons. *N. Engl. J. Med.* 354: 1629–1632.

Loscalzo, J. (2012). Personalized cardiovascular medicine and drug development: time for a new paradigm. *Circulation* 125: 638–645.

Loscalzo, J., Kohane, I., and Barabasi, A.L. (2007). Human disease classification in the postgenomic era: a complex systems approach to human pathobiology. *Mol. Syst. Biol.* 3: 124.

Luck, K., Kim, D.K., Lambourne, L. et al. (2020). A reference map of the human binary protein interactome. *Nature* 580: 402–408.

Luzarowski, M., Vicente, R., Kiselev, A. et al. (2021). Global mapping of protein–metabolite interactions in *Saccharomyces cerevisiae* reveals that Ser-Leu dipeptide regulates phosphoglycerate kinase activity. *Commun. Biol.* 4: 181.

Ly, T., Ahmad, Y., Shlien, A. et al. (2014). A proteomic chronology of gene expression through the cell cycle in human myeloid leukemia cells. *Elife* 3: e01630.

Ly, T., Endo, A., and Lamond, A.I. (2015). Proteomic analysis of the response to cell cycle arrests in human myeloid leukemia cells. *Elife* 4: e04534.

Ly, T., Whigham, A., Clarke, R. et al. (2017). Proteomic analysis of cell cycle progression in asynchronous cultures, including mitotic subphases, using PRIMMUS. *Elife* 6: e27574.

Maiorino, E. and Loscalzo, J. (2023). Phenomics and robust multiomics data for cardiovascular disease subtyping. *Arterioscler., Thromb., Vasc. Biol.* 43: 1111–1123.

Maron, B.A. and Loscalzo, J. (2009). The treatment of hyperhomocysteinemia. *Annu. Rev. Med.* 60: 39–54.

Maron, B.A., Wang, R.S., Shevtsov, S. et al. (2021). Individualized interactomes for network-based precision medicine in hypertrophic cardiomyopathy with implications for other clinical pathophenotypes. *Nat. Commun.* 12: 873.

Maslov, S. and Sneppen, K. (2002). Specificity and stability in topology of protein networks. *Science* 296: 910–913.

Mathieson, T., Franken, H., Kosinski, J. et al. (2018). Systematic analysis of protein turnover in primary cells. *Nat. Commun.* 9: 689.

Menche, J. and Barabási, A.L. (2016). Introduction to network analysis. In: *Network Medicine: Complex Systems in Human Disease and Therapeutics* (ed. J. Loscalzo, A.-L. Barabási, and E.K. Silverman), 17–43. Cambridge, Massachusetts: Harvard University Press. ISBN 9780674436534.

Menche, J., Sharma, A., Kitsak, M. et al. (2015). Disease networks. Uncovering disease-disease relationships through the incomplete interactome. *Science* 347: 1257601.

Mohammadi, S., Davila-Velderrain, J., and Kellis, M. (2019). Reconstruction of cell-type-specific interactomes at single-cell resolution. *Cell Syst.* 9: 559–568. e4.

Martinez Molina, D., Jafari, R., Ignatushchenko, M. et al. (2013). Monitoring drug target engagement in cells and tissues using the cellular thermal shift assay. *Science.* 341: 84–87.

Mulvey, C.M., Breckels, L.M., Geladaki, A. et al. (2017). Using hyperLOPIT to perform high-resolution mapping of the spatial proteome. *Nat. Protoc.* 12: 1110–1135.

Mund, A., Brunner, A.D., and Mann, M. (2022a). Unbiased spatial proteomics with single-cell resolution in tissues. *Mol. Cell* 82: 2335–2349.

Mund, A., Coscia, F., Kriston, A. et al. (2022b). Deep visual proteomics defines single-cell identity and heterogeneity. *Nat. Biotechnol.* 40: 1231–1240.

Nieminen, J. (1974). On the centrality in a graph. *Scand. J. Psychol.* 15: 332–336.

Ohsumi, Y. (2006). Protein turnover. *IUBMB Life* 58: 363–369.

Paci, P., Fiscon, G., Conte, F. et al. (2022). Comprehensive network medicine-based drug repositioning via integration of therapeutic efficacy and side effects. *npj Syst. Biol. Appl.* 8: 12.

Piazza, I., Kochanowski, K., Cappelletti, V. et al. (2018). A map of protein-metabolite interactions reveals principles of chemical communication. *Cell* 172: 358–372. e23.

Pratt, J.M., Petty, J., Riba-Garcia, I. et al. (2002). Dynamics of protein turnover, a missing dimension in proteomics. *Mol. Cell. Proteomics* 1: 579–591.

Przytycka, T.M., Singh, M., and Slonim, D.K. (2010). Toward the dynamic interactome: it's about time. *Briefings Bioinf.* 11: 15–29.

Pushpakom, S., Iorio, F., Eyers, P.A. et al. (2019). Drug repurposing: progress, challenges and recommendations. *Nat. Rev. Drug Discovery* 18: 41–58.

Qin, W., Cho, K.F., Cavanagh, P.E., and Ting, A.Y. (2021). Deciphering molecular interactions by proximity labeling. *Nat. Methods* 18: 133–143.

Rafieian-Kopaei, M., Setorki, M., Doudi, M. et al. (2014). Atherosclerosis: process, indicators, risk factors and new hopes. *Int. J. Prev. Med.* 5: 927–946.

Raj, A. and Van Oudenaarden, A. (2008). Nature, nurture, or chance: stochastic gene expression and its consequences. *Cell* 135: 216–226.

Ramazi, S. and Zahiri, J. (2021). Posttranslational modifications in proteins: resources, tools and prediction methods. *Database (Oxford)* 2021: baab012.

Rao, V.S., Srinivas, K., Sujini, G.N., and Kumar, G.N. (2014). Protein-protein interaction detection: methods and analysis. *Int. J. Proteomics* 2014: 147648.

Richards, A.L., Eckhardt, M., and Krogan, N.J. (2021). Mass spectrometry-based protein-protein interaction networks for the study of human diseases. *Mol. Syst. Biol.* 17: e8792.

Roberts, P.M. (2006). Mining literature for systems biology. *Briefings Bioinf.* 7: 399–406.

Rolland, T., Taşan, M., Charloteaux, B. et al. (2014). A proteome-scale map of the human interactome network. *Cell* 159: 1212–1226.

Rosenberger, F.A., Thielert, M., Strauss, M.T. et al. (2023). Spatial single-cell mass spectrometry defines zonation of the hepatocyte proteome. *Nat. Methods* 20: 1530–1536.

Ross, A.B., Langer, J.D., and Jovanovic, M. (2021). Proteome turnover in the spotlight: approaches, applications, and perspectives. *Mol. Cell. Proteomics* 20: 100016.

Rual, J.F., Venkatesan, K., Hao, T. et al. (2005). Towards a proteome-scale map of the human protein-protein interaction network. *Nature* 437: 1173–1178.

Ruwolt, M., Schnirch, L., Borges Lima, D. et al. (2022). Optimized TMT-based quantitative cross-linking mass spectrometry strategy for large-scale interactomic studies. *Anal. Chem.* 94: 5265–5272.

Sadegh, S., Skelton, J., Anastasi, E. et al. (2021). Network medicine for disease module identification and drug repurposing with the NeDRex platform. *Nat. Commun.* 12: 6848.

Samokhin, A.O., Stephens, T., Wertheim, B.M. et al. (2018). NEDD9 targets COL3A1 to promote endothelial fibrosis and pulmonary arterial hypertension. *Sci. Transl. Med.* 10: eaap7294.

Sanada, H., Jones, J.E., and Jose, P.A. (2011). Genetics of salt-sensitive hypertension. *Curr. Hypertens. Rep.* 13: 55–66.

Savitski, M.M., Reinhard, F.B., Franken, H. et al. (2014). Tracking cancer drugs in living cells by thermal profiling of the proteome. *Science.* 346: 1255784.

Schopper, S., Kahraman, A., Leuenberger, P. et al. (2017). Measuring protein structural changes on a proteome-wide scale using limited proteolysis-coupled mass spectrometry. *Nat. Protoc.* 12: 2391–2410.

Silverman, E.K. and Loscalzo, J. (2013). Developing new drug treatments in the era of network medicine. *Clin. Pharmacol. Ther.* 93: 26–28.

Silverman, E.K. and Loscalzo, J. (2016). Scientific basis of network medicine. In: *Network Medicine: Complex Systems in Human Disease and Therapeutics* (ed. J. Loscalzo, A.-L. Barabási, and E.K. Silverman), 1–16. Cambridge, Massachusetts: Harvard University Press. ISBN 9780674436534.

Sonawane, A.R., Aikawa, E., and Aikawa, M. (2022). Connections for matters of the heart: network medicine in cardiovascular diseases. *Front. Cardiovasc. Med.* 9: 873582.

Stanhewicz, A.E. and Kenney, W.L. (2017). Role of folic acid in nitric oxide bioavailability and vascular endothelial function. *Nutr. Rev.* 75: 61–70.

Stelling, J., Sauer, U., Szallasi, Z. et al. (2004). Robustness of cellular functions. *Cell* 118: 675–685.

Stelzl, U., Worm, U., Lalowski, M. et al. (2005). A human protein-protein interaction network: a resource for annotating the proteome. *Cell* 122: 957–968.

Steuer, R. and Lopez, G.Z. (2008). Global network properties. In: *Analysis of Biological Networks* (ed. B.H. Junker and F. Schreiber), 31–63. Hoboken, New Jersey: Wiley. ISBN: 978-0-470-04144-4.

Tay, A.P., Pang, C.N.I., Winter, D.L., and Wilkins, M.R. (2017). PTMOracle: a cytoscape app for covisualizing and coanalyzing post-translational modifications in protein interaction networks. *J. Proteome Res.* 16: 1988–2003.

Tay, A.P., Liang, A., Wilkins, M.R., and Pang, C.N.I. (2019). Visualizing post-translational modifications in protein interaction networks using PTMOracle. *Curr. Protoc. Bioinformatics* 66: e71.

Venkatesan, K., Rual, J.F., Vazquez, A. et al. (2009). An empirical framework for binary interactome mapping. *Nat. Methods* 6: 83–90.

Verhaert, D., Richards, K., Rafael-Fortney, J.A., and Raman, S.V. (2011). Cardiac involvement in patients with muscular dystrophies: magnetic resonance imaging phenotype and genotypic considerations. *Circ.: Cardiovasc. Imaging* 4: 67–76.

Vidal, M. (2001). A biological atlas of functional maps. *Cell* 104: 333–339.

Vidal, M., Cusick, M.E., and Barabási, A.L. (2011). Interactome networks and human disease. *Cell* 144: 986–998.

Wang, R.S. and Loscalzo, J. (2018). Network-based disease module discovery by a novel seed connector algorithm with pathobiological implications. *J. Mol. Biol.* 430: 2939–2950.

Wang, S., Osgood, A.O., and Chatterjee, A. (2022). Uncovering post-translational modification-associated protein-protein interactions. *Curr. Opin. Struct. Biol.* 74: 102352.

Wang, R.S., Maron, B.A., and Loscalzo, J. (2023). Multiomics network medicine approaches to precision medicine and therapeutics in cardiovascular diseases. *Arterioscler., Thromb., Vasc. Biol.* 43: 493–503.

Wanjare, M. and Huang, N.F. (2017). Regulation of the microenvironment for cardiac tissue engineering. *Regen. Med.* 12: 187–201.

Warrick, J.W., Murphy, W.L., and Beebe, D.J. (2008). Screening the cellular microenvironment: a role for microfluidics. *IEEE Rev. Biomed. Eng.* 1: 75–93.

Watts, D.J. and Strogatz, S.H. (1998). Collective dynamics of 'small-world' networks. *Nature* 393: 440–442.

Welch, G.N. and Loscalzo, J. (1998). Homocysteine and atherothrombosis. *N. Engl. J. Med.* 338: 1042–1050.

Wiśniewski, J.R., Zougman, A., Nagaraj, N., and Mann, M. (2009). Universal sample preparation method for proteome analysis. *Nat. Methods* 6: 359–362.

Wu, Y., Wang, H., Li, Z. et al. (2021). Subtypes identification on heart failure with preserved ejection fraction via network enhancement fusion using multi-omics data. *Comput. Struct. Biotechnol. J.* 19: 1567–1578.

Yan, K., Wang, K., and Li, P. (2019). The role of post-translational modifications in cardiac hypertrophy. *J. Cell. Mol. Med.* 23: 3795–3807.

Yildirim, M.A., Goh, K.I., Cusick, M.E. et al. (2007). Drug-target network. *Nat. Biotechnol.* 25: 1119–1126.

Zhong, Q., Simonis, N., Li, Q.R. et al. (2009). Edgetic perturbation models of human inherited disorders. *Mol. Syst. Biol.* 5: 321.

Building directly on the principles discussed in the above book chapter, the work presented herein applies tools from network medicine to analyze unbiased, primary proteomics data generated from hearts of male L-2-hydroxyglutarate dehydrogenase knock-out (*L2hgdh*$^{-/-}$) and wild-type (*L2hgdh*$^{+/+}$) mice exposed to *ex vivo* ischemia. Rather than interpreting differentially expressed proteins in isolation, we embed these data within PPI networks to identify proteins whose network context suggests biological relevance to *L2hgdh* deficiency during ischemia. Using this holistic approach, we identify the major vault protein (MVP), the principal structural component of vault ribonucleoprotein particles[2-4], as a differentially regulated node associated with *L2hgdh* deficiency in ischemic hearts. As a proof of concept, this network-derived hypothesis is subsequently validated in cardiac microvascular endothelial cells, illustrating how network medicine can be used not only to contextualize proteomics datasets, but also to uncover previously unrecognized molecular links that merit targeted experimental validation.

4.2 Methods and materials

Except where otherwise specified below, the Materials and Methods for the present chapter are identical to those described in Sections 2.2.1 (Chemicals and reagents), 2.2.6 (LC–MS-based proteomics, with the exception of data analysis, which was performed as described in Section 4.2.2), 2.2.8 (Immunoblotting, with the following antibodies at 1:1000 (v/v) dilutions: MVP, cat no. ab273093, Abcam; PARP4, cat. no. ab133745, Abcam; TEP1, cat. no. NBP1-77285, Novus Biologicals; α-tubulin, cat. no. 9099S, Cell Signaling Technology), and 2.2.13 (2.2.13.1 Animal housing ethics compliance and 2.2.13.3 Langendorff perfusion).

4.2.1 Cell culture and treatments

Primary human cardiac microvascular endothelial cells (MVECs, cat. no. CC-7030, Lonza) were cultured in endothelial basal media (cat. no. CC-3156, Lonza) with supplements (cat. no. CC-4147, Lonza). For hypoxic experiments, MVECs were exposed to 0.5% (v/v) O_2 for 3–24 h using a modular hypoxia chamber.

4.2.2 Proteomics data analysis

Proteomics data were analyzed as previously described[5]. Briefly, LC-MS/MS datasets were median-normalized to common-channel tandem mass tag (TMT) reporter ion intensities and subsequently $\log_2$-transformed. Protein-level quantification across replicate experiments was obtained using a weighted median approach, with weights assigned according to the number of peptide spectral matches contributing to each protein measurement, as implemented in R. Only proteins identified by a minimum of two unique peptides were considered for downstream analysis. Proteins with fewer than 50% missing quantitative values were retained for statistical testing. Pairwise comparisons were performed using Student's t-tests, as implemented in Perseus[6]. Proteins were considered significantly altered based on a threshold of $p < 0.05$ (Student's t-tests, reflecting biological variance) in combination with an absolute *z*-score ≥ 1.0, corresponding to ranked $\log_2$ fold-change variability. In contrast to the fold-change threshold (> ±1.5-fold change) applied in Section 2.3.5, protein-level significance in this analysis was alternatively defined using an absolute *z*-score ≥ 1.0. This approach was adopted from Li *et al.* to capture more subtle but coordinated changes in protein abundance that may be biologically meaningful yet fall below arbitrary fold-change cutoffs[5]. Unlike absolute fold-change thresholds, which impose a fixed effect-size criterion independent of data structure, *z*-score–based filtering accounts for the underlying distribution of protein-level variation across the dataset, thereby identifying proteins that deviate meaningfully from the global behavior of the proteome. This distinction is particularly important for network-based analyses, which rely on sufficient node density to resolve higher-order connectivity and modular structure[1]. Application of stringent fold-change cutoffs alone resulted in sparse networks that were insufficient for robust interactome reconstruction, whereas *z*-score–based filtering enabled inclusion of proteins exhibiting modest but statistically coherent changes required for downstream network medicine analyses. The proteomics dataset is provided in **Supplementary Data S4.1**.

4.3 Results

4.3.1 Construction and validation of an ischemia network module

The proteomic dataset analyzed in this chapter was generated by TMTpro-based quantitative MS of whole-heart lysates from male *L2hgdh*$^{-/-}$ and *L2hgdh*$^{+/+}$ mice subjected *ex vivo* to fatty acid-

deprived baseline perfusion or low-flow ischemia (LFI) using the Langendorff protocol described in Section 2.2.13.3 (samples: wild-type baseline, n = 5; knock-out baseline, n = 5; wild-type LFI, n = 4; knock-out LFI, n = 5; spanning two TMTpro experiments). After upstream MS-pipeline filtering (≥2 unique peptides; <50% missing-value cut-off), 3,983 proteins were retained for downstream analysis. Principal component analysis (PCA) of the full dataset is provided as a quality-control panel in **Supplementary Data S4.1**. Differentially regulated proteins were then defined using the z-score–based filtering criterion described in Section 4.2.2 for input into the network analyses below.

We first sought to construct a PPI network derived from proteins differentially expressed during ischemia, restricting the analysis to wild-type mice to exclude genotype-dependent effects. Differentially expressed proteins were mapped onto a reference human interactome (formatted as a list of edges, *i.e.*, protein pairs whose physical interaction has been validated experimentally, see Section 16.2.7 of the book chapter above) by retaining only the edges in the edge list for which both interacting partner proteins were differentially expressed in the proteomics dataset. This filtering strategy was chosen over inclusion of all edges containing at least one differentially expressed protein because the high connectivity of the human interactome otherwise yields an excessively dense network comprising hundreds of nodes and thousands of edges. Such networks are likely to introduce substantial biological redundancy, as differential regulation of a single protein arguably does not justify inclusion of all its direct interaction partners. The resulting network, hereafter referred to as the *ischemia module*, is depicted with nodes representing proteins and edges representing physical interactions, with upregulated proteins shown in red and downregulated proteins shown in green (**Fig. 4.1**).

Given that a less stringent yet biologically relevant statistical criterion based on *z*-scores was used to define differential protein regulation (see Section 4.2.1), we sought to independently assess whether the ischemia module derived from experimentally identified differentially expressed proteins reflects biologically meaningful processes. To this end, we constructed an independent myocardial infarction (MI) reference module by compiling genes implicated in human MI from multiple disease-curation resources, including Open Targets[7], Phenopedia[8], and DisGeNET[9]. These genes were not restricted to cardiac tissue or circulating compartments, as spatial or tissue-specific annotations are not consistently available across these databases. We then quantified the

degree of overlap between the experimentally derived ischemia module and the literature-curated MI module, under the premise that significant concordance would support the biological relevance of the ischemia module. Indeed, a statistically significant overlap between the two gene sets was observed (**Fig. 4.2**), as assessed by a hypergeometric test implemented in the Nematode Bioinformatics Analysis Tools database[10].

4.3.2 Construction of a L2HGDH network module with enhanced connectivity

We next constructed an analogous PPI network to capture proteins differentially regulated by *L2hgdh* deficiency under ischemic conditions. Using the same network-construction strategy applied to the ischemia module (**Fig. 4.1**), differentially expressed proteins were mapped onto the reference human interactome, which was filtered to retain only edges for which both interacting partner proteins were differentially expressed in response to *L2hgdh* deficiency during ischemia. This approach was used to limit network complexity and avoid inclusion of indirect or redundant interactions arising from the high baseline connectivity of the interactome. The resulting network, hereafter referred to as the "L2HGDH module*"* (**Fig. 4.3**), represents protein interactions specifically associated with L2HGDH deficiency in the ischemic context. Because the L2HGDH module contained multiple disconnected components composed of small protein pairs or isolated network motifs (see Section 16.5.1 of the book chapter above), we sought to enhance network connectivity using the Seed Connector Algorithm (SCA[11], see Section 16.7 of the book chapter above). The SCA operates by iteratively identifying intermediate "connector" proteins from the reference interactome that optimally link initially disconnected seed nodes, while minimizing the number of added nodes and preserving network specificity. In doing so, the algorithm increases internal connectivity without indiscriminately expanding the network (see **Figure 16.6** in Section 16.7 of the book chapter above). Application of the SCA resulted in a more cohesive interaction module (**Fig. 4.4**), in which the original seed proteins (red and green nodes) were connected through a limited set of connector proteins (yellow nodes), yielding a less sparse and more interpretable network structure.

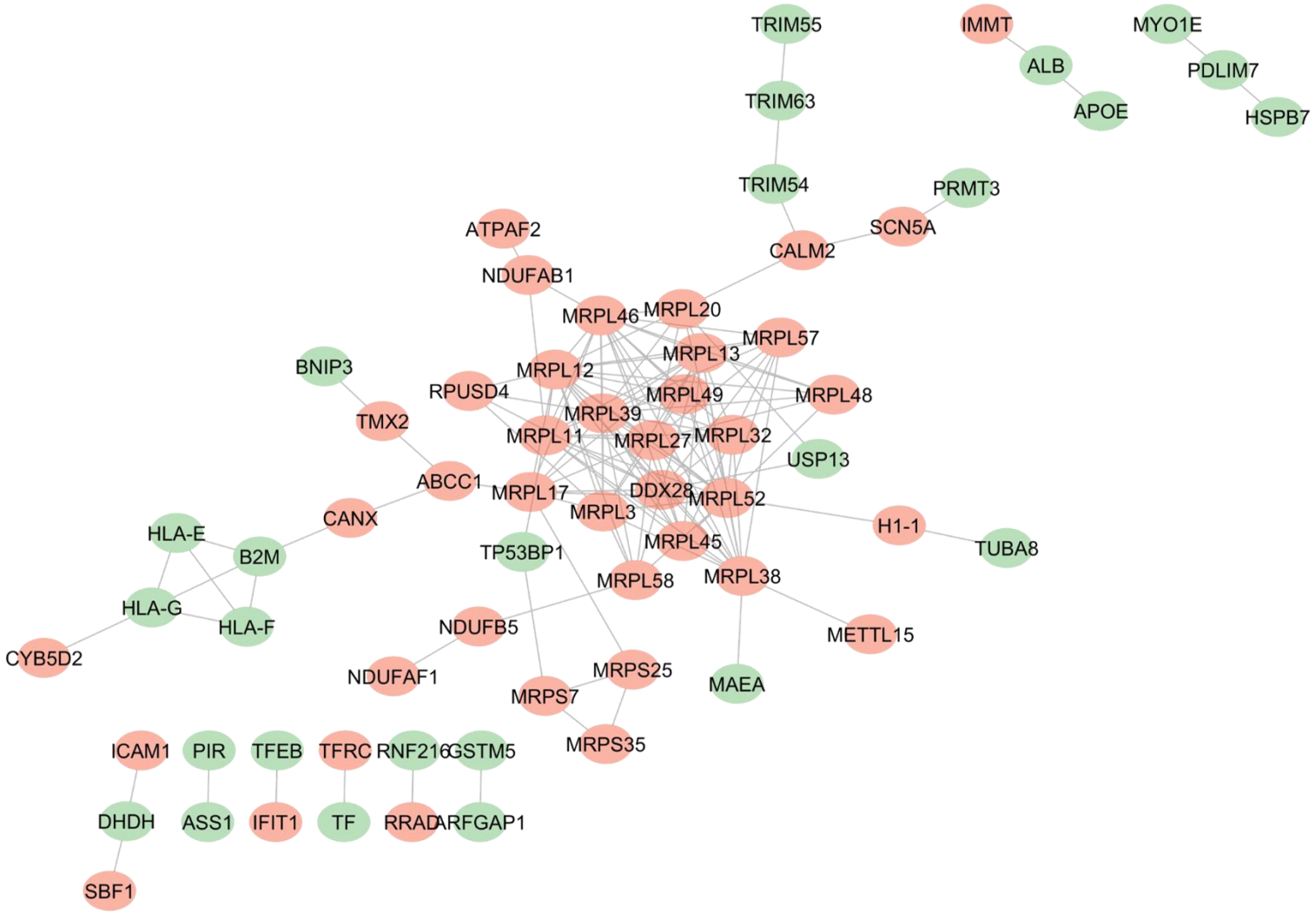

Figure 4.1. Protein–protein interaction (PPI) network of proteins differentially expressed by myocardial ischemia (ischemia module). Differentially expressed proteins, defined as described in the main text (see Section 4.2.2), were mapped onto a reference human PPI interactome (see Section 4.3.1). The reference human interactome was filtered to retain only edges for which both interacting partner proteins were differentially expressed. Nodes represent proteins, and edges indicate documented PPIs. Proteins upregulated in ischemia are shown in red, whereas downregulated proteins are shown in green. The network was visualized using Cytoscape v3.10.1.

Importantly, these connector proteins may highlight previously unrecognized components of the *L2hgdh*-deficiency–associated network, including proteins that were not detected in the proteomic dataset due to low abundance, technical limitations, or context-dependent expression, thereby providing hypotheses for additional nodes potentially involved in L2HG-mediated regulation. For example, one connector protein identified by the SCA was *N*-acylethanolamine-hydrolyzing acid amidase (NAAA), an enzyme involved in the hydrolysis of fatty acyl ethanolamides, including palmitoylethanolamide[12]. Given that fatty acyl ethanolamides are structurally and metabolically linked to ethanolamine-containing lipid pools, the emergence of NAAA within the L2HGDH module is notable considering our previous findings that L2HG perturbs PEtn and PE metabolism (see Chapter 3). This interpretation remains speculative and will require targeted biochemical and functional studies to determine whether NAAA activity or regulation is altered in the context of L2HG accumulation.

4.3.3 MVP emerges as a convergent network node at the intersection of ischemia, hypoxia, and *L2hgdh* deficiency

We next leveraged the constructed interaction networks to identify potential nodal proteins associated with *L2hgdh* deficiency in myocardial ischemia. Specifically, we assessed the network overlap between the ischemia module (**Fig. 4.5A**), the L2HGDH module (**Fig. 4.5B**), and the set of direct protein neighbors of hypoxia inducible factor 1-α (HIF-1α, denoted in the modules as HIF1A) and HIF1A inhibitor (HIF1AN), obtained from the reference human interactome, given the well-established roles of these factors in hypoxia and ischemic signaling[13-15] (**Fig. 4.5C**). Notably, only a single protein, major vault protein (MVP), was common to all three networks (**Fig. 4.5D)**. MVP was significantly upregulated by *L2hgdh* deficiency in ischemia (**Fig. 4.3**). On the basis of this convergent network-level association, we selected MVP for further investigation, first through additional network-based analyses and subsequently through targeted experimental validation.

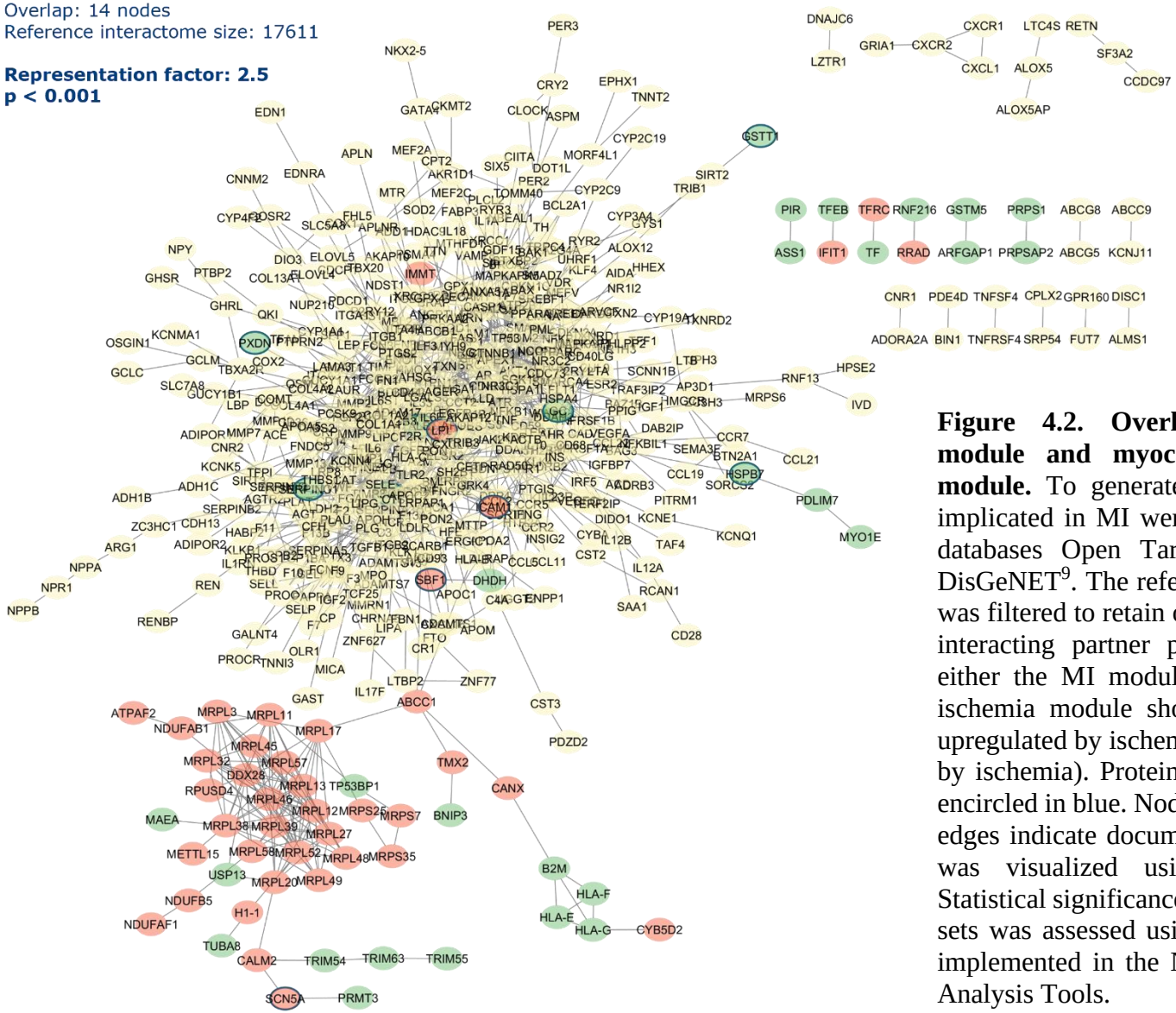

Figure 4.2. Overlap between ischemia module and myocardial infarction (MI) module. To generate the MI module, genes implicated in MI were compiled from disease databases Open Targets[7], Phenopedia[8], and DisGeNET[9]. The reference human interactome was filtered to retain only edges for which both interacting partner proteins were present in either the MI module (yellow nodes) or the ischemia module shown in **Figure 4.1** (red, upregulated by ischemia; green, downregulated by ischemia). Proteins present in modules are encircled in blue. Nodes represent proteins, and edges indicate documented PPIs. The network was visualized using Cytoscape v3.10.1. Statistical significance of overlap between gene sets was assessed using a hypergeometric test implemented in the Nematode Bioinformatics Analysis Tools.

To further strengthen the inference that MVP represents a biologically relevant node linking *L2hgdh* deficiency and myocardial ischemia, we assessed the overlap between the direct protein interaction neighborhood of MVP and the ischemia as well as L2HGDH modules. Direct MVP neighbors were extracted from the reference human interactome. In both cases, a statistically significant overlap was observed, indicating that proteins interacting with MVP are non-randomly embedded within networks associated with both *L2hgdh* deficiency (**Fig. 4.6**) and ischemic injury (**Fig. 4.7**).

To experimentally validate the network-based prediction implicating MVP in *L2hgdh* deficiency during myocardial ischemia, we assessed MVP protein abundance in cardiac tissue by immunoblotting. Consistent with the proteomics and network analyses, MVP protein abundance was increased in ischemic *L2hgdh*-deficient hearts when compared to ischemic controls, thereby providing orthogonal validation of this finding (**Fig. 4.8A–B**).

Notably, inspection of the L2HGDH module (**Fig. 4.3** and **4.4**) revealed that two direct MVP interactors, protein mono-ADP-ribosyltransferase (PARP4) and nuclear cap-binding protein subunit 1 (NCBP1), were also downregulated under conditions of *L2hgdh* deficiency in ischemia. This observation prompted a targeted literature review to assess whether these proteins are functionally linked. Indeed, MVP is the core structural component of vault nanoparticles, large and highly conserved ribonucleoprotein assemblies originally discovered and characterized through the seminal work of Leonard Rome and colleagues[2-4]. Vault particles are among the largest known ribonucleoprotein complexes in eukaryotic cells and exhibit a distinctive barrel-shaped architecture. They are ubiquitously expressed across mammalian tissues[16], yet their precise physiological roles remain incompletely defined[17], contributing to their long-standing characterization as enigmatic cellular structures. PARP4 and telomerase protein component 1 (TEP1) are established constituents of the vault complex, supporting the biological coherence of the network-derived associations.

To assess whether regulation of vault components could be modeled *in vitro*, we next examined microvascular endothelial cells (MVECs) exposed to hypoxia at 0.5% (v/v) O_2 for 3–24 h. Immunoblots and densitometric quantification revealed that all three major vault components, MVP, PARP4, and TEP1, were downregulated following hypoxic exposure at both early (3 h) and

later (24 h) time points (**Fig. 4.8C–F**). The absence, or reduced magnitude, of changes at 6 h suggests a temporal signature to hypoxia-mediated regulation of vault nanoparticles (**Fig. 4.8C–F**). Nevertheless, these findings suggest that vault-associated proteins are responsive to hypoxic stress in MVECs and are regulated in a coordinated manner.

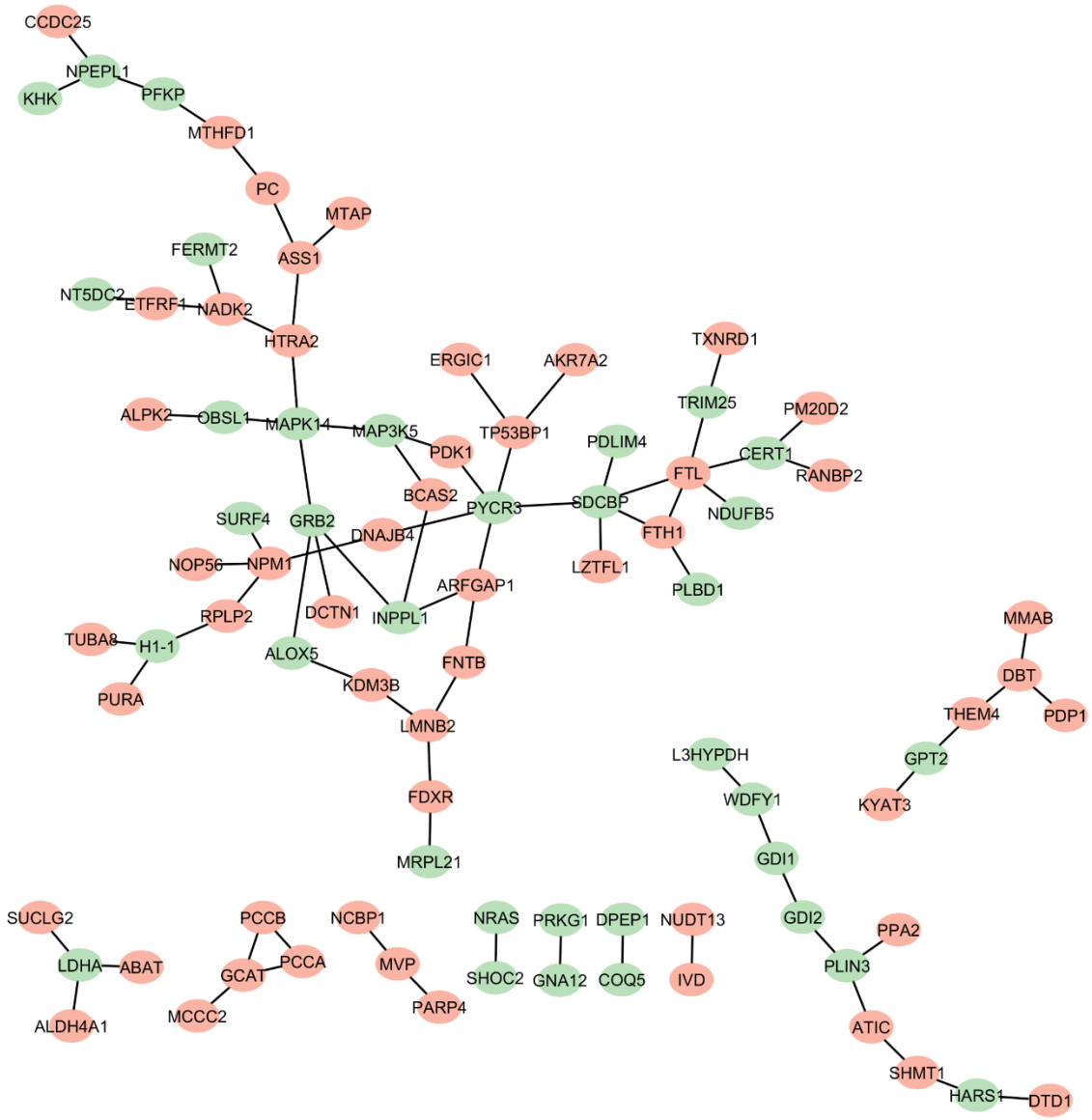

Figure 4.3. Protein–protein interaction (PPI) network of proteins differentially expressed by *L2hgdh* deficiency during myocardial ischemia (L2HGDH module). Differentially expressed proteins, defined as described in the main text (see Section 4.2.2), were mapped onto a reference human PPI interactome (see Section 4.3.1). The reference human interactome was filtered to retain only edges for which both interacting partner proteins were differentially expressed. Nodes represent proteins, and edges indicate documented PPIs. Proteins upregulated in *L2hgdh*$^{-/-}$ hearts are shown in red, whereas downregulated proteins are shown in green. The network was visualized using Cytoscape v3.10.1.

4.4 Discussion

The present chapter applies a network medicine framework to unbiased cardiac proteomic data to interrogate how perturbation of *L2hgdh* intersects with ischemia-associated proteome remodeling. Rather than prioritizing proteins solely on the magnitude of differential expression, we embedded quantitative proteomic changes within PPI networks or modules to identify nodes whose topological position and contextual connectivity suggest potential biological relevance. Using this systems-level approach, we identify MVP as a convergent node linking *L2hgdh* deficiency, ischemic stress, and hypoxia-associated signaling. These findings provide proof-of-concept that network-based analysis can reveal molecular associations that would likely remain obscured by conventional reductionist approaches.

A central motivation for applying network medicine in this chapter was the recognition that many biologically meaningful phenotypic shifts are often nuanced[18], and that biological significance need not manifest as large fold changes in individual proteins[19,20]. By incorporating *z*-score–based filtering rather than relying exclusively on arbitrary fold-change thresholds, we preserved sufficient node density to resolve higher-order network structure while still restricting analysis to statistically coherent protein changes.

The biological validity of this approach is supported by the significant overlap observed between the experimentally derived ischemia module and an independently curated MI module. This overlap provides an important external benchmark, demonstrating that the ischemia module captures disease-relevant biology despite the relatively permissive statistical filtering required for network reconstruction. Importantly, this validation step addresses a common critique of network-based analyses – namely, that network structure may reflect database-specific connectivity rather than underlying biology – by showing that the experimentally derived module converges with prior disease knowledge.

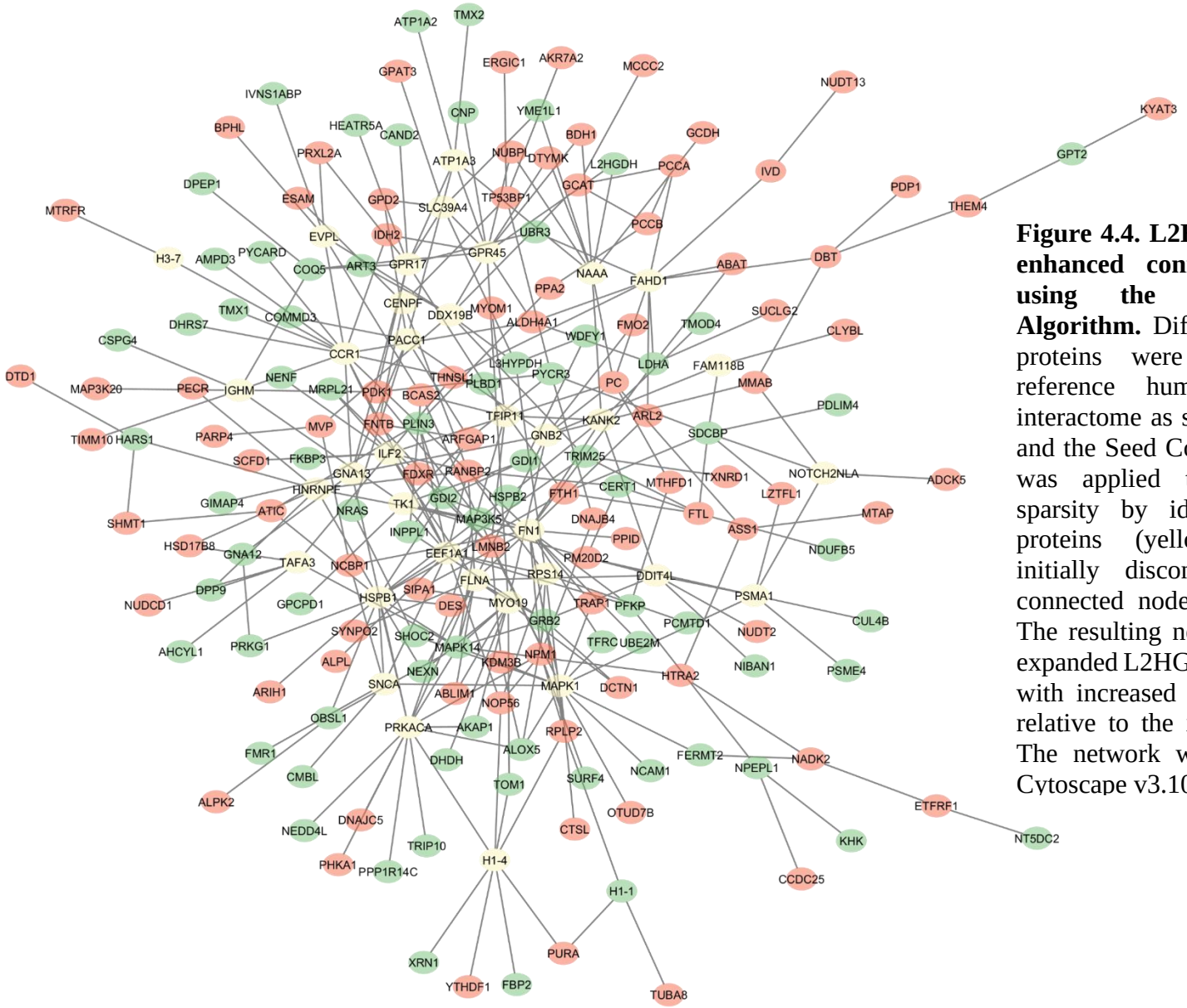

Figure 4.4. L2HGDH module with enhanced connectivity identified using the Seed Connector Algorithm. Differentially expressed proteins were mapped onto a reference human protein–protein interactome as shown in **Figure 4.3**, and the Seed Connector Algorithm[11] was applied to reduce network sparsity by identifying additional proteins (yellow) that connect initially disconnected or weakly connected nodes (see Section 4.1). The resulting network represents an expanded L2HGDH-centered module with increased internal connectivity relative to the initial seed network. The network was visualized using Cytoscape v3.10.1.

Construction of a network module specific to *L2hgdh* deficiency under ischemia revealed relatively fragmented topology, consisting of multiple disconnected components. This observation likely reflects both biological and technical factors. Biologically, L2HG accumulation may perturb multiple partially independent processes rather than inducing a single dominant pathway response. Technically, incomplete proteome coverage and context-dependent protein expression limit the detection of all relevant network nodes. Application of the SCA[11] improved this fragmentation by identifying a minimal set of connector proteins that increased internal connectivity without indiscriminately expanding the network. These connector proteins were not selected based on differential expression, but rather on their ability to link existing seed nodes within the interactome. As such, they represent network-predicted candidates whose relevance emerges from topology rather than abundance. The appearance of NAAA as a connector node is particularly intriguing in light of findings from Chapter 3 implicating L2HG in perturbations of ethanolamine-containing lipid metabolism. While speculative, this observation illustrates how network expansion can generate mechanistically testable hypotheses that extend beyond the immediate proteomic dataset.

MVP emerged as the only node common to three independently defined networks: the ischemia module, the L2HGDH module, and the interaction neighborhoods of hypoxia-responsive regulators HIF1A and HIF1AN. The appearance of MVP at the intersection of these networks suggests a specific embedding within biological programs engaged during metabolic stress and ischemic injury. Further support for MVP's relevance is provided by the significant overlap between its direct interaction neighborhood and both ischemia- and L2HGDH-associated modules, indicating that MVP does not merely appear as an isolated shared node but is embedded within a broader subnetwork that is non-randomly associated with both perturbations. In network medicine terms, MVP occupies a position of network proximity to disease-relevant modules, a property that has been associated with functional relevance in multiple disease contexts (see Section 16.10.1 of the book chapter above). Importantly, our findings are consistent with the work of Iwashita *et al.*[21] demonstrating that *MVP* silencing using RNA interference results in elevated HIF-1α protein accumulation under both hypoxic conditions and treatment with hypoxia-mimicking agents in adenocarcinoma cells. In the same study, the authors showed that this effect occurs independently of changes in *HIF1A* transcript abundance but rather is linked to reduced ubiquitination and proteasomal turnover of HIF-1α.

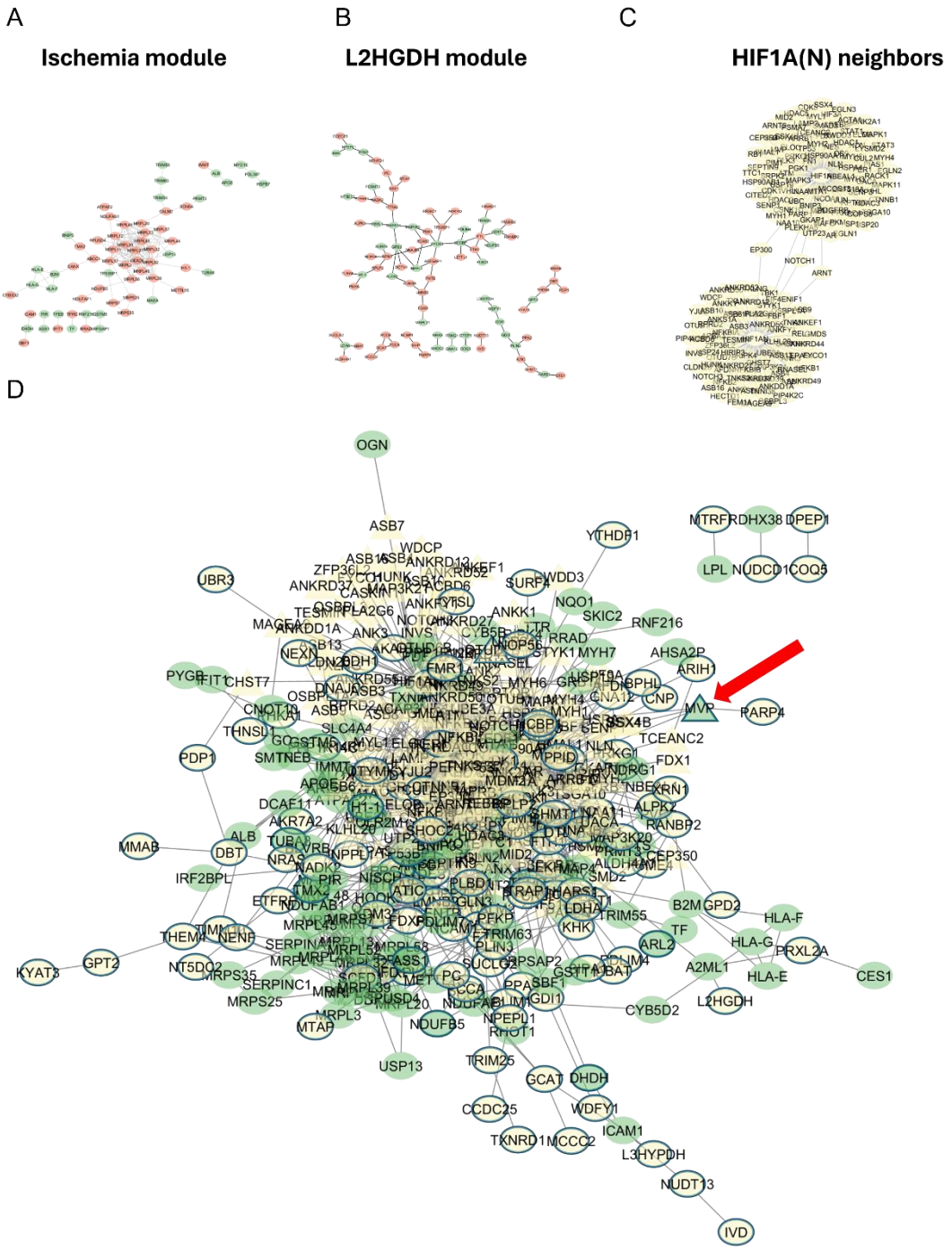

Figure 4.5. Integrated network representation of ischemia-, L2HGDH-, and HIF1A/HIF1AN-associated modules. Protein–protein interaction (PPI) networks corresponding to the ischemia-associated module (**A**), the L2HGDH-centered module (**B**), and direct neighbors of HIF1A and HIF1AN (**C**) were overlaid to generate an integrated network. Nodes shown in green represent proteins belonging to the ischemia module, nodes outlined in blue indicate proteins within the L2HGDH module, and triangular nodes denote direct neighbors of HIF1A or HIF1AN. Yellow nodes represent proteins unique to a single network. Edges indicate documented PPIs. The only node shared across all three networks was major vault protein (MVP, indicated by the red arrow). The network was visualized using Cytoscape v3.10.1.

Not less important, MVP was upregulated in ischemic *L2hgdh*-deficient hearts, and this regulation was independently validated at the protein level by immunoblotting. This orthogonal validation is critical, as it demonstrates that the network-derived association reflects a true biological signal rather than an artifact of computational analysis or statistical filtering.

Inspection of the L2HGDH module revealed that two established MVP interactors, PARP4 and NCBP1, were also differentially regulated in *L2hgdh*-deficient ischemic hearts. This observation prompted a focused literature review, which revealed that MVP, PARP4, and TEP1 are core constituents of vault nanoparticles[2-4]. The identification of multiple vault components (MVP and PARP4) within the same network module provides important biological coherence to the network-derived findings. Vault particles are among the largest ribonucleoprotein complexes in eukaryotic cells and are assembled in a highly stoichiometric manner, suggesting regulated biogenesis rather than incidental aggregation[2-4]. Despite extensive structural characterization, the physiological functions of vaults remain incompletely defined, and they have long been described as enigmatic cellular structures[17]. Proposed roles include drug resistance[22], intracellular transport[23], radiation response[24], and formation of nuclear core complexes[25], but no unifying function has emerged. More recently, MVP and vaults have been implicated in cardiovascular disease, including atherosclerotic plaque destabilization[26] and vascular remodeling[27].

Although the present data do not establish a direct mechanistic link between *L2hgdh* deficiency and vault abundance and/or function, recent structural insights suggest a plausible point of convergence. Vaults are now recognized as metabolite-responsive assemblies, with MVP forming a scaffold that binds NAD^+ and recruits regulatory components such as PARP4, thereby positioning the vault to sense and integrate changes in cellular metabolic state[28]. In the context of *L2hgdh* deficiency and ischemia, where redox balance and NAD^+ homeostasis are perturbed (see Section 1.3), altered metabolite availability could influence vault assembly or cargo selection rather than acting through changes in transcription. Given prior evidence that vaults associate with HIF-1α and components of its degradation machinery[21], such remodeling could indirectly modulate hypoxia signaling by affecting HIF-1α stability. Under this model, increased MVP abundance in *L2hgdh*-deficient ischemic hearts reflects adaptive regulation of a stress-responsive signaling scaffold.

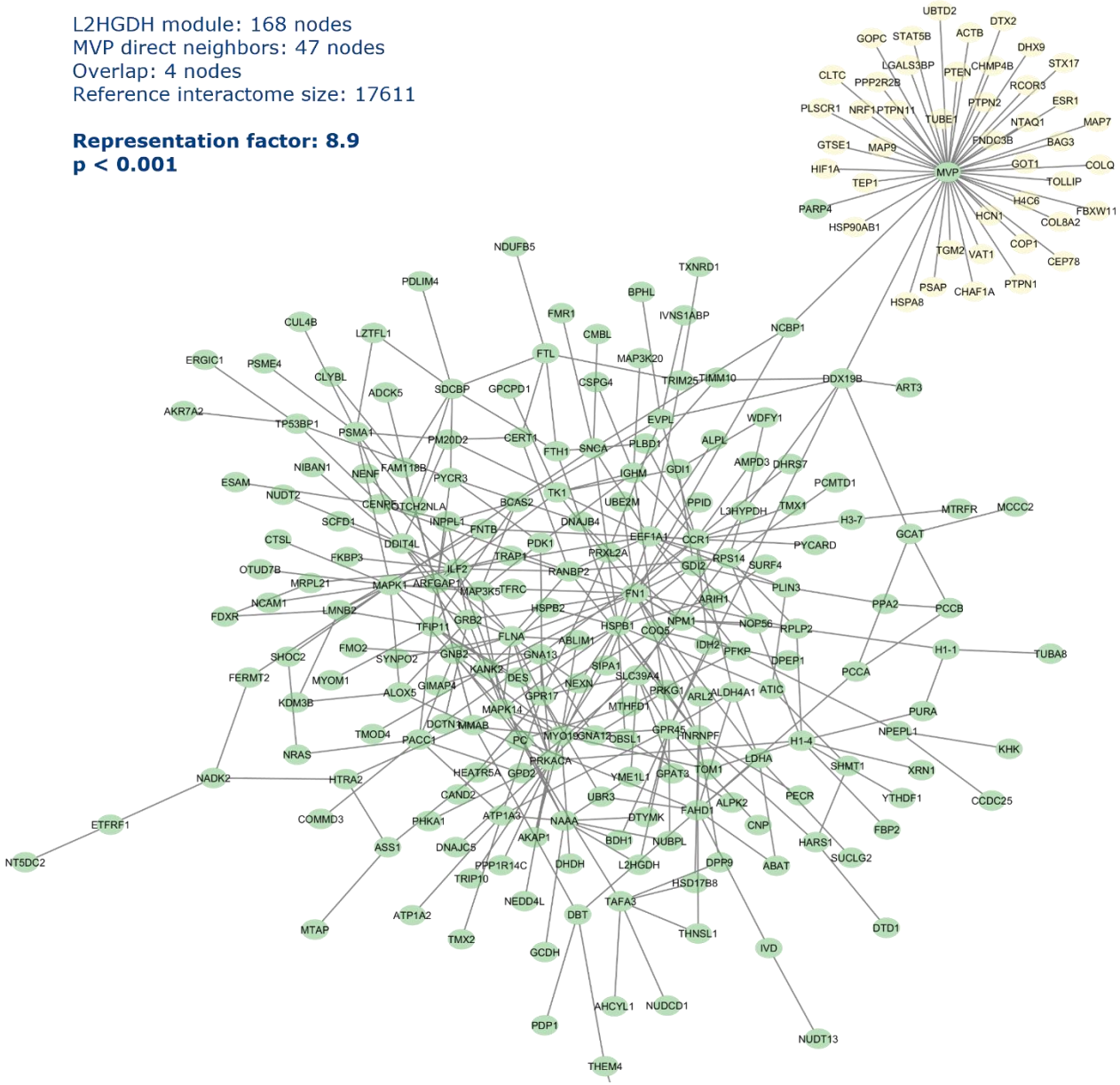

Figure 4.6. Overlap between L2HGDH module and MVP direct neighbors. The reference human interactome was filtered to retain only edges for which both interacting partner proteins were present in either the L2HGDH module (green nodes) or among direct neighbors of MVP (yellow nodes). Nodes represent proteins, and edges indicate documented PPIs. The network was visualized using Cytoscape v3.10.1. Statistical significance of overlap between gene sets was assessed using a hypergeometric test implemented in the Nematode Bioinformatics Analysis Tools.

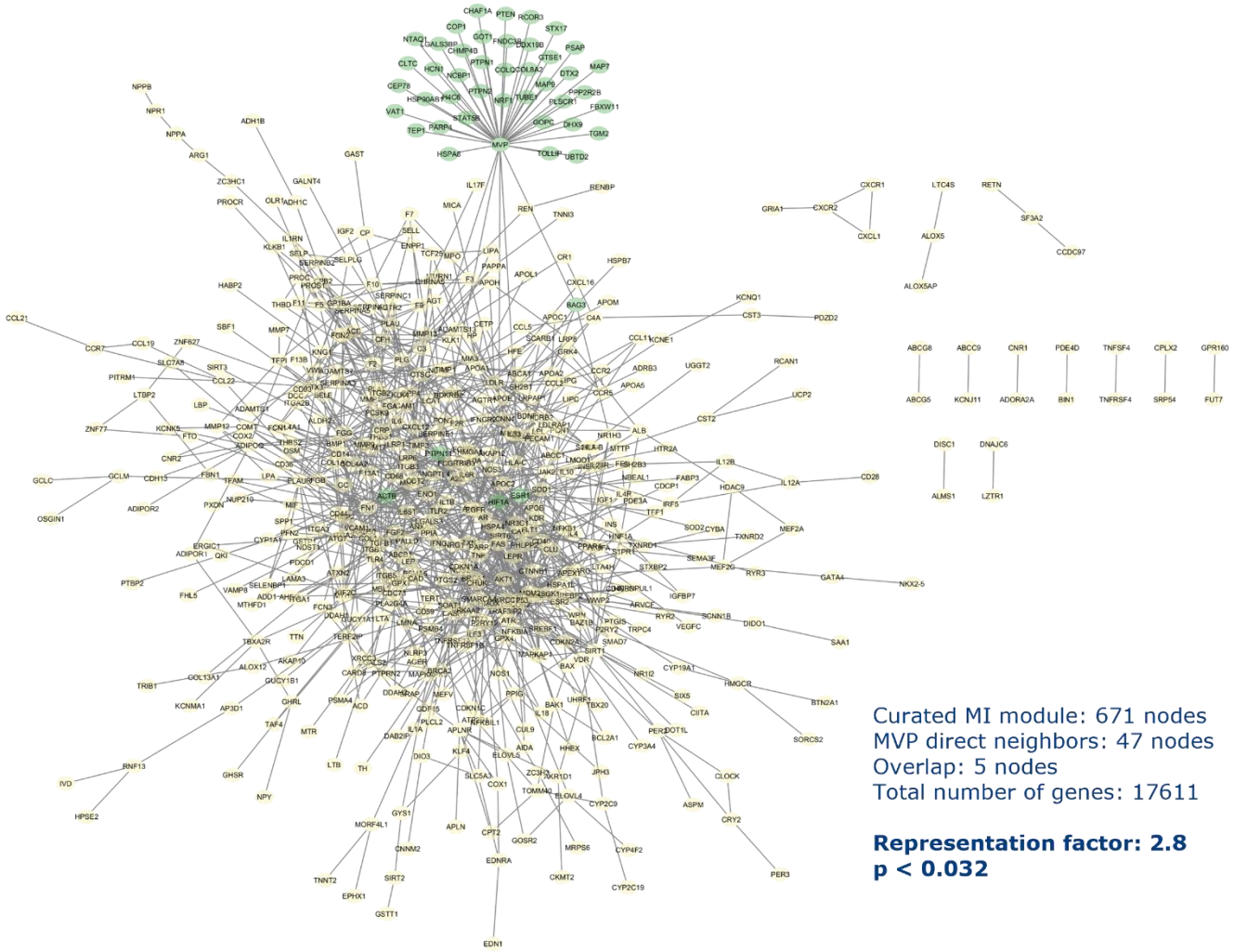

Figure 4.7. Overlap between MI module and MVP direct neighbors. The reference human interactome was filtered to retain only edges for which both interacting partner proteins were present in either the MI module (green nodes) or among direct neighbors of MVP (yellow nodes). Nodes represent proteins, and edges indicate documented PPIs. The network was visualized using Cytoscape v3.10.1. Statistical significance of overlap between gene sets was assessed using a hypergeometric test implemented in the Nematode Bioinformatics Analysis Tools.

Several limitations warrant consideration. First, the use of a reference human interactome to analyse murine proteomics data introduces species-related assumptions, although conservation of core protein interactions mitigates this concern. Furthermore, murine proteins identified as differentially expressed were mapped to their corresponding human orthologs prior to network construction, including cases in which gene or protein nomenclature differed between species. Second, network analyses are inherently constrained by the completeness and accuracy of interaction databases, which remain biased toward well-studied proteins (inspection bias, see Section 16.3.1 of book chapter above). Third, network overlap and proximity do not establish causality; they identify associations that require targeted mechanistic testing, which was beyond the scope of this thesis chapter. Establishing causality will require genetic or pharmacological manipulation of vault components in appropriate *in vivo* and *in vitro* models. In addition, MVP regulation is associated with *L2hgdh* deficiency but cannot be unequivocally attributed to L2HG accumulation *per se*, given potential L2HG-independent roles of L2HGDH (see Section 1.5.4). Also, MVP validation was restricted to cardiac microvascular endothelial cells (~30% of total heart cells); future work should test MVP induction under hypoxia in cardiomyocytes and other cardiac cell types. Additionally, MVP biochemically fractionates almost exclusively with assembled vaults in cells[29], so MVP immunoblot signal reflects vault levels; functional perturbation studies remain valuable future work. Lastly, the reference human interactome used here is not tissue-specific (see book chapter in Section 4.1), and incorporation of tissue-resolved interactomes represents a valuable refinement for future work.

4.5 Conclusion and future directions

In summary, this chapter demonstrates that network medicine can be used to extract biologically meaningful hypotheses from discovery-driven proteomics datasets, even when individual protein changes are modest. By prioritizing proteins based on network context rather than magnitude alone, we identify MVP as a convergent node linking *L2hgdh* deficiency, myocardial ischemia, and hypoxia-associated signaling. The coordinated regulation of multiple vault components further supports the biological coherence of this finding. These results position vault nanoparticles, and MVP in particular, as previously underappreciated elements of the cardiac stress response that merit further investigation. More broadly, this work illustrates how network-based frameworks can bridge the gap between high-dimensional omics data and mechanistically grounded

hypotheses, reinforcing the value of systems-level approaches in cardiovascular and metabolic disease research.

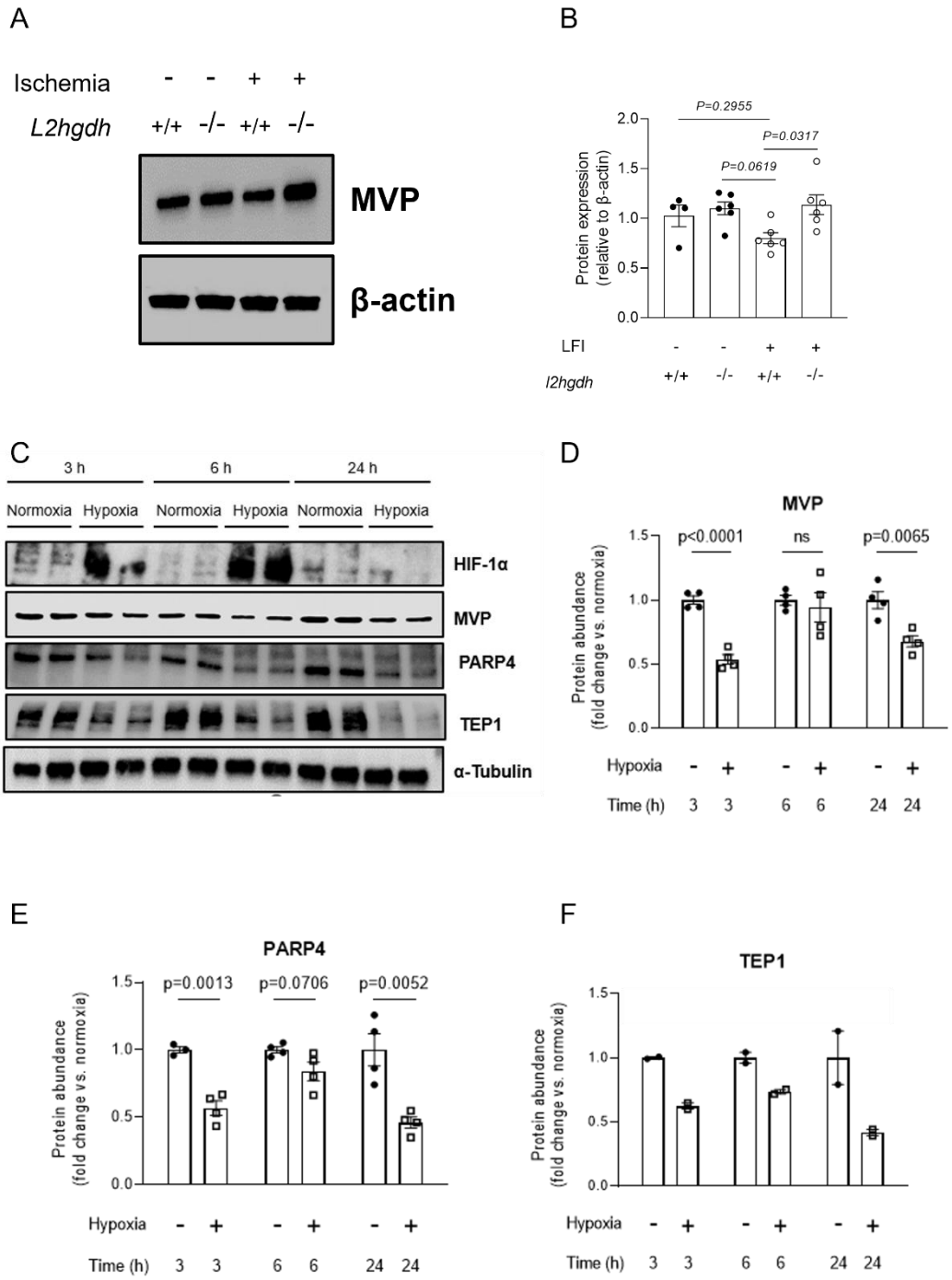

Figure 4.8. Validation of L2HG- and ischemia/hypoxia-mediated regulation of MVP. A, Representative immunoblot and **B**, densitometric quantification of MVP protein abundance in hearts from *L2hgdh*$^{-/-}$ *vs. L2hgdh*$^{+/+}$ mice subjected to baseline perfusion or low-flow ischemia. **C**, Representative immunoblots and **D**–**F**, densitometric quantification of HIF-1α, MVP, PARP4, and TEP1 in microvascular endothelial cells following exposure to hypoxia for 3, 6, or 24 h. Data are presented as mean ± SEM. Data were tested for normality by Shapiro–Wilk test. Normal data were analyzed by unpaired *t*-test. Non-normal data were analyzed by the Mann–Whitney test. *Note: No statistical analysis was performed for panel **F** due to limited sample size (n = 2).*

4.6 References

1 Vigder, N., Cordwell, S. J. & Loscalzo, J. in *Cardiovascular Proteomics Techniques* (ed C. Banfi) 449–485 (John Wiley & Sons, Inc., 2026).

2 Kedersha, N. L. & Rome, L. H. Isolation and characterization of a novel ribonucleoprotein particle: large structures contain a single species of small RNA. *Journal of Cell Biology* **103**, 699–709 (1986).

3 Frascotti, G. *et al.* The Vault Nanoparticle: A Gigantic Ribonucleoprotein Assembly Involved in Diverse Physiological and Pathological Phenomena and an Ideal Nanovector for Drug Delivery and Therapy. *Cancers* **13** (2021).

4 Kong, L. B., Siva, A. C., Rome, L. H. & Stewart, P. L. Structure of the vault, a ubiquitous celular component. *Structure* **7**, 371–379 (1999).

5 Li, D. K. *et al.* Multi-omics of a pre-clinical model of diabetic cardiomyopathy reveals increased fatty acid supply impacts mitochondrial metabolic selectivity. *Journal of Molecular and Cellular Cardiology* **164**, 92–109 (2022).

6 Tyanova, S. *et al.* The Perseus computational platform for comprehensive analysis of (prote)omics data. *Nature Methods* **13**, 731–740 (2016).

7 Buniello, A. *et al.* Open Targets Platform: facilitating therapeutic hypotheses building in drug discovery. *Nucleic Acids Research* **53**, D1467–d1475 (2025).

8 Yu, W., Clyne, M., Khoury, M. J. & Gwinn, M. Phenopedia and Genopedia: disease-centered and gene-centered views of the evolving knowledge of human genetic associations. *Bioinformatics* **26**, 145–146 (2010).

9 Piñero, J. *et al.* DisGeNET: a comprehensive platform integrating information on human disease-associated genes and variants. *Nucleic Acids Research* **45**, D833–d839 (2017).

10 Lund, J. *Statistical significance of the overlap between two groups of genes,* <http://nemates.org/MA/progs/overlap_stats.html>

11 Wang, R. S. & Loscalzo, J. Network-Based Disease Module Discovery by a Novel Seed Connector Algorithm with Pathobiological Implications. *Journal of Molecular Biology* **430**, 2939–2950 (2018).

12 Piomelli, D. *et al.* N-Acylethanolamine Acid Amidase (NAAA): Structure, Function, and Inhibition. *Journal of Medicinal Chemistry* **63**, 7475–7490 (2020).

13 Lee, J. W., Ko, J., Ju, C. & Eltzschig, H. K. Hypoxia signaling in human diseases and therapeutic targets. *Experimental & Molecular Medicine* **51**, 1–13 (2019).

14 Hewitson, K. S. *et al.* Hypoxia-inducible factor (HIF) asparagine hydroxylase is identical to factor inhibiting HIF (FIH) and is related to the cupin structural family. *Journal of Biological Chemistry* **277**, 26351–26355 (2002).

15 Lando, D. *et al.* FIH-1 is an asparaginyl hydroxylase enzyme that regulates the transcriptional activity of hypoxia-inducible factor. *Genes & Development* **16**, 1466–1471 (2002).

16 Kedersha, N. L., Miquel, M. C., Bittner, D. & Rome, L. H. Vaults. II. Ribonucleoprotein structures are highly conserved among higher and lower eukaryotes. *Journal of Cell Biology* **110**, 895–901 (1990).

17 Rome, L., Kedersha, N. & Chugani, D. Unlocking vaults: organelles in search of a function. *Trends in Cell Biology* **1**, 47–50 (1991). https://doi.org/10.1016/0962-8924(91)90088-q

18 Otto, D. J. *et al.* Comparing phenotypic manifolds with Kompot: Detecting differential abundance and gene expression at single-cell resolution. *bioRxiv* (2025). https://doi.org/10.1101/2025.06.03.657769

19 Kammers, K., Cole, R. N., Tiengwe, C. & Ruczinski, I. Detecting Significant Changes in Protein Abundance. *EuPA Open Proteomics* **7**, 11–19 (2015).

20 McCarthy, D. J. & Smyth, G. K. Testing significance relative to a fold-change threshold is a TREAT. *Bioinformatics* **25**, 765–771 (2009).

21 Iwashita, K. *et al.* Major vault protein forms complexes with hypoxia-inducible factor (HIF)-1alpha and reduces HIF-1alpha level in ACHN human renal adenocarcinoma cells. *Cancer Science* **101**, 920–926 (2010).

22 Scheffer, G. L. *et al.* The drug resistance-related protein LRP is the human major vault protein. *Nature Medicine* **1**, 578–582 (1995).

23 van Zon, A. *et al.* Vault mobility depends in part on microtubules and vaults can be recruited to the nuclear envelope. *Experimental Cell Research* **312**, 245–255 (2006).

24 Lara, P. C., Pruschy, M., Zimmermann, M. & Henríquez-Hernández, L. A. MVP and vaults: a role in the radiation response. *Radiation Oncology* **6**, 148 (2011).

25 Vollmar, F. *et al.* Assembly of nuclear pore complexes mediated by major vault protein. *Journal of Cell Science* **122**, 780–786 (2009).

26 Liu, Q. *et al.* Major Vault Protein Prevents Atherosclerotic Plaque Destabilization by Suppressing Macrophage ASK1-JNK Signaling. *Arteriosclerosis, Thrombosis, and Vascular Biology* **42**, 580–596 (2022).

27 Jiang, B. *et al.* Endothelial major vault protein alleviates vascular remodeling via promoting Parkin-mediated mitophagy. *Nature Communications* **16**, 4365 (2025).

28 Lodwick, J. E. *et al.* Structural Insights into the Roles of PARP4 and NAD^+ in the Human Vault Cage. *bioRxiv* (2024). https://doi.org/10.1101/2024.06.27.601040

29 Poderycki, M. J. *et al.* The vault exterior shell is a dynamic structure that allows incorporation of vault-associated proteins into its interior. *Biochemistry* **45**, 12184–12193 (2006).

Chapter 5

Conceptual Integration of 2HG-Mediated Phenotypic Alterations Identified in This Thesis

5.1 From unbiased discovery to targeted mechanism: integrating hypothesis-generating and hypothesis-driven approaches to study 2HG

A central challenge in experimental design lies in balancing hypothesis-driven and hypothesis-generating approaches, each of which addresses a different stage of biological understanding[1]. Hypothesis-driven experiments are powerful when the molecular players and pathways are already well defined, enabling precise testing of mechanistic predictions[2]. In contrast, hypothesis-generating, discovery-driven strategies are particularly valuable when a perturbation is known to be biologically relevant, yet its downstream molecular consequences remain incompletely characterized[2]. Rather than existing in opposition, these approaches are most effective when deployed complementarily, with unbiased discovery often informing targeted mechanistic interrogation.

The work presented in this thesis was motivated by prior evidence implicating 2HG in cardioprotection during hypoxia[3,4] and ischemic stress[5], yet relatively little was known about the metabolic and/or molecular programs engaged by exogenous 2HG exposure, particularly at the level beyond central carbon metabolism (*i.e.*, glycolysis and oxidative phosphorylation). Given this limited mechanistic framework, a purely hypothesis-driven approach would have constrained the investigation to a narrow subset of anticipated pathways. Instead, the initial phases of this work adopted an intentionally unbiased, multi-omics strategy to capture the global metabolic, lipidomic, and proteomic landscape associated with 2HG accumulation.

This discovery-driven approach proved instrumental in revealing several classes of molecular phenotypic alterations that were not readily predictable *a priori*[6]. 2HG exposure was associated with pronounced remodeling of neutral lipids, including accumulation of triglycerides (TGs) and expansion of lipid droplets (LDs), accompanied by altered expression of LD–associated proteins such as perilipin 2 (PLIN2). Furthermore, unbiased analysis of the lipidome in response to 2HG accumulation revealed broad shifts in phospholipid composition, including changes in phosphatidylethanolamine (PE) relative to phosphatidylcholine (PC), suggesting coordinated regulation of glycerolipids and glycerophospholipids by 2HG. Importantly, these observations did not themselves constitute mechanistic explanations. Rather, they served as data-driven entry points for subsequent hypothesis formulation and targeted experimentation. The identification of LD

expansion motivated focused analyses of TG synthesis and turnover using targeted flux analyses (Chapter 2); changes in PE prompted examination of biosynthetic intermediates (Chapter 3); and protein-level alterations revealed by unbiased proteomics and contextualized by network medicine tools guided investigation into important nodes altered by *L2hgdh* deficiency, leading to the discovery of a regulatory link between L2HG and vault nanoparticles (Chapter 4). In this way, the unbiased multi-omics datasets functioned as hypothesis generators that shaped the trajectory of later, more mechanistically precise studies.

Beyond enabling discovery, this integrative strategy offered key advantages in the context of 2HG biology. Because 2HG is a pleiotropic metabolite with the potential to influence multiple cellular processes simultaneously[7,8], single-pathway readouts risk providing an incomplete or misleading picture. By measuring metabolites, lipids, and proteins in parallel, this work was able to situate individual phenotypes, such as TG accumulation or PE depletion, within a broader molecular framework, reducing the likelihood of over-interpreting isolated changes. At the same time, the complexity revealed by this approach underscores an important limitation of discovery-driven studies: identifying phenotypic alterations is only the first step, and their interpretation often requires careful consideration of confounding variables. As explored in the remainder of this chapter, this challenge becomes particularly salient in the context of stereoselectivity, where differences between L2HG and D2HG may arise from intrinsic stereochemical specificity, from differences in intracellular accumulation, or from nonlinear, dynamic-range–dependent responses. Nevertheless, it is precisely the unbiased nature of the initial approach that exposed these complexities, enabling a more rigorous and nuanced discussion of mechanism.

5.2 Interpreting apparent stereoselectivity in the context of biphasic and multiphasic 2HG responses

A recurring theme in studies of 2HG biology is the tendency to examine the L and D enantiomers in isolation[9], often with the implicit assumption that phenotypic differences observed between them necessarily reflect intrinsic stereochemical specificity. While this approach has proved informative, it also risks obscuring the extent to which shared mechanisms and concentration-dependent effects contribute to observed phenotypes. This concluding section highlights this complexity and underscores the need to interpret enantiomer-specific alterations in the broader

context of intracellular 2HG abundance, dynamic range, and nonlinear cellular responses. Particularly, the following discussion argues that molecular phenotypic differences observed following treatment with OL2HG *vs.* OD2HG cannot be assumed to arise solely from the stereochemistry of liberated L2HG *vs.* D2HG, respectively, but must additionally be considered in light of potential differences in intracellular exposure over time. Accordingly, these limitations merit a zoomed-out view of the findings presented in this thesis, organizing them conceptually around the notion of stereoselectivity while explicitly acknowledging the confounding influence of metabolite accumulation and dynamic range effects.

Following 24 h of treatment, both OL2HG and OD2HG resulted in comparable accumulation of total intracellular O2HG (**Fig. 2.1A**). Although indirect, this observation suggests that uptake of the derivatized compounds and/or their initial intracellular hydrolysis may not be strongly stereoselective. One possible interpretation is that O2HG enters cells *via* non-chiral mechanisms and undergoes de-esterification through spontaneous processes or the promiscuous activity of intracellular hydrolases that do not discriminate between enantiomers, a notion that is supported by previous work[10]. However, because measurements at this time point integrate uptake, hydrolysis, metabolism, and efflux, one cannot draw definitive conclusions. Properly resolving whether these early steps are stereoselective will require short time-scale experiments using, for example, $^{13}C_5$-labeled OL2HG and OD2HG, capturing intracellular O2HG and liberated 2HG within seconds to minutes of exposure in order to minimize confounding effects of downstream metabolism.

Despite comparable O2HG accumulation, treatment with OD2HG resulted in substantially greater increases in total intracellular 2HG compared with OL2HG, with differences on the order of three- to four-fold after 24 h (**Fig. 2.1B**). This divergence has far-reaching implications for the interpretation of all downstream phenotypes described in this thesis. One explanation is differential catabolism of L2HG and D2HG back to α-ketoglutarate (αKG) by their respective dehydrogenases, potentially reflecting differences in their expression levels and/or enzymatic activities. Nevertheless, the expression of *L2HGDH* and *D2HGDH* was similar in several cell types, as evidenced by comparable transcript per million readouts in our RNA-sequencing datasets (**Supplementary Data S2.2–3**). Alternatively, differential efflux of L2HG *vs.* D2HG could contribute, a possibility that would require measurement of extracellular 2HG in the culture media

to assess. Regardless of the underlying mechanism, the unequal intracellular accumulation of total 2HG introduces a critical confounder: phenotypic differences between OL2HG and OD2HG treatments may reflect differences in intracellular concentration of liberated 2HG rather than (or in addition to) intrinsic stereoselectivity.

This distinction gives rise to the possibility that 2HG-mediated effects are nonlinear and may exhibit biphasic or multiphasic dose-response behavior. Support for this notion is further provided by our observations that a relatively lower dose (0.5 mM) of unmodified L2HG increased total TG levels in PAECs to a greater extent than higher doses (1–2 mM) (data not shown), despite inducing a smaller increase in total intracellular 2HG (**Fig. 2.4A**). This inverse relationship between phenotypic magnitude and intracellular 2HG accumulation suggests that lipid remodeling may be maximal within a restricted concentration window of 2HG and attenuated at higher levels, consistent with a biphasic or multiphasic response rather than a monotonic dose dependence. Under such a model, specific phenotypic alterations may emerge only within a defined dynamic range of intracellular 2HG and may diminish, plateau, or even reverse when concentrations exceed that range, as observed previously for other classes of molecules[11-13]. For example, increases in intracellular TGs and decreases in PEs following OL2HG treatment, but not OD2HG treatment, could reflect stereochemical specificity, but may alternatively arise because OD2HG drives total 2HG accumulation beyond the permissive range for these responses, effectively masking effects that would otherwise be shared between the enantiomers.

In contrast, some phenotypes were shared between OL2HG and OD2HG despite substantial differences in total intracellular 2HG accumulation. Notably, both enantiomers increased intracellular diacylglycerol (DAG) levels to similar extents (**Fig. 2.1E**). If this effect were strictly dependent on total 2HG concentration, one might expect divergent magnitudes between treatments. Instead, the similarity of this response raises the possibility that certain pathways are either insensitive to absolute 2HG levels beyond a threshold or may indeed reflect stereoselective engagement that is uncoupled from intracellular concentration. In contrast, OL2HG-induced accumulation of intracellular oleate was partially recapitulated by OD2HG in a cell-type-specific manner (**Fig. 2.2A** and **D**), suggesting that stereochemical effects may intersect with cellular context and metabolic state. Protein-level changes, including differential regulation of PLIN2 (**Fig. 2.3E** and **F**), opposing effects on HIF-1α stabilization in smooth muscle cells (**Fig. 2.9C** and **D**),

and stronger induction of SREBP1 by OL2HG relative to OD2HG (**Fig. 2.10G** and **H**), point toward selective engagement of regulatory networks.

Collectively, these observations underscore that discriminating true stereochemical specificity from concentration-dependent, biphasic or multiphasic effects will require dose-response paradigms in which OL2HG and OD2HG are explicitly calibrated to achieve comparable intracellular levels of total 2HG. Only under such matched conditions can phenotypic divergence be confidently ascribed solely to stereochemistry itself, rather than to nonlinear responses arising from differences in intracellular metabolite abundance. While such analyses extend beyond the scope of the present thesis, they define a central direction for future work in our laboratory. Forthcoming studies will be positioned to disentangle how stereochemistry, intracellular metabolite levels, and nonlinear pathway behavior intersect to shape the cellular consequences of 2HG accumulation in health and disease.

5.3 Future directions and outstanding questions

While the present study provides evidence that L2HG regulates lipid metabolism and promotes TG accumulation alongside PE depletion, several important questions remain unresolved and warrant further investigation. One important future direction would be the implementation of absolute lipid quantification approaches rather than reliance on relative fold-change measurements alone. Although relative quantification is highly informative for identifying altered lipid species and pathway-level remodeling, absolute quantification would provide deeper insight into the stoichiometric accumulation of TG and depletion of PE induced by L2HG, including whether the magnitude of TG accumulation could quantitatively account for the observed PE depletion, thereby providing evidence for or against direct fatty acyl recycling between these two lipid groups[14]. Such analyses may help determine whether these lipid alterations are mechanistically linked through coordinated lipid remodeling pathways or instead represent independent downstream consequences of L2HG signaling. This remains technically challenging in lipidomics not least because lipid classes such as TG and PE are not single molecular entities, but rather heterogeneous groups composed of numerous species differing in acyl-chain length and saturation[15]. Generating individual calibration curves for every lipid species is therefore impractical. One potential strategy to overcome this limitation would be to assume relatively similar ionization efficiencies in the MS

source across species within a given lipid class and employ a representative standard for that class (*e.g.*, a representative TG species) to generate a single calibration curve. The summed signal intensities of all detected species within the lipid class could then be converted into an estimated absolute abundance of the total TG or PE pool. While such an approach would still involve assumptions regarding ionization behavior, it could provide a practical framework for estimating global lipid pool sizes and strengthen interpretation of the biological significance of the observed lipid remodeling.

An additional limitation of the current LC–MS/MS workflow used in this study is its inability to directly determine the positional isomerism of double bonds within lipid acyl chains. Consequently, lipid species containing identical total carbon and unsaturation compositions but differing in double-bond position could not be distinguished. Future studies employing advanced fragmentation approaches, such as oxygen attachment dissociation (OAD)[16], could enable direct structural characterization of double-bond positional isomers and provide deeper insight into whether L2HG preferentially alters specific lipid desaturation patterns or acyl-chain remodeling pathways.

Another important consideration is that many experiments in this thesis utilized OL2HG, a membrane-permeable derivative designed to facilitate intracellular delivery of L2HG. Although OL2HG is widely used experimentally[17], it is not identical to endogenous unmodified L2HG and may possess distinct biological properties arising from the octyl moiety itself (see Section 1.6.1.1). Consequently, it would be important to repeat key experiments using unmodified L2HG to confirm that the observed lipogenic and lipolytic flux alterations are attributable specifically to L2HG rather than effects unique to OL2HG treatment. Such validation would substantially strengthen the physiological relevance of the findings presented in this thesis. Conversely, if important differences between OL2HG and unmodified L2HG were observed, this could itself reveal additional mechanistic insights into how metabolite transport, membrane permeability, or lipid conjugation influence cellular metabolic responses, as shown previously for αKG[10].

A further avenue of investigation would involve more detailed characterization of the spatial compartmentalization of L2HG signaling and metabolism. Increasing evidence suggests that metabolite signaling can be highly compartment-specific, with metabolites exerting distinct effects

depending on their subcellular localization and accessibility to different protein targets[18]. Future studies could therefore employ recently developed compartment-specific biosensors capable of monitoring L2HG dynamics within individual organelles or cellular compartments[19] (see Section 1.6.2.2). Such approaches may reveal whether mitochondrial, cytosolic, nuclear, or other localized pools of L2HG exert distinct biological effects on lipid metabolism. Complementary biochemical approaches such as organelle fractionation followed by compartment-resolved lipidomics could further determine whether the TG accumulation and PE depletion observed in this thesis occur uniformly throughout the cell or preferentially within specific organelles, as discussed previously in Ref.[20]. Understanding the spatial organization of L2HG signaling may therefore provide important mechanistic insight into how this metabolite regulates lipid homeostasis.

Finally, additional work is needed to define the molecular mechanisms linking L2HG to TG accumulation and PE depletion more comprehensively. While the present study establishes a robust phenotypic association, the precise signaling pathways, regulatory nodes, and molecular targets responsible for this effect remain incompletely understood. One approach would involve systematic genetic perturbation experiments targeting candidate regulators of TG metabolism, including transcriptional regulators such as peroxisome proliferator-activated receptor gamma (PPARγ[21]) and other genes involved in lipid storage, lipogenesis, and LD biology. Assessing whether knock-down or inhibition of such factors attenuates or rescues the TG accumulation phenotype could help establish causal relationships within the pathway. More advanced MS-based approaches could also provide mechanistic insight into the direct molecular interactions of L2HG. For example, future studies could investigate both non-covalent interactions between L2HG and protein targets (*e.g.*, using limited proteolysis approaches[22,23]), as well as covalent modifications such as the recently discovered *O*-2-hydroxyglutarylation[24] (see Section 1.5.3). Taken together, such studies would contribute toward the development of a more comprehensive mechanistic framework describing how L2HG functions as a metabolic signaling molecule regulating lipid metabolism.

5.4 References

1 Biesecker, L. G. Hypothesis-generating research and predictive medicine. *Genome Research* **23**, 1051–1053 (2013).

2 Misra, D. P. *et al.* Formulating Hypotheses for Different Study Designs. *Journal of Korean Medical Science* **36**, e338 (2021).

3 Oldham, W. M., Clish, C. B., Yang, Y. & Loscalzo, J. Hypoxia-Mediated Increases in L-2-hydroxyglutarate Coordinate the Metabolic Response to Reductive Stress. *Cell Metabolism* **22**, 291–303 (2015).

4 Intlekofer, A. M. *et al.* Hypoxia Induces Production of L-2-Hydroxyglutarate. *Cell Metabolism* **22**, 304–311 (2015).

5 He, H. *et al.* L-2-Hydroxyglutarate Protects Against Cardiac Injury via Metabolic Remodeling. *Circulation Research* **131**, 562–579 (2022).

6 Luo, Y., Zhao, C. & Chen, F. Multiomics Research: Principles and Challenges in Integrated Analysis. *BioDesign Research* **6**, 0059 (2024).

7 Du, X. & Hu, H. The Roles of 2-Hydroxyglutarate. *Frontiers in Cell and Developmental Biology* **9**, 651317 (2021).

8 Hao, J. *et al.* Deciphering the multifaceted roles and clinical implications of 2-hydroxyglutarate in cancer. *Pharmacology Research* **209**, 107437 (2024).

9 Struys, E. A. 2-Hydroxyglutarate is not a metabolite; D-2-hydroxyglutarate and L-2-hydroxyglutarate are! *Proceedings of the National Academy of Sciences of the United States of America* **110**, E4939 (2013).

10 Parker, S. J. *et al.* Spontaneous hydrolysis and spurious metabolic properties of α-ketoglutarate esters. *Nature Communications* **12**, 4905 (2021).

11 Jodynis-Liebert, J. & Kujawska, M. Biphasic Dose-Response Induced by Phytochemicals: Experimental Evidence. *Journal of Clinical Medicine* **9** (2020).

12 Ramesh, V. & Krishnan, J. A unified approach to dissecting biphasic responses in cell signaling. *Elife* **13** (2023).

13 Calabrese, E. J. Biphasic dose responses in biology, toxicology and medicine: Accounting for their generalizability and quantitative features. *Environmental Pollution* **182**, 452–460 (2013).

14 Wunderling, K., Zurkovic, J., Zink, F., Kuerschner, L. & Thiele, C. Triglyceride cycling enables modification of stored fatty acids. *Nature Metabolism* **5**, 699–709 (2023).

15 Schoeny, H. *et al.* Achieving Absolute Molar Lipid Concentrations: A Phospholipidomics Cross-Validation Study. *Analytical Chemistry* **94**, 1618–1625 (2022).

16 Takeda, H. *et al.* Dual fragmentation via collision-induced and oxygen attachment dissociations using water and its radicals for C=C position-resolved lipidomics. *Communications Chemistry* **8**, 148 (2025).

17 Xu, W. *et al.* Oncometabolite 2-hydroxyglutarate is a competitive inhibitor of α-ketoglutarate-dependent dioxygenases. *Cancer Cell* **19**, 17–30 (2011).

18 Bar-Peled, L. & Kory, N. Principles and functions of metabolic compartmentalization. *Nature Metabolism* **4**, 1232–1244 (2022).

19 Kang, Z. *et al.* An Ultrasensitive Biosensor for Probing Subcellular Distribution and Mitochondrial Transport of l-2-Hydroxyglutarate. *Advanced Science* **11**, e2404119 (2024).

20 Sarmento, M. J. *et al.* The expanding organelle lipidomes: current knowledge and challenges. *Cellular and Molecular Life Sciences* **80**, 237 (2023).

21 Montaigne, D., Butruille, L. & Staels, B. PPAR control of metabolism and cardiovascular functions. *Nature Reviews Cardiology* **18**, 809–823 (2021).

22 Li, K. *et al.* A peptide-centric local stability assay enables proteome-scale identification of the protein targets and binding regions of diverse ligands. *Nature Methods* **22**, 278–282 (2025).

23 Wang, K. *et al.* Peptide-centric local stability assay (PELSA) for sensitive identification of ligand-targeting proteins and binding sites at proteome scale. *Nature Protocols* (2026).

24 Zhang, Z. *et al.* Discovery of chirally dependent protein modifications by D- and L-2-hydroxyglutarates. *Nature Chemistry* (2026).